THE BELL SYSTEM
TECHNICAL JOURNAL

The TM-1/TL-2 Short Haul Microwave Systems

By R. W. FRIIS, J. J. JANSEN, R. M. JENSEN, and
H. T. KING

This paper describes the design and discusses the performance of the TM-1 and TL-2 radio relay systems designed for short haul service in the 5925 to 6425 megacycle and the 10,700 to 11,700 megacycle common carrier bands, respectively. Used as a crossband diversity pair, they provide a highly reliable broadband message channel for up to 600 circuits and require little maintenance and relatively low power. These systems are also used to transmit television.

TABLE OF CONTENTS

I. INTRODUCTION AND BACKGROUND

Bell System short haul microwave was launched in 1958 with the completion of the development of the 11-gc TJ Microwave

1

Radio Relay System.[1] Generally well received, this all-electronic tube system suffered somewhat from an economic standpoint because of its relatively large power requirements (just under one-half kilowatt) and the expense entailed in providing standby power at remote locations. The TJ system had a radio frequency power output of at least one-half watt. Initially characterized as a 240-circuit system, its message capability has been gradually improved to its present capacity of 600 circuits with a noise performance of 35 dbrnc0 for a 250-mile ten-hop system.*

With the development of high-frequency capabilities of solid-state devices, the design of a lower cost and more economically operated system for the 11-gc band was undertaken. The new system, TL radio,[2] now referred to as TL-1, used solid-state circuitry throughout the system except for the employment of klystrons as the transmitter oscillator and the receiver beat frequency oscillator. The new transmitter-receiver required only 170 watts, which eliminated the need for an emergency 60-cycle power plant, permitting the equipment to operate directly from a 24-volt storage battery. The message capability for a ten-hop, 250-mile system was 240 circuits at 38 dbrnc0 including the multiplex. The use of solid-state devices in both the radio and power equipment permitted reduction in size hitherto not possible. The TL-1 radio system was notable, then, for its extensive use of semiconductors, low cost, simplicity and reliability.

Even as this new system was first being applied in the field, the need arose for greater circuit capacity, for improved noise performance, and for television capability. The development of the TL-2 Radio was then undertaken, followed in short succession by the companion TM-1 Radio System operating in the 6-gc common carrier band. The latter system was designed to provide, with TL-2, a crossband diversity arrangement by which further improvements in reliability might be obtained. The use of the crossband feature, involving transmission at both 6 and 11 gc, places reduced demands on the crowded 6-gc band yet provides the diversity pair with the greater freedom from rain fades which is inherent in the lower frequency band.

It should be emphasized that a change was taking place in the short haul radio field. When the earlier systems were conceived, they were intended for lightly loaded routes; but, as demands for message circuits mounted, and the existing cable network began to reach the ultimate in expansion capabilities which short haul carrier could sup-

---

* The measurement of noise is reviewed briefly in the appendix.

ply, the importance of the newer transmission medium was emphasized. Circuit cross sections were growing rapidly and new services such as data, commercial TV, and educational and industrial TV were coming to the fore. The new diversity pair was designed to provide TV capabilities and a highly reliable message transmission medium capable of handling 600 circuits with the basic transmission performance improved over the earlier systems.

II. SYSTEM OBJECTIVES

2.1 General

The general objectives for the TM-1/TL-2 radio pair are somewhat more severe than for TL-1 radio. TL-2 and TM-1 are intended to yield higher reliability, carry heavier message loads, give better noise performance, and furnish TV capability in the short haul field. Like the TL-1 radio, they are intended to provide short haul and tributary trunk facilities (*i*) in difficult geographical situations; (*ii*) where wire line facilities would prove uneconomical; (*iii*) where open wire requires replacement; (*iv*) where existing cable routes are being exhausted; and (*v*) as spurs leading from heavy route microwave systems. In addition, they can be used to provide order wire and alarm facilities for heavy route radio systems as well as to furnish facilities for television transmission in the TV broadcast network, or in industrial and educational fields.

2.2 Telephone Message Capacity

Both systems are designed to transmit up to 600 circuits of L-carrier, meeting modern noise objectives of 35 dbrnc0 over 10 hops covering a distance of approximately 250 miles.

2.3 Power Drain and Reserve

These systems employ all solid-state circuitry, except for the transmitter and receiver klystrons, and consume approximately 170 watts of power for a transmitter-receiver combination. Depending somewhat upon the battery supply arrangements, sufficient reserve is normally provided to carry the system for approximately 24 hours in the event the commercial ac power fails.

2.4 *Order Wire and Alarm*

The order wire and alarm system provided for the TL-1 system has been adapted with minor changes for use with the TL-2 and TM-1 systems.[2]

2.5 *Economics*

The objective is to provide, at low cost, a radio facility which, a short time ago, would have been considered a "heavy route" radio facility. Simplicity and compactness have been emphasized in design. Maintenance procedures and equipment have been held to a minimum consistent with the increased load requirements. Outdoor cabinets and standard shelters have been provided which may be shipped to the station site completely equipped, thus minimizing engineering and installation expense. Low-cost antennas and antenna supporting structures have also been made available for minimizing over-all station costs.

2.6 *Reliability*

The reliability of a radio system is expressed as the percentage of outage time that may be expected with respect to the total time. Reliability objectives in short haul radio have been raised steadily over the past few years due to customer demands and to the increasing dependence upon radio as the message loads on short haul systems have increased. The current reliability objective for the TM-1/TL-2 diversity pair is set at 0.02 percent for a 10-hop system.

Hazards to service which may cause outages include not only power and equipment problems, but also atmospheric phenomena. In TM-1 and TL-2, outages due to power failures are reduced by the employment of storage batteries with sufficient reserve to carry the equipment for a reasonable period. Equipment hazards are largely eliminated by full diversity operation. Outages caused by atmospheric conditions such as inversion, reflective layer phenomena and rain are combatted by means of a broad range AGC. However, because the raindrop size is an appreciable part of a wavelength at 11 gc these frequencies suffer much greater rain attenuation than the lower frequencies. For this reason the 6-gc band is measurably more reliable than the 11-gc band.

Experience has shown that the 0.02 percent reliability objective would be difficult to meet, and would involve an economic penalty with an 11-gc system, in areas subject to heavy rain incidence. The use of a 6/11-gc crossband diversity arrangement yields a highly reli-

able system with the advantage of 6 gc in connection with rain attenuation. By relying on the 11-gc band for the other half of the diversity pair, the dependence on 6 gc (and therefore, the congestion of that band) is reduced by one-half.

2.7 *Transmission Objectives*

To meet the general objectives set forth for these systems, the following transmission objectives were established.

	TM-1	TL-2
RF frequency range	5.925–6.425 gc	10.7–11.7 gc
Frequency plan	modified TH plan	modified TJ plan
Number of available RF channels	32 (split channel TH plan)	24 (TJ plan)
	12 (staggered channel TH plan)	24 (staggered channel TJ plan)
	16 (TH co-channel plan)	
Minimum transmitted power with TM-A1 amplifier	+20 dbm	+20 dbm
	+33 dbm	
Transmitter frequency stability	±0.02%	±0.05%
Minimum design receiver input	−45 dbm	
Receiver noise figure (receiver inputs of −45 dbm or lower)	11 db	
Fading margin (minimum)	30 db	
IF center frequency	70 mc	
Baseband width	10 cps-6 mc	
Pre-emphasis		
600 message circuits	9 db	
Television	7 db	
Maximum hops per alarm section	10	
System length		
message (10 hops)	250 miles	
ETV-ITV (10 hops)	250 miles	
NTSC-TV (6 hops)	150 miles	
Ambient temperature	−40°F to 120°F	

2.8 *Power Amplifier*

In order to lengthen a hop where circumstances demand, a power amplifier can be used with the TM-1 transmitter. The TM-A1 traveling wave tube power amplifier described in Section VI increases the power output from +20 dbm to +33 dbm. Coupled with a diversity switch that normally reverts to the preferred channel, the power amplifier permits the repeater spacing to be increased substantially with no appreciable degradation of system performance or reliability.

III. ENGINEERING CONSIDERATIONS

3.1 *Antennas*

Several types of antennas and antenna systems are available for the TM-1/TL-2 combination. A 6-foot parabolic antenna and a 10-foot

parabolic antenna, each handling two polarizations at 11 gc and one polarization at 6 gc are available for use as direct radiators. A periscopic system is obtained with these antennas when used with appropriate reflectors.[3] The 6-foot antenna is illustrated in Fig. 1. The dual-frequency antennas are always furnished with radomes. Two 11-gc connections (WR90) and one 6-gc connection (WR159) are required for both sizes of antennas. A horn-reflector antenna may also be used in the TM-1/TL-2 systems.[4] In this case, WC281 circular waveguide is used from the antenna to the associated waveguide networks near the base of the tower. The minimum midband gain for these antennas compared to an isotropic radiator is as follows:

| Antenna	Minimum midband gain over isotropic antenna	
	6175 mc	11,200 mc
6 ft dual-frequency antenna including radome	37.9 db	42.5 db
10 ft dual-frequency antenna including radome	42.3 db	46.7 db
Horn-reflector antenna	43.1 db	47.7 db
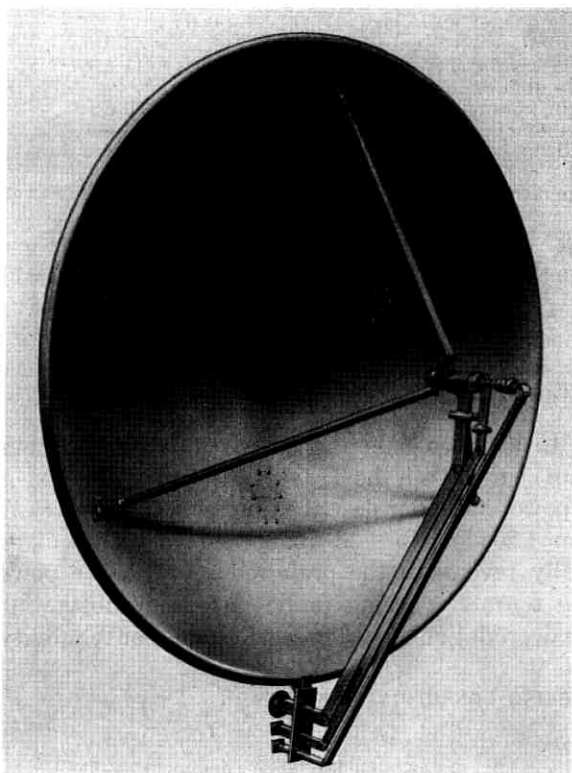
Fig. 1 — Dual-frequency antenna with radome removed.

The gain of the parabolic antennas used in conjunction with flat reflectors is shown in Fig. 2 where the effect of antenna-reflector separation is included.

The parabolic antennas and reflectors may be mounted on a wide variety of towers. The type of tower is dependent upon the wind loading for the area used as well as the size of the antenna or passive reflector. A somewhat more limited selection of tower designs is available for the horn-reflector antenna.

3.2 *The Design of a Typical Hop*

The expected performance of a hop may be computed for TL-2 and TM-1 based on the following assumptions:

	TM-1	*TL-2*
Path loss for 25 miles	140.4 db	145.6 db
Loss of waveguide components in radio equipment	3.4 db	5.5 db
Waveguide losses (40 ft) for a periscope system	1.0 db	1.6 db
Total losses	144.8 db	152.7 db
Minimum transmitter power	+20 dbm	+20 dbm
Gain of two 10-ft dual-frequency antennas	84.6 db	93.4 db
Gain of two 10-ft × 15-ft reflectors 180 ft away from antennas	−0.8 db	−0.8 db
Sum	103.8 db	112.6 db
Received carrier power	−41.0 dbm	−40.1 dbm
Assumed maintenance margin*	3 db	3 db
Received carrier power	−44.0 dbm	−43.1 dbm

* This factor is introduced to allow for some misalignment of the antenna system, etc.

The above calculation illustrates that in a typical hop, the received power for TM-1 and TL-2 are nearly the same. The increased path loss and waveguide component losses at 11 gc are balanced by an increased antenna gain.

In a low-index FM system, the thermal noise power in the highest frequency telephone circuit at the 0 TL point may be expressed by[5]

$$P_n = P_s + 20 \log \frac{f_1}{\Delta F} + 10 \log \frac{2 \, \Delta f \, N}{P_c}$$

where

P_s is the power of a baseband sine wave at the 0 TL point that will produce a peak deviation of ΔF megacycles. This is taken as the Dixon-Holbrook multiload factor and is +23.5 dbm for a 600-circuit load.
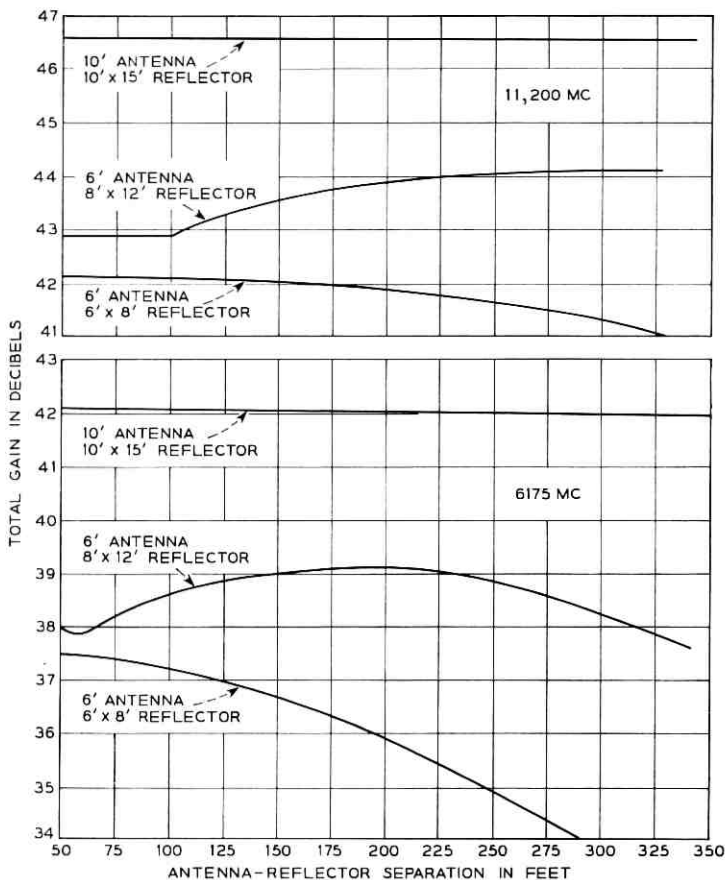
Fig. 2 — Periscope antenna gain vs separation for 6- and 10-foot dual-frequency antennas.

ΔF the peak deviation, is set to achieve an approximate balance between thermal and modulation noise. In TL-2 and TM-1, $\Delta F = 5$ mc.

f_1 is the location of the highest frequency multiplexed telephone circuit. For a 600-circuit load this is 2788 kc.

Δf is the nominal bandwidth of a telephone circuit, 3 kc.

N is the noise power per cycle, $(-174 + NF$ dbm$)$/cycle. In these systems $N = -174 + NF = -163$ dbm.

P_c is the received carrier power. For TM-1, $P_c = -44.0$ dbm and for TL-2, $P_c = -43.1$ dbm.

The values of P_n for TM-1 and TL-2 are, therefore, -62.8 dbm and -63.7 dbm, respectively.

In the Bell System, noise measurements are made using a 3A noise measuring set with C-message weighting and the values of P_n just computed will read as 25.2 dbrn for TM-1 and 24.3 dbrn for TL-2.*

Other noise contributions, based on factory measurements of transmitter receiver units, must be included as follows:

	TM-1	TL-2
FM thermal noise	25.2 dbrnc0	24.3 dbrnc0
Klystron noise	18.0	16.0
Modulation noise	22.0	23.0
Total noise	27.4	27.1
Pre-emphasis advantage†	3.5	3.5
Expected per hop noise performance	23.9 dbrnc0	23.6 dbrnc0

† The pre-emphasis characteristic specified for TM-1/TL-2 is shown in Fig. 3.

The noise performance of the 0.1-watt TM-1 and TL-2 systems in a typical 25-mile hop is expected to be nearly alike and, in the general case, there is no advantage in assigning a preferred status to one system over the other. Geographical situations do occur, however, where a higher transmitted power is required to transmit a greater distance.

The TM-A1 amplifier is available as a hop stretcher. A traveling-wave tube amplifier, providing at least 13-db gain is capable of raising the transmitted power of TM-1 to 2 watts. The power of the TL-2 system is not increased, but a revertive diversity switch is used at the receiver to take advantage of the better signal-to-noise ratio on the TM-1 channel when the power amplifier is used.

Carrying through the calculations for a 75-mile hop, but retaining all the earlier assumptions, we have:

	TM-1	TL-2
Received carrier power		
TM-1 @ +33 dbm	-40.6 dbm	
TL-2 @ +20 dbm		-52.7 dbm
Expected per hop noise performance of the highest frequency telephone circuit	22.2 dbrnc0	30.6 dbnrc0

Under these conditions, TM-1 is the preferred channel, and a diversity switch that reverts to TM-1 would be used. The TL-2 channel provides protection against TM-1 fades and equipment failures. The combination of a 2-watt TM-1 system and a 0.1-watt TL-2 system is capable of meeting over-all system reliability objectives.

* For the reasons given in the appendix, these readings will be referred as dbrnc0.
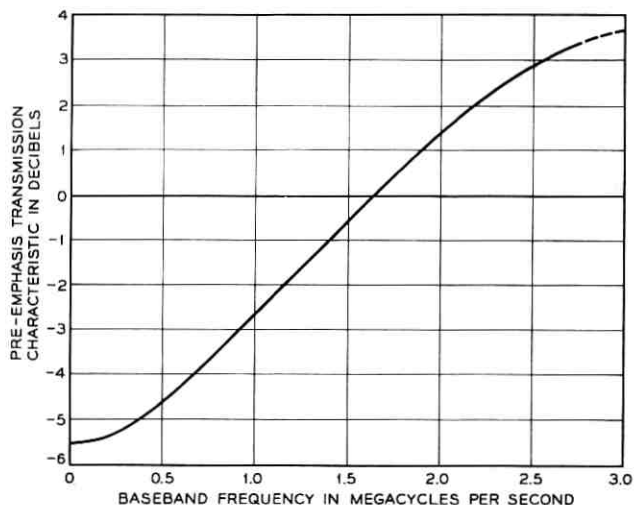
Fig. 3 — Message pre-emphasis characteristic.

IV. TRANSMISSION PLAN

4.1 *Frequency Plans*

The number of two-way diversity channels which may be provided by TM-1/TL-2 combinations depends upon several factors. Where the normal TM-1 and TL-2 allocations are employed, the antenna system becomes the deciding factor. With the dual-frequency parabolic antennas, limited to a single polarization at 6 gc while providing two polarizations at 11 gc, a maximum of four two-way crossband channels may be provided. When two polarizations in both bands are available, as with the horn-reflector antenna, six two-way crossband diversity channels are possible.

Basically, the normal TL-2 frequencies are the same as those of the TJ and TL plans (Fig. 4). The staggered plan shifts all the A frequencies 20 mc higher and the B frequencies 20 mc lower. In the case of TM-1, several frequency allocations exist as shown in Fig. 5. The normal or split channel plan provides two TM-1 channels in the frequency space set aside for each TH channel.[7] The staggered allocation provides a more limited number of TM channels which are located between TH channel assignments. This allocation is used to minimize interference in cases where a TM-1 route crosses a TH route. A third

allocation, the co-channel plan, is the TH frequency plan which is used where TM and TH will share the same route. In this instance, the normal or staggered plans would not be suitable. It should be pointed out that in all cases, the preferred order of channel growth in TM-1 is the reverse of the preferred use order in TH to minimize interference possibilities.

Although TM-1 and TL-2 Radio Systems may be operated on a non-
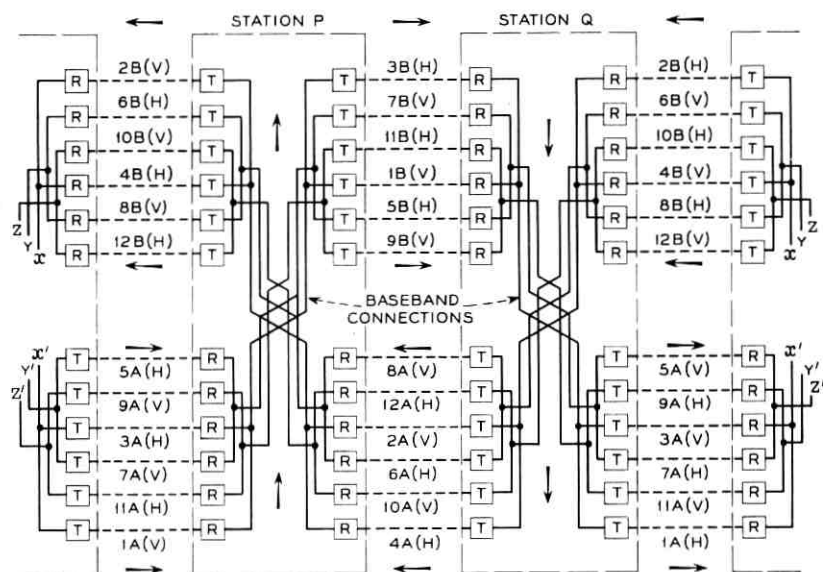
Channel number	Transmitter frequency, gc	Beat oscillator frequency, gc	Channel number	Transmitter frequency, gc	Beat oscillator frequency, gc
4A	10.715	10.785	9B	11.245	11.315
1A	10.755	10.825	12B	11.285	11.355
10A	10.795	10.865	5B	11.325	11.255
11A	10.835	10.905	8B	11.365	11.295
6A	10.875	10.805	1B	11.405	11.335
7A	10.915	10.845	4B	11.445	11.375
2A	10.955	11.025	11B	11.485	11.555
3A	10.995	11.065	10B	11.525	11.595
12A	11.035	11.105	7B	11.565	11.495
9A	11.075	11.145	6B	11.605	11.535
8A	11.115	11.045	3B	11.645	11.575
5A	11.155	11.085	2B	11.685	11.615

Fig. 4 — TL-2 frequency allocation plan.
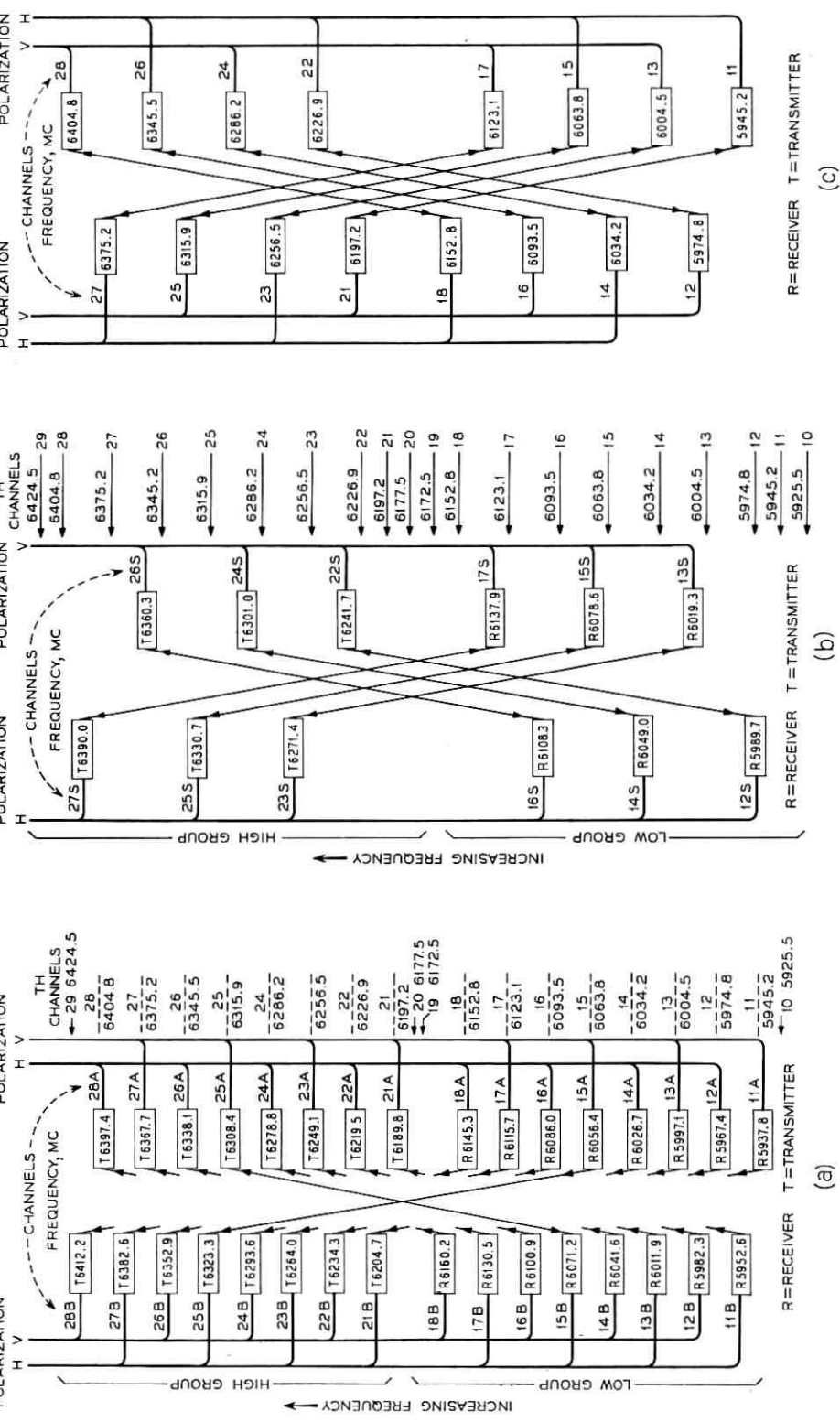
Fig. 5 — Frequency plans—TM-1 microwave high-group transmitting repeater: (a) normal channel frequency plan, (b) staggered channel frequency plan, (c) ...

12

diversity basis, or in diversity with other channels within their individual bands, these cases will not be discussed here. Generally speaking, in message service, the increasing size of circuit groups and the more severe reliability objectives makes nondiversity operation undesirable. For educational TV, industrial or closed circuit video, however, nondiversity operation is usually acceptable.

Fig. 6 shows a possible growth plan for a TM-1/TL-2 crossband diversity system. Both the TM-1 and TL-2 systems normally employ a four-frequency plan using each RF frequency only once at a repeater which is required when periscope antenna systems are employed. These frequency plans achieve the following results:

(i) There is adequate separation between transmitters and receivers by using the upper (or lower) half of the band for transmitting and the lower (or upper) half for receiving. This arrangement is inverted at alternate stations.

(ii) Polarization of adjacent channels alternates between vertical and horizontal to provide maximum frequency separation between channels of the same polarity.

(iii) "Over-reach" interference is reduced by alternating horizontal and vertical polarization of a given frequency. A frequency having a horizontal polarization in one hop will occur again two hops away but will be vertically polarized.

4.2 Diversity Operation

The beat frequency oscillator is always kept within the assigned common carrier band, but its frequency may be above or below the frequency of the incoming RF carrier. Hence, since all other phase relationships are identical, the two halves of a diversity pair could have baseband outputs of opposite polarity. A polarity inverter is therefore included in the TM-1 transmitter baseband amplifier to insure in-phase signals at the baseband switch points to provide hitless diversity switching.

Two forms of diversity switch may be employed with the TM-1/TL-2 combination. The simple bistable switch has been described in detail in an earlier paper.[2] Where the performance of the two systems of a diversity pair is comparable, this type of switch is fully adequate, but where the performance of one of the systems is better than the other, a revertive switch, described in Section VII, is normally used. A typical two-hop system is illustrated in Fig. 7.

Fig. 6 — A growth plan for a TM-1/TL-2 crossband diversity system.
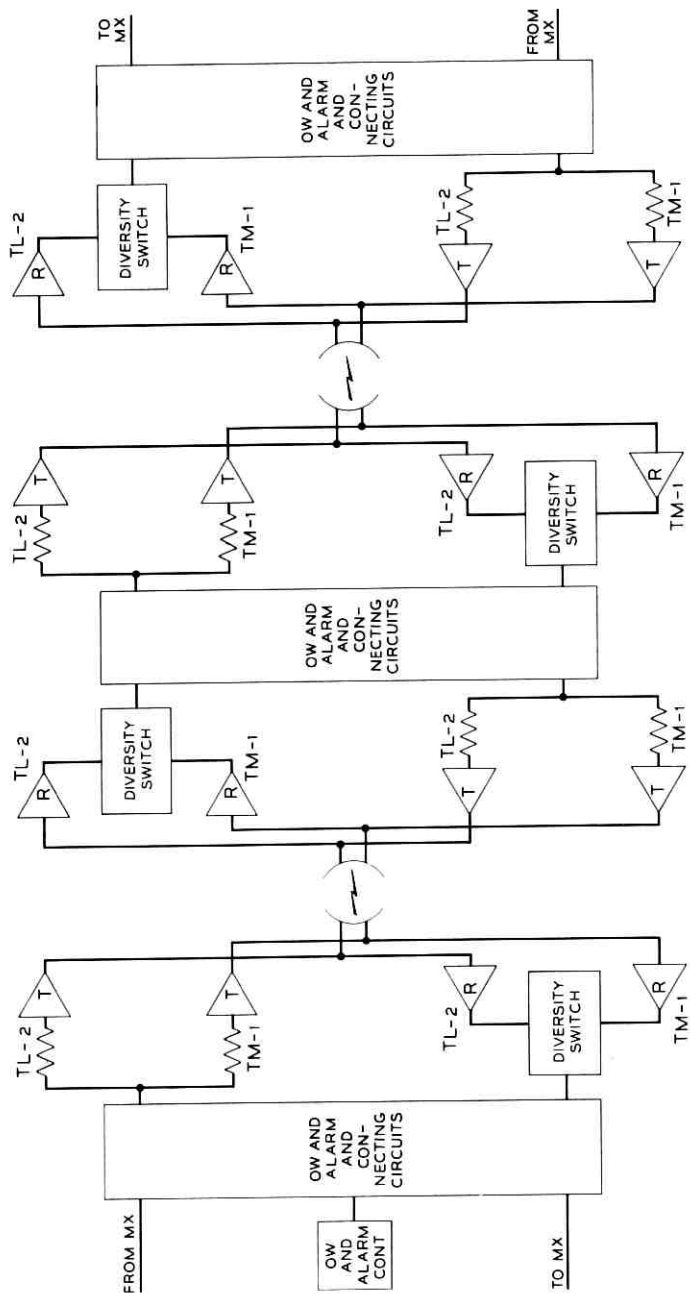
Fig. 7 — A typical two-hop TM-1/TL-2 diversity system.

V. MICROWAVE MULTIPLEXNG NETWORKS

5.1 *Antenna Multiplexing Networks*

The dual-frequency antennas mentioned in the previous section accept two polarizations at 11 gc and one polarization at 6 gc for a total of six 11-gc radio channels and four 6-gc radio channels. For crossband diversity usage this is limited to four diversity radio channels. Where load requirements are greater, the horn-reflector antenna may be used and here a microwave multiplexing network is required which will permit the multiplexing of more radio channels.

The block schematic of Fig. 8 illustrates how six two-way radio channels may be operated in crossband diversity. The two groups of TL-2 channels are combined in a 1405A polarizer network. The three TM-1 channels to be polarized horizontally and the three TM-1 chan-
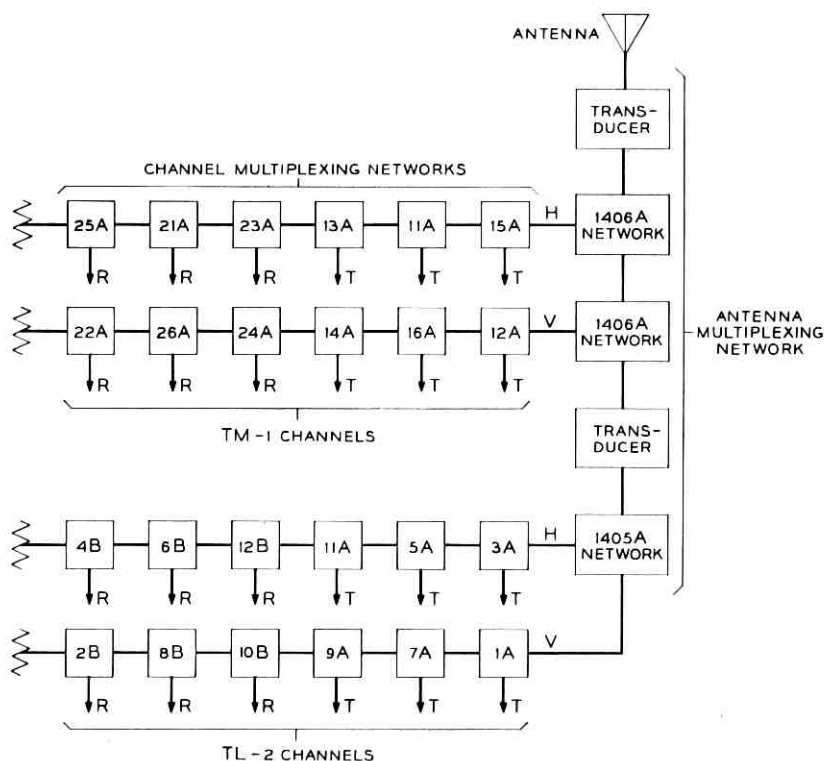

Fig. 8 — Use of microwave multiplexing networks in a TM-1/TL-2 installation.

nels to be polarized vertically are connected to separate 1406A networks which are multihole directional couplers having square through arms that support 6- and 11-gc orthogonally polarized waves. One 1406A network is rotated 90° with respect to the other. A transducer is required between the 1405A network and the 1406A networks, and another between the 1406A networks and the antenna. The networks are, of course, bilateral and have been described fully in previous literature.[8]

5.2 Channel Multiplexing Networks

The use of channel multiplexing networks is also illustrated in Fig. 8. Transmission through a network is nearly lossless for all channels except for the assigned channel where the through loss is very high but the loss to the drop is low. Fig. 9 illustrates a TM-1 channel multiplexing network. It consists of two channel rejection filters inserted between two short-slot directional couplers. The directional couplers are terminated in end pieces that provide the desired access for 3 ports and a termination for the fourth port. The manner in which a channel multiplexing network operates may be described by referring to the schematic shown in Fig. 10. A signal incident to port 1 is divided into two equal signals that differ in phase by 90° appearing at ports 5 and 6. These signals then pass into the filters and if the filters are tuned to the frequency of the signals, they are reflected back into the coupler. Each reflected signal is then divided into equal components with an additional 90° phase difference at ports 1 and 2. The components at port 1 are 180° out-of-phase and cancel while the components at port 2 are in-phase and add to give the original signal for the dropped channel. If the filters are not tuned to the signal frequency, the two signals pass freely through the filters and emerge in phase at port 3, and out-of-phase at port 4. Port 4 is terminated to present a good impedance looking into the other ports.

The performance of a representative network is shown by the transmission characteristics in Fig. 11. The in-band loss between ports 1 and 2 is less than 0.5 db for a 20-mc band while the loss between ports 1 and 3 is less than 0.1 for frequencies in the 5925 – 6425-mc band outside of the $f_m \pm$ 59.3-mc region. In the standard frequency plan, the center frequencies of the other channels are at least 59.3 mc removed from f_m. The return loss of any port with the other two ports terminated is greater than 35 db from 5925 to 6425 mc.

The filters used in the channel multiplexing networks are constant-k.

PORT 3

516A TERMINATION

20A DIRECTIONAL COUPLER

1318 TYPE FILTER

20A DIRECTIONAL COUPLER

20A BEND

PORT 2

PORT 1
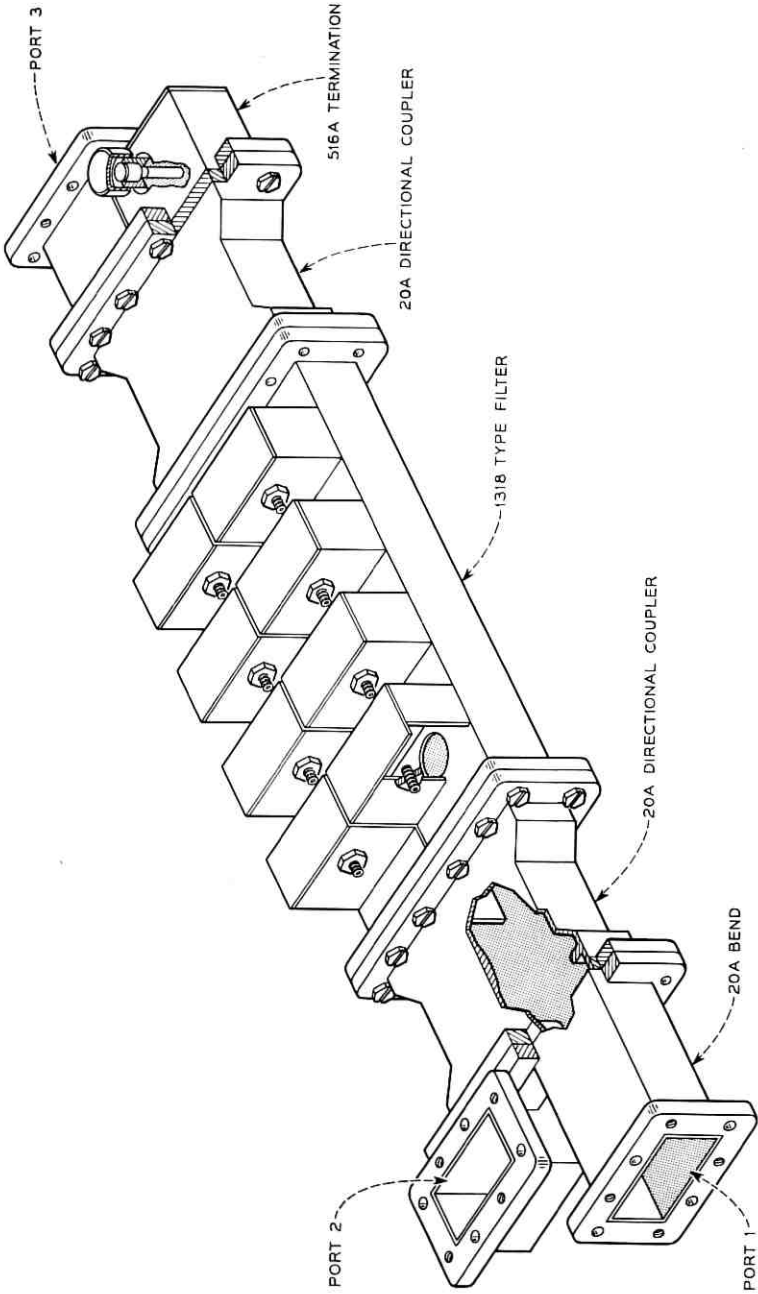
Fig. 9 — TM-1 channel multiplexing network.
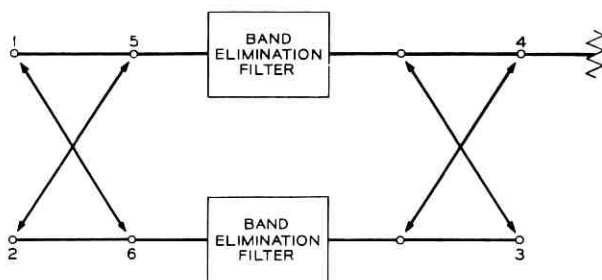
Fig. 10 — Channel multiplexing network schematic.

Each filter consists of four aperture-coupled cavities spaced $\frac{3}{4}$ λ along a section of waveguide. This type of cavity can be closely approximated by a series parallel-tuned circuit over a narrow band of frequencies.

The channel separating networks for TL-2 have been described previously.[1] Typical performance characteristics are given in Fig. 12.

VI. RADIO TRANSMITTERS

6.1 *General*

The block diagram of Fig. 13 describes both the TM-1 and the TL-2 radio transmitters. The baseband signal is amplified by the transmitter
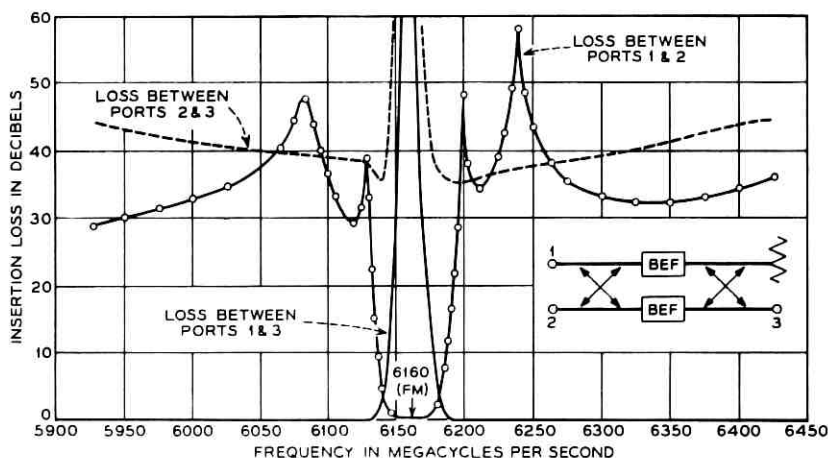
Fig. 11 — Insertion loss characteristic of TM-1 channel multiplexing network.
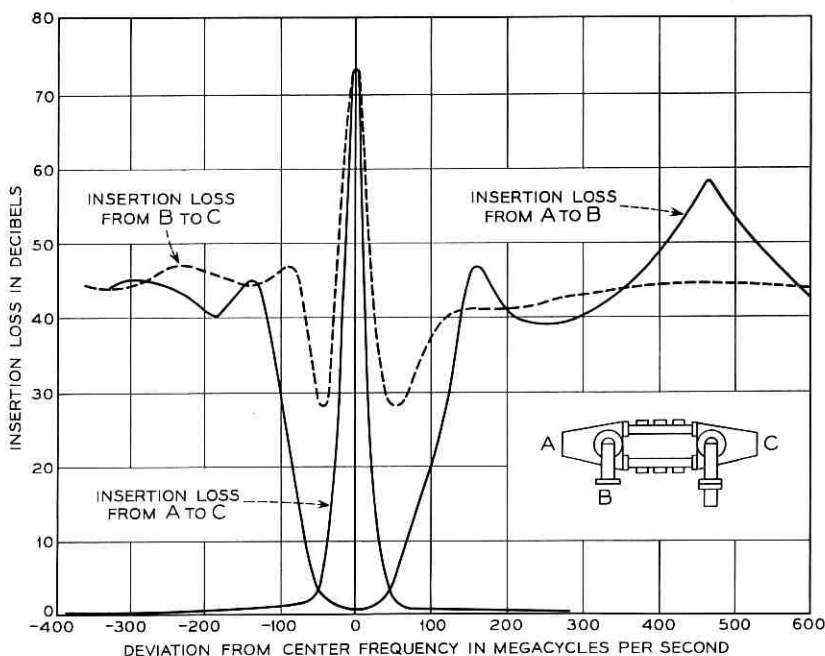
Fig. 12 — Transmission characteristic of channel multiplexing networks for TL-2.

baseband amplifier and is applied to the repeller of the klystron oscillator causing the frequency of oscillation to be deviated about the assigned channel frequency. The resulting band of RF frequencies is fed to the antenna networks through an isolator, directional couplers to permit frequency and power monitoring, a waveguide switch, and a channel separation network. Photographs of the transmitter portions of TM-1 and TL-2 are shown in Figs. 14(a) and (b). The klystrons and the isolators are not visible in these photographs.

6.2 Transmitter Baseband Amplifiers

The transmitter baseband amplifier for TL-2 is a three-stage feedback amplifier using Western Electric 15C germanium diffused base transistors. It provides a nominal voltage gain of 31 db from the 75-ohm unbalanced input to the high impedance of the klystron repeller, supplying a maximum voltage of 8 volts peak-to-peak. A gain control of ±4 db is provided to accommodate the modulation sensitivity of all klystrons. The amplifier has a frequency characteristic that is nomi-

small frequency errors due to this effect are unacceptable. The basic time constant is still approximately C_1R_1, but in the circuit of Fig. 16 leakage currents in C_1 flow in R_2 rather than R_1. Both C_2 and R_2 are large compared to C_1 and R_1. The voltage across C_2 is essentially zero.
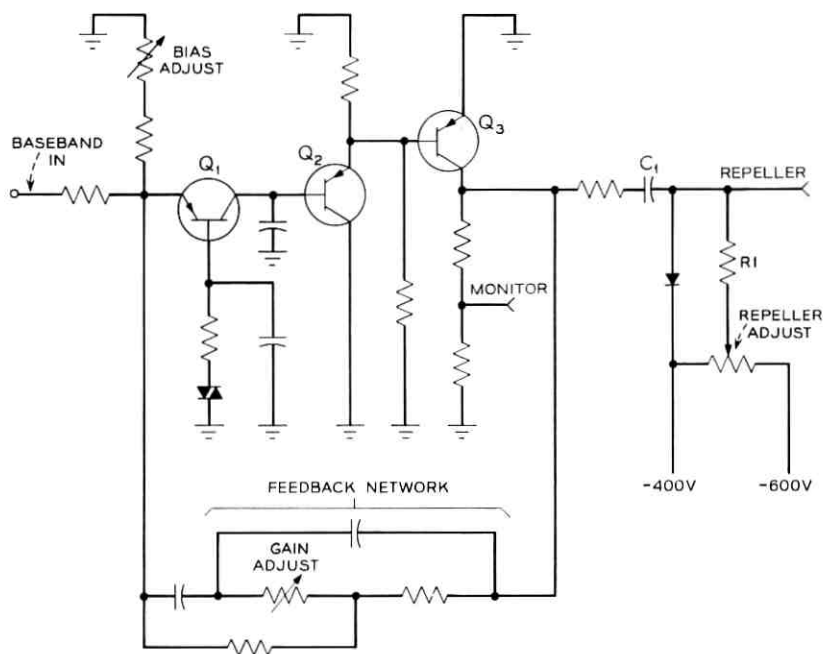

Fig. 15 — TL-2 transmitted baseband amplifier.

6.3 *Transmitter Klystrons**

The **459**-type klystron is an external cavity klystron designed specifically for the TM-1 system. The tube is both cooled and temperature stabilized by clamping it to a vapor phase cooling boiler by means of the output flange. It has a specially designed temperature compensator which provides a frequency temperature coefficient of less than ±0.1 megacycle per degree Fahrenheit.

The external cavity design was chosen in order to achieve a relatively high modulation sensitivity comparable to that of the 457A 11-gc klystron. Even though the efficiency of an external cavity structure

---

* This section was written by Mr. E. J. Panner.
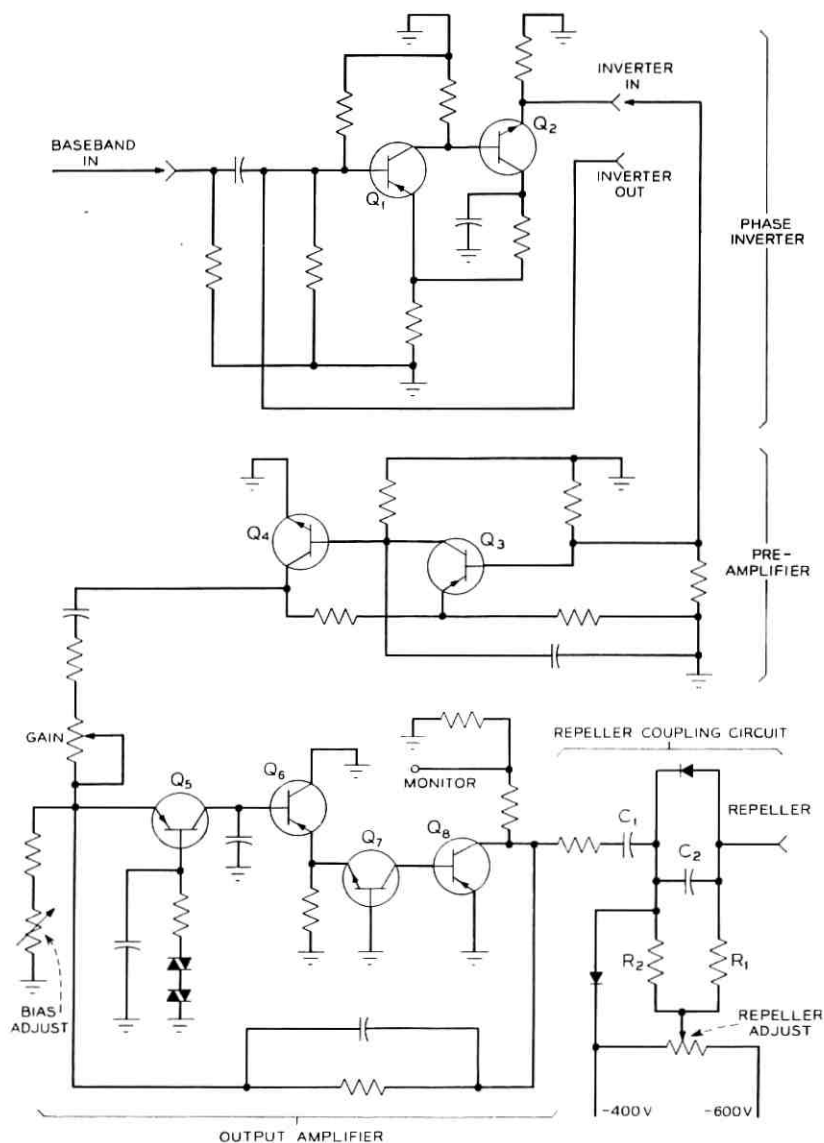
Fig. 16 — TM-1 transmitter baseband amplifier.

is somewhat lower than that of an internal cavity tube, some of this loss of efficiency is regained by operating the tube in the $2\frac{3}{4}$ mode. In addition, the higher output power tubes are coded 459A for use in transmitters while the lower end of the distribution is coded 459B for use as local oscillators in receivers.

Tuning is accomplished through the use of a contacting tuning plunger which is coupled to a frequency indicator and is driven by a slotted tuning nut. Mechanical tuning is possible without removing the insulating cover in the TM-1 bay. The entire tube is gold plated to raise the Q of the cavity and reduce the effects of oxidation.

The WE457A klystron, used in TL-2, has been described in connection with the TL Radio System.[9]

Fig. 17 is a photograph showing both the 459A and the 457A klystrons while typical output power versus frequency characteristics of both tubes are shown in Fig. 18. Typical operating characteristics of both tubes are summarized in Table I.

6.4 Isolators*

New high reverse loss isolators were designed for these systems to be used at the outputs of the transmitter klystrons to prevent frequency pulling that would give rise to intermodulation distortion.[10] Fig. 19 shows the dielectric loaded full-height E-plane structures used and typical performance characteristics for both isolators. This structure was chosen to maximize the reverse loss per unit length to obtain a minimum length isolator.

The isolators consist of a thin ferrite slab (nickel aluminum ferrite) bonded to a ceramic loading of aluminum oxide which is approximately ten times thicker than the ferrite. The ferrite-ceramic loading is positioned in the waveguide at a nearly circular point of polarization of the microwave magnetic field. In addition to supporting the ferrite, the ceramic increases the microwave energy in the ferrite and decreases the frequency dispersion of the point of circular magnetic field polarization by lowering the cut-off frequency of the waveguide. The ferrite is biased to ferri-magnetic resonance with and external "C" magnet which is potted in glass filled nylon and bonded to the waveguide. The magnet length is critically determined to realize a variation in applied magnetic field along the ferrite, increasing the bandwidths of the reverse loss (isolation) characteristic. Matching is accomplished with linear tapers ground in both ends of the ceramic loading. The TM-1

---

* This section was written by Mr. J. J. Degan.

457A FOR
TL-2

459A FOR
TM-1
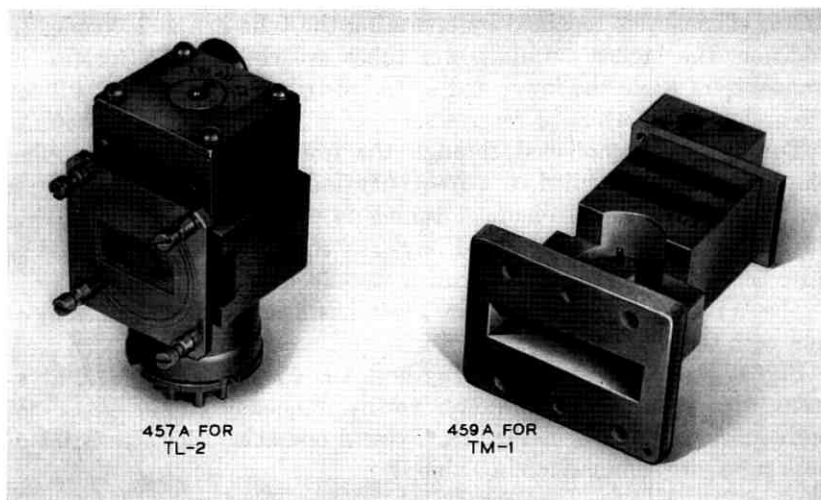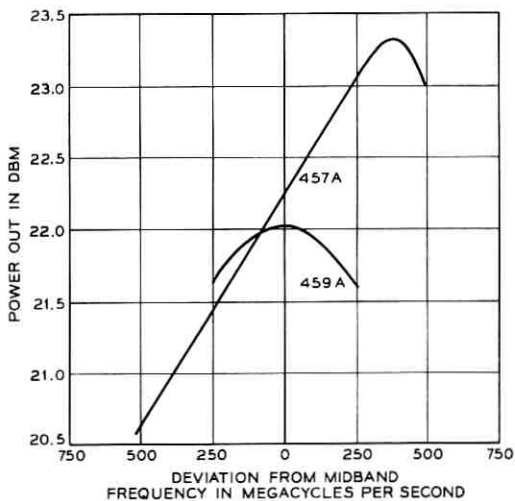
Fig. 17 — Klystrons.

Fig. 18 — Typical power output vs frequency for 457A and 459A klystrons.

TABLE I—TYPICAL OPERATING CHARACTERISTICS

|	459A Klystron	457A Klystron
RF power output	0.1w (min)	0.1w (min)
Resonator voltage	400v	400v
Repeller voltage	−120v	−115v
Repeller modulation sensitivity	1.7 mc/volt	2.3 mc/volt
Electronic tuning range	75 mcs	100 mcs
Heater current	0.88 amp	0.90 amp
Cathode current	43 ma	43 ma
Frequency-temperature coefficient	<0.1 mcs/°F	<0.15 mcs/°F
Oscillating mode	$2\frac{3}{4}$	$3\frac{3}{4}$

system isolators are temperature compensated by a shunt strap of magnetic material whose permeability changes rapidly with temperature.

An additional feature of the high reverse loss isolator in the TM-1 system is its built-in harmonic absorption. Harmonic outputs from the klystron tend to pull the klystron frequency, causing modulation distortion unless these harmonics are properly terminated. The ceramic-ferrite loading of the isolator preferentially mode converts the harmonic energy into the TE_{30} mode. On the other hand, energy at the fundamental frequency remains in the dominant mode (TE_{10}) in the desired signal band and is concentrated into the high dielectric loading. The resulting distribution of fundamental and harmonic electric field intensities is shown in Fig. 20. The result is a large differential in the value of electric field intensity near the side walls of the waveguide. Resistive vanes are placed in a position to provide several db of loss at the harmonic frequencies with less than 0.2 db of additional loss at the desired signal frequency. The vanes are bonded to a dielectric slab which in turn is bonded to the waveguide wall. Fig. 21 is a cut-away view of the isolator showing details of construction.

6.5 *Vapor Phase Cooling System Designs**

The frequency stability of the TM-1 and TL-2 transmitters is obtained in part by carefully controlling the temperature of the klystrons. This method was successfully used for TL-1 and the technique was improved for TM-1 and TL-2. Also, since TM-1 and TL-2 are designed to fit in the same panel space and to operate in diversity ar-

---

* This section was prepared by Mr. W. G. Stieritz.
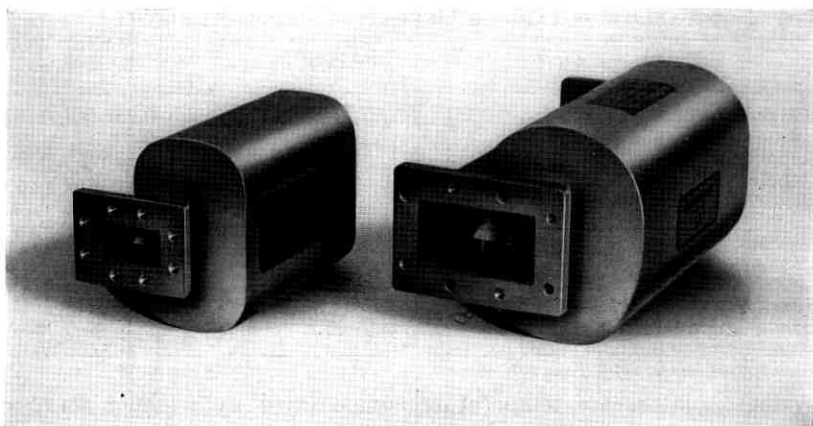
(a)
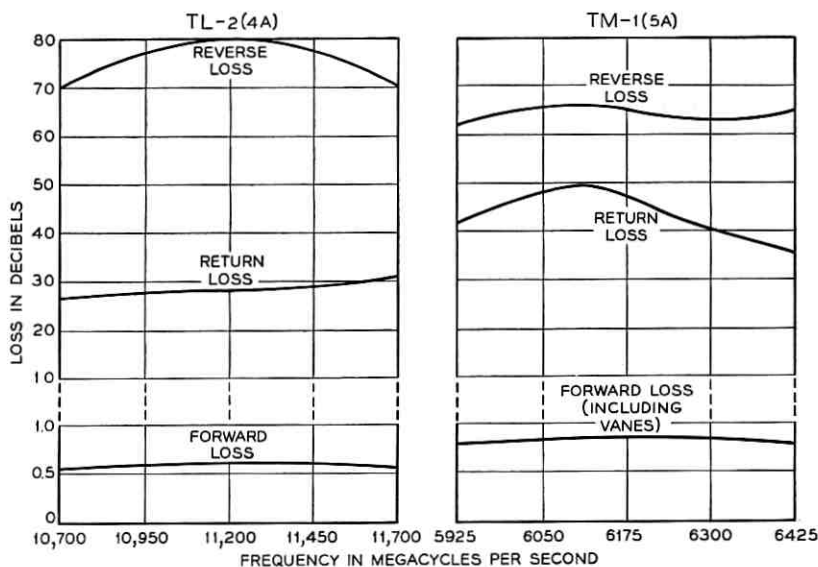
(b)

Fig. 19 — (a) Transmitter isolators. (b) Typical isolator characteristics.
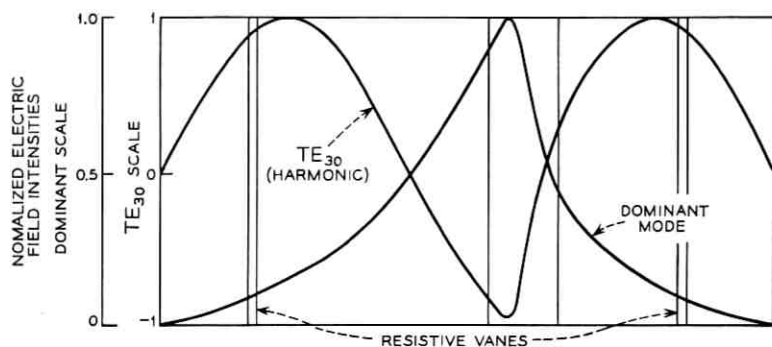
Fig. 20 — Comparison of dominant mode and TE₃₀ transverse E fields in dielectric loaded guide.
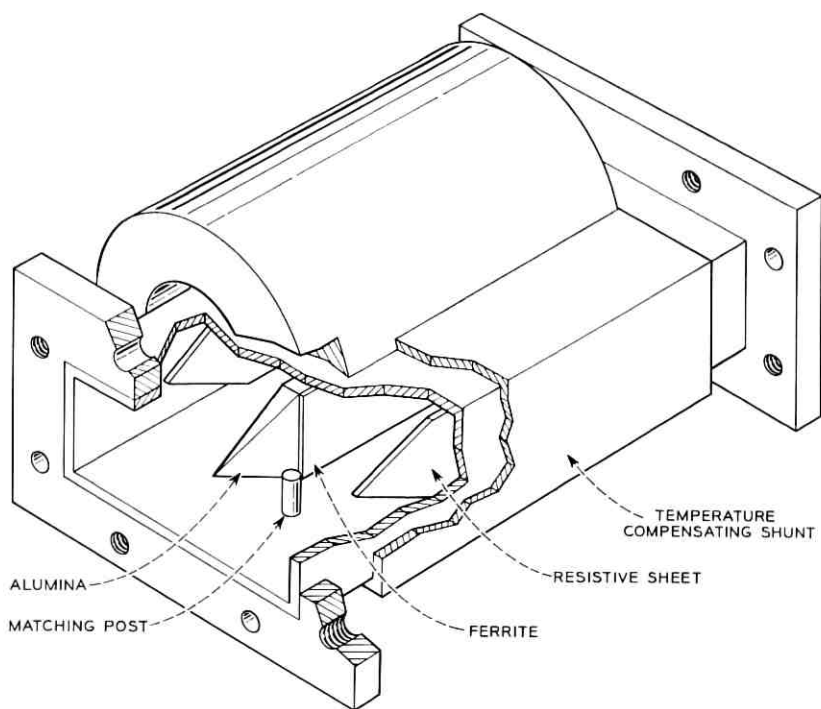

Fig. 21 — 5A isolator, cut-away view.

rangements with each other in the same shelters, it was advantageous to use a common equipment design.

The radio equipment is designed to be mounted in unattended shelters or in pole-mounted cabinets. The power dissipated in these enclosures will produce a temperature rise of about 20°F at low temperatures. The radio equipment must therefore operate in an environment of −20°F to +120°F corresponding to an outside ambient ranging from −40°F to +120°F. (At high ambient temperatures an exhaust fan is used.) Over a nominal 3-month maintenance interval the range of ambient temperature variation is not likely to exceed 100°F, however. To meet the ±0.05 percent frequency accuracy for TL-2 and the ±0.02 percent requirement for TM-1, the klystron temperature must be held to ±3°F. Klystron voltages must also be closely regulated, as described in Section VIII.

The major elements of the TL-2 vapor phase cooling system are shown disassembled in Fig. 22. The heat source is a pair of klystrons clamped to each side of a copper boiler. The boiler and klystrons are enclosed in a fiberglass insulated chamber to reduce the effect of ambient temperature variation. The boiler is filled with a heat transfer fluid, FC-75 fluorochemical which is a liquid that has a boiling point of 214°F at standard atmospheric pressure of 29.98 inches of mercury. The vapor from the boiling liquid which has absorbed the klystron heat is led by an inclined stainless steel pipe to the copper condenser block. Here the vapors are condensed back to the liquid phase, and returned to the boiler. This condenser is in turn bolted to the equipment mounting panel which serves as a heat sink to ambient. A rubber bladder connects to the condenser outlet and allows for expansion of the gases inside the system without allowing their escape. The flexible bag permits substantial changes in volume of the enclosed system without appreciable changes in pressure. This is required since otherwise changes in heat input to the boiler caused by ambient temperature changes would result in pressure changes inside the system, hence changes in the boiling temperature of the liquid. This equipment is capable of holding temperature changes of the klystrons of about 5°F over an ambient temperature change from −20°F to +140°F.

While the design of the TM-1 vapor phase cooling system is based on the earlier TL-2 design, the two systems differ considerably in detail. The differences may be attributed to physical and thermal differences between the 11- and 6-gc components.

The TM-1 solution, which was achieved by heat flow analysis and
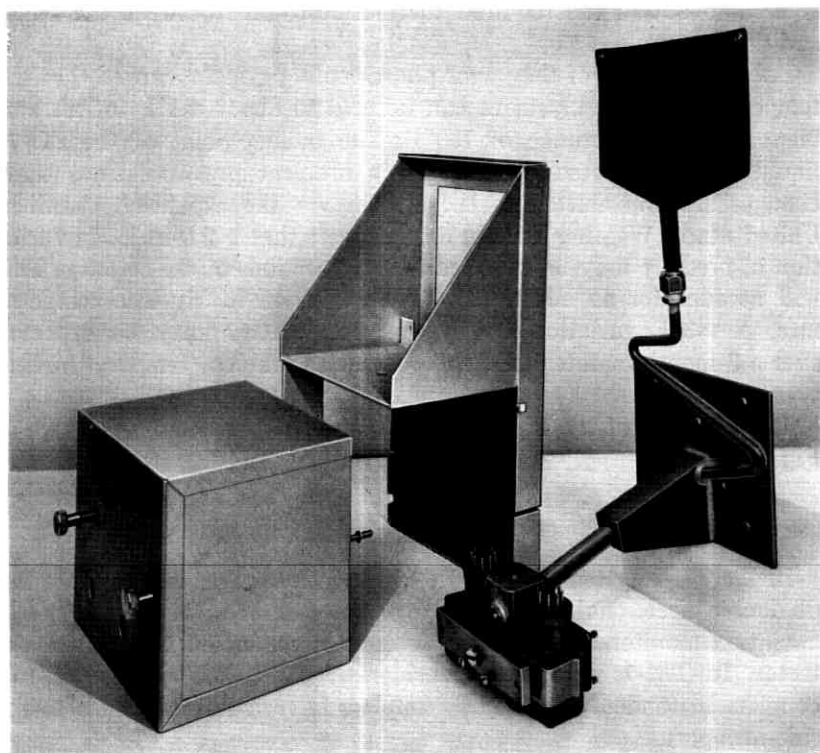
Fig. 22 — TL-2 vapor phase cooling system.

experimental verification, includes the following refinements over TL-2:

(*i*) The boiler, in the shape of a double waveguide flange, was thermally isolated from each waveguide by a section of internally plated plastic guide to eliminate heat flow through the large mass of the waveguide.

(*ii*) Foamed plastic blocks about ¼-inch thick are inserted in the plastic waveguides, and cemented to the narrow dimension of the guides. These blocks isolated the klystrons from air currents in the waveguides.

(*iii*) The cover assembly for the klystron chamber is insulated with polyurethane foam, rather than fiberglass as used in TL-2. A thermostatically controlled heater was also added to hold the temperature in the klystron chamber to about 110°F ±5° at lower ambient temperatures.

(*iv*) Synthetic rubber tubing between the boiler and the condenser

is used to obtain the required thermal resistance between the boiler and the frame.

Laboratory tests of the vapor phase cooling system showed that the temperature of the klystrons can be held to about ±1°F for an ambient temperature range of 100°F. The boiling point of the FC-75 liquid is also affected by changes in ambient pressure, since these changes are transmitted to the system via the expansion chamber. United States Weather Bureau data suggest that a 2.0-inch Hg variation in pressure may be expected in some sections of the country. This will account for an additional ±2°F variation in klystron temperature. A ±3°F variation in klystron temperature may be expected over a 3-month maintenance interval due to ambient temperature and pressure chages.

The elements of the TM-1 vapor phase cooling system are shown in Fig. 23.

6.6 *Frequency and Deviation Monitor*

In the TL-2 system the output of the isolator is connected to a 20-db double directional coupler where one output feeds the frequency and deviation monitor and the other output is connected to a power detector. In TM-1, equipment considerations dictated the use of two couplers in tandem where both couplers have a loss of 17 db to the side-arm port.

The frequency accuracy of the transmitter is dependent upon the accuracy of the microwave reference cavity. The frequency stability requirement for TM-1 particularly, resulted in the following design:

(*i*) The cavity was constructed from specially heat treated and machined invar.

(*ii*) Provision was made to annul the small but finite expansion of invar using a brass detail compensator.

(*iii*) The cavity was filled with dry argon and sealed to minimize any variation of the dielectric constant with humidity.

(*iv*) Individual cavities were designed for each channel because it was felt that tuning mechanisms covering a wider frequency range might not be sufficiently stable.

Fig. 24 shows a cut-away view of the TM-1 reference cavity. It is a TE_{011} cavity aperture-coupled to rectangular guide. The dimensions of the cavity are proportioned to provide single mode operation and the apertures are proportional to achieve the narrow-band insertion loss characteristic shown in Fig. 25. The aperture tolerances are held
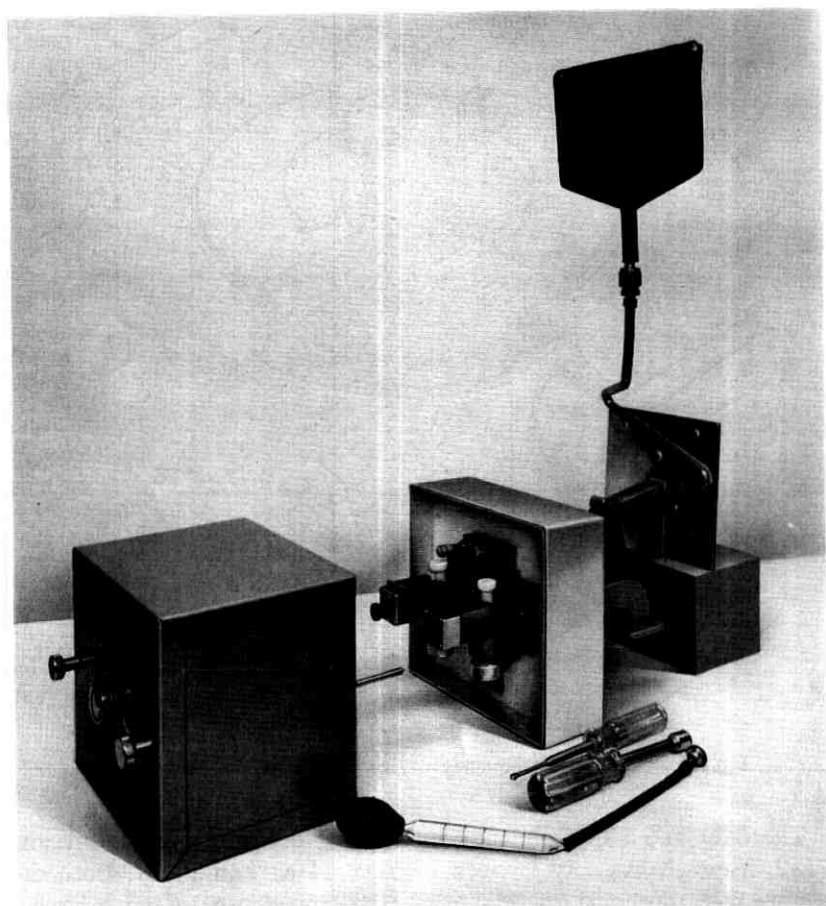
Fig. 23 — TM-1 vapor phase cooling system.

tightly to give accurate bandwidth control. The details of construction
are shown in Fig. 24 including the brass temperature compensator. A
typical cavity is stable to ±300 kc over the temperature range of
−40°F to +140°F.

The frequency stability requirements for the TL-2 reference cavity
are more lenient than those for TM-1, hence the compensation
for the expansion of the invar was omitted. The tuning mechanism,
consisting of a screw that is solder-sealed after cavity adjustment, is
simpler than that used in TM-1. The transmission characteristic of the
TL-2 reference cavity is shown in Fig. 26.
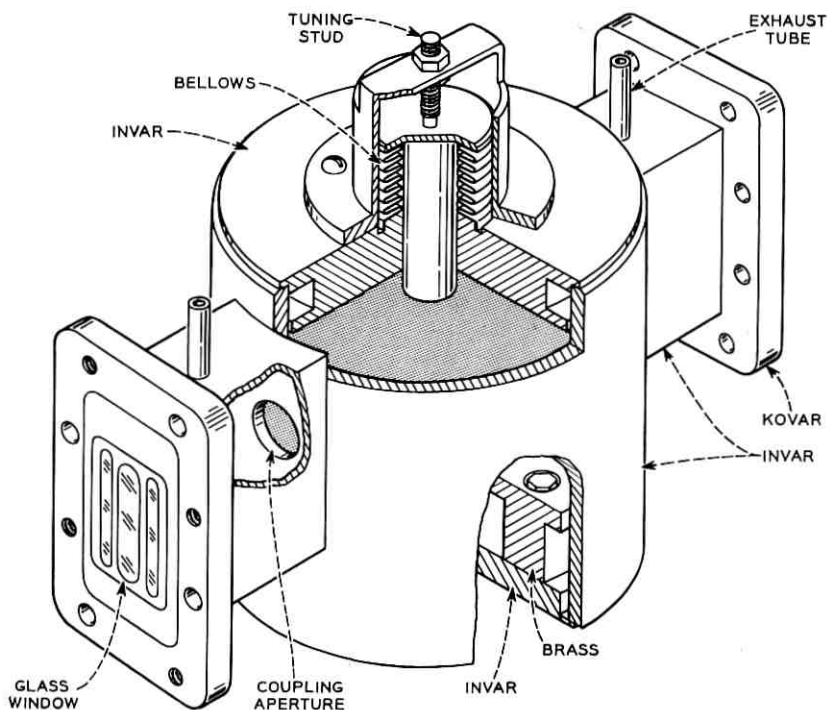
Fig. 24 — Reference frequency cavity for TM-1, cut-away view.

The 54D and 53A frequency monitoring detectors, for TM-1 and TL-2, respectively, may be seen in Figs. 14(a) and 14(b). Both detectors were designed to present a good impedance to the reference cavities as well as a flat transmission characteristic over a wide band.

In both TM-1 and TL-2, the waveguide attenuator is an integral part of the coupler and can be set to either of two positions. One position is virtually no loss while the loss for the other position (ranging from 2.5 to 3.5 db) is carefully set at the time of manufacture to permit a simple field adjustment of deviation. When the unmodulated transmitter is "on frequency", the detector meter readings will be maximum. When the transmitted RF carrier is frequency modulated, the detected output through the cavity filter will decrease because the filter selectivity attenuates the sidebands that are generated. The reduction obtained can be calibrated for a given deviation, modulating frequency, and cavity filter. This calibration is made in the two-position attenuator in its "loss" position. Thus, by applying say 100 kc at

a given level, the transmitter baseband gain control can be adjusted to give the same output from the cavity filter as is obtained when the attenuator is in its loss position and the carrier is unmodulated.

6.7 *Power Monitors and Waveguide Switches*

The power monitor detectors may be seen in the left-hand side of Fig. 14(a) for TM-1 and in the upper right-hand corner of Fig. 14(b) for TL-2. While the 53A detector used in TL-2 is identical to the frequency monitor, the power detector for TM-1 is built integrally with a 17-db directional coupler to better fit the TM-1 equipment design.

The waveguide switches may also be seen in Figs. 14(a) and 14(b). These switches are required in tests, such as the initial tuning of klystrons, where the transmitters must be effectively disconnected from the antenna. Each switch consists of a short section of waveguide with a narrow slot to accept a double-ended vane. The vane is properly positioned in the slot by means of detents and leakage from the slot is minimized by choke rings. The switch provides more than 60-db attenuation in the "off" position and a return loss of more than 40 db in its "on" position.
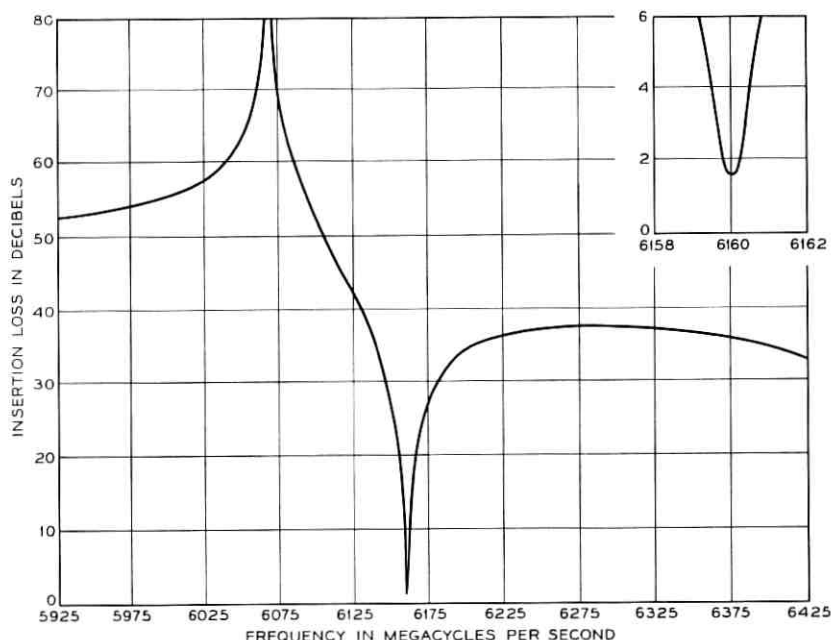
Fig. 25 — Transmission characteristic of reference cavity for TM-1.

6.8 *Stability of the TM-1 Transmitted Frequency*

The maintenance objectives for these systems are that a quarterly adjustment of frequency will be made using the built-in frequency and deviation monitor. A 100°F variation in temperature may be encountered over this interval. Laboratory measurements on a number of
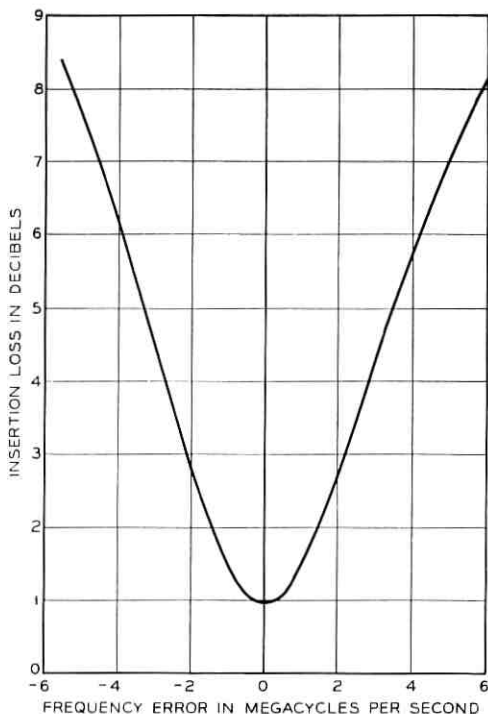
Fig. 26 — Transmission characteristic of reference cavity for TL-2.

transmitters (see Fig. 27) indicate that the TM-1 frequency is within ±0.02 percent of the assigned channel frequency for temperatures varying between −20°F and +120°F and the expected pressure variations that will be encountered during the maintenance interval.

6.9 *The TM-A1 Power Amplifier**

Fig. 28 shows a block schematic of the power amplifier and how it is used with a TM-1 transmitter to achieve an RF output of 2 watts.

* This section was written by Mr. L. K. S. Haas.
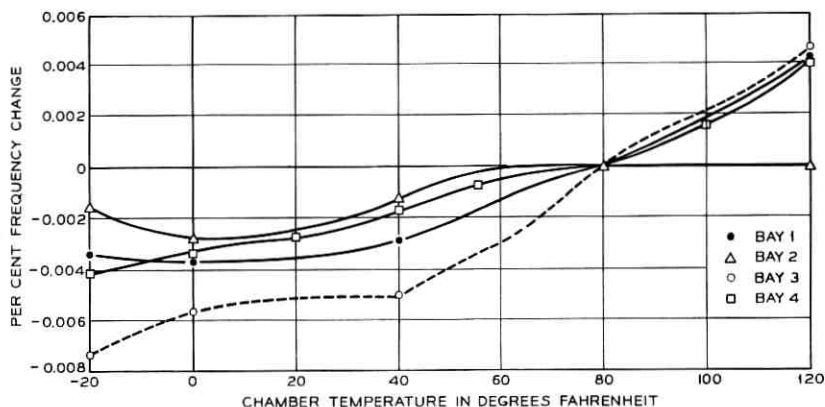
Fig. 27 — Transmitter frequency stability vs temperature for TM-1 transmitters.

The concept followed in the development of the 462A traveling-wave tube is that of a tube and circuit package in which all adjustments of electron beam focus and helix-to-waveguide match are made at the factory. To minimize the effects of defocusing, the helix diameter of the traveling-wave tube (TWT) is slightly larger than optimum for band flatness, and as a result, the gain characteristic has a slope of about 2 db over the 500-mc TM band. In the event of a tube failure, the package is returned to the factory for a new tube. Provision is made for an interlocking circuit so that the power supply cannot be turned on unless connection is made to the 462A package.

Focus of the TWT is accomplished by means of a repeating magnetic field pattern along the length of the tube provided by a stack of alternating Alnico VIII magnets and iron pole pieces. Magnets of this material were chosen because of its stability with changes in temperature.

RF input and output to the amplifier are made through reduced height waveguides which require waveguide transformers to match the standard WR-159 waveguide used elsewhere in the TM bay. The smaller waveguide inside dimensions are 0.318 by 1.590 inches for the input and 0.100 by 1.590 for the output.

The important parameters of the traveling-wave tube package are given in Table II. Nominal values are shown.

Cooling of the collector is accomplished by thermal contact between a cooling block on the 462A package and a heat sink which is part of the TM bay. A photograph of the 462A package is shown in Fig. 29.
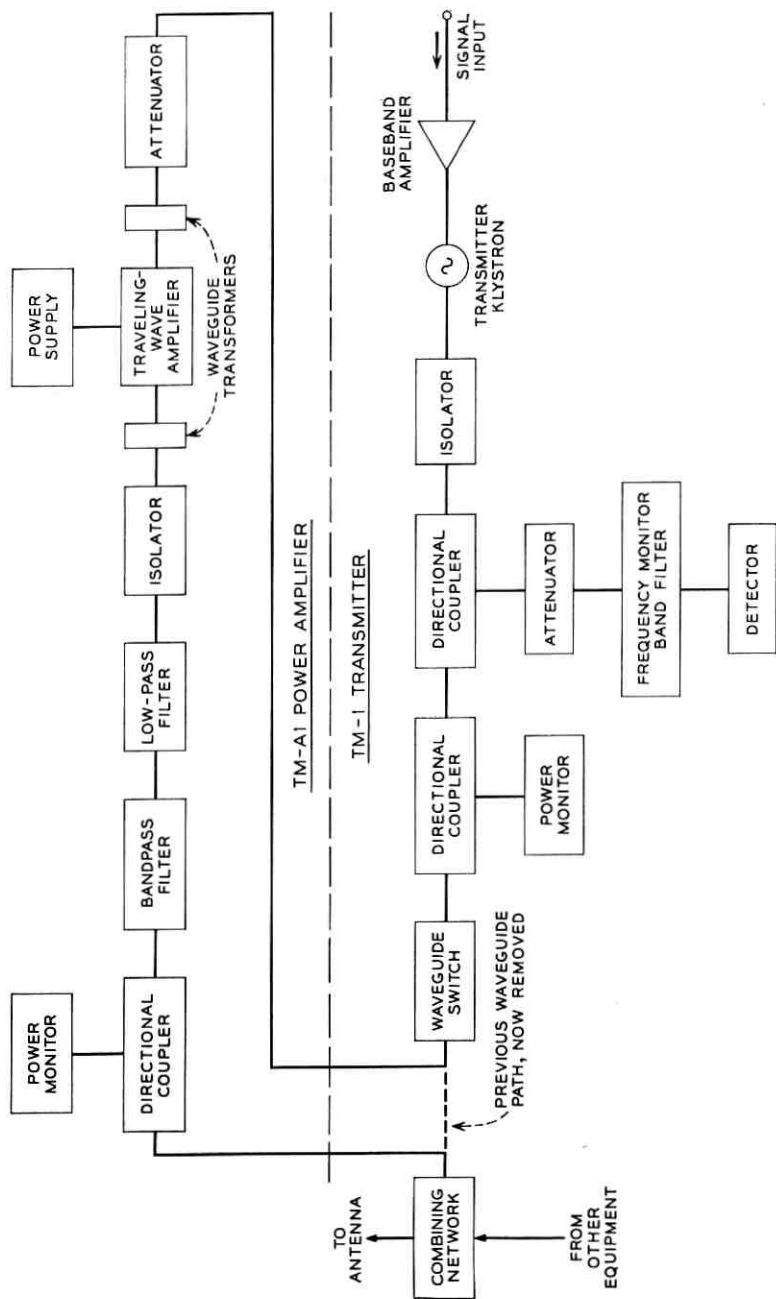
Fig. 28 — TM-A1 amplifier block schematic showing how amplifier may be added to a TM-1 transmitter.

TABLE II

Heater voltage	6.5v
Anode voltage	+2500 with respect to cathode
	+400 with respect to helix
Helix voltage	+2100 with respect to cathode
Cathode voltage	−1200v with respect to ground
Collector voltage	ground
Beam current	32 milliamperes
Collector dissipation	38 watts
Hot input return loss	17 db over entire TM band
Gain	21 db
Noise figure	25 db
Saturation power	+36 dbm
AM-PM conversion at +33 dbm output	2.5°/db
Spurious noise	20 db above background (max)

Provision is made in the TM-A1 amplifier to measure output power as shown in Fig. 28. The low-pass filter is provided to attenuate second harmonics generated in the traveling-wave tube while the purpose of the bandpass filter is to prevent wideband noise produced by the TWT from reaching receivers on the same waveguide run.

Performance tests made of a TM-1 system with a TM-A1 amplifier show that the amplifier introduces negligible transmission impairments in raising the outpuut power to 2 watts.
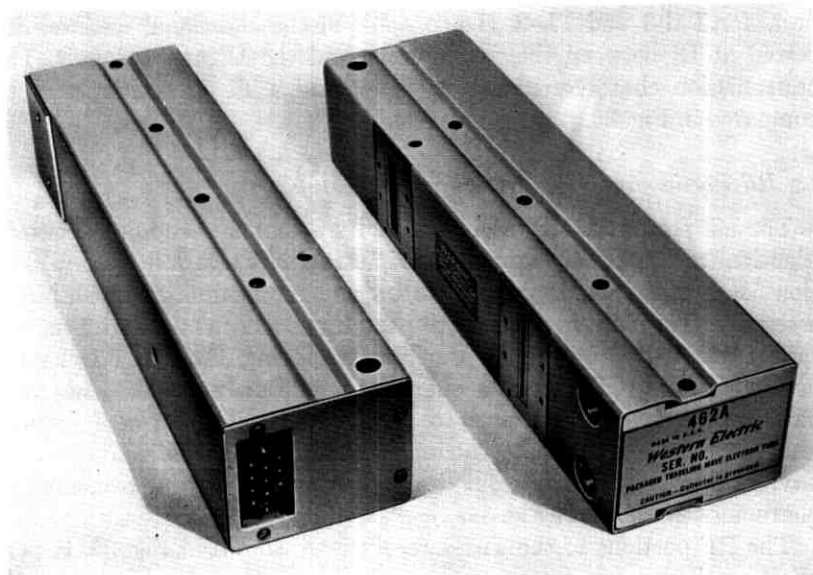
Fig. 29 — 462A packaged traveling-wave tube.

VII. RADIO RECEIVERS

7.1 *General*

The receiver portion is generally located on the right-hand portion of the RF panel as shown on the TM-1 photograph of Fig. 30. All the non-microwave circuits of the receiver except the preamplifier are contained in the IF and baseband plug-in unit that is the same for both TM-1 and TL-2, the general construction of which may be seen in Fig. 31. The box is divided into four shielded compartments with all the IF and baseband circuitry being divided among four printed wiring boards.

Fig. 32 shows the block diagram of either system. The functions served by the IF and BB unit and the receiver control unit are indicated. The IF bandpass filter and delay equalizer, used in TM-1 only, is the unit to the far right in Fig. 30.

With TM-1 channels spaced more closely than TL-2 channels, it was necessary to provide more discrimination against adjacent channels in TM-1 than in TL-2. Adding sufficient discrimination to the TM-1 RF bandpass filter would have been costly in terms of meeting stability requirements with temperature and the use of a narrower IF filter following the input IF amplifier would have meant separate IF and BB units for TM-1 and TL-2. Hence, some of the additional loss was inserted at IF between the preamplifier and the IF and BB unit. The transmission characteristics of a TM-1 and a TL-2 receiver may be compared in Fig. 33.

7.2 *RF Portion and IF Preamplifier for TM-1*

The RF portion of the receiver includes a channel-dropping network, identical to the TM-1 channel multiplexing network described in Section 5.3, a bandpass filter, an isolator, and the modulator preamplifier assembly. The design of the bandpass filter reflects the stringent requirements imposed by the close channel spacing. Each TM-1 channel uses a 5-cavity filter plus a channel separation network. The filter cavities are spaced $\frac{3}{4} \lambda$ apart to minimize coupling between sections and the filter is aligned by variable capacitance adjustments in each cavity. It is a maximally flat design having the typical transmission characteristic shown in Fig. 34.

The RF portions of the TM-1 receiver are shown in Fig. 35. It is in effect, a three-layer arrangement with the channel-dropping network mounted against the back plate of the RF panel. In a tandem ar-

Fig. 30 — Receiver portion for TM-1.
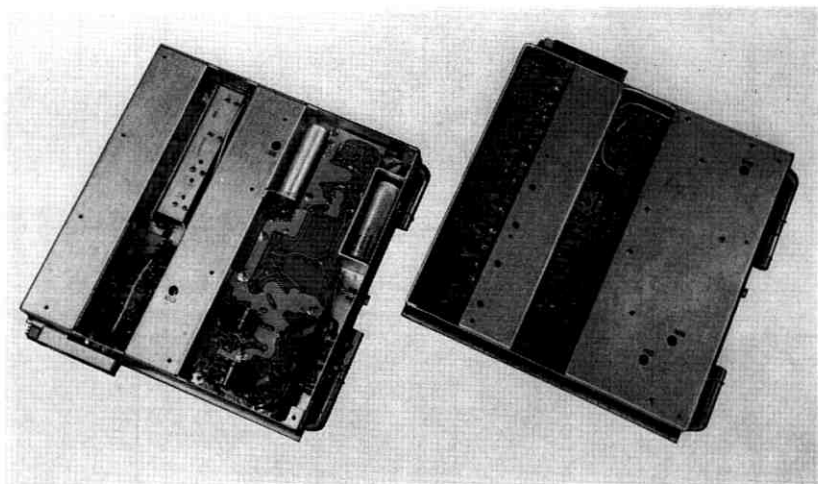
Fig. 31 — IF and baseband unit showing internal construction.

rangement of several receivers, the termination at the upper port of the channel-dropping network is replaced by a waveguide connection to the next receiver. The bandpass filter is located in the middle layer followed by a waveguide low-pass filter and the receiver isolator.

To meet over-all transmission objectives, the bandpass filter must present a good impedance to the channel separation network. This is very difficult to accomplish if the bandpass filter is terminated by the modulator, and therefore a receiver isolator is used between the filter and the modulator. Since this isolator is broadband, the filter is terminated by a network that is not frequency selective. The isolator also protects other receivers against beat oscillator energy that is present at the modulator signal input port. The isolator characteristics are shown on Fig. 36.

The transmitter and receiver isolators are resonance-type isolators, and the reverse loss to second harmonics is fairly low. Since the insertion loss of the bandpass filter to second harmonics is also low, a waveguide low-pass filter is required immediately ahead of the isolator as shown in Fig. 35. This filter attenuates the second harmonic of the beat oscillator (generated in the modulator) and prevents this energy from entering the modulator of another receiver and generating in-band interference products.

A 459-type klystron, operated in the same mode as the transmitter klystron, serves as the local oscillator. It is held at thermal equilibrium

Fig. 32 — Receiver block diagram.
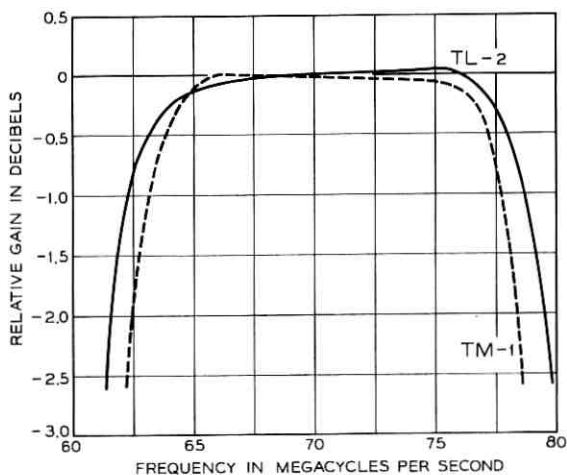
Fig. 33 — Relative receiver gain from RF input to IF output for TM-1 and TL-2.
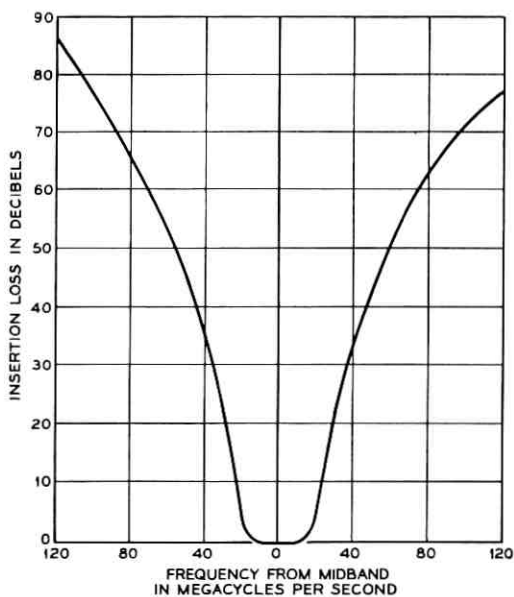
Fig. 34 — Transmission characteristic of TM-1 bandpass filter.
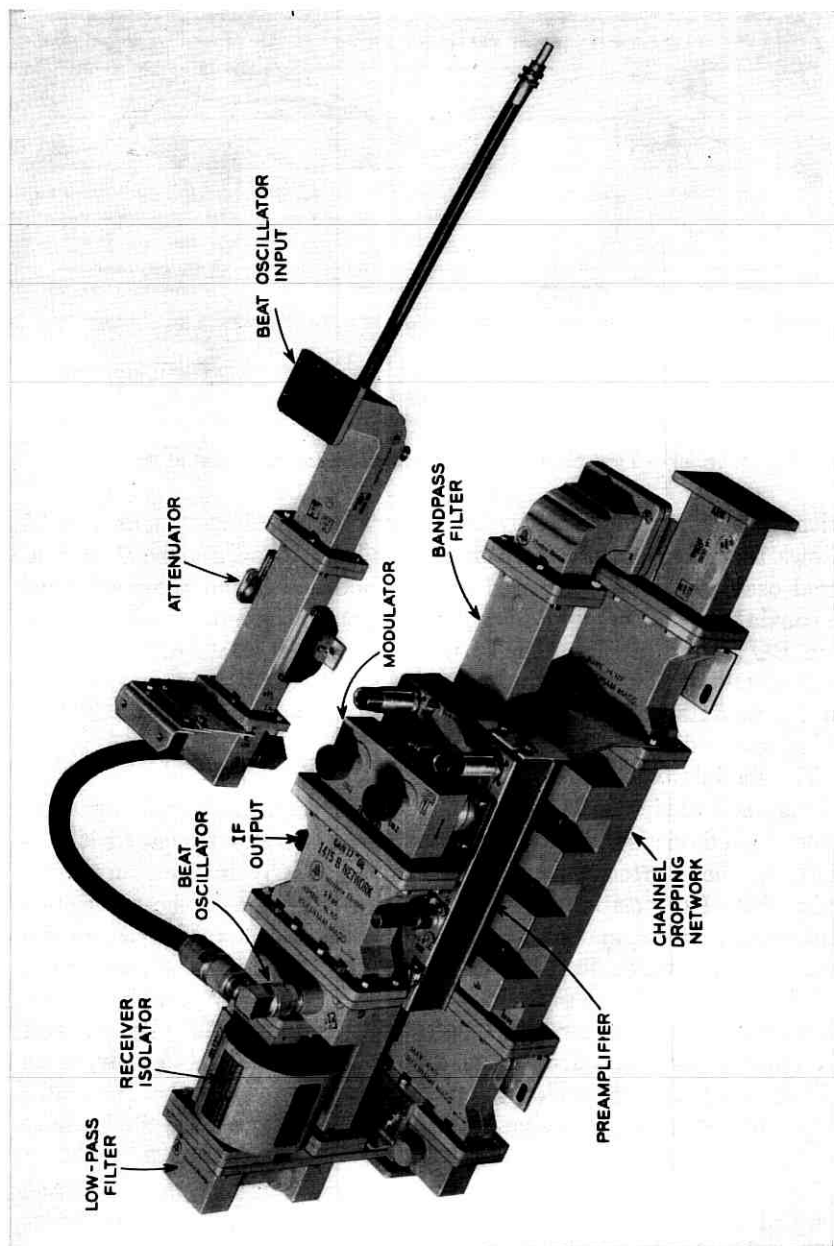
Fig. 35 — RF portions of a TM-1 receiver.
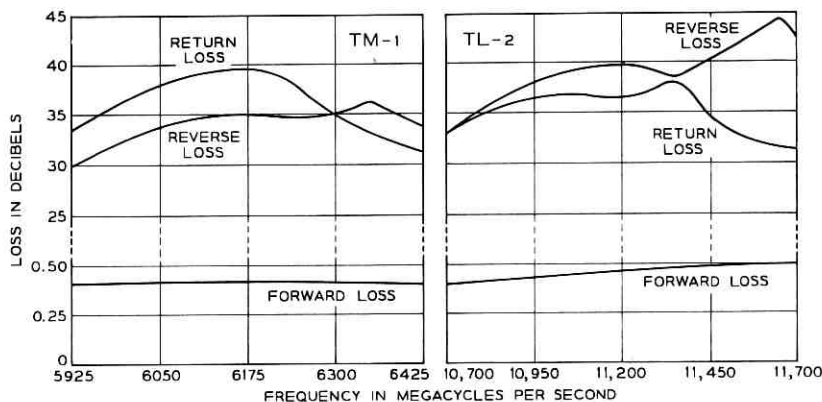
Fig. 36 — Typical isolator characteristics for receiver isolators.

with its transmitting mate by the vapor phase cooling system. Fig. 35 shows the waveguide attenuator that is used to adjust the 0 dbm of local oscillator power required by the modulator, and the waveguide to coaxial transducers used in the connection to the modulator. The RF and BO powers are applied to the input ports of a 3-db short slot coupler and are divided equally between the output ports that connect to the modulator. Isolation between the RF and BO sources is provided by the directivity of the coupler.

The modulator consists of two parallel guides equipped with a pair of matched diodes in the manner shown by Fig. 37. In this arrangement, each diode is coupled to the waveguide energy by locating it partially in the shorted waveguide line and partially in the shorted coaxial line. The position of the diode and locations of the waveguide and coaxial shorts, and the shape of the outer conductor of the coaxial line inside the waveguide are selected to give optimum performance.

The IF signal is separated from the RF signal by radial cavities. The cavities are stagger-tuned to provide optimum RF filtering over the 500-mc band and are spaced along the coaxial line to provide an RF short at the waveguide-to-coaxial interface. Since the modulator is broadband, a single design covers all channels, and the diodes may be replaced without retuning.

The two IF output signals from the modulator are paralleled and coupled to a transistor preamplifier as shown in Fig. 38. The interface or coupling network consists of a shunt tunable inductor paralleled by parasitic capacitance. The inductor is factory tuned to give a maxi-

mally flat transmission for channel 28B, and may be used for any other channel without retuning.

The preamplifier consists of two low-noise grounded-emitter stages plus a grounded-base stage. It has a noise figure of about 4 db. The nominal performance characteristics from the RF input to the microwave bandpass filter to the IF output of the preamplifier are:

RF to IF conversion gain.................................... 18 db
Noise figure.. 10.5 db
Transmission flatness over the 64–76 mc band................ 0.2 db

7.3 *RF Portion and IF Preamplifier for TL-2*

The channel-dropping networks and bandpass filters used in TL-2 were designed originally for the TJ Radio System, and the filters are of two types. Three cavity bandpass filters are used in all cases except for the last receiver in a lineup if the standard frequency plan is followed. Here a 4-cavity filter is specified and the channel-dropping net-
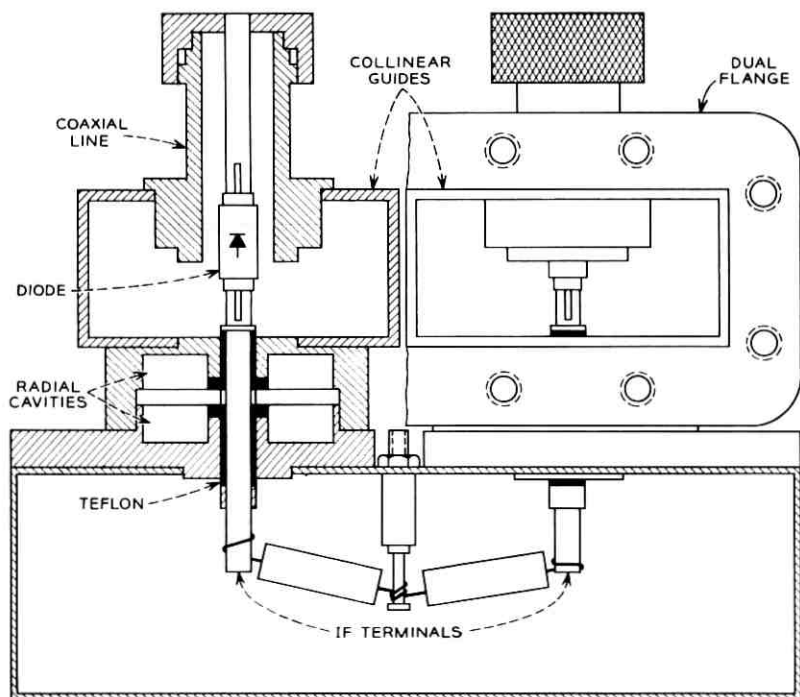
Fig. 37 — Internal configuration of modulator.
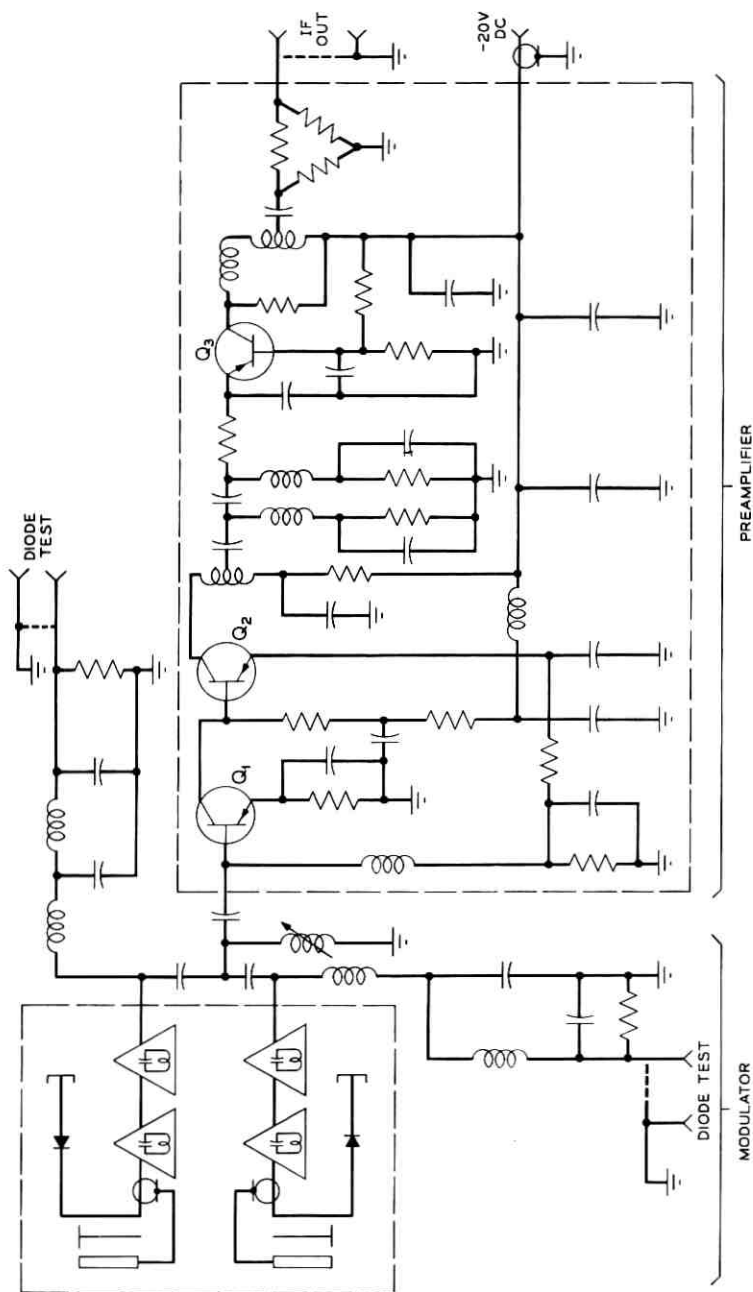
Fig. 38 — TM-1 modulator-preamplifier schematic.

work may be omitted. The transmission characteristics for the two types of filters are shown in Fig. 39; the characteristics of the channel-dropping network are given on Fig. 12.

The modulator-preamplifier assembly for TL-2 is shown in Fig. 40 where the 4-cavity filter, the receiver isolator and the modulator block may be identified readily. The preamplifier is housed in the section to the rear of the modulator block. The isolator serves the same purpose as the isolator in TM-1 and its performance characteristics are also
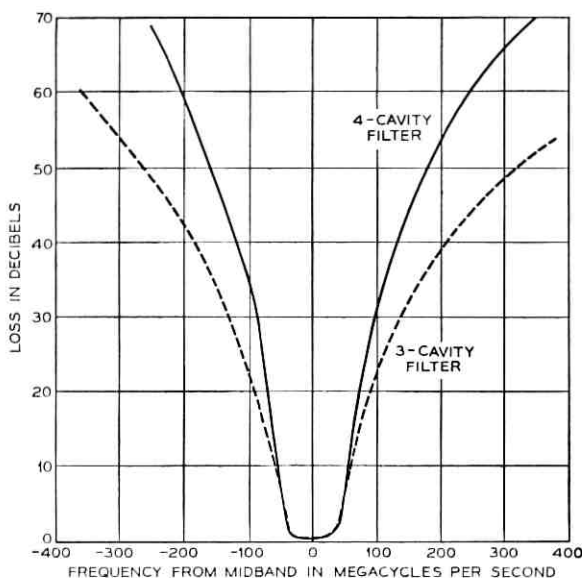
Fig. 39 — Representative transmission characteristic of TL-2 bandpass filters.

shown in Fig. 36.* Here again, the use of the isolator makes the modulator-preamplifier a broadband device, and a bandpass filter, an isolator, and a modulator-preamplifier may be assembled and used without making any over-all adjustments.

Beat oscillator power at about 0 dbm is applied to the modulator at the waveguide port that is visible at the front of the block. A low-pass filter in the signal waveguide path has not been found necessary since

---

* In early TL-2 production a tuner was used rather than an isolator. The tuner was adjusted for an optimum impedance into the bandpass filter. Thus, in the earlier design, the modulator-preamplifier assembly was a frequency sensitive entity.
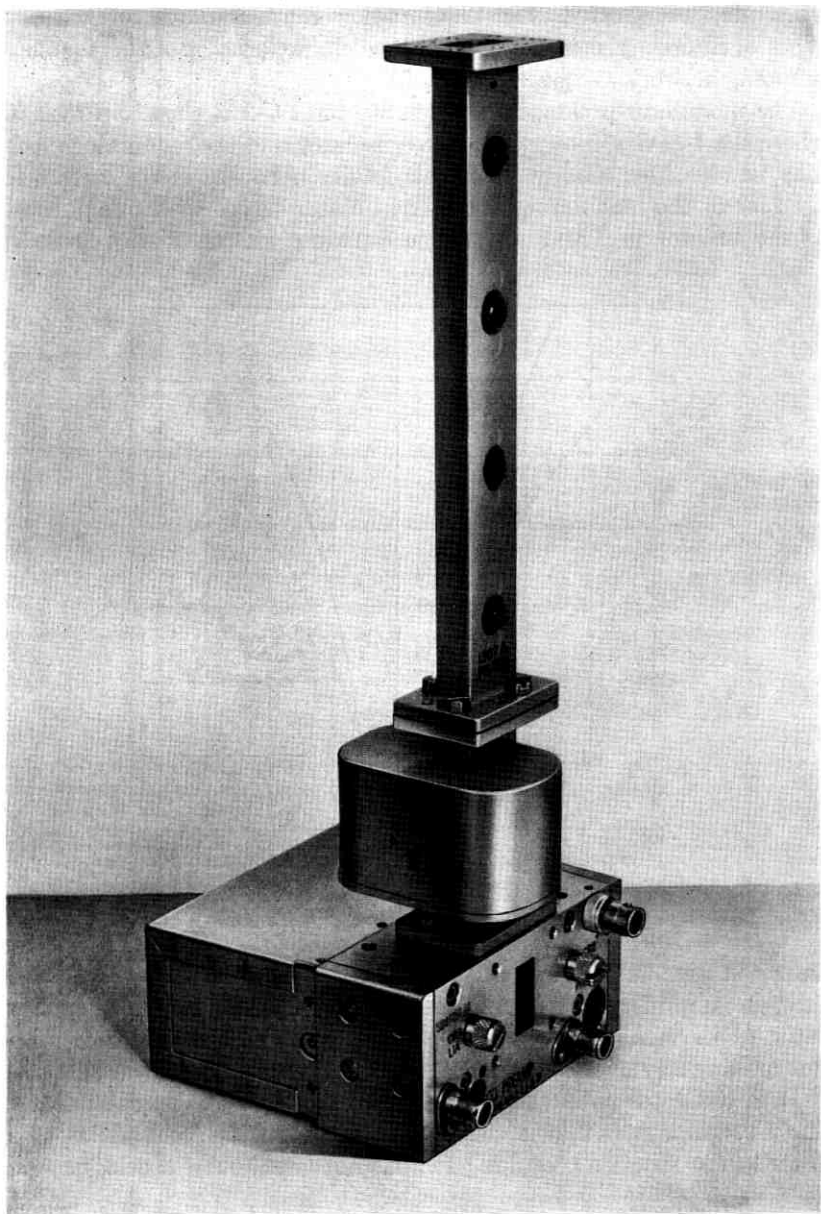
Fig. 40 — TL-2 receiver-modulator preamplifier.

nally flat from less than 10 cycles to over 6 mc. A schematic of the amplifier is shown in Fig. 15. The amplifier is packaged in the transmitter control unit.

The nominal deviation sensitivity of the TM-1 klystron is less than that of the TL-2 klystron, hence the TM-1 input amplifier requires additional gain. The schematic for TM-1 is shown in Fig. 16 where the output amplifier is similar to the TL-2 amplifier and the preamplifier provides the added gain. The maximum gain of the amplifier is 34 db, and it is capable of supplying a maximum voltage of 12 volts peak-to-peak. The transmission characteristic is essentially flat from less than 10 cycles to over 6 mc.

As described previously, the phase inverter is required to obtain hitless switching. By providing for reversal of the baseband signal in the inverter of the TM-1 amplifier, the proper polarity of the diversity switch in the next receiver can be obtained.

The repeller coupling circuits for the two systems are also shown in Figs. 15 and 16. In TL-2, the time constant R_1C_1 is sufficiently long to insure good low frequency performance and the breakdown diode protects the repeller against voltages that are positive with respect to the klystron cathode. The voltage across C_1 is about 500 volts however, and changes in leakage current will result in frequency errors. In TM-1, with the more stringent requirements on frequency stability, the
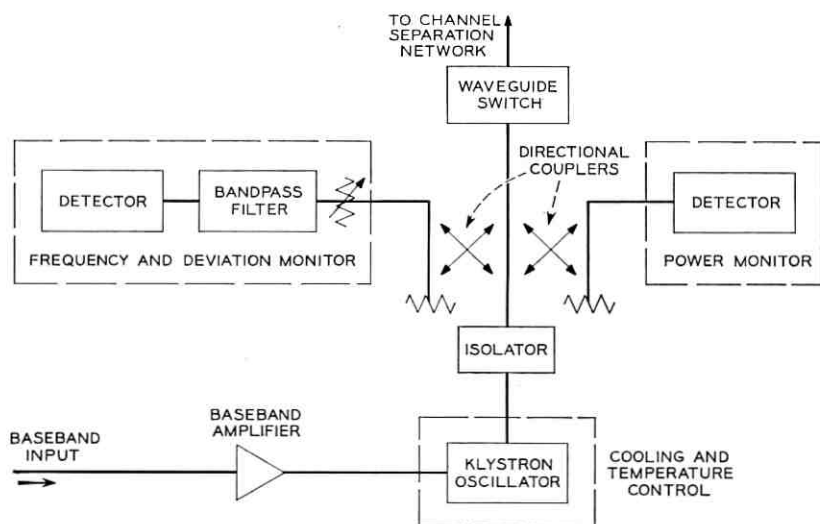
Fig. 13 — Transmitter block schematic.
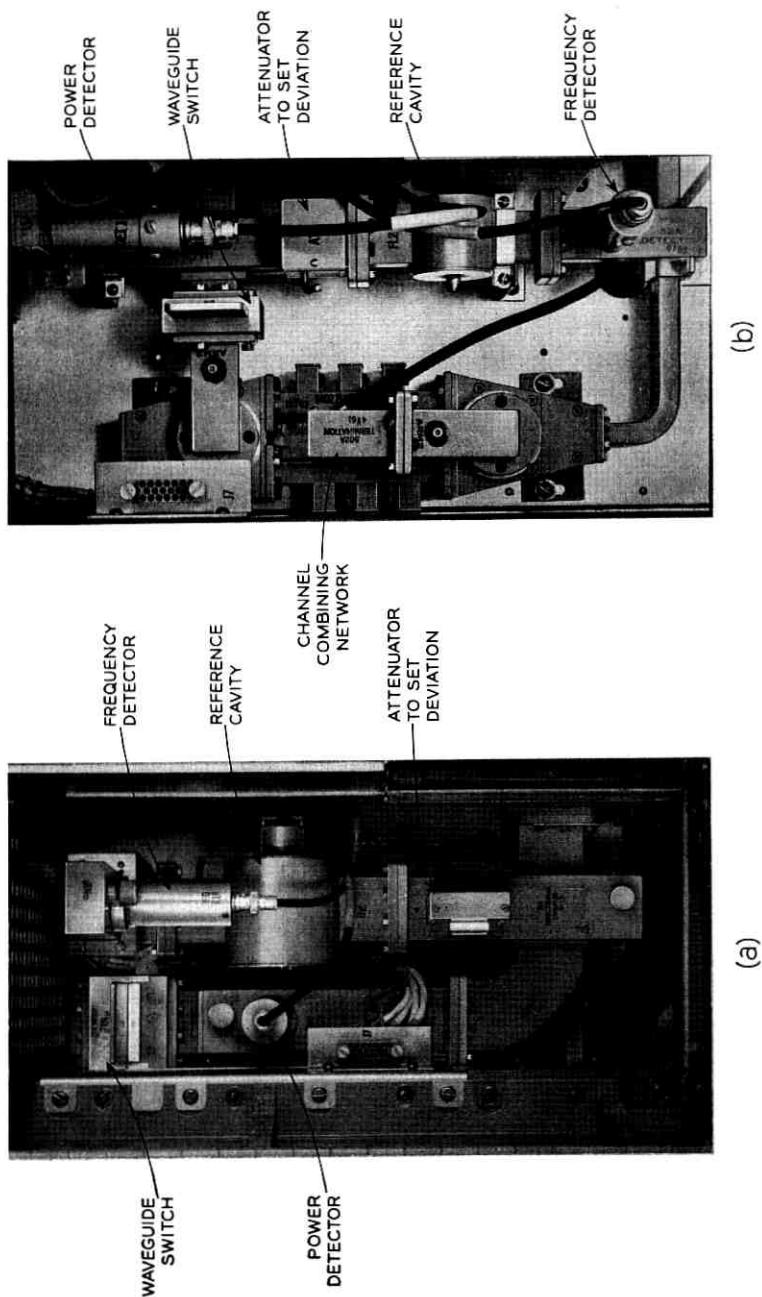
Fig. 14 — (a) TM-1 transmitter. (b) TL-2 transmitter.

the TL-2 receiver modulator design provides sufficient balance against the second harmonic of the local oscillator.

The circuit of the TL-2 preamplifier is shown in Fig. 41. The important difference between this preamplifier and the one for TM-1 obtains at the modulator-preamplifier interface. Where TM-1 is tuned, TL-2 is broadband; the output capacitance of the TL-2 modulator is too high to accommodate the TM-1 circuit. While the untuned circuit provides less gain, it was possible to optimize the noise performance of the circuit with the input transformer and to make up the gain by using additional grounded-base stages. The nominal conversion gain of
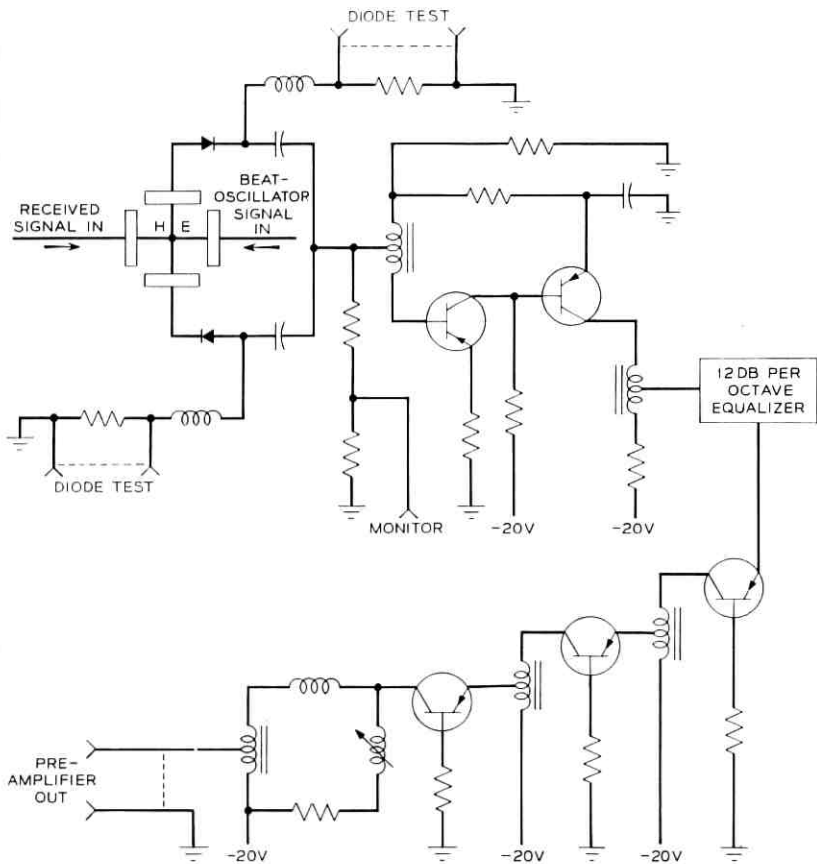
Fig. 41 — TL-2 preamplifier simplified schematic.

this modulator-preamplifier is also 18 db and its nominal noise figure, referred to the input of the mixer, is 10.5 db.

7.4 *The IF Amplifier*

Nearly all the IF stages in the IF input and output amplifiers are grounded base stages as shown in Fig. 42(a).[11] Using 2:1 interstage transformers as shown, the theoretical current gain per stage is 6.0 db but due to transformer losses, the practical current gain is about 5.5 db. To a first approximation, and neglecting the transformer step-up, the equivalent circuit is as given in Fig. 42(b), where L is the sum of the transformer leakage and emitter inductance, R is a damping resistor and the capacitors are the collector and transformer shunt ca-
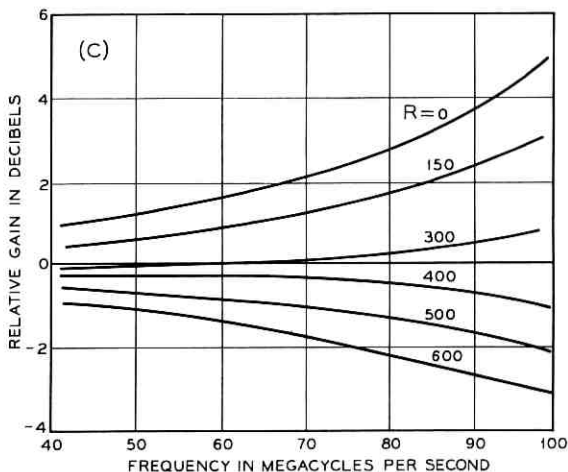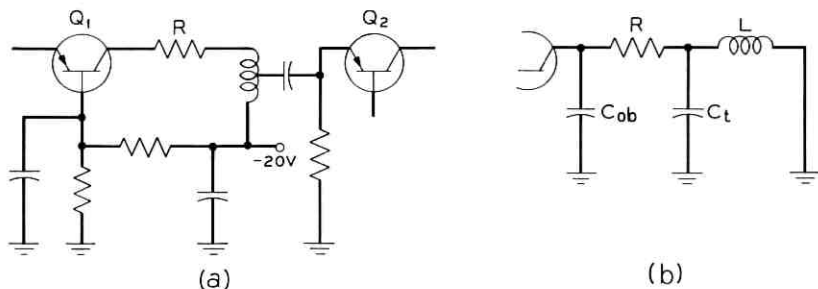
Fig. 42 — IF interstage; (a) typical IF stage, (b) equivalent circuit, (c) relative transmission characteristic for several values of damping resistance.

pacitances. Without damping, such an interstage peaks at about 135 mc for the transistors, transformers, and printed board design used. The damping resistance is selected for a maximally flat transmission, and Fig. 42(c) illustrates the relationship between damping and transmission. By designing the active circuits for a wide transmission band, it is possible to use a passive network to limit the band to the desired 64–76 mc. This is the purpose of the IF bandpass filter and equalizer shown in Fig. 32.

The input IF amplifier shown in Fig. 32 includes three variolossers controlled by an AGC circuit to hold constant the IF power delivered to the limiter over a fade range of at least 35 db. Each variolosser is of the form shown in Fig. 43. The losser element is a point contact germanium diode shunted across the circuit. Control current from the AGC detector is made to flow through this diode; a high value of control current, corresponding to a high RF input to the receiver, produces a low impedance path to ground, and hence, a high loss in the variolosser section. The series resistance, $R_1 + R_2$, serves again to damp the transmission characteristic. The relative transmission characteristic of the stage can be held very nearly fixed over a wide range
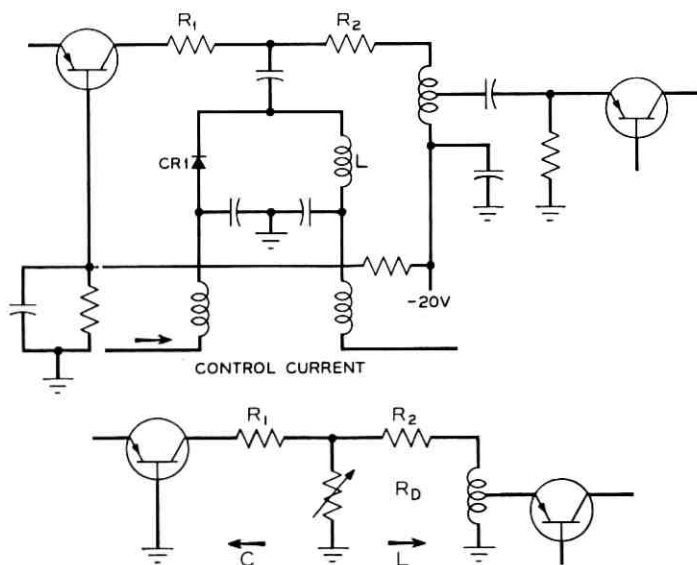
Fig. 43 — A variolosser stage.
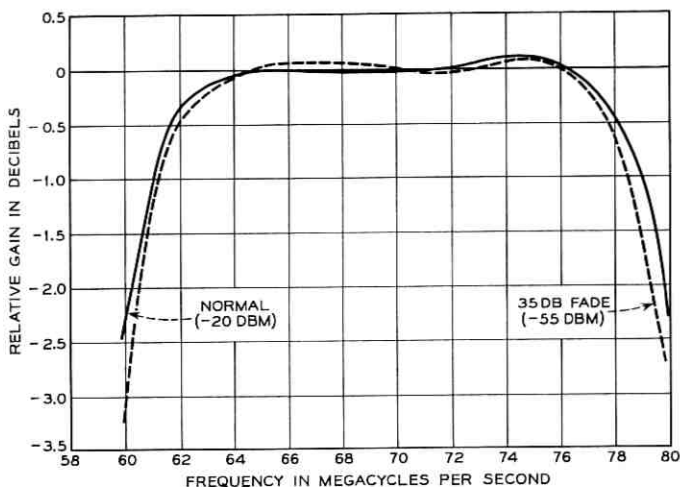
Fig. 44 — Transmission characteristic of the IF amplifier for normal and faded inputs.

of loss, if the variolosser diode is located at a constant resistance point. This is achieved if

$$R_1 = R_2 = \sqrt{\frac{L}{C}},$$

where C is the parasitic collector capacitance and L is the parasitic inductance contributed by the transformer, the wiring, and the following transistor. The maximum flat design is obtained when

$$R_1 + R_2 = \sqrt{\frac{2L}{C}} \sqrt{1 - \left(\frac{f_c}{f_p}\right)^2}$$

where f_p is the peak frequency of the interstage and f_c is the center of the band. The variolossers therefore, contribute a small negative transmission slope that is overcome by slightly peaking the other IF stages. Fig. 44 shows transmission characteristics of a typical IF amplifier for a normal input and for an input corresponding to a 35-db fade.

The location of variolossers in the circuit is critical. They are preferably used at low-level points to minimize AM-to-PM conversion in the receiver but if located too near the input of the receiver, the signal power level at the stage following the variolosser could be lower than the signal power level at the input for normal operating conditions.

Under these conditions the later stages could contribute significantly to the noise figure of the receiver.

The variolosser line-up in the receiver is shown in Fig. 45(a). Since the AGC circuit holds P_{out} to a fixed value, and the maximum gain is known, the loss L of each variolosser is fixed for a given value of input power. Fig. 45(b) shows a measurement of noise figure of a TL-2 receiver versus input power.

The complete IF amplifier (apart from the preamplifier) includes 12 stages ahead of the bandpass filter and 7 stages following the filter. The nominal maximum IF gain is 92 db, but some 19 db of padding is provided nominally as shown in Fig. 45(a) to insure good impedance terminations for the filter and equalizer. The exact value of padding is adjusted as part of the manufacturing testing routine. A minor adjustment of the delay equalizer is also made after the other adjustments of the IF and baseband unit are completed.

An IF output is available from the receiver at the IF monitor jack as shown in Fig. 32 to permit an IF connection at 70 mc to other microwave systems. The power output at this point is 0 dbm.

(a)

(b)
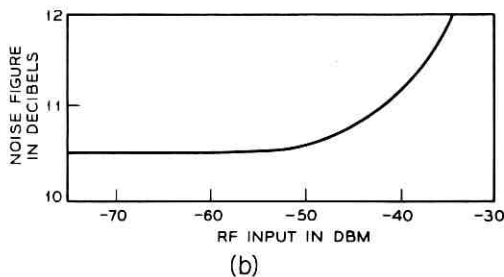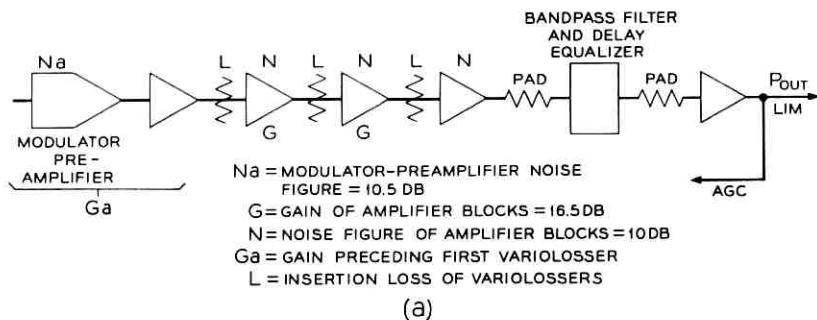
Fig. 45 — Thermal noise performance; (a) gain allocation in the receiver, (b) receiver noise figure vs RF input.
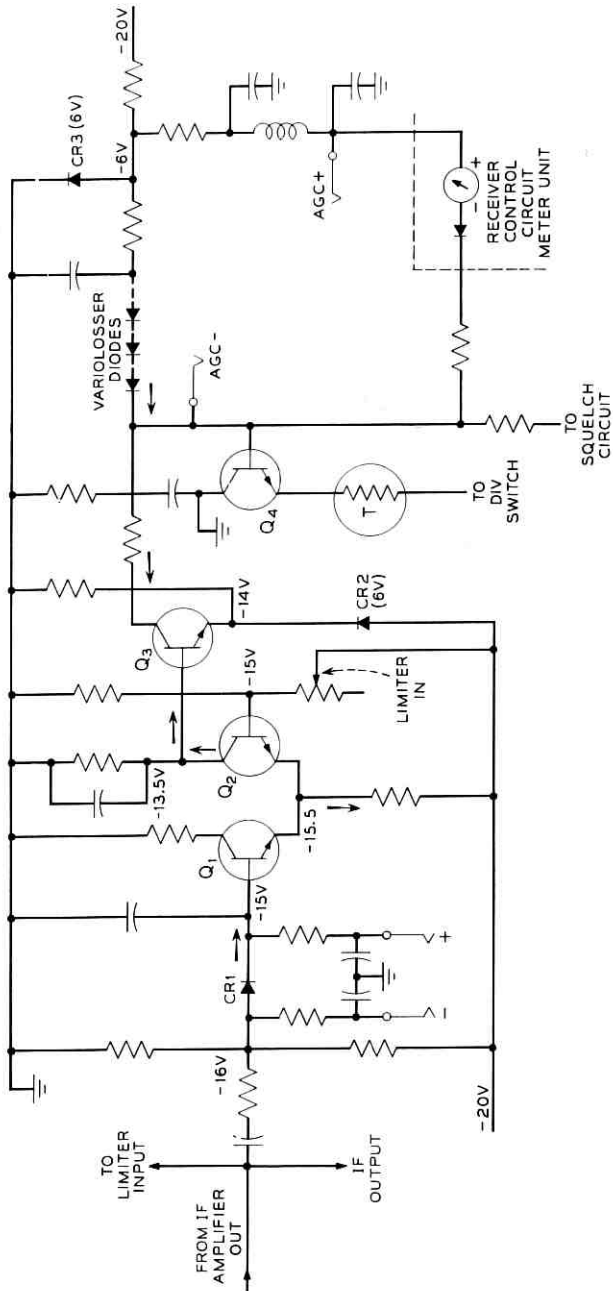
Fig. 46 — Automatic gain control circuit.

7.5 AGC Circuit, Squelch Operation and Diversity Drive

The elements of the AGC circuit are shown in Fig. 46. The output from the final IF stage is divided among three loads; the limiter (+11.5 dbm), the IF output (0 dbm), and the AGC detector. The AGC rectifier, CR_1, is followed by a three-stage dc amplifier. Since the variolossers are shunted across the transmission path, a high loss corresponds to a high-control current. When the IF output power increases, additional dc currents flow in the amplifier in the directions shown in Fig. 46. The gain of the circuit is such that when the feedback loop is open, a change in the IF power of 0.1 db is sufficient to swing the dc amplifier over its entire operating range. The LIM IN potentiometer is used to adjust the operating range of the AGC amplifier, hence the desired IF output power.

When the input to the receiver is reduced, the collector current of Q_3 decreases and the voltage at the base of Q_4 decreases linearly with input power in db. At the end of the regulating range when the current through the variolosser diodes is zero, the voltage at the base of Q_4 is −6 volts. A slight further reduction in IF power will result in zero collector current for Q_3 with the Q_4 base voltage going to zero. Typical operating characteristics of the circuit are shown in Fig. 47. The abrupt change in the squelch voltage from −6 to 0 results in a positive trigger for the squelch circuit. The IF power to the limiter is held essentially constant up to the end of the regulating range beyond which the output decreases db for db with the input. In this circuit, the squelch point is determined by the available IF gain. There are no adjustments in the control circuit to set the point at which the receiver squelches. The total IF gain of the IF and baseband unit is, therefore, adjusted at the time of manufacture.

The above description is simplified in that noise was not considered. Practically, as the gain of the receiver is increased, the noise will also increase and the AGC circuit operates to hold the output of signal plus noise constant. In a practical case then, the operating characteristic conforms to the carrier plus noise curve. It is apparent that if the maximum gain of the receiver is too high, the resulting high noise will prevent receiver squelch. For this reason, the gain of the preamplifier is restricted. Any IF and baseband unit can work with any modulator-preamplifier.

In the receivers for the TM-1 and TL-2 systems, the maximum gain from the input of the RF band filter to the monitor jack, shown in Fig. 32, is about 80 db. This allows approximately 35-db fade margin for a
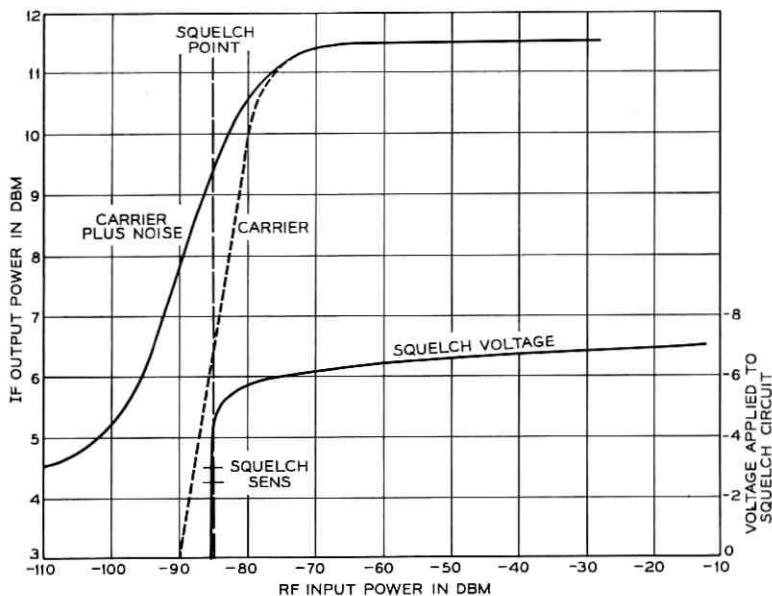
Fig. 47 — Operation of the automatic gain control and squelch circuits vs RF input power.

normal input of −45 dbm, and provides approximately 6-db margin against squelch malfunction due to excessive noise.

It is important that the receiver be squelched when the input signal drops below a given power. Unbalances in the discriminator characteristic can result in the AFC circuit being biased off when the receiver goes to full noise. Under these conditions, there is a danger that the circuit will not restore when the RF signal becomes normal again. Full noise in a radio channel could also cause interference in other facilities since groups of voice circuits from the radio facility in question are frequently combined with other groups of voice circuits transmitted by other radio or cable facilities.

The squelch relay has two transfers. One circuit is used to open the AFC loop when the receiver goes to full noise, while the other transfer is used to place a short circuit across the output of the receiver baseband amplifier under these conditions.

The linear portion of the squelch voltage characteristic shown in Fig. 47 between 6 and 7 volts provides information regarding RF input power. It serves as the control characteristic for the diversity switch. The circuit has been designed so that the slope of the control

characteristic is essentially the same in all receivers and is nearly independent of temperature. The temperature correction is provided by the temperature sensitive resistor following the emitter of Q_4 (Fig. 46).

The operation of the bistable diversity switch is not affected by temperature-sensitive control circuits so long as the control characteristics of the two receivers are alike. For the revertive switch, however, where the control voltage is compared with a fixed voltage, the control voltage must be independent of temperature.

7.6 Discriminator and Receiver Baseband Amplifier

The receiver baseband amplifier for the TL-2 and TM-1 systems is designed to provide television and telephone service. This required extending the low frequency cut-off to below one cycle and, in the case of the receiver amplifier, providing adequate linearity so that the amplifier contributes negligible intermodulation noise, differential phase and differential gain.

The receiver baseband amplifier, shown in Fig. 48, consists of two feedback amplifiers in tandem. The input amplifier is a three-stage amplifier with a loop feedback connection between the emitters of the first and third stages. A minimum feedback of 20 db is maintained at 4 mc, with feedback increasing to about 30 db at low frequencies. The input coupling circuit was designed for minimum loss between the discriminator and the amplifier which is also the condition for minimum thermal noise.

The receiver gain control is located between the two baseband amplifiers and has a range of 6 db. The output amplifier is a two-stage feedback amplifier with the second stage employing two transistors in a compound connection. Its output capability exceeds +10 dbm. For a 4-mc deviation of the RF signal, the normal sine wave output is +6.5 dbm. The inductor in the output collector insures that virtually all the signal current flows into the load and the feedback circuit includes compensation for the low-frequency transmission characteristic caused by the inductor. The feedback trimmer capacitor is adjusted at the time of manufacture to set the transmission characteristic of the overall video amplifier.

7.7 Receiver AFC

Except for time constants, the receiver AFC circuits are essentially the same as for the TL-1 design.[11] A system having a transmission
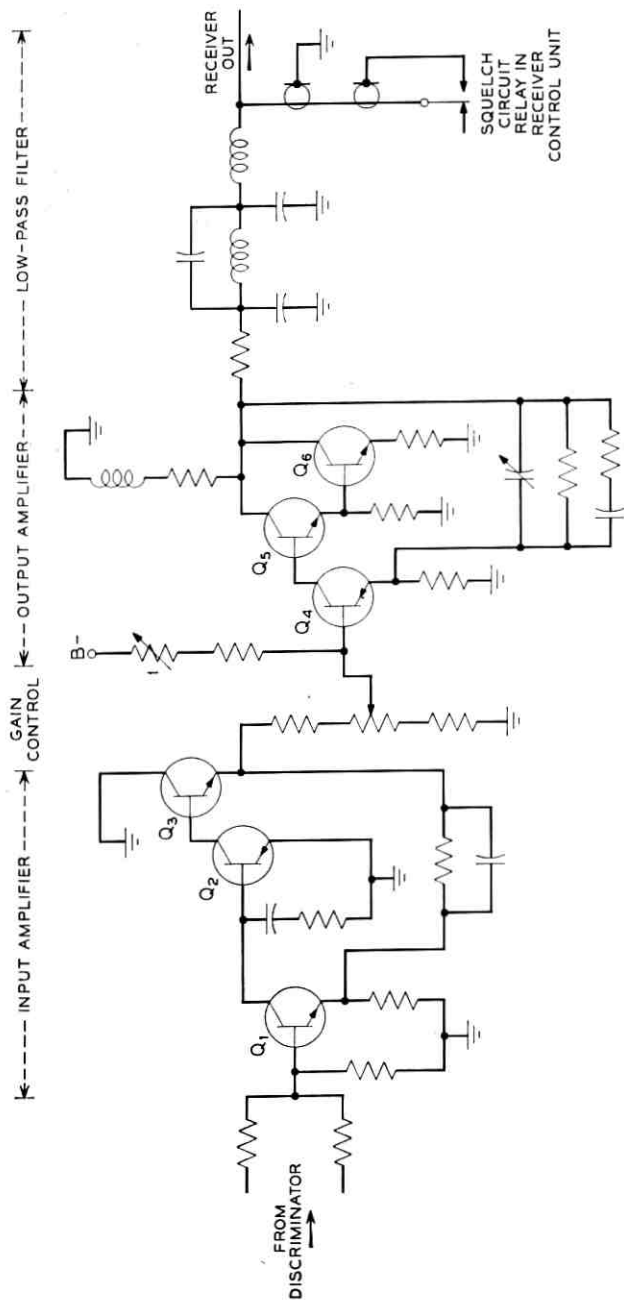
Fig. 48 — Receiver baseband amplifier.

characteristic that extends to the order of 1 cycle per second requires a slowacting AFC circuit. The cut-offs in the AFC feedback characteristic must be well separated in frequency to avoid gain enhancement and the lowest frequency cut-off must be well below the band of interest to avoid erasing signal information. The first two cut-off frequencies in the AFC circuit for the TM-1 and TL-2 receivers occur at 0.03 cycle per second and about 0.5 cycle per second.

7.8 *Revertive Diversity Switch*

Two forms of diversity switches may be employed with the TM-1/TL-2 combination. The simple bistable switch furnished with the TL-1 system has previously been described in detail.[2] In the bistable switch, the AGC signals of the diversity pair are compared; the difference signal is fed to a Schmitt trigger circuit which activates the switch when the input of the working receiver drops below the input to the standby receiver by a predetermined amount. If the nominal received RF power for one system is appreciably stronger than the nominal received power for the other system, it is desirable to have the switch revert to the system having the stronger received signal. This is accomplished in the revertive switch by using switching logic which orders that transmission be via the preferred channel unless and until its incoming radio signal power drops below a predetermined absolute value. At this predetermined level, the logic block is removed and the switch functions in the bistable manner, causing a switch if the received power of the preferred channel compares unfavorably with the incoming received power of the other system. The block schematic of Fig. 49 illustrates how the revertive comparator may be associated with either receiver, or not used at all for bistable operation. It is recommended that the switch be set up on a revertive basis only if the normal incoming level of the two systems is appreciably different (say 5–6 db), or if the performance of one of the two systems is appreciably superior to the other.

The operation of the revertive switch may be illustrated by means of Fig. 50. If a point whose coordinates are given by the received power of channel A (preferred) and channel B (protection) falls in the shaded area, the switch will select channel A. If that point falls in the crosshatched area, it will switch to channel B. If the point falls in the clear area, the switch will not operate — it will hold whatever position it has. The width of both corridors in Fig. 50 are adjustable.

The bistable switch operates similarly except that the bistable cor-
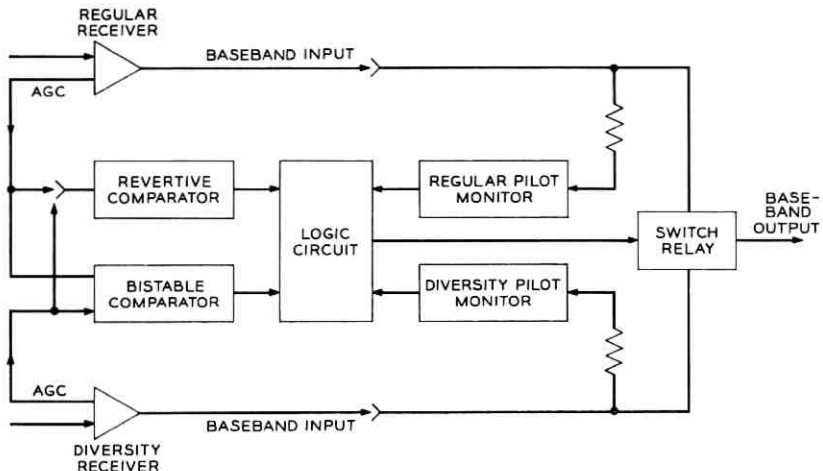
Fig. 49 — Block schematic showing use of a revertive diversity switch at a receiver location.
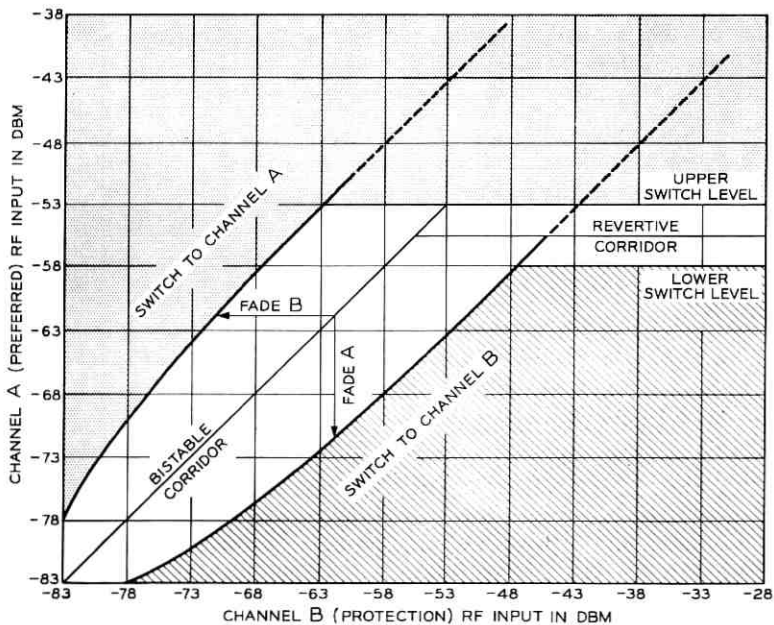
Fig. 50 — Typical TM-1/TL-2 revertive switch characteristic based on RF inputs.

ridor is extended as indicated by the broken lines and all the area below the corridor is assigned to channel B.

7.9 Other Features

Order wire and alarm arrangements, and all other circuits not mentioned specifically above, are very similar to the designs for the TL receiver. The reader is referred to the earlier article for details.[2,11]

VIII. POWER SYSTEM*

8.1 General

Power to the TM-1/TL-2 system is maintained during commercial ac power outages through the use of batteries which are an integral part of the power plant. The batteries are charged to float voltage and act as a filter for the output of the ac rectifier unit when ac power is present. Continuous power is provided to the radio bays since the batteries are always in the circuit and no transfer of power source is required when ac fails.

The block diagram of Fig. 51 shows the power design for TM-1/TL-2 radio. The battery charger, fed from 117-volt commercial ac power, supplies the stabilized dc voltage to float-charge 6-volt batteries in series-parallel combinations whose number depends upon the desired reserve capacity. Power for the transistor circuits of each RF panel is supplied through a voltage regulator, while a second regulator powers a dc-to-dc converter and related circuits to provide the required klystron voltages. Provision is also made to power the traveling-wave tubes in those stations where TM-A1 amplifiers are employed. Each TM-1 or TL-2 RF panel (typically one transmitter and one receiver) requires up to about 8 amperes maximum, hence the 48-ampere charger can service 6 RF panels. An allowance of 8 amperes should also be made for a TM-A1 power amplifier. A 16-ampere charger is available for small installations.

The batteries are housed in a separate cabinet with the large charger, or on shelves on the radio bay where the small charger is used. There is often a preference for connecting fewer than the maximum number of RF panels to a charger and battery unit in order to increase the reserve capacity.

The −24-volt office battery may be used to power the radio equipment in central office installations.

---

* This section was prepared by Mr. P. W. Ussery.
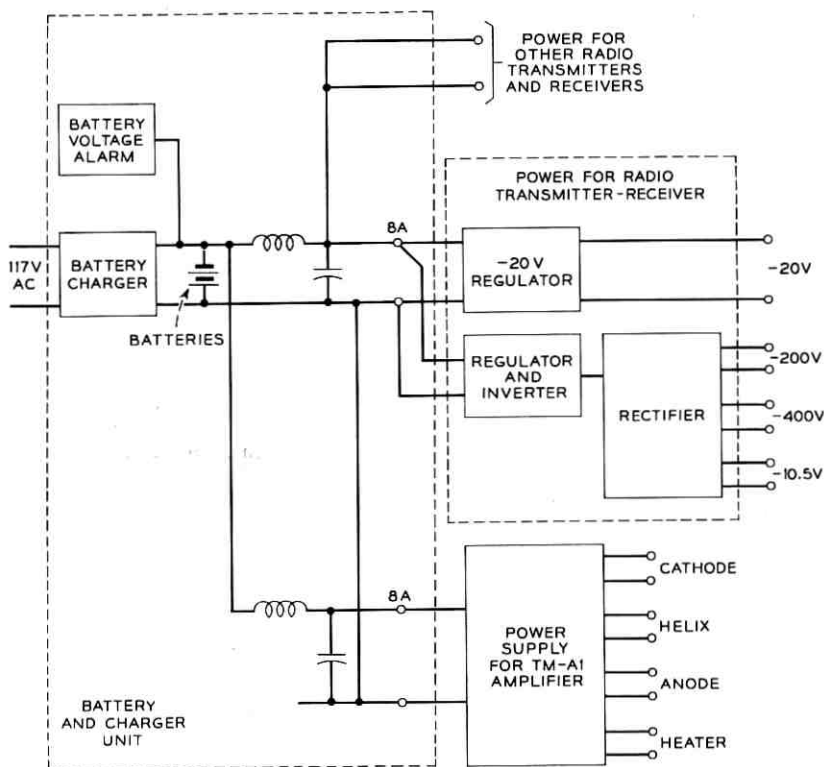
Fig. 51 — Power system block schematic.

8.2 *The Charger Unit*

A simplified schematic of the 48-ampere charger is shown in Fig. 52. The ferroresonant transformer in the battery charger regulates the ac voltage applied to the rectifier of the battery charger. Silicon diodes in a full-wave bridge arrangement give a dc output which is applied to the batteries for floating or charging.

The batteries are high specific gravity, lead-acid types connected in series, and float at 27.6 volts. They were chosen to provide maximum reserve at minimum cost for severe environments involving wide temperature swings from $-20°F$ to $+120°F$. Most of the time the batteries are being float-charged and this condition contributes to very low battery maintenance. The high specific gravity aids both in protecting
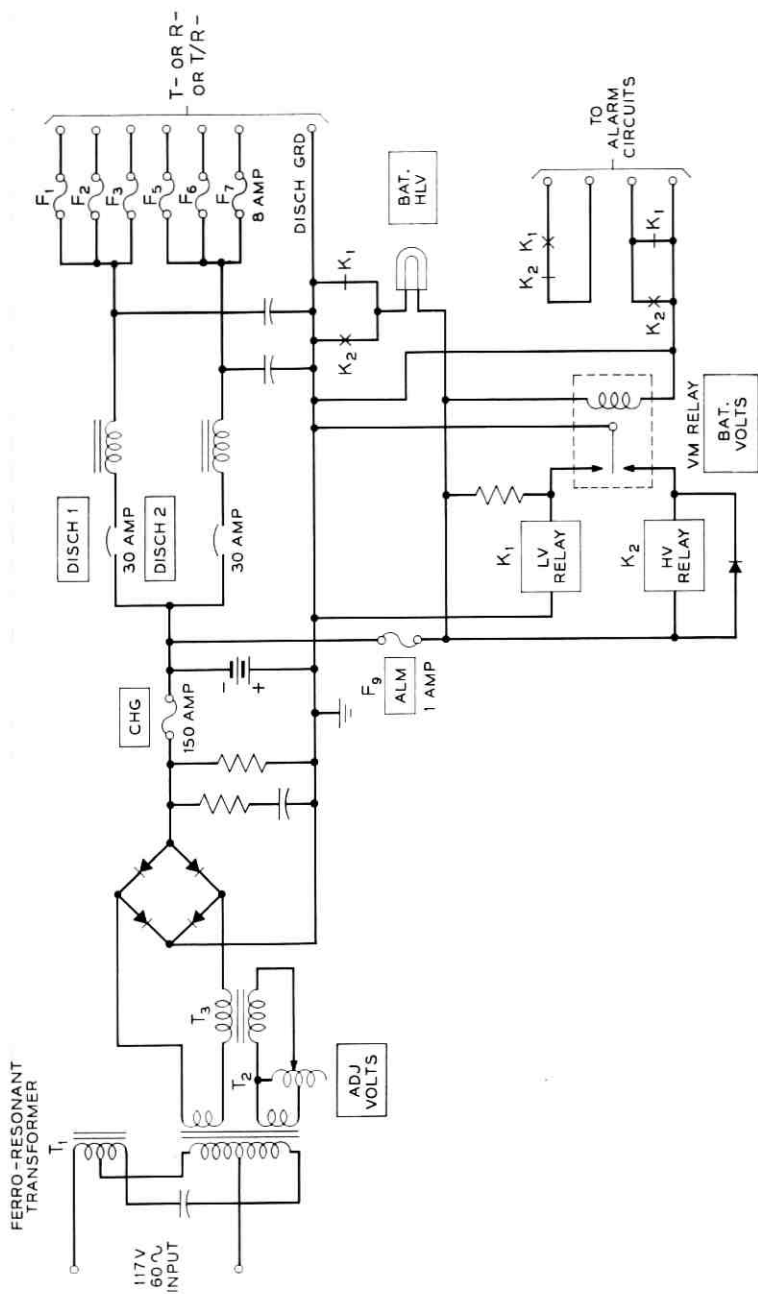
Fig. 52 — 48-ampere battery charger and power supply, simplified schematic.

the batteries and increasing their hours of reserve at low temperatures. At −40°F they do not freeze, even if fully discharged.

The battery chargers incorporate a battery voltage alarm to operate an alarm lamp on the front panel of the charger when the battery voltage falls outside the normal limits and to send an alarm to the central office when the battery voltage is below normal. The power cabinet containing the 48-ampere charger is shown in Fig. 53.

8.3 *Power for the Radio Equipment*

The radio equipment requires −20 volts for the transistor circuits, −400 volts for the klystron cathode, 10.5 volts as a klystron heater supply voltage, and a voltage that can be varied between −400 volts and −600 volts for the klystron repeller. The latter requirement is satisfied by a −200-volt supply that is connected in series with the −400-volt supply. An 1800-cycle square wave is used to operate the magnetic amplifier in the receiver AFC circuit. The klystron voltages must be very precisely regulated in order to achieve the required stability of the average transmitted frequency. Also, the noise on the output voltages of the power supply must be very low to obtain the signal-to-noise ratio required to meet the message and television transmission limits for the system. These factors contribute to very demanding requirements on the stability of the power supply.

Voltage stability requirements were derived based on an allocation of permissible frequency errors and the known sensitivities of the 457A and 459A klystrons. The stability requirements are given below:

Voltage	TL-2	TM-1	Currents for 2 Tubes
−400V	±0.45%	±0.10%	100 ma
−200V	±0.45%	±0.05%	10 ma
10.5V	±0.75%	±0.75%	1800 ma

These objectives should be met over a three months maintenance interval that may include temperature changes up to 100°F and ac line voltage changes from 105 to 129 volts. In order to meet the more stringent TM-1 requirements, several refinements of the initial TL-2 design were required. Regulators were added to both the −200-volt and −400-volt supplies and these regulating circuits are located in temperature-controlled ovens.

The other power supply requirements, common to the two systems, are as follows:

Voltage	Stability	Currents
−20V	±1%	1.1 amp (max)
43V ac(1800 cps)	±0.45%	10 ma
27.6V	battery	750 ma (max)
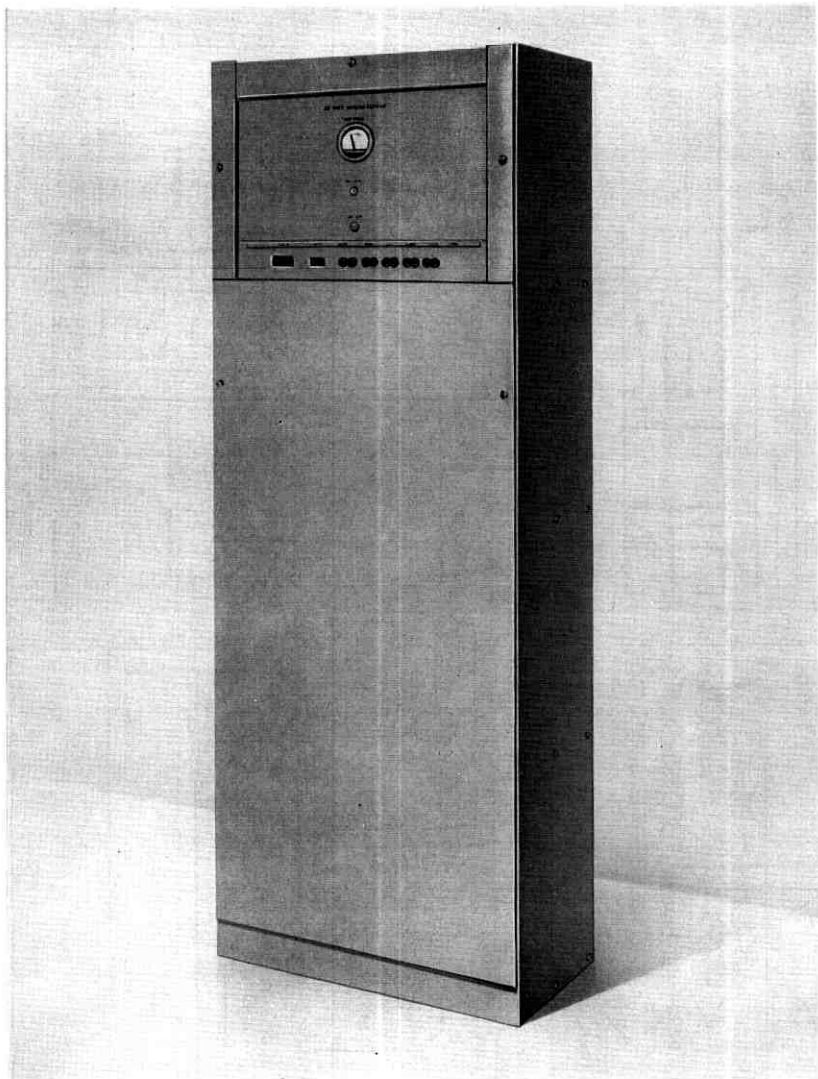
Fig. 53 — Cabinet containing 48-ampere charger and batteries.

Circuit-wise, the power supply is divided conveniently into three parts: a −20-volt regulator, an inverter operating at about 1800 cycles, and a rectifier to supply the klystron voltages. The same regulator and inverter are used for both TL-2 and TM-1. Fig. 54 gives a simplified schematic of the TM-1 power supply. TL-2 is substantially the

68
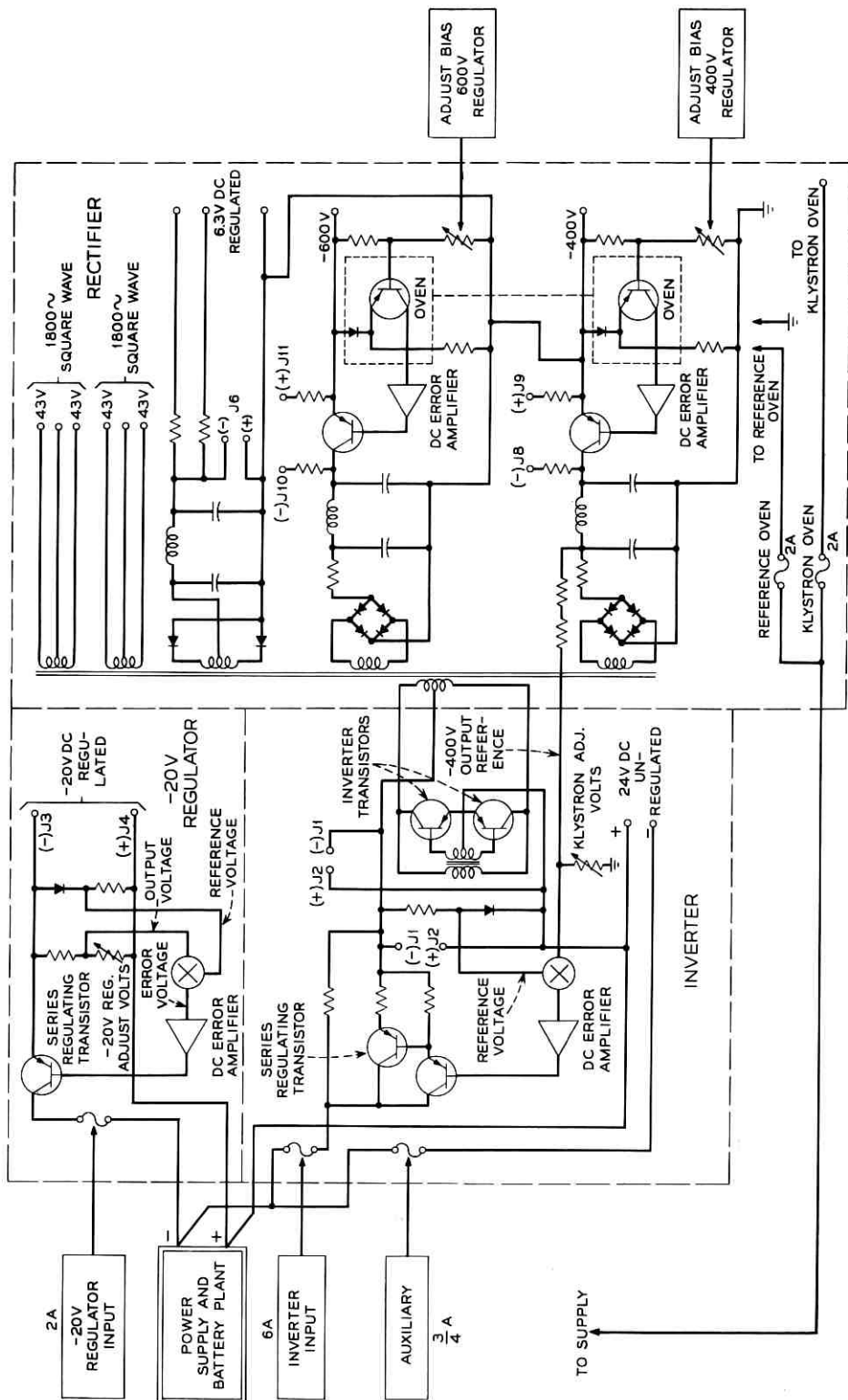
same except that the regulators shown in the −400-volt and −200-volt supplies are not present.

The −20-volt supply for the solid-state IF and baseband circuitry is obtained through a series transistor regulator which is controlled by an error-voltage amplifier. The reference voltage is obtained from a temperature-compensated voltage reference diode.

The dc-to-ac inverter consists of two transistors and a saturable transformer switching at a frequency of 1800 cps. The square wave output is stepped up in a power transformer and rectified to provide the klystron voltages. The klystron cathode voltage is −400 volts with respect to the cavity resonator which is grounded. Since the repeller operates between 100 and 200 volts more negative than the cathode, its voltage is obtained by connecting the output of another rectifier in series with the −400-volt supply. Other windings on the power transformer provide a 43-volt center-tapped square wave voltage for the receiver AFC magnetic amplifier. Another winding is used for the 10.5-volt dc klystron heater supply which is fed to ballast resistors in series with the heater of each klystron which drop the voltage to 6.3 volts. The heater supply is operated essentially on a constant power basis to gain longer life and greater frequency stability from the klystron. The output of the −400-volt rectifier is also used to control the regulator preceding the inverter. This provides regulation for the −200, 10.5, and the square wave voltages since these will all track the −400-volt output. In the TM-1, the −400 and −200-volt supplies are regulated independently as shown.

Photographs of the TM-1 and TL-2 power supply units are given in Fig. 55.

8.4 *Power for the TM-A1 Amplifier*

An electronically regulated power supply is used for the TM-A1 amplifier to obtain the required voltages for the traveling-wave tube. It also draws its input power from the battery-charger combination described above.

Fig. 56 gives a block schematic of the supply. The inverter delivers a 48-volt, 2000-cycle square wave to four separate circuits from which are derived the anode, the helix, the cathode, and the heater potentials. The anode and the helix voltages are jointly regulated with respect to the cathode, and the heater is regulated separately.

The helix supply is regulated to $\pm\frac{1}{2}$ percent of the nominal helix to cathode voltage. A sample of the helix-to-cathode output voltage is
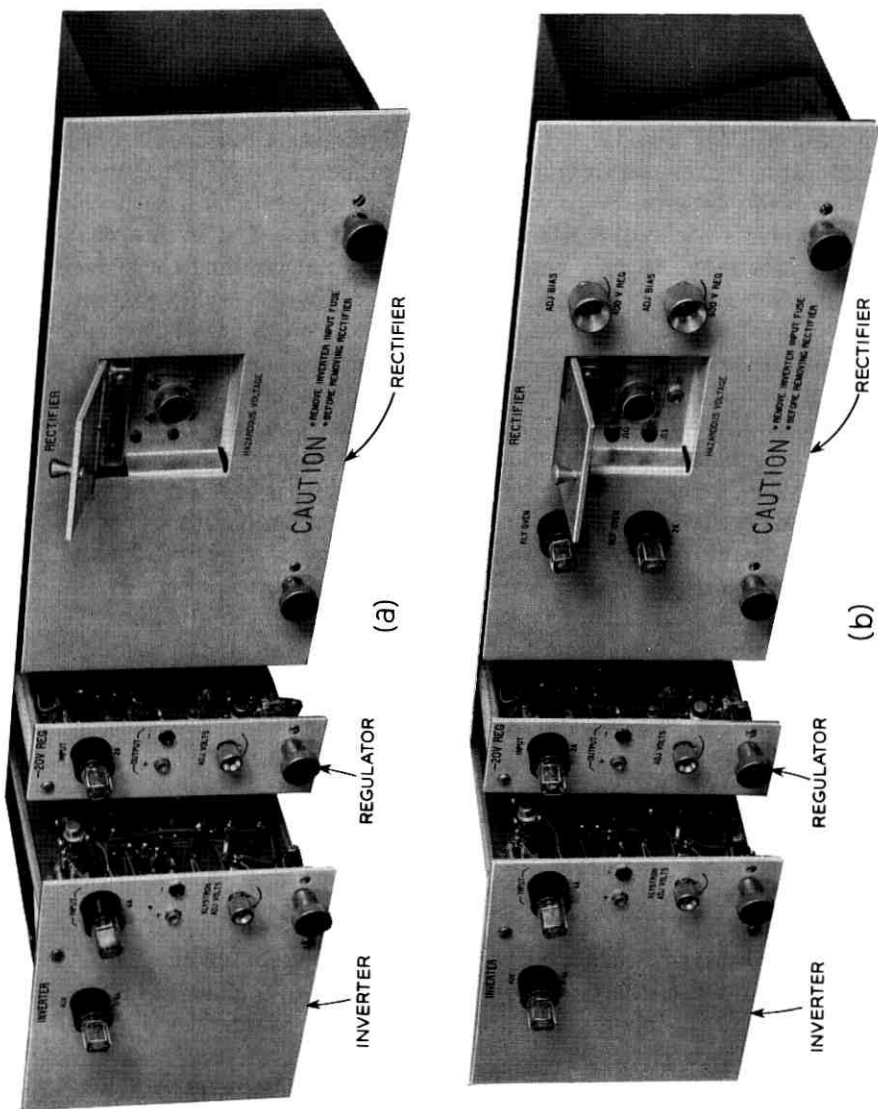
Fig. 55 — Power supply for (a) TL-2 and (b) TM-1.
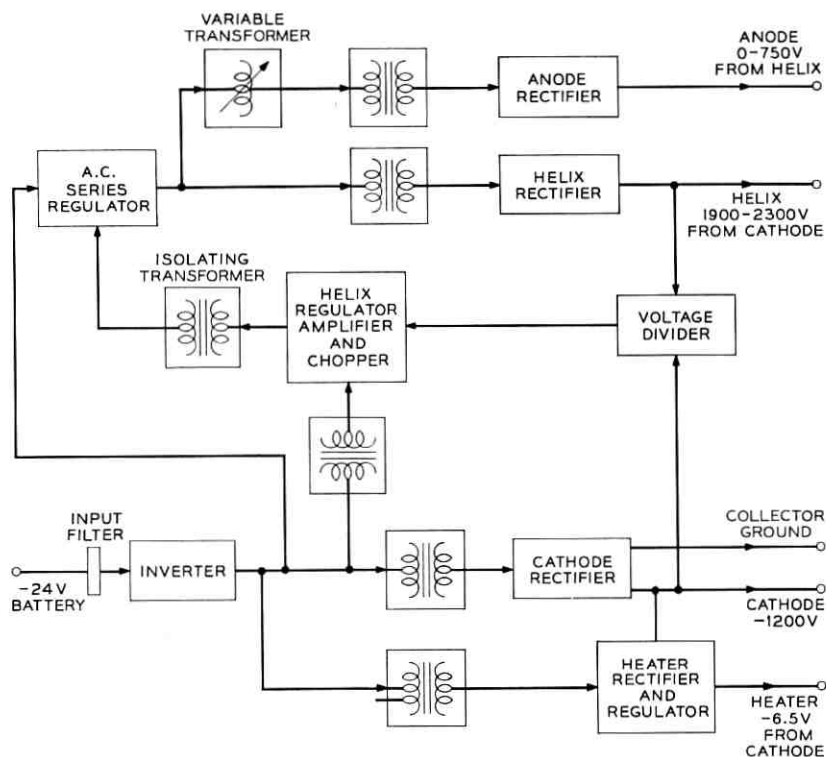
Fig. 56 — TWT power supply, block schematic.

compared with a reference voltage and the difference voltage (the error) is amplified by a dc amplifier. The amplified error signal is then "chopped" and the resulting square wave applied to a rectifier and applied to the ac series regulator. The isolating transformer in the control path isolates the regulator from the high helix voltage. The anode voltage will track the helix voltage as shown in Fig. 56.

A series transistor regulator is used to regulate the heater voltage, the positive side of which is connected directly to the cathode, nominally held at −1200 volts.

The power supply includes four meters to read collector current, helix current, anode-to-cathode voltage and heater voltage. Adjustments for cathode and heater voltages are provided; the heater voltage is set precisely in the factory. The power supply may be seen in the photograph of Fig. 57. The following table summarizes the performance of the power supply.

Fig. 57 — Power supply for traveling-wave tube amplifier.

	Nominal Operation (−27V @ 4.5A)	Regulation (−21.5V to −29V)
Anode-cathode	2500 volts 0–1 ma	±45 volts
Helix-to-cathode	2100 volts 0–4 ma	±12 volts
Cathode	−1200 volts 30 ma	−900 to −1300 volts
Heater-to-cathode	−6.5 volts 0.8 to 0.95 ampere	±0.13 volts

IX. EQUIPMENT DESIGN FEATURES

9.1 *Radio Equipment*

Fig. 58 illustrates a typical TM-1/TL-2 single channel bay intended for installations with very limited or no growth potential. The 7-foot high by 23-inch wide bay houses a single TM-1 or TL-2 RF panel (transmitter-receiver plus plug-in power units), four 6-volt high spe-
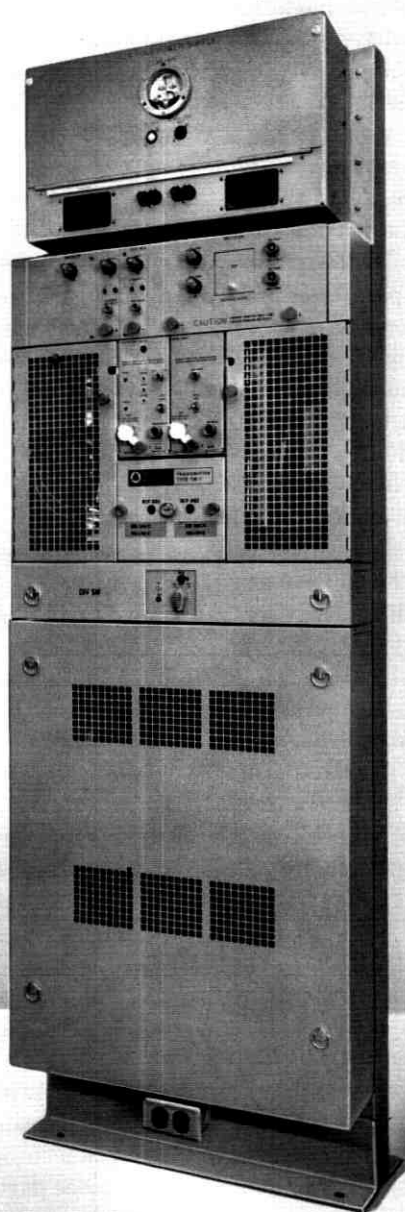
Fig. 58 — Single channel transmitter-receiver bay complete with batteries and charger.

cific gravity lead-acid batteries, and the charging rectifier. Space is provided for an order wire alarm panel in one bay or a diversity switch panel in the associated bay of a diversity system. Such a bay may serve as a radio terminal for a two-way single channel non-diversity system. Two bays would be required at a two-way, single channel non-diversity repeater station.

For applications where there is an appreciable growth potential, the TM-1/TL-2 equipment may be obtained with one, two, or three RF panels in a 7-foot by 23-inch bay. Fig. 59 illustrates such a bay with three RF panels plus their associated order wire or diversity switch panels. The bay can be ordered fully equipped with three RF panels or partially equipped with one or two RF panels and the remaining units added in the field as the need develops for additional circuits. The batteries and their associated charging rectifier in such an application are housed in a separate 30-inch by 16-inch by 7-foot high power cabinet as shown in Fig. 53.

A 9-foot by 23-inch bay arrangement housing as many as four broadband channels is also available for central office, TD-2, or TH radio rooms. The 24-volt battery power for these 7- or 9-foot high bays may also be obtained from central office 24-volt battery plants when available.

Greater flexibility has been realized in the TM-1/TL-2 equipment arrangements which facilitate their application for network, educational or industrial television system. Since ETV needs may frequently call for groups of six channels, a 7-foot bay may be readily equipped with 6 transmitters as a transmitting video terminal, or 6 receivers as a receiving video terminal. The 4-inch by 23-inch space normally allocated on message systems to the order wire alarm or diversity switch panels may be used in television systems for video repeater or video terminal amplifiers and equalizers depending upon the needs of a particular application.

The frontal dimensions of a typical TM-1 or TL-2 transmitter-receiver panel, as shown on Fig. 58 or 59, are 23-inches wide by 21-inches in height, inclusive of the power supply. The TM-1 and TL-2 transmitter-receiver panels are essentially identical in appearance. Equipment arrangements for the two systems are similar so as to facilitate their ordering, installation, and operation in 6- and 11-gigacycle crossband diversity applications. Common piece parts and common circuitry and equipment units are used whenever possible for the two systems to reduce costs and ease field maintenance problems.

Fig. 60 illustrates a 7-foot bay housing two RF panels with their
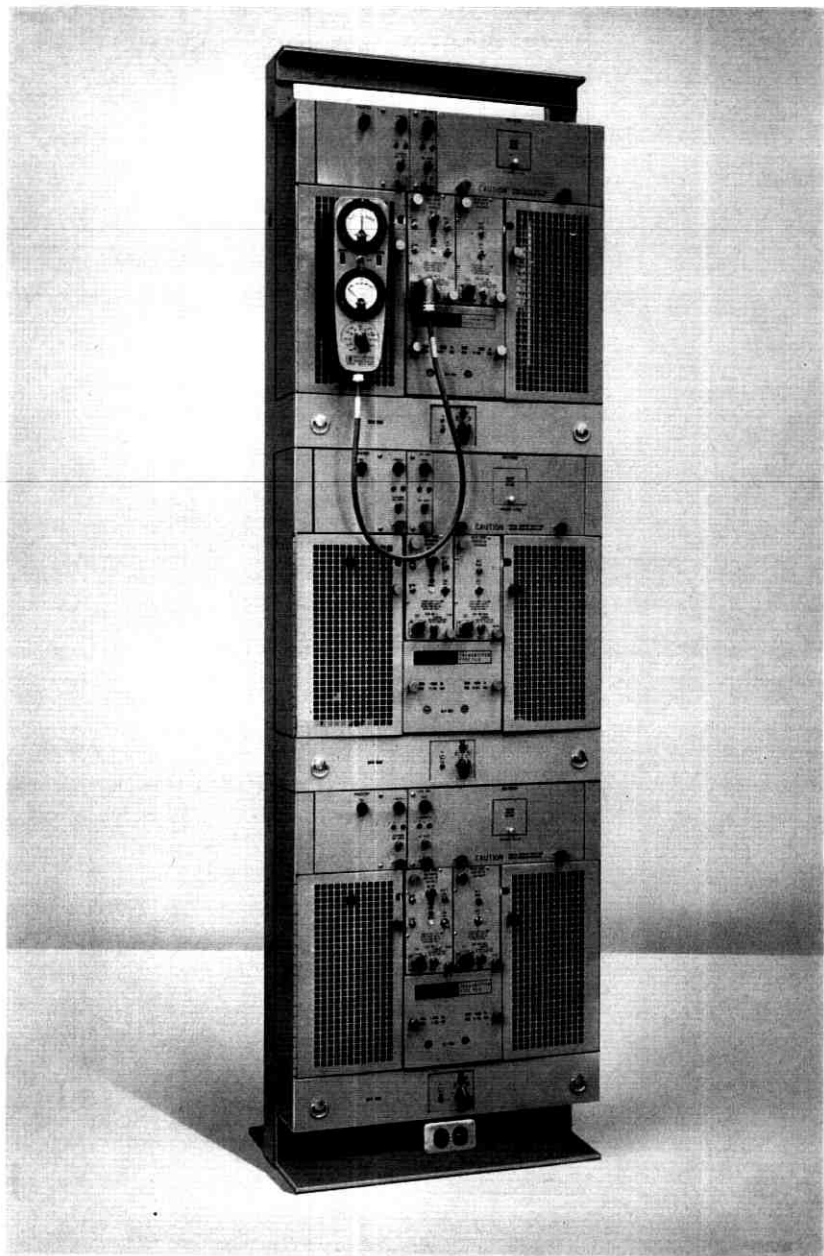
Fig. 59 — A 7-foot bay equipped with three transmitter-receiver units, power supplies, and diversity switches.
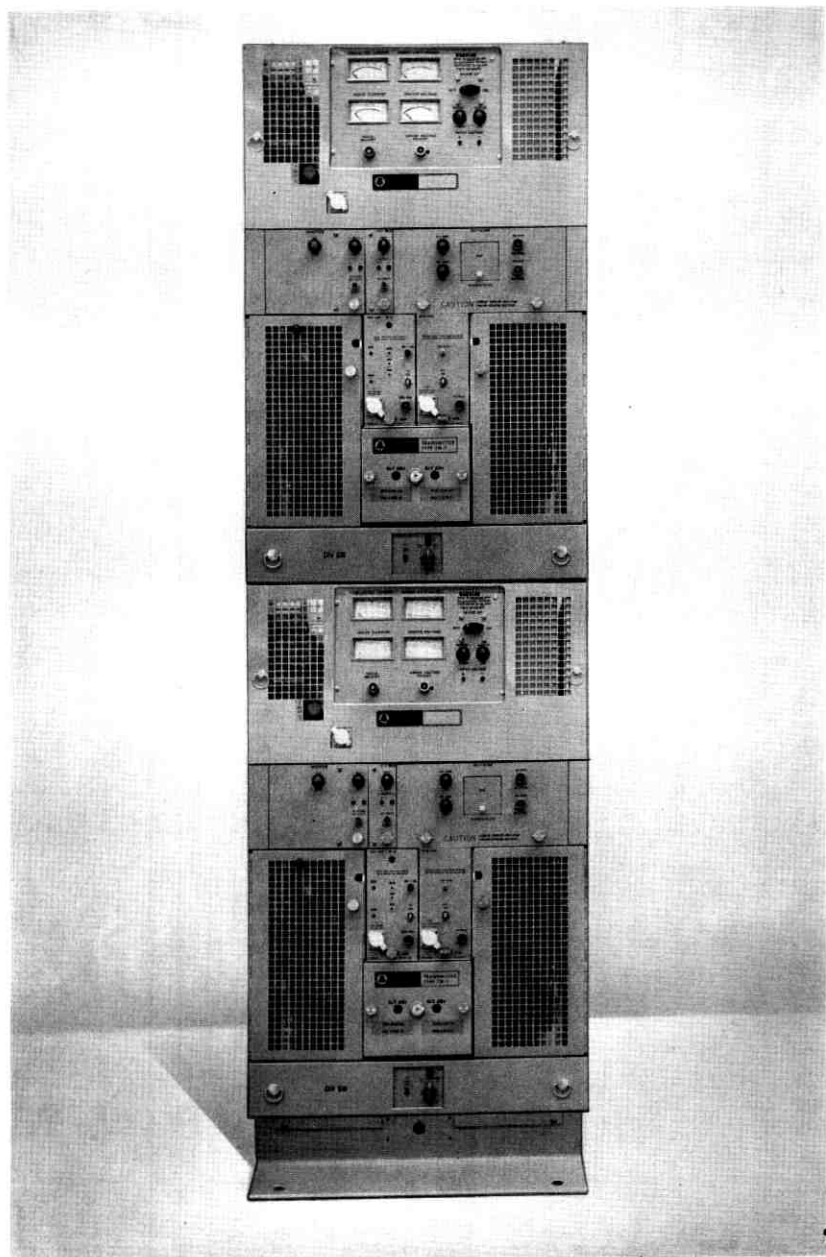
Fig. 60 — A 7-foot bay equipped with two transmitter-receiver units and their associated TM-A1 amplifiers.

associated TM-A1 amplifiers. The plug-in traveling-wave tube amplifier power supply is mounted on the TM-A1 amplifier panel and furnishes all required voltages for the amplifier. The power supply operates from the same battery source as the TM-1 transmitter-receiver.

9.2 *Equipment Shelters*

One of the earlier concepts of short-haul, light-route microwave radio relay systems[2] eliminated the need for a building or shelter to house the equipment and substituted a relatively small and less expensive weatherproof cabinet. The type of equipment cabinet developed for TL-1 was continued for TL-2 and TM-1, but the smaller TM-1/TL-2 package permitted the design of the equipment cabinet illustrated in Fig. 61 which houses twice as many RF panels as the earlier cabinet. This thermally insulated cabinet houses either a TL-2 and a TM-1
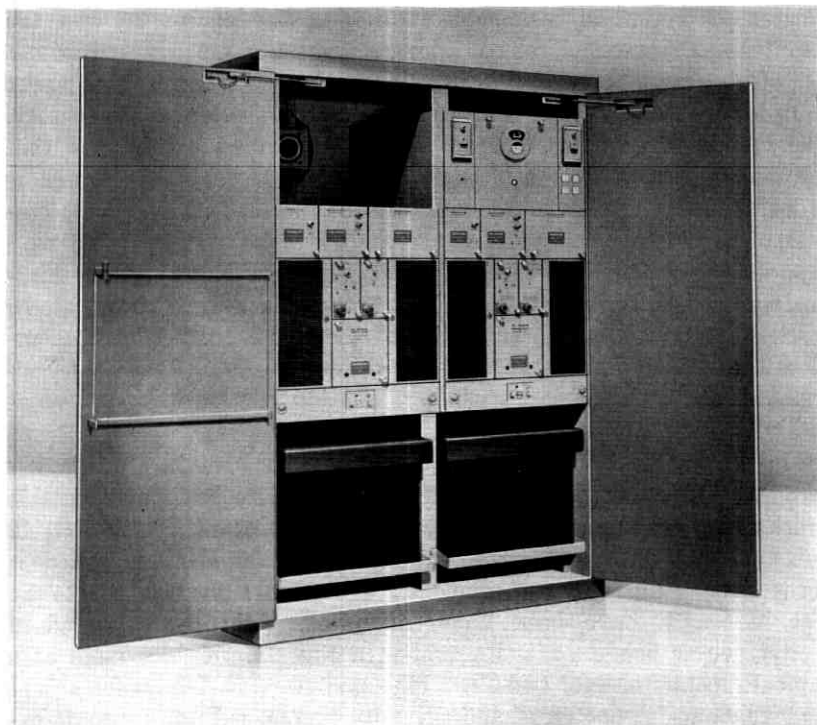
Fig. 61 — Equipment cabinet for two transmitter-receiver panels plus batteries and charger.

RF panel, or two TL-2 or two TM-1 panels with their associated power supplies, batteries, and order wire and alarm, diversity switch, or video panels. The cabinet is 57-inches wide by 76½-inches high by 21-inches deep. Only one cabinet is now required for a diversity terminal or at a repeater point for a non-diversity system. Two cabinets are required at a diversity two-way repeater station. However, the use of cabinets is limited to single broadband channel message systems with no growth potential beyond the initial 600-message circuit capacity or for video service limited to two two-way or four one-way channels. While these solid-state TL-2 and TM-1 systems have demonstrated excellent reliability, and are designed to facilitate maintenance with the quick replacement of plug-in units, the above growth limitations and the problems of the maintenance personnel during possible difficult winter operating conditions has limited the use of such cabinets.

Like TL-1 radio, TL-2 and TM-1 radio systems make use of the equipment shelter illustrated in Fig. 62. This shelter not only provides greater protection in inclement weather to the equipment and the maintenance personnel, but it also removes the growth limitations. All of the radio, carrier line interconnecting equipment, and power equipment, less batteries, can be installed in a shelter at the factory. The installation includes the ac, dc, and transmission cabling within the shelter, as well as all the interconnecting waveguide which is brought out to hatches in the side wall of the shelter. The completeness of the installation permits the shelter to be system tested with experienced personnel before shipment from the factory, thus minimizing job engineering and installation time, effort, and expense at the repeater station sites. The majority of the few items needed to complete the installation in the field are shipped properly crated and secured to the floor within the shelter. The batteries are shipped separately.

The TM-1/TL-2 shelter is standardized at present in a thermally insulated truck body type of aluminum structure having an outside width of 7 feet, a height of 8 feet, and a length of either 7½ feet, 12 feet, or 16 feet. For special applications where more space is needed for radio spur or multiplex equipment, shelters up to 24 feet in length have been made available. The 12-foot standard shelter, whose floor plan is illustrated in Fig. 63, provides room at a typical repeater site for two TL-2 bays and two TM-1 bays for a 6/11 gigacycle one-for-one crossband diversity system with an ultimate capacity of 3-broadband channels or 1800-message circuits. Space is provided for three power cabinets with their self-contained 24-volt bat-
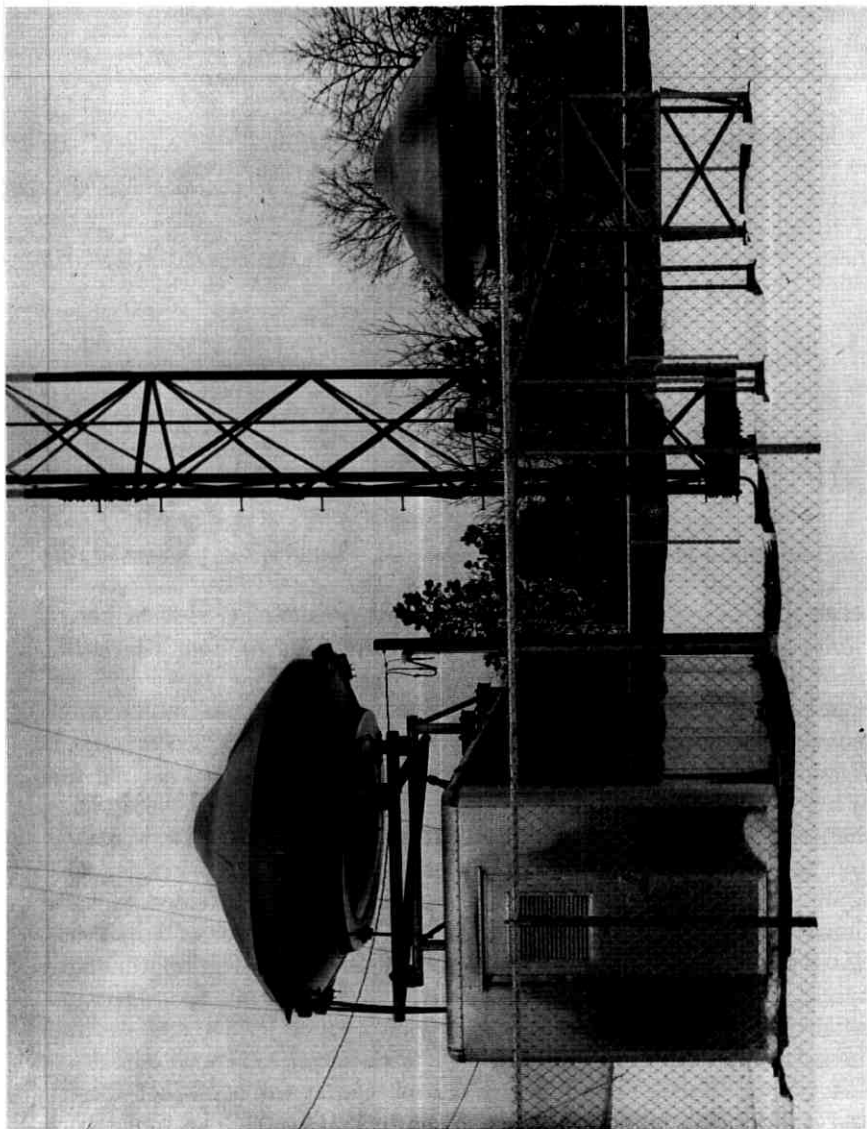
Fig. 62 — TM-1/TL-2 repeater station showing equipment shelter, antennas, and guyed tower.
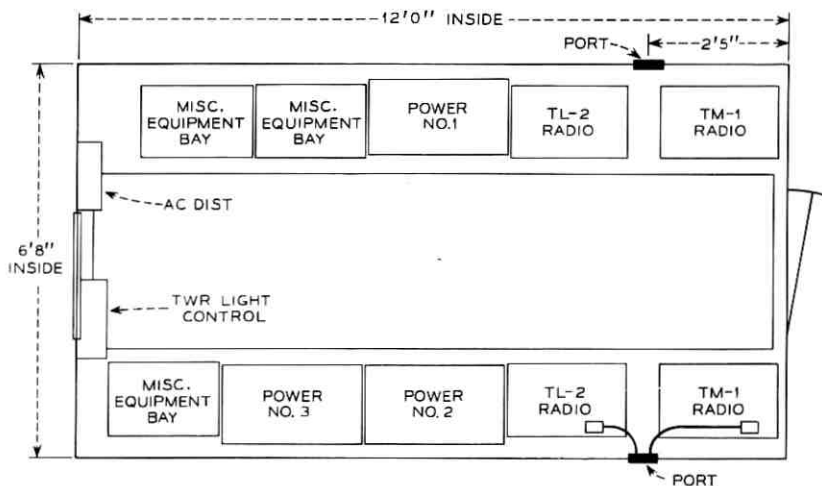
Fig. 63 — Floor plan for a TM-1/TL-2 equipment shelter showing growth plan.

teries and chargers. The single 30-inch by 16-inch by 84-inch power cabinet, provides about 24 hours battery reserve for the four RF panels illustrated in Fig. 64 in the event of commercial ac power failure. Space is also provided for a miscellaneous bay for multiplex equipment at stations where message circuits are to be dropped or added. Windows are omitted for security reasons, but either a ventilating fan or a $\frac{1}{2}$ or $\frac{3}{4}$ HP room air conditioner can be installed at one end of the shelter. The air outlet in the door and the intake port are screened and provided with dust filters. Interior lighting, ac wiring for test equipment and a power distribution cabinet are all provided. Fig. 64 shows the ac distribution box at the end of the shelter and its associated tower lighting panel underneath the air filter. The approximate weight of an unequipped 12-foot shelter is 2000 pounds, the maximum weight fully equipped for shipment by rail or truck is 4300 pounds; and the maximum in-place installed weight with batteries is 6900 pounds.

A typical TM-1/TL-2 repeater station employing a 16-foot shelter and a periscopic antenna system is shown in Fig. 65. The roof structure of the shelter supports a ten-foot diameter dual-frequency 6/11 gc paraboloidal dish antenna that illuminates the 12- by 15-foot plane reflector. A second 10-foot dish supported by a triangular pylon illuminates the reflector facing the rear. The guyed tower is 120 feet in height with a triangular base four feet on a side.

9.3 *Maintenance*

The maintenance philosophy for the TM-1/TL-2 short-haul systems is to minimize testing and to use relatively simple test equipment that will enable the craftsman to locate troubles quickly and eliminate them by the substitution of spare plug-in units. He is not expected to make field repairs on any plug-in unit.

A portable meter unit, shown plugged into the top RF panel in Fig.

Fig. 64 — Interior view of an equipment shelter at a repeater station equipped for a diversity message system (ultimate capacity is 3 diversity systems).
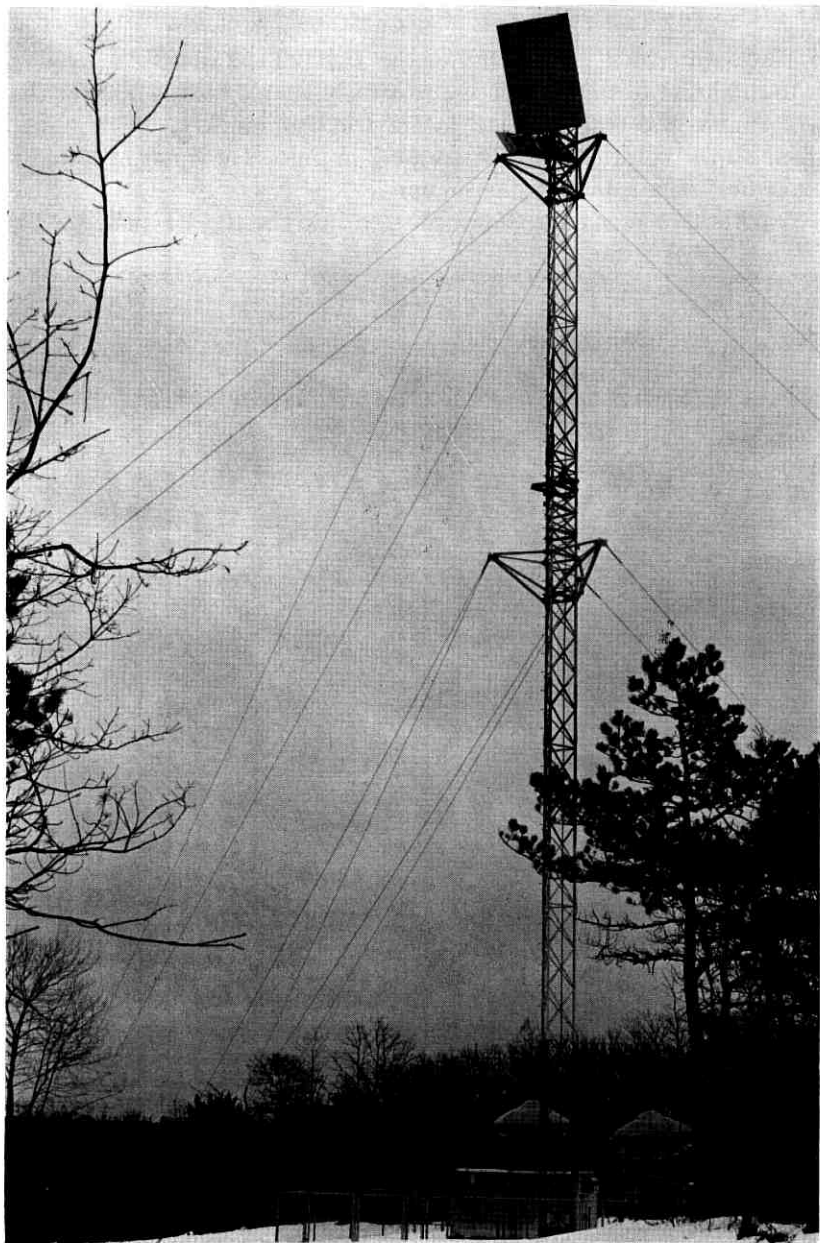
Fig. 65 — Typical TM-1/TL-2 repeater station.

59, provides the means of making certain maintenance tests and adjustments and for monitoring various currents and voltages within the transmitter-receiver panel. A light, portable, solid-state test set[2] which can be carried from station to station provides the test facilities for maintenance and trouble location at terminal or repeater stations. The test set provides oscillators for all required baseband and intermediate frequency testing and a solid-state voltmeter for measuring transmission levels and baseband response up to 4.5 mc. The test set is 16-inches long, 10-inches wide, and 10-inches deep and weighs 35 pounds.

While this test equipment is adequate for making all tests and adjustments on lightly loaded systems, more specialized and more precise instruments are available for tests to ensure high performance on systems carrying 600 message channels or broadcast quality television.

Two fiberglass cases, each limited in weight to about 40 pounds provide the recommended spare parts and tools that may be required by a craftsman in the on-site maintenance of a TL-2/TM-1 radio system. Each of the cases shown in Fig. 66 is 20 by 16 by 10 inches. The spare parts are protected in transit by encasement in cavities moulded into the soft polyurethane foam liner. The No. 1 case contains the volt-ohmmeter, fluorochemical for the boiler, spare TM-1 and TL-2 klystrons, a receiver IF/baseband amplifier and those other tools and spares having a higher probability of use in the routine maintenance of a remote station. The No. 2 case contains TM and TL receiver modulators and preamplifiers, transmitter baseband amplifiers, and a plug-in diversity switch comparator and pilot monitor.

X. THE INITIAL INSTALLATION

10.1 *Description of the System and Test Results*

The first TM-1/TL-2 crossband diversity system was installed between Charlottesville and Richmond, Virginia. The layout and description of the route is given in Fig. 67. The table indicates what antennas were used, whether direct radiators or periscope systems, the length of the waveguide runs, and the measured received signal powers.

Several weeks were devoted to making performance tests of this system before it was placed in service. Noise loading tests and transmission tests were made on the individual hops as well as on several combinations of hops in tandem. The single-hop noise loading results of a nominal length section, the Carter Mountain-Shannon Hill hop, are given in Fig. 68(a). The 4 hops (two TL-2 and two TM-1) were connected in tandem and the results are given in Fig. 68(b).
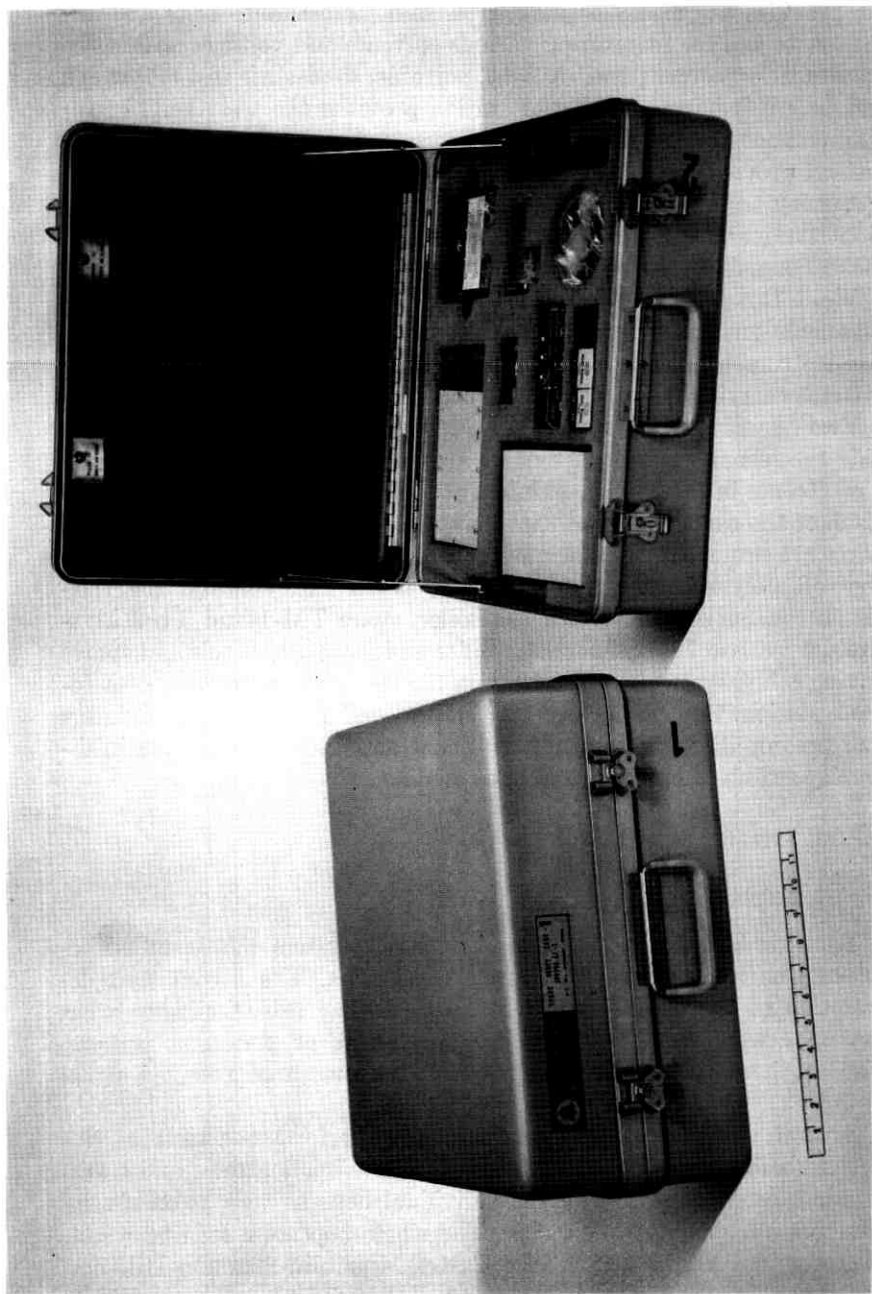
Fig. 66 — Spare parts cases for TM-1/TL-2.

CHARLOTTESVILLE
3.5 MILES
CARTER MOUNTAIN
24.9 MILES
SHANNON HILL
20.8 MILES
OILVILLE
19.8 MILES
RICHMOND
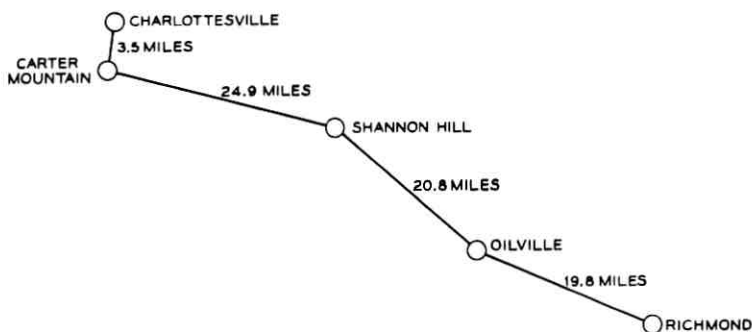
	CHARLOTTES-VILLE	CARTER		SHANNON		OILVILLE		RICHMOND
ANTENNA (DIAMETER-FEET)	6	6	10	10*	10*	10*	10*	HR
*PERISCOPE (10×15)								
LENGTH WAVEGUIDE	50	75	70	10	20	100	40	90

TM-1
-35 → -42 → -44 → -39 →
← -31.5 ← -43.5 ← -42.5 ← -40.5

TL-2
-31.5 → -41.5 → -44 → -39 →
← -29 ← -43.5 ← -41.5 ← -42

Fig. 67 — Charlottesville-Richmond diversity system.

Also shown are the results for a 10-hop system that included a loop from Carter Mountain to Richmond in tandem with a loop from Carter Mountain to Oilville. The 10-hop system included six TL-2 hops and four TM-1 hops, a combination that could occur easily if a system were equipped with bistable diversity switches. In all of the noise loading results the test signal was a 60–2540-kc band of noise and the noise power applied to the transmitter baseband input corresponding to 0 db in the figures gave 5-mc peak deviation. The pre-emphasis network, used in some of the tests, had a transmission characteristic as shown in Fig. 3. The transmission characteristic of the 10-hop system is given in Fig. 69 while a thermal noise characteristic of 8 of these hops is given in Fig. 70. (The two Oilville-Richmond hops were not available for this test.) A de-emphasis network was not used in the noise measurement.

10.2 *Some Factors that Influence Performance*

The linearity and the delay characteristics of the receivers in the TM-1 and TL-2 systems are determined mainly by factory adjust-
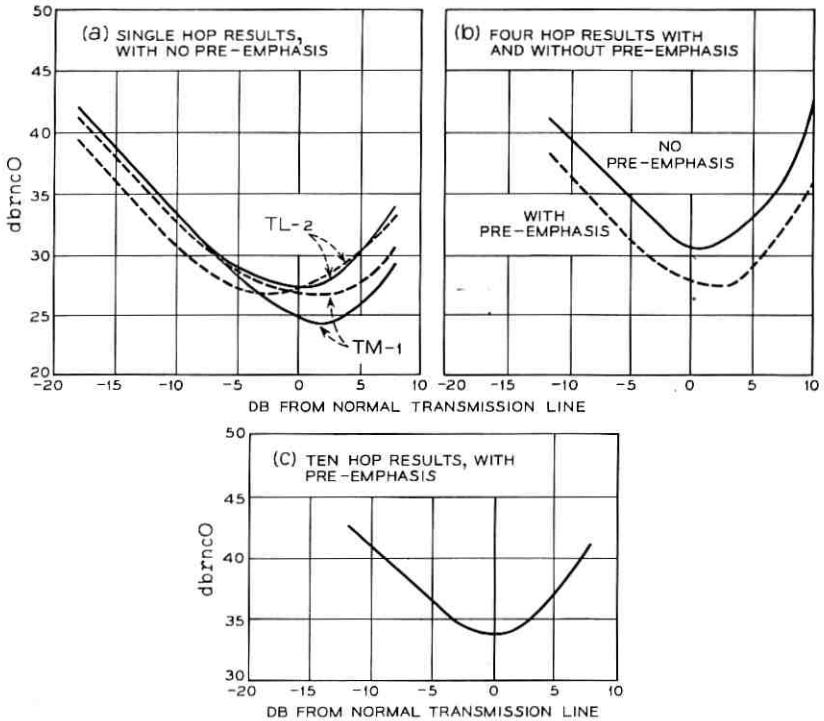
Fig. 68 — 600 circuit noise loading results (slot at 2438 kc).

ments. These are expected to hold essentially for the life of the equipment. The linearity of the transmitter klystron is adjustable, however. It has been found that optimum linearity of a reflex klystron obtains at the repeller voltage for which the deviation sensitivity is minimum and so the repeller bias may be adjusted to minimize the small signal FM deviation produced by a small voltage variation.[12] The minimum is very shallow, however.

The repeller voltage may also be adjusted to optimize the noise loading performance of a hop. This may be done by adjusting for minimum modulation noise in the 70-kc slot and is the technique that was employed in these tests.

Echoes in the RF paths can result in substantial performance degradations. The return loss of the parabolic dish antenna and the radio equipment are such that echoes should be down from the main signal by 50 db or more. A significantly larger echo will degrade the performance severely if the two impedance mismatches are separated by sufficient waveguide (75 feet or more).

This kind of trouble was encountered in the Carter Mountain-Charlottesville section. Initially, the noise loading result corresponded to the "Before" curve of Fig. 71. Investigation showed that the sum of the return losses at Carter Mountain was only 42 db and that the waveguide was noticeably dented close to the antenna. Replacing this section of guide improved the return loss by 6 db and the noise loading characteristic to the "after" curve of Fig. 71.

Another factor, encountered in crossband systems, was insufficient isolation in dual-frequency dish antennas. Energy at 11 gc can couple into the 6-gc port of the antenna from whence it propagates down the 6-gc waveguide, is reflected by the TM-1 radio equipment and radiates from the antenna as an echo. Since the echo delay will cause a changing phase across a given channel bandwidth, the resulting phase distortion produces higher than normal cross modulation. This problem was solved by adding a low-pass filter in the 6-gc waveguide as close to the antenna as possible in all such installations.

XI. TELEVISION TRANSMISSION

11.1 *General*

The objectives for television transmission in TM-1/TL-2 included meeting NTSC color transmission requirements for six hops and educational television requirements for 10 hops. All input and output
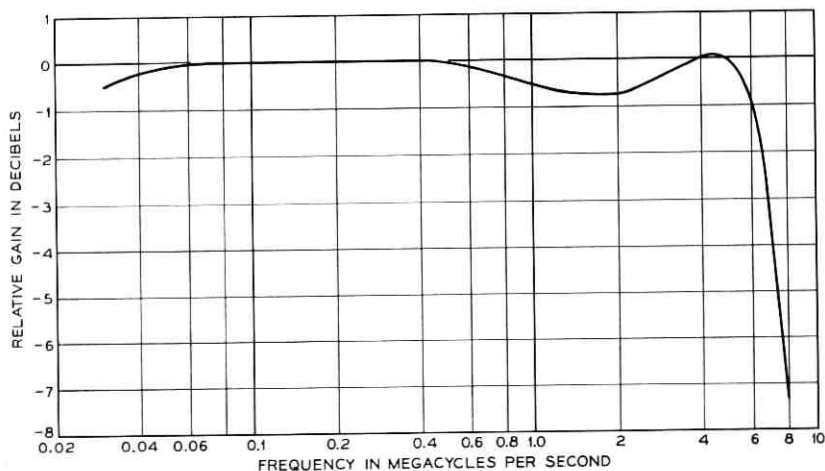
Fig. 69 — Transmission characteristic of 10 hops in tandem.
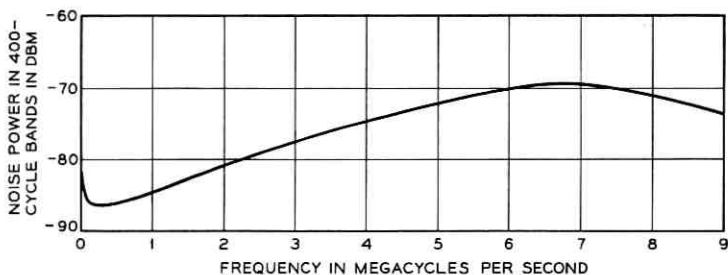
Fig. 70 — Thermal noise characteristic of eight hops.

impedances are 75 ohms and the system delivers a 1 volt peak-to-peak output signal. The plan for television transmission that was adopted originally is given in Fig. 72 showing arrangements at a transmitting terminal, at a repeater, and at a receiving terminal.

A pre-emphasis network and an adjustable attenuator to set deviation are included at the transmitting terminal. Fixed attenuators are used at repeaters, while a receiving terminal includes a de-emphasis network and a television terminal amplifier. The final amplifier insures a 1-volt peak-to-peak output, it provides some $\sqrt{f}$ adjustable equalization, and includes a signal inverter that may be used to obtain the desired signal polarity at the output of the system. The very low frequency transmission of the system was extended by adding large capacitors in the shunt legs of attenuators.

Extensive tests were made on the TL-2 installation at the New York World's Fair involving ten television channels in each direction be-
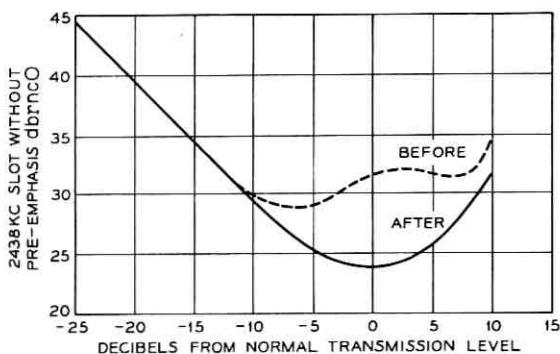
Fig. 71 — Effect of reducing amplitude of echo in waveguide in the TM-1 system between Charlottesville and Carter Mountain.
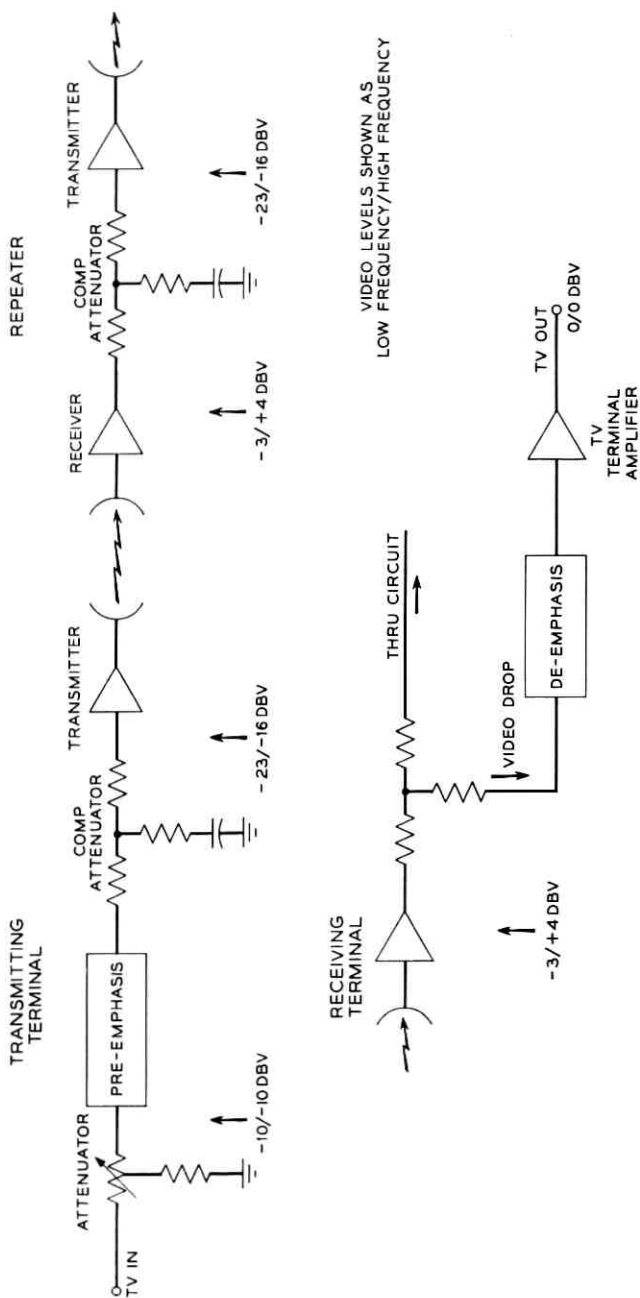
Fig. 72 — Basic television transmission plan.

tween Manhattan and the Fair. As a result of these tests, a number of refinements of the basic plan are being introduced into production.

The performance data and the further description of the system given below, are based on the revised block schematic shown in Fig. 73. All the equalizers, networks, attenuators, and the terminal video amplifier will be mounted on the video panels as described in Section X.

11.2 *Low-Frequency Equalization*

Even though individual baseband amplifiers in TM-1/TL-2 were designed to have a low-frequency cut-off under one cycle per second, the tandem combination of many amplifiers does result in the systematic addition of many very small deviations. For example, a 10-hop TM-1 system includes at least 40 baseband amplifiers since each receiver baseband amplifier and each transmitter baseband amplifier includes two feedback amplifiers in tandem.
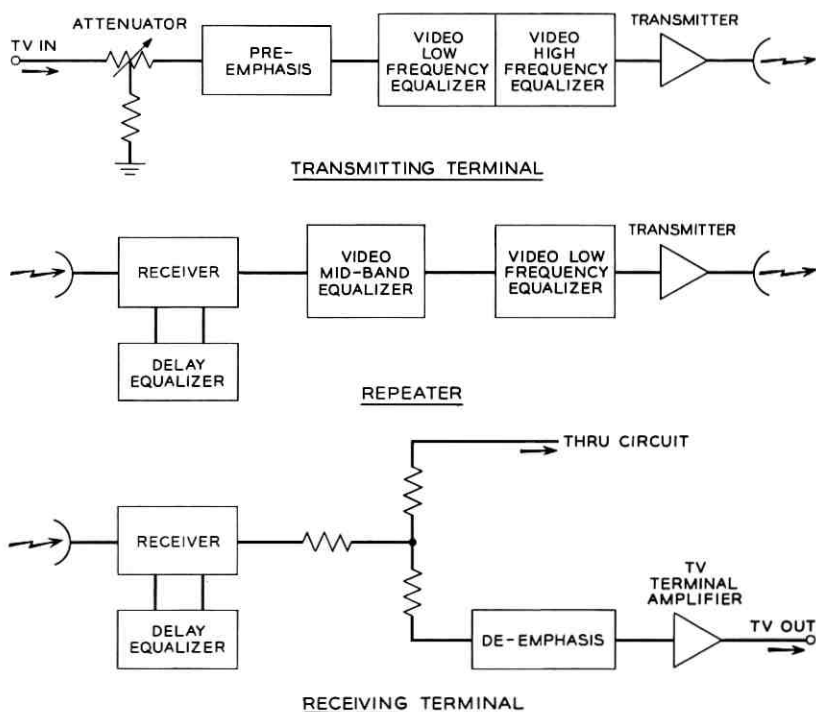
Fig. 73 — Television transmission.

The very low end of the characteristic is controlled by taking advantage of loss pads at the transmitter and at repeaters. The low-frequency equalizers, shown in Fig. 73 are similar to the compensated attenuators of Fig. 72 except that provision is made for selecting the shunt-leg capacitors. The adjustment is made to obtain minimum slope across a 60-cycle square wave at the time of installation or as part of a maintenance routine. Fig. 74 illustrates the performance that has been measured for a six-hop system.

Equalization is also required to mop-up small systematic effects between about 500 cycles and 50 kc that would produce some horizontal smearing of the picture. These equalizers, called video midband equalizers, are fixed equalizers and are to be applied at every third repeater.

11.3 *High-Frequency Equalization*

Equalization at the upper end of the band is to be provided by a video high-frequency equalizer located at the transmitting terminal. It provides a $\sqrt{f}$ characteristic having a range of about ±4 db at 6 mc. To conserve loss, the high-frequency equalizer and the low-frequency equalizers for the transmitter terminal will be combined in
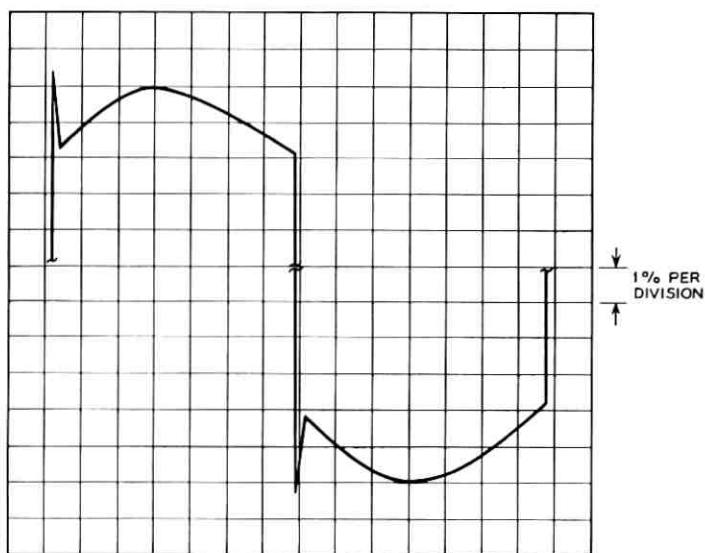
Fig. 74 — Expanded presentation of a 60-cycle square wave transmitted over 6 hops.

a single design. The video terminal amplifier for the Fig. 73 plan will not have a $\sqrt{f}$ adjustment.

11.4 *Differential Phase and Gain*

For television transmission, the transmitter klystrons are adjusted to minimize differential gain. Not only is the procedure different, but optimum klystron tuning for television transmission is not the same as the klystron tuning that minimizes cross-modulation in message systems.

Differential phase is minimized by a factory adjustment of the IF equalizer in the IF and baseband unit, and by the use of additional delay equalizers. These equalizers are selected from a family of equalizers, at the time a system is installed, based on differential phase measurements. They are inserted between the output of the pre-amplifier and input to the IF and baseband unit at some repeater locations.

Differential phase and gain performance can be improved by the use of pre-emphasis. Television systems in TM-1/TL-2 are operated at a peak deviation of 4 mc with 7 db of pre-emphasis such that a high-frequency sine wave deviates the carrier ±4 mc while a low-frequency sine wave deviates it ±1.8 mc. The emphasis characteristics are shown in Fig. 75. While the use of more pre-emphasis would be helpful as far as differential phase and gain are concerned, it would penalize low-frequency noise performance.
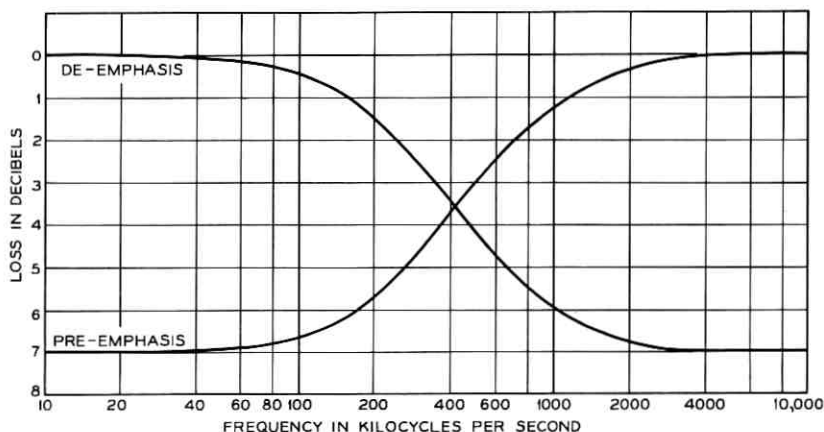
Fig. 75 — Loss of pre-emphasis and de-emphasis networks for television transmission.

By adjusting the transmitter klystrons and by the use of auxiliary delay equalizers, it is possible to obtain differential gain and phase performance of 1 db and 2 degrees for 6 hops with proportionate increases for 10 hops.

Fig. 76 shows the transmission of two common television test signals over a 6-hop TL-2 system at the Fair. The video mid-band equalizers, designed to be applied on every third hop, were not available for these tests and this accounts for the window signal tilt that may be seen. There was no difficulty in meeting thermal noise objectives.

XII. ACKNOWLEDGMENT

The systems described here are the result of the efforts of many members of the Bell Telephone Laboratories in the research, systems development, device development, outside plant, and systems engineering departments. The cooperation of the American Telephone and
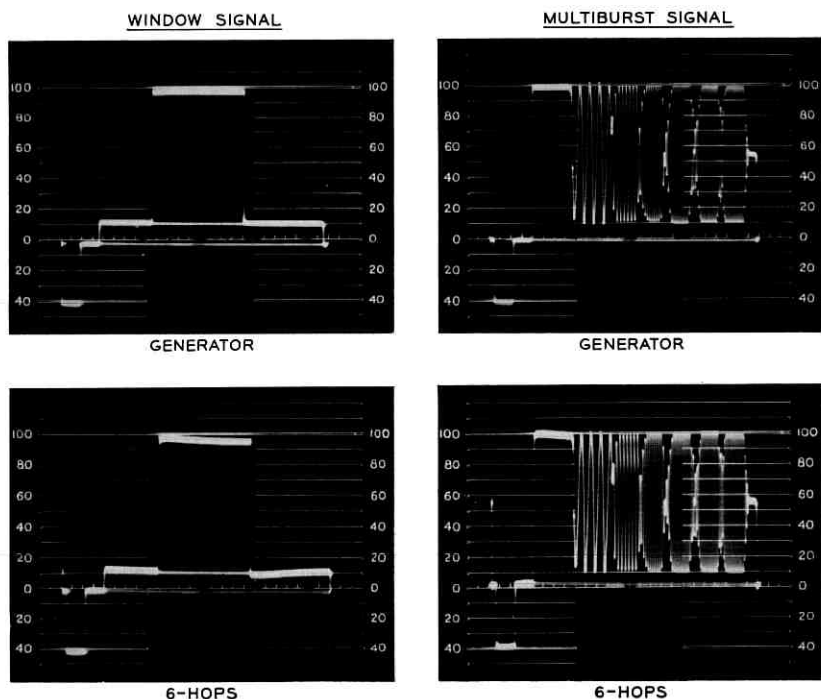
Fig. 76 — Television test signals transmitted over a 6-hop TL-2 system.

Telegraph Company and of the Western Electric Company was important to the success of this undertaking.

APPENDIX

The performance of transmission systems is rated in terms of the interfering noise power that may be measured in a telephone circuit at the reference transmission level point — the 0TL point. As the technology has advanced, the methods of measurement have changed with the result that several units of measurement are found in the literature. The purpose of this note is to relate these units.

A 3A noise measuring set is currently used in the Bell System. Readings are generally made using C-message weighting and the set is calibrated in dbrn or db above reference noise. The 2B noise measuring set was used prior to the advent of the 3A instrument. Its weighting curve was dbrn adjusted (adjusted with respect to an earlier value of reference noise) and generally called dba.

When measurements are made at the 0 TL point, the readings are frequently given in dba0 or dbrn0. Since the 3A noise set can be used with flat weighting as well as C-message weighting, it has become common to state the reading as dbrnc0 when C-message weighting is used.

Noise readings on the 2B and 3A sets may be summarized as follows:

| | Readings due to 0dbm of | |
Set	1000 Cycles	0–3kc White Noise
2B	85 dba	82 dba
3A	90 dbrn	88 dbrn

The international standard weighting characteristic is the CCIF psophometric curve. It is similar to the FIA weighting curve, but a reference frequency of 800 cycles rather than 1000 cycles is used. A 300 – 3400-cycle band of uniform noise is attenuated 2.5 db by the CCIF weighting network. In CCIF terms, a picowatt (pw) is -90 dbm, and a psophometrically weighted picowatt (pwp) is -87.5 dbm for a band of flat noise (300 – 3400 cycles). Hence

$$0 \text{ dba} = 3.55 \text{ pwp}$$

and

$$0 \text{ dbrnc} = 0.89 \text{ pwp}.$$

REFERENCES

1. Gammie, J. and Hathaway, S. D., The TJ Radio System, B.S.T.J., *39*, July, 1960, p. 821.
2. Ruthroff, C. L. and Tillotson, L. C., An Experimental Short Hop Microwave System, Bell Labs Record, June, 1960, p. 202. Hathaway, S. D., Sagaser, D. D., and Word, J. A., The TL Radio System, B.S.T.J., *42*, Sept., 1963, p. 2297.

3. Jakes, W. C., Jr., A Theoretical Study of an Antenna System, Proc. IRE, 41, 1953, p. 272.
4. Friis, R. W. and May, A. S., A New Broadband Microwave Antenna System, AIEE, 77, 1958, p. 97.
5. Transmission Systems for Communications by Members of the Technical Staff of Bell Telephone Laboratories, Chapter 20.
6. Cochran, W. T. and Lewinski, D. A., A New Measuring Set for Measuring Message Circuit Noise, B.S.T.J., 39, 1960, p. 911. Cochran, W. T., A New Noise Measuring Set, Bell Laboratories Record, June, 1960, p. 227.
7. Kinzer, J. P. and Laidig, J. F., Engineering Aspects of the TH Microwave Relay System, B.S.T.J., 40, November, 1961, p. 1459.
8. Harkless, E. T., A Network for Combining Radio Systems at 4, 6, and 11 KMC, B.S.T.J., 38, September, 1959, p. 1253.
9. Gucker, G. B., Long Term Frequency Stability for a Reflex Klystron without the use of External Cavities, B.S.T.J., 41, May, 1962, p. 945.
10. Lax, B. and Button, K. J., Microwave Ferrites and Ferrimagnetics, McGraw-Hill, 1962, Chapter 12. Degan, J. J., Waveguide Resonance Isolators, B.S.T.J., to be published.
11. Ballentine, W. E., Saari, V. R., and Witt, F. J., The Solid-State Receiver in the TL Radio System, B.S.T.J., 41, November, 1962, p. 1831.
12. Houghton, E. W. and Hatch, R. W., FM Terminal Transmitter and Receiver for the TH Radio System, B.S.T.J., 40, November, 1961, p. 1587.

Light Transmission in a Multiple Dielectric (Gaseous and Solid) Guide

By E. A. J. MARCATILI

A low-loss transmission medium for optical frequencies consisting of a thin-wall dielectric tube that separates an internal high-density gas from an external low-density gas is proposed. Approximate transmission characteristics of the coaxial structure are derived via the analysis of a two-dimensional model.

The multiple dielectric guide behaves similarly to a dielectric waveguide, and the fundamental mode attenuation due to losses in the solid tube is calculated to be small even at the worst possible choice of the tube wall thickness.

Assuming (i) an internal diameter of 5×10^{-4} m, (ii) wall thickness of 10^{-5} m, (iii) loss in the solid dielectric of 1 neper/m, and (iv) internal and external gases, CO_2 and air, respectively, both at 20 atmospheres, the theoretical attenuation for the fundamental mode is of the order of 0.05 db/km and the attenuation of each mode is roughly four times smaller than that of the next higher one.

I. INTRODUCTION

Hollow metallic and dielectric waveguides for long distance optical transmission were suggested by the author and R. A. Schmeltzer.[1] An alternative, proposed by S. E. Miller, is the coaxial structure shown in Fig. 1. The internal medium $r \leqq a$, as well as the external one, $r \geqq b$, are gases of refractive indexes n_1 and n_3 such that $n_1 > n_3$. Both gases are kept apart by a dielectric tube of thickness $c = b - a$ and refractive index n_2.

Since n_1 and n_2 are both bigger than n_3, the structure will guide modes similarly to a dielectric waveguide, but it is of interest to find out if there are modes with most of their power traveling within the internal gas and not in the dielectric tube. If these modes exist, they
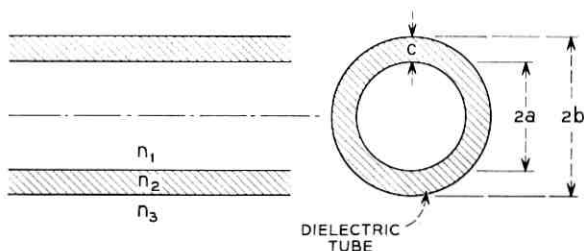
Fig. 1 — Multiple dielectric guide. $(n_3 - n_1)/(n_2 - n_1) \ll 1$.

will have relatively low losses originating from Rayleigh scattering, from scattering due to geometrical and dielectric imperfections, and from small absorption in the dielectric tube.

It is shown here that such modes indeed exist, and the losses due to absorption in the dielectric tube are calculated.

II. SOLUTION OF MAXWELL'S EQUATIONS

Instead of solving the equations for the three-dimensional cylindrical structure of Fig. 1, we solve them for the two-dimensional model of Fig. 2. The simplification is justified by the results obtained in Ref. 1; the propagation constants of modes in a hollow dielectric waveguide of circular cross section turn out to be comparable to the propagation constants of modes in the two-dimensional model, independently of the polarization.

We look for TE modes with electric field only along the y axis and independent of y. The field components are then, E_y, H_x, and H_z. The components in the three regions 1, 2, and 3, that will be needed to match the boundary conditions, are

$$
\left.
\begin{aligned}
E_{y1} &= \cos k_1 x \\[4pt]
H_{z1} &= \frac{k_1}{i\omega\mu} \sin k_1 x \\[4pt]
E_{y2} &= A \cos (k_2 x + \varphi) \\[4pt]
H_{z2} &= \frac{A k_2}{i\omega\mu} \sin (k_2 x + \varphi) \\[4pt]
E_{y3} &= B\, e^{-ik_3 x} \\[4pt]
H_{z3} &= \frac{B k_3}{\omega\mu}\, e^{-ik_3 x}
\end{aligned}
\right\} e^{-i\gamma z}
\qquad (1)
$$

where A, B, and φ are constants to be determined; ω is the angular
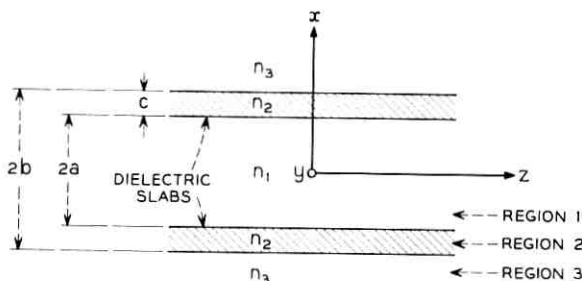
Fig. 2 — Two-dimensional version of the multiple dielectric waveguide.

frequency; μ is the magnetic permeability; k_1, k_2, and k_3 are the propagation constants along the x axis in the three regions and γ is the propagation constant along z. The electric field has been chosen symmetric with respect to the plane of symmetry $x = 0$, but the results will be extended later to antisymmetric modes.

For simplicity, we refer the refractive indexes to that of the internal gas. Therefore,

$$n_1 = 1. \tag{2}$$

The propagation constants in the three media are related to the propagation constant in free space $k = \omega\sqrt{\mu\epsilon}$ by

$$k_1^2 = k^2 - \gamma^2$$
$$k_2^2 = k^2 n_2^2 - \gamma^2 \tag{3}$$
$$k_3^2 = k^2 n_3^2 - \gamma^2.$$

From (1) the continuity of tangential components at the discontinuities ($H_{z1}/E_{y1} = H_{z2}/E_{y2}$ at $x = \pm a$ and $H_{z2}/E_{y2} = H_{z3}/E_{y3}$ at $x = \pm b$) yield two equations

$$k_1 \tan k_1 a = k_2 \tan (k_2 a + \varphi)$$
$$k_2 \tan (k_2 b + \varphi) = ik_3 \tag{4}$$

which, together with those in (3), are enough to calculate the five unknowns k_1, k_2, k_3, γ, and φ. In particular, the characteristic equation which determines γ is derived from (4) eliminating φ between the two equations:

$$k_1 \tan k_1 a = \frac{-k_2 \tan k_2 c + i k_3}{1 + i \dfrac{k_3}{k_2} \tan k_2 c}. \tag{5}$$

Substituting k_1, k_2, and k_3 by their equivalents (3), we have a transcendental equation in γ. To solve it in closed form we make several assumptions:

(i) The propagation constant is close to that of a plane wave in medium (1) Fig. 2. Therefore,

$$\gamma = k(1 - \delta) \tag{6}$$

and

$$\delta \ll 1. \tag{7}$$

Powers of δ bigger than one will be neglected.

(ii) Most of the power flows within the internal gas and consequently the electric field is close to zero in the vicinity of $x = \pm a$. Then from (1), (3), and (6)

$$k_1 a = ka \sqrt{2\delta} \cong (2p + 1) \frac{\pi}{2} \tag{8}$$

where p is an integer.

Since $\delta \ll 1$, it follows from this equation that the free space wavelength must be much shorter than the internal gas gap. That is,

$$\frac{\lambda}{a} \ll 1. \tag{9}$$

With these assumptions and some algebra, the value of δ derived from (5) and substituted in (6) yields the propagation constant

$$\gamma = k \left\{ 1 - \frac{1}{2} \left(\frac{\pi q}{2ka} \right)^2 \right.$$

$$\left. \cdot \left[1 + \frac{2}{ka} \frac{1 + i \sqrt{\dfrac{n_3^2 - 1 + \left(\dfrac{\pi q}{2ka} \right)^2}{n_2^2 - 1}} \tan kc \sqrt{n_2^2 - 1}}{\sqrt{n_2^2 - 1} \tan kc \sqrt{n_2^2 - 1} - i \sqrt{n_3^2 - 1 + \left(\dfrac{\pi q}{2ka} \right)^2}} \right] \right\}. \tag{10}$$

The integer $2p + 1$ has been replaced by another integer, q. If q is odd, the propagation constant (10) is that of a symmetric mode. If q is even, the propagation constant is that of an antisymmetric mode (electric field zero in the plane of symmetry $x = 0$, Fig. 2).

III. DISCUSSION OF PARTICULAR CASES AND CONCLUSIONS

As expected, if n_2 is real and $n_3^2 < 1 - (\pi q/ka)^2$ * the propagation constant γ given in (10) is real, that is, the mode of order q propagates without loss. Nevertheless, the dielectric sheets separating the gases have some loss and their refractive index can be rewritten

$$n_2 = n \left(1 - i \frac{\alpha}{kn} \right) \tag{11}$$

where n is the real part of the refractive index and α is the plane wave attenuation constant in the dielectric. Since the light attenuation in a low-loss solid dielectric is of the order of 1 db/m,

$$\frac{\alpha}{kn} \ll 1, \tag{12}$$

and powers of α/kn bigger than one will be neglected.

Now, let us substitute the value n_2 given in (11) into equation (10) and furthermore, let us consider two extreme cases of slab thickness.

3.1 *First Case*

The dielectric slabs are resonant: each slab contains an integer number s of half wavelengths. This requires

$$kc \sqrt{n^2 - 1} = s\pi. \tag{13}$$

Then,

$$\gamma_1 = k \left[1 - \frac{1}{2} \left(\frac{\lambda q}{4a} \right)^2 \left(1 - \frac{2}{ka} \frac{\sqrt{1 - n_3^2} - i\alpha nc}{1 - n_3^2 + \alpha^2 n^2 c^2} \right) \right]. \tag{14}$$

3.2 *Second Case*

The slabs are antiresonant, that is, each contains an odd number $2s + 1$, of quarter wavelengths, which requires that

$$kc \sqrt{n^2 - 1} = (2s + 1) \frac{\pi}{2}, \tag{15}$$

and consequently,

$$\gamma_2 = k \left[1 - \frac{1}{2} \left(\frac{\lambda q}{4a} \right)^2 \left(1 - \frac{2}{ka} \frac{\sqrt{1 - n_3^2} - i\alpha nc}{n^2 - 1} \right) \right]. \tag{16}$$

---

* The reader is reminded that n_2 and n_3 are refractive indexes normalized to n_1.

In both cases, the phase constant is very close to

$$\text{Re } \gamma_1 \cong \text{Re } \gamma_2 \cong k \left[1 - \tfrac{1}{2} (\lambda q/4a)^2\right], \tag{17}$$

which coincides with that of TE_{qo} modes far from cut-off in oversize rectangular waveguides.

In general, since $n_3 \cong 1$,

$$n^2 - 1 \gg 1 - n_3^2 + \alpha^2 n^2 c^2. \tag{18}$$

Therefore, the attenuation constant

$$\text{Im } \gamma_1 = - \left(\frac{\lambda q}{4a}\right)^2 \frac{\alpha n c}{a} \frac{1}{1 - n_3^2 + \alpha^2 n^2 c^2} \tag{19}$$

in the first case (resonant slabs) is larger. Small attenuation requires n_3 as large as possible,

$$\frac{a}{\lambda} \gg 1, \tag{20}$$

and

$$\frac{\alpha n c}{1 - n_3^2} \ll 1. \tag{21}$$

These inequalities indicate that for small losses the internal gap must be large compared to the wavelength and that the attenuation through the solid dielectric thickness c must be small compared to the difference between refractive indices of the two gases.

Since the attenuation constant is proportional to q^2, the attenuation discrimination between the q_1th and the q_2th mode is $(q_1/q_2)^2$. Better discrimination is predicted with modes in hollow metallic optical waveguides.[1]

Let us put in some numbers. For

$$a = 0.25 \ 10^{-3} \text{ m},$$
$$\lambda = 10^{-6} \text{ m},$$
$$\alpha = 1 \text{ neper/m},$$
$$n = 1.5,$$
$$c = 10^{-5} \text{ m},$$

and using CO_2 and air for the internal and external gases, respectively, both at 20 atmospheres, which yield

$$1 - n_3^2 \cong 0.01,$$

the attenuation in db for the fundamental mode would be

$$8.686 \text{ Im } \gamma_1 = 0.052 \text{ db/km}.$$

In order to get an idea about how critical it is to maintain the wall thickness uniformity, we calculate the propagation constant of modes assuming an extreme case in which the external surface of the dielectric is very rough and scatters. This transmission medium is equivalent to that of Fig. 2 with dielectric slabs infinitely thick. Then the propagation constant is derived from (10) making $n_3 = n_2 = n$. Thus,

$$\gamma_3 = k \left[1 - \frac{1}{2} \left(\frac{\lambda q}{4a} \right)^2 \left(1 + \frac{i2}{ka\sqrt{n^2 - 1}} \right) \right]. \tag{22}$$

The ratio between the attenuation constants of the medium with infinite and finite dielectric slab is

$$\frac{\text{Im } \gamma_3}{\text{Im } \gamma_1} = \frac{1 - n_3^2}{anc \sqrt{n^2 - 1}} = 595.$$

The fundamental mode in the guide made with CO_2 backed with hard dielectric is 595 times more lossy than the mode in the guide made with CO_2 and air separated by the hard dielectric.

For comparison, we reproduce some of the results obtained for hollow metallic and dielectric waveguides in Ref. 1. An aluminum straight waveguide of 0.25 mm radius operating at $\lambda = 1 \, \mu$ was calculated to have a TE_{01} mode loss of 1.8 db/km, and this loss doubled for the case where the axis of the guide had a radius of curvature of 48 m. Using glass instead of aluminum, the lowest loss mode EH_{11} was calculated to be attenuated 118 db/km.

Therefore, from the example in this paper, we conclude that if the wall thickness can be perfectly controlled, the multiple dielectric waveguide should be approximately one order of magnitude less lossy than the hollow metallic waveguide; at the other extreme, if the wall thickness cannot be controlled at all, the multiple dielectric waveguide should be roughly one order of magnitude lossier than the metallic waveguide.

We have only scratched the surface of the problem and the results are attractive. Many questions though remain unanswered. What thickness uniformity, and consequently, loss can be achieved in practice, what is the loss increase due to (i) the presence of supports for the dielectric tube, (ii) lack of straightness, and (iii) unwanted thermal gradients, etc.

REFERENCES

1. Marcatili, E. A. J. and Schmeltzer, R. A., Hollow Metallic and Dielectric Waveguides for Long Distance Optical Transmission and Lasers, B.S.T.J., *43*, July, 1964, pp. 1783–1810.

Ray Propagation in Beam-Waveguides with Redirectors

By E. A. J. MARCATILI

In a beam-waveguide, wanted and unwanted lens displacements from a straight line cause the beam propagating in either direction to depart severely from the guide axis. By including beam redirectors at each lens, it is shown that it is possible to reduce those displacements by amounts which depend (i) on the relative position of the lens where the beam deflection is sampled and of the redirector into which that information is fed, and (ii) on whether redirectors are sensitive to one or both directions of propagation.

If transmission takes place in one direction only, it is better to place each redirector before its deflection sampling point (feed-forward control). If transmission occurs in both directions, it is advantageous to place each redirector after its deflection sampling point (feed-back control).

I. INTRODUCTION

Correlated and uncorrelated transverse displacements of the lenses of a beam-waveguide[1,2,3,4,5] cause a propagating light beam to deviate from the axis of the guide. Since that deviation can grow proportionally to the number of lenses, the tolerance requirements on the lenses alignment become quite severe when the lenses are closelo spaced, as in beam-waveguides made with gaseous lenses.[6,7]

In order to relax those tolerances, devices have been proposed that sense the position of the beam and introduce deflections tending to re-align the beam with the guide axis.*

In this paper, the steady-state ray trajectories of beams traveling in opposite directions through a sequence of misaligned lenses are derived for several possible arrangements of iterated redirectors.

These calculations answer the following questions:

(*i*) Considering a single beam and assuming that the displacement

---

* Redirectors of this nature were proposed long ago by R. Kompfner and L. U. Kibler for beam-waveguides with widely separated lenses.

of the ray from the center of each lens will be used as an error signal to deflect the beam, where is it more advantageous to introduce each deflection, immediately ahead of or behind the deflection sampling point?

(*ii*) How effective is each method?

(*iii*) If the displacements of a beam are kept within tolerable limits because of the use of redirectors, are the displacements of another beam traveling in the opposite direction also within those tolerable limits?

(*iv*) For beams traveling in opposite directions, what reduces more the displacements, redirectors sensitive to one of the beams or to both of them?

II. ANALYSIS OF THE PROBLEM

Consider a sequence of aberration-free cylindrical lenses (two-dimensional problem) of focal length f and spacing L, Fig. 1, arbitrarily aligned in the plane of the drawing. The normals at the center point of each segment connecting the centers of successive lenses determine the lengths R_n which characterize the lens positions. Superimposed with each lens are four variable prisms, though for simplicity we have indicated only those at the nth lens. Lenses and prisms are idealized in the sense that they introduce phase shift in infinitely small thickness.

In a practical case, it is not necessary to have separate lens and prisms; they may be one and the same device. For example, a lens laterally displaced from the axis of the beam-waveguide is equivalent to a centered lens plus a prism.

Prisms number 1 and 2 are controlled by beam sensors,* S_1 and S_2, which are sensitive only to an east-bound ray. Those prisms deflect the beam at the nth lens by an angle

$$A\,\frac{r_{n-1}}{L} + B\,\frac{r_{n+1}}{L},$$

which is proportional to the beam displacements r_{n-1} and r_{n+1} normalized to the lens spacing L. The constants of proportionality, A and B, are determined by the amplifiers connecting each sensor with each prism.

Similarly, wedges 3 and 4 are controlled by sensors S_3 and S_4 sensitive only to a west-bound ray. The angular deflections introduced by those prisms at the nth lens is $C(\rho_{n-1})/L + D(\rho_{n+1})/L$.

---

* By beam sensor I mean any photosensitive device that measures the beam displacement from the center of the lens.
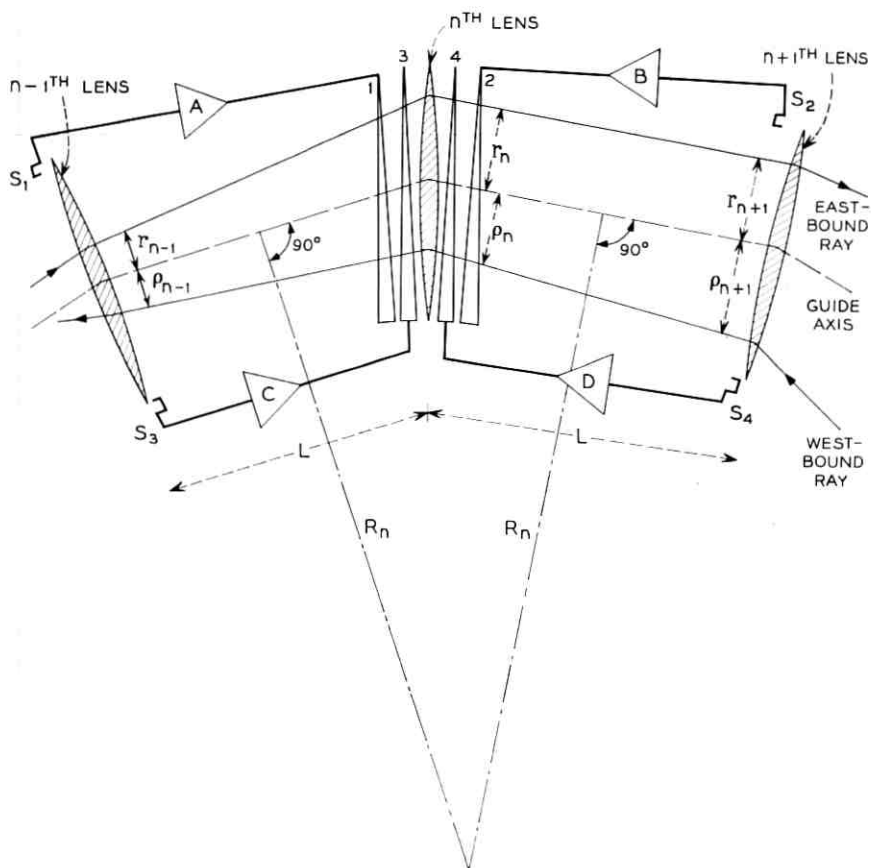
Fig. 1 — Sequence of misaligned lenses with redirectors.

The difference equation for the east-bound paraxial ray can be derived by inspection of Fig. 1,

$$r_{n+1} = r_{n-1} + \left(\frac{r_n - r_{n-1}}{L}\right) 2L - \frac{L}{f} r_n$$
$$- A r_{n-1} - B r_{n+1} - C \rho_{n-1} - D \rho_{n+1} + \frac{L^2}{R_n}.$$

This equation is easy to interpret by noting that the deflection r_{n+1} at the $(n + 1)$th lens is equal to the sum of several partial deflections. The first two measure the deflection at the $(n + 1)$th lens as if the nth lens, prisms, and curvature of the guide axis did not exist; the third

term is the deflection introduced by the nth lens; the fourth, fifth, sixth, and seventh terms are those introduced by the prisms; the last is the deflection introduced by the lenses misalignment. Cross product terms do not appear because the ray is considered paraxial.

Rearranging terms in that equation, introducing a similar expression for the west-bound ray and calling

$$1 - L/2f = \cos \theta, \tag{1}$$

two simultaneous difference equations are obtained

$$r_{n+1}(1 + B) - 2r_n \cos \theta + r_{n-1}(1 + A) + C\rho_{n-1} + D\rho_{n+1} = \frac{L^2}{R_n}$$

$$\rho_{n-1}(1 + C) - 2\rho_n \cos \theta + \rho_{n+1}(1 + D) + Ar_{n-1} + Br_{n+1} = \frac{L^2}{R_n} \tag{2}$$

that permit the determination of r_n and ρ_n.

We are not interested in the general solution of (2), but rather in four particular cases. Before considering them, and to compare results, we solve first the set of equations (2) assuming no redirectors, $A = B = C = D = 0$. Using standard techniques to solve difference equations,[8]

$$r_n = M \cos n\theta + N \sin n\theta + \frac{L^2}{\sin \theta} \sum_{m=0}^{n-2} \frac{\sin (n - m - 1)\theta}{R_{m-1}}$$

$$\rho_n = P \cos n\theta + Q \sin n\theta - \frac{L^2}{\sin \theta} \sum_{m=n+2}^{\nu} \frac{\sin (n - m + 1)\theta}{R_{m-1}}. \tag{3}$$

M, N, P, and Q are constants of integration determined by the initial conditions of the east- and west-bound rays. The lenses have been numbered from 0 to ν inclusively. Assuming further that the curvature of the guide axis $1/R_n$ has a Fourier component of amplitude $1/R$ and period θ, we can neglect the other spectral components[1] and in (3) replace the function $1/R_k$ by $(\sin k\,\theta)/R$, after which, keeping only the terms proportional to n, we obtain

$$r_n \cong -n \frac{L^2}{2R} \frac{\cos n\theta}{\sin \theta}$$

$$\rho_n \cong (\nu - n) \frac{L^2}{2R} \frac{\cos n\theta}{\sin \theta}. \tag{4}$$

If there are no redirectors, both rays increase their deflections proportionally to the number of lenses. These results, which already have been found by other people,[1,2,3] will be compared with those obtained when redirectors are included.

Now let us consider four particular cases.

First case: only east-bound correction; each beam deflection is fed to a correcting prism at the next lens following the direction of the ray. This implies

$$A \neq 0 \qquad B = C = D = 0$$

and (2) reduce to

$$r_{n+1} - 2r_n \cos \theta + (1 + A) r_{n-1} = \frac{L^2}{R_n}$$

$$\rho_{n-1} - 2\rho_n \cos \theta + \rho_{n+1} + A r_{n-1} = \frac{L^2}{R_n}. \tag{5}$$

Using standard techniques[8] to solve difference equations, the general solution of (5) is found to be

$$r_n = M_1(\cos \theta + S)^n + N_1(\cos \theta - S)^n$$
$$+ \frac{L^2}{2S} \sum_{m=0}^{n-2} \frac{(\cos \theta + S)^{n-m-1} - (\cos \theta - S)^{n-m-1}}{R_{m-1}} \tag{6}$$

$$\rho_n = P_1 \cos n\theta + Q_1 \sin n\theta$$
$$- \frac{L^2}{\sin \theta} \sum_{k=n+2}^{\nu} \left(\frac{1}{R_{k-1}} - \frac{A r_{k-2}}{L^2} \right) \sin (n - k + 1)\theta \tag{7}$$

where

$$S = \sqrt{-A - \sin^2 \theta};$$

$\nu + 1$ is the total number of lenses numbered from 0 to ν, and M_1, N_1, P_1, and Q_1 are constants of integration to be determined by the initial conditions of the east- and west-bound rays. The east-bound ray, r_n, has minimum deflection from the guide axis if

$$A = -1$$
$$\cos \theta = 1 - \frac{L}{2F} = 0. \tag{8}$$

The first equation implies that for the east-bound beam, the deflection introduced by prism number 1 at the $(n + 1)$th lens must be equal to minus the deflection of the beam at the $(n - 1)$th lens; the second equation indicates that the sequence of lenses must be confocal. In order to see what is the effect of small departures from conditions (8), we assume

$$A = -1 - \delta$$
$$\cos \theta = \varepsilon \tag{9}$$

with $|\delta| \ll 1$ and $|\varepsilon| \ll 1$, and then recalculate the deflections of the opposite traveling beams by substituting (9) in (6) and (7). Neglecting terms with powers of δ and ε bigger than one leads to

$$r_n = L^2 \left(\frac{1}{R_{n-1}} + \frac{2\varepsilon}{R_{n-2}} + \frac{\delta}{R_{n-3}} \right) \tag{10}$$

$$\rho_n = P_1 \cos n\theta + Q_1 \sin n\theta$$
$$\tag{11}$$
$$-L^2 \sum_{k=n+2}^{\nu} \left(\frac{1}{R_{k-1}} + \frac{1+\delta}{R_{k-3}} + \frac{2\varepsilon}{R_{k-4}} + \frac{\delta}{R_{k-5}} \right) \sin (n - k + 1)\theta.$$

The east-bound ray displacement, r_n, does not grow proportionally to n as it would if the redirectors were not present (4). The small departure ε and δ, from the ideal conditions (8) change only slightly the minimum possible beam displacement, $r_{n \min} = L^2/R_{n-1}$.

Furthermore, assuming as before that the curvature of the guide axis $1/R_k$ is Fourier-analyzed and we replace its value in (11) by the component $(\sin k\,\theta)/R$, the resulting west-bound ray displacement

$$\rho_n = P_1 \cos n\theta + Q_1 \sin n\theta \tag{12}$$

not only does not grow but besides, is insensitive to a first order, to the departures δ and ε from the ideal conditions (8).

The only drawback of this system is that the amplifiers connecting sensors with prisms must be stable to maintain $A \cong -1$.

Second case: east- and west-bound correction; the beam deflection at each lens is fed to a correcting prism at the next lens following the ray. These conditions require

$$A = D \qquad C = B = 0.$$

The governing equations are obtained by replacing these values in (2)

$$r_{n+1} - 2r_n \cos \theta + r_{n-1}(1 + A) + A \rho_{n+1} = L^2/R_n \tag{13}$$

$$\rho_{n-1} - 2\rho_n \cos \theta + \rho_{n+1}(1 + A) + A r_{n-1} = L^2/R_n. \tag{14}$$

Calculating ρ_n from (13) and substituting in (14) we derive a difference equation for r_n,

$$r_{n+2} - 2\frac{2+A}{1+A} r_{n+1} \cos \theta + 2 \left(1 + \frac{2\cos^2 \theta}{1+A} \right) r_n$$
$$- 2\frac{2+A}{1+A} r_{n-1} \cos \theta + r_{n-2} = \frac{L^2}{1+A} \left[\frac{1}{R_{n+1}} + \frac{1}{R_{n-1}} - \frac{2\cos\theta}{R_n} \right], \tag{15}$$

the solution of which is

$$r_n = M_2 \cos n\,\theta + N_2 \sin n\,\theta + P_2 \cos n\,\alpha + Q_2 \sin n\,\alpha$$
$$+ \frac{L^2}{(1+A)\sin\alpha} \sum_{m=0}^{n-2} \frac{\sin\,(n-m-1)\alpha}{R_{m+1}}. \tag{16}$$

M_2, N_2, P_2, and Q_2 are constants of integration that depend on initial conditions of the east- and west-bound rays, and

$$\alpha = \cos^{-1}\frac{1 - L/2f}{1 + A}. \tag{17}$$

The solution for the west-bound ray is similar to (16).

Minimum deflection of the east-bound beam, r_n, is obtained by selecting the amplifiers such that

$$|A| \gg 1. \tag{18}$$

The deflection, r_n, deduced from (16) and (18) is then

$$r_n \cong M_2 \cos n\,\theta + N_2 \sin n\,\theta + P_2 \cos n\,\alpha + Q_2 \sin n\,\alpha$$
$$+ \frac{L^2}{A} \sum_{m=0}^{n-2} \frac{\sin\,(n-m-1)\alpha}{R_{m+1}}. \tag{19}$$

If the curvature of the guide axis, $1/R_m$, is replaced by the Fourier component $(\sin m\,\alpha)/R$, the deflection r_n for $n \gg 1$ is

$$r_n \cong -\frac{nL^2}{2AR} \cos n\alpha. \tag{20}$$

Therefore, deflections are A times smaller than in the absence of redirectors (4), but much larger than in the previous case of redirectors sensitive only to one direction of propagation (10), (12).

Third case: only east-bound correction; each beam deflection is fed back into a correcting prism at the preceding lens. This means

$$A = C = D = 0, \qquad B \neq 0 \tag{21}$$

and (2) reduce to

$$(1 + B)\,r_{n+1} - 2r_n \cos\theta + r_{n-1} = L^2/R_n$$
$$\rho_{n+1} - 2\rho_n \cos\theta + \rho_{n-1} + B\,r_{n+1} = L^2/R_n. \tag{22}$$

Their solutions are

$$r_n = \frac{M_3 \sin n\beta + N_3 \cos n\beta}{(1+B)^{n/2}} + \frac{L^2}{\sin \beta} \sum_{m=0}^{n-2} \frac{\sin (n-m-1)\beta}{R_{m+1}(1+B)^{n-m/2}}$$

$$\rho_n = P_3 \sin n\theta + Q_3 \cos n\theta$$

$$+ \frac{L^2}{\sin \theta} \sum_{k=n+2}^{\nu} \left[\frac{1}{R_{k-1}} - \frac{Br_k}{L^2} \right] \sin (n-k+1)\theta \tag{23}$$

where, similarly to the previous cases, $\nu + 1$ is the total number of lenses, M_3, N_3, P_3, and Q_3 are integration constants and

$$\beta = \cos^{-1} \frac{1 - L/2f}{\sqrt{1+B}}. \tag{24}$$

East- and west-bound rays have small deflections if one chooses the proportionality constant of the amplifier

$$|B| \gg 1 \tag{25}$$

and also lenses far from plane or concentric

$$\frac{L}{2f} \neq \begin{cases} 0 \\ 2 \end{cases}. \tag{26}$$

Under these conditions, deflections (23) become

$$r_n \cong \frac{M_3 \sin n\beta + N_3 \cos n\beta}{B^{n/2}} + \frac{L^2}{R_{n-1} B}$$

$$\rho_n \cong P_3 \sin n\theta + Q_3 \cos n\theta + \frac{L^2}{B \sin \theta} \sum_{k=n+2}^{\nu} \frac{\sin (n-k+1)\theta}{R_{k-1}}. \tag{27}$$

Assuming perfect beam launching from both ends, $M_3 = N_3 = P_3 = Q_3 = 0$, and, as in previous cases, replacing $1/R_k$ by the Fourier component $(\sin k\theta)/R$, both rays are described by

$$r_n = \frac{L^2}{BR_{n-1}}$$

$$\rho_n = -\frac{(\nu - n)L^2 \cos n\theta}{2BR \sin \theta}. \tag{28}$$

Deflections in the east-bound ray, r_n, do not grow and they are B times smaller than in the first case (10). West-bound ray deflections, ρ_n, are only B times smaller than those in the absence of redirectors (4).

Fourth case: east- and west-bound correction; the deflection of each beam is fed into a correcting prism at the preceding lens. To achieve these conditions we must choose

$$A = D = 0, \qquad B = C \neq 0, \tag{29}$$

and (2) become

$$r_{n+1} (1 + B) - 2r_n \cos \theta + r_{n-1} + B \rho_{n-1} = L^2/R_n \qquad (30)$$

$$\rho_{n+1} - 2\rho_n \cos \theta + \rho_{n-1} (1 + B) + B r_{n+1} = L^2/R_n . \qquad (31)$$

A difference equation in r_n exclusively is obtained by calculating ρ_n from (30) and substituting the result in (31). Thus,

$$r_{n+2} - 2\frac{2 + B}{1 + B}r_{n+1} \cos \theta + 2\left(1 + \frac{2 \cos^2 \theta}{1 + B}\right)r_n - 2\frac{2 + B}{1 + B} r_{n-1} \cos \theta$$
$$+ r_{n-2} = \frac{L^2}{1 + B} \left(\frac{1}{R_{n-1}} + \frac{1}{R_{n+1}} - \frac{2 \cos \theta}{R_n}\right). \qquad (32)$$

Its solution, similar to that of the second case, is

$$r_n = M_4 \cos n \theta + N_4 \sin n \theta + P_4 \cos n \beta + Q_4 \sin n \beta$$
$$+ \frac{L^2}{(1 + B) \sin \beta} \sum_{m=0}^{n-2} \frac{\sin (n - m - 1) \beta}{R_{m+1}} . \qquad (33)$$

M_4, N_4, P_4, and Q_4 are the constants of integrations and β has been defined in (24). The west-bound ray is described by an expression similar to (33).

The beam displacement, r_n, is minimized by selecting

$$| B | \gg 1.$$

As before, if the curvature of the axis, $1/R_m$, has a Fourier component, $(\sin m \beta)/R$, the deflection, r_n, of the east-bound beam grows proportionally to the number of lenses n traversed by the beam. For $n \gg 1$, and neglecting terms not proportional to n, expression (33) becomes

$$r_n \cong -nL^2/(2BR) \cos n \beta. \qquad (34)$$

Deflections are B times smaller than those in the absence of redirectors (4).

III. CONCLUSIONS

In a beam waveguide with misaligned lenses, large beam departure from the guide axis can be drastically reduced by selecting a confocal sequence of lenses and by using a beam redirector at every lens sensitive to only one direction of propagation and such that it displaces the beam at the following lens by a length equal and of opposite sign to the beam displacement on the preceding lens. Under these conditions, the waveguide axis is rectified and, for the beam that sensitizes the redirectors, the ray displacement at the nth lens is

$$r_n = \frac{L^2}{R_{n-1}}$$

where L equals the separation between lenses and $1/R_{n-1}$ equals the curvature of the guide axis at the $n - 1$th lens. For the opposite beam, the displacement at the same lens is

$$\rho_n = P_1 \cos \frac{n\pi}{2} + Q_1 \sin \frac{n\pi}{2}$$

where P_1 and Q_1 are constants that define the input of this beam.

These results are not substantially varied if the conditions of confocality and deflection per redirector are not fulfilled rigorously (see (10) and (12)).

The feed-forward control system appears so effective that a guide with small beam deflections should be obtained by using redirectors not continuously but only at discrete intervals.

If the redirectors are sensitive to one direction of propagation and each deflects the beam proportionally to the beam displacement in the following lens, the displacements of the beam are small indeed,

$$r_n = L^2/BR_{n-1}$$

where $B \gg 1$ is the constant of proportionality provided by the feedback system. On the other hand, the ray traveling in the opposite direction behaves only as if the radii of curvature of the guide axis had been increased B times, (28). Therefore, only if the guide must transmit in a single direction is the feed-back control system more effective than the previous one.

No improvement is obtained by providing redirectors sensitive to both directions of propagation or by making the deflections proportional to the beam displacement at the lens where the redirector is located.

All we have said is applicable to steady-state trajectories, but we don't know if those trajectories are stable. Without studying any transient, though, we can conclude that in the first case, where sensitivity exists for one direction of propagation and each redirector is located after the sampling point, the trajectories are indeed stable. In effect, any displacement in the $(n - 1)$th lens, will produce a change in prism 1, Fig. 1, but since there is no loop to feed back this change to the sensor S_1, there is no loop where instability can exist.

REFERENCES

1. Hirano, J. and Fukatsu, Y., Stability of a Lightbeam in a Beam Waveguide, Proc. IEEE, *52*, Nov., 1964, pp. 1284–1292.

2. Marcuse, D., Statistical Treatment of Light-Ray Propagation in Beam-Wave-guides, B.S.T.J., *44*, Nov., 1965, pp. 2065–2082.
3. Berreman, D. W., Growth of Oscillations of a Ray About the Irregularly Wavy Axis of a Lens Light Guide, B.S.T.J., *44*, Nov., 1965, pp. 2117–2132.
4. Unger, H. G., Light Beam Propagation in Curved Schlieren Guides, Arch. Elektr. Ubertr., *19*, April, 1965, pp. 189–198.
5. Rowe, H. E., unpublished work.
6. Marcuse, D. and Miller, S. E., Analysis of a Tubular Gas Lens, B.S.T.J., *43*, July, 1964, pp. 1759–1982.
7. Berreman, D. W., A Lens or Light Guide Using Convectively Distorted Thermal Gradients in Gases, B.S.T.J., *43*, July, 1964, pp. 1469–1475.
8. Hildebrand, F. B., *Methods of Applied Mathematics*, Prentice-Hall, Inc., pp. 242–249.

Delta Modulation Quantizing Noise Analytical and Computer Simulation Results for Gaussian and Television Input Signals

By J. B. O'NEAL, Jr.

Quantizing noise in delta modulation systems falls into two categories, granular noise and slope overload noise. Granular noise exists because the decoded output signal can assume only a specified number of levels in the range of interest. Slope overload noise occurs when the slope of the input signal is greater than the delta modulator is capable of reproducing. When the S/N ratio is not too small, the noise power from these two sources is additive.

A formula for the slope overload noise power for Gaussian input signals is derived. This is used with an earlier result for the granular noise to give over-all signal-to-quantizing-noise ratios. It is shown by computer simulation that the assumptions employed in deriving these signal-to-quantizing-noise ratios are valid and that the analytical results provide good estimates of the true values of these ratios. Computer simulation of the Picturephone* visual telephone, a low-bandwidth television system, illustrates that the formulas derived for Gaussian signals apply quite well to video signals. Estimates are given for the S/N ratios theoretically possible when a 4.5-mc monochrome television signal is transmitted by delta modulation.

The characteristics of delta modulation quantizing noise may cause it to be subjectively less annoying than an equivalent amount of additive Gaussian noise.

I. INTRODUCTION

Delta modulation (ΔM) is one way in which an analog signal may be converted into pulses suitable for transmission over binary channels. Since the modulation process may be simpler and cheaper for ΔM than for standard pulse code modulation (PCM), there is considerable interest in determining how the performance of ΔM relates to that of

---

* *Picturephone* is a service mark of the Bell System.

standard PCM. Digital transmission of an analog signal is one way to effectively trade bandwidth for noise immunity in the transmission medium. Indigenous to this trade, however, is the introduction of quantizing noise in the encoding and decoding processes. Bennett[1] has studied this problem for standard PCM. De Jager[2] and Van de Weg[3] have studied quantizing noise for ΔM, but their results are somewhat restricted due to the difficulties encountered in analyzing a nonlinear feedback system such as ΔM. Zetterberg[4] discusses ΔM through the discipline of information theory.

This study was initiated primarily to determine what kind of performance could be expected if ΔM were used for narrow-band television signals such as *Picturephone* signals, but more general results are also presented. The metric used as a figure of merit is the ordinary signal-to-quantizing-noise ratio S/N. Recently, the concept of delta modulation has been subject to a rash of embellishments and modifications, some of which may improve its ability to transmit television signals and all of which add equipment complexity. This study, however, is limited to the simplest type of single-integration ΔM system with a uniform constant step size. Formulas for S/N ratio are found which apply when the S/N ratio is large, which is the region of greatest interest. The formulas derived apply to Gaussian signals with arbitrary spectra. The results are verified by simulating various ΔM systems on an IBM 7094 digital computer and analyzing their performance with Gaussian input signals. A practical ΔM system designed for the transmission of a *Picturephone* signal is simulated, and the results illustrate that the formulas derived for Gaussian signals apply quite well to monochrome television signals.

II. THEORY

Delta modulation is a simple type of predictive quantizing system.[5,6] This means that the value of the signal is predicted at each sample time and only the difference between the actual signal value and this predicted value is transmitted. At the receiver, the value of the decoded signal at every sample time is predicted to be the same as that at the previous sample time. At each sample time, the transmitted signal is simply a correction which, when added to the decoded signal at the previous sample time, gives (to an approximation) the signal at the current sample time. Systems of this kind are also called differential feedback PCM systems.

The basic single integration ΔM system is shown in Fig. 1. The adder and delay element in the feedback loop around the quantizer simply
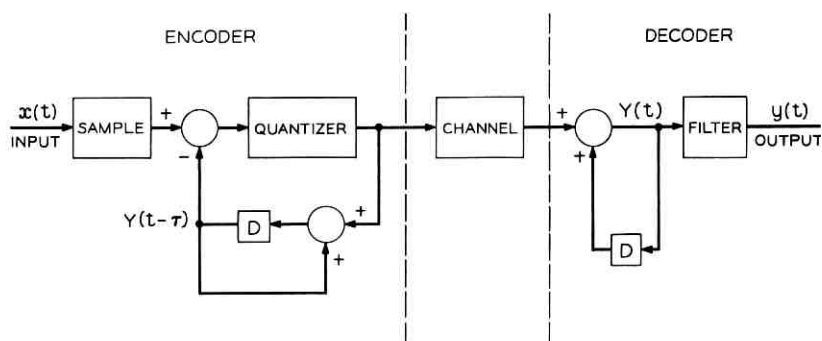
Fig. 1 — Basic binary ΔM system.

form an accumulator. The transfer function of the feedback loop is $D/(1 - D)$ where D is the unit delay operator $e^{-s\tau}$ and represents a delay of one sample interval τ. Since

$$D/(1 - D) = D + D^2 + D^3 \cdots,$$

the signal being fed back is simply the sum of all previously transmitted samples. It is also identical to the decoded signal at the receiver and represents the signal value predicted for the next sample time. The difference between the input signal and this predicted signal is quantized and transmitted through a discrete channel. In practice, it is necessary to insert a leak, or amplifier with gain less than one, in the feedback loop. Systems with leak are discussed in Section VII.

For the most part we restrict ourselves to 2-level quantizers whose outputs can assume only the levels $\pm k$, where k is called the step size. In this paper, the term delta modulation (ΔM) when used without qualifications implies a 2-level quantizer. The extension of our results to multi-level quantizers is simple and is covered in Section X. Systems with 2-level quantizers are of greater practical interest because, in this case, the equipment required for ΔM is simple and cheap compared to standard PCM systems. Since the quantizer levels are $\pm k$, the decoded output before filtering $Y(t)$ can assume the values $\pm ik$, $i = 1, 2, \cdots$.

We assume that the input signal $x(t)$ has zero mean, unit variance, and is bandlimited to the frequency band $(0, f_o)$. The sampling rate f_s is typically many times the bandwidth and, for a 2-level system, is identical to the bit rate.

In ΔM systems there are two types of quantizing noise, granular noise and overload noise. Granular noise is similar to the quantizing noise of PCM. It is caused by the fact that the output samples can assume only

discrete values which in ΔM are multiples of the step size k. Overload noise is a result of the fact that the maximum slope a ΔM system may reproduce is limited to kf_s.

Typical signals in a ΔM system are shown in Fig. 2. $Y(t)$ is the reconstructed output signal before filtering. The noise is defined as

$$n(t) = x(t) - y(t), \tag{1}$$

where $x(t)$ is the input signal and $y(t)$ is the output signal. In the example illustrated in Fig. 2 the noise $n(t)$ is granular before time t_o. At time t_o the slope of the input $x(t)$ exceeds that which the delta modulator is capable of transmitting. The period of slope overload in the case shown is from t_o to t_1 and the noise during this period is

$$n(t) = x(t) - [y(t_o) + (t - t_o)x_o'] \qquad t_o \leqq t \leqq t_1,$$

where $x_o' = kf_s$ is the maximum slope the delta modulator is capable of reproducing.

The quantizing noise is not independent of the signal. Fig. 2 illustrates that granular noise is determined by the instantaneous amplitude of the input signal and overload noise is determined by the slope of the input signal. For very large step sizes almost all of the noise is granular. As the step size is decreased the output signal loses its ability to rise and fall rapidly and overload noise becomes dominant. As the step size approaches zero so does the output $y(t)$. Due to the definition in (1) the noise $n(t)$ approaches the signal $x(t)$ and the S/N ratio, which is 10 log $\overline{x^2}/\overline{n^2}$, approaches zero db as the output $y(t)$ approaches zero.
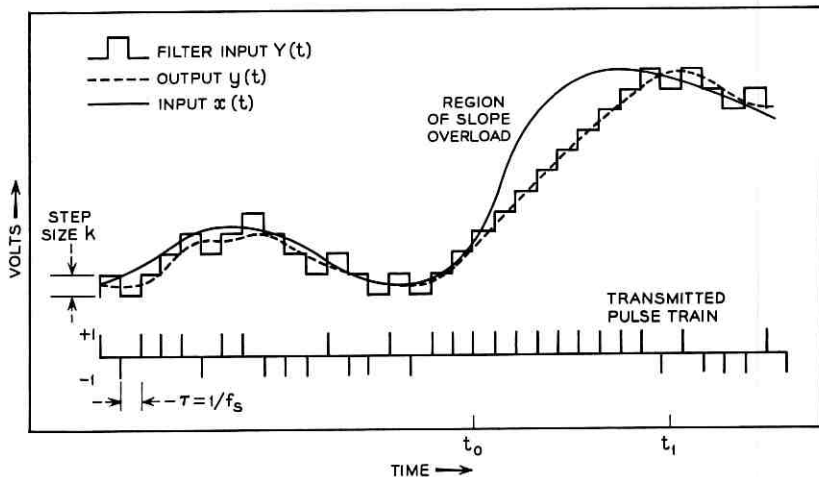
Fig. 2 — Signals in a ΔM system.

Clearly, this definition of the noise and of the S/N ratio must be used with discretion when the S/N ratio is small.

Any plot of S/N ratio versus step size will show a general tendency to approach the three asymptotes shown in Fig. 3. In Appendix A, S. O. Rice has computed an approximation for slope overload noise N_o for Gaussian input signals. This approximation is valid only when the maximum slope x_o' is somewhat larger than the rms value of $x'(t)$. In a previous paper[3] Van de Weg has found an approximation for the granular noise N_g, and his expression for N_g is used in this paper. If the overload noise is small it occurs in short bursts. During a burst, the overload noise is the dominant source of noise. When there is no overload burst all noise present is granular noise. The total noise power N can, therefore, be approximated by the sum of N_o and N_g. If we normalize our results so that the rms value of the input $x(t)$ is unity, then our approximation for the total noise power is

$$N = N_o + N_g, \tag{2}$$

$$N_o = \frac{3^5}{4\sqrt{2\pi}} \left(\frac{b_o^2}{b_2}\right) \left(\frac{f_s k}{\sqrt{b_o}}\right)^{-5} \exp\left(-\frac{f_s^2 k^2}{2b_o}\right), \tag{3}$$

$$N_g = \frac{8k^2}{\pi^2 F_s} \left[\frac{\pi^2}{12} + \sum_{n=1}^{\infty} \sum_{l=1}^{\infty} (-1)^{nl} \frac{\sin 2\pi n/F_s}{2\pi n/F_s} \frac{1}{l^2}\right.$$
$$\left. \exp\left(-\frac{\pi^2 l^2}{k^2}(1 - a_n)\right)\right], \tag{4}$$
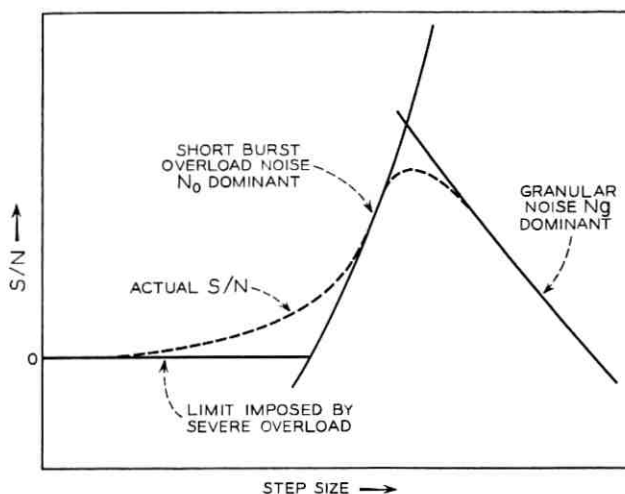
Fig. 3 — Asymptotes for S/N ratios in ΔM for $f_s \gg f_o$.

where

f_s = sampling frequency

$F_s = f_s/f_o$ = sampling frequency as a multiple of the bandwidth f_o

$a_n = \psi(n/f_s)$ where $\psi(\tau)$ is the autocovariance function of $x(t)$

k = step size

b_o = variance of $x'(t)$

b_2 = variance of $x''(t)$.

Equation (3) is obtained by substituting $f_s k$ for x_o' in (22) of Appendix A. Equation (4) is taken from page 382 of Ref. 3. These equations show that the noise power is a function of the power density spectrum of the input signal $x(t)$ since b_o, b_2, and $\psi(\tau)$ are determined by this spectrum. Since (2), (3), and (4) apply to an input signal with an rms value of 1, the rms signal to rms noise ratio in db is $S/N = -10 \log_{10} N$.

III. FLAT BANDLIMITED GAUSSIAN SIGNALS

For flat signals bandlimited to $(0, f_o)$ the expressions for b_o and b_2, which are computed from (17) in Appendix A, and $\psi(\tau)$ are

$$b_o = \frac{(2\pi f_o)^2}{3},$$

$$b_2 = \frac{(2\pi f_o)^4}{5},$$

$$\psi(\tau) = \frac{\sin 2\pi f_o \tau}{2\pi f_o \tau}, \tag{5}$$

Fig. 4 shows plots of S/N ratio for a flat bandlimited Gaussian input signal. Points from some simulated delta modulation systems are also illustrated. Sampling rates of 4, 8, 16, 32, and 64 times the bandwidth are shown. The S/N ratios are plotted as a function of the quantity $kf_s/f_o = kF_s$ which, for any given sampling rate, may be thought of as the normalized step size. As an example of the use of these curves, we see that for a sampling rate of 32 times the bandwidth the maximum S/N ratio is about 29 db and it will occur when the step size is about 12/32. If the rms value of the input signal were not 1 but σ then, of course, the maximum S/N ratio of 29 db would occur when the step size is $12\sigma/32$. To the left of the S/N peaks the noise is primarily overload noise N_o while to the right of these peaks the noise is primarily granular noise N_g. The optimum value of kF_s maximizes the S/N ratio by providing the proper balance between N_o and N_g.
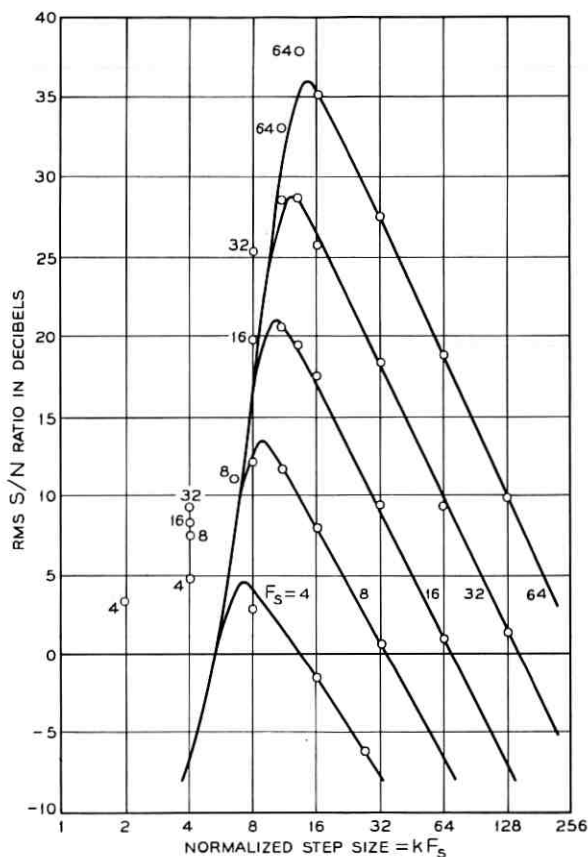
Fig. 4 — S/N ratio for bandlimited flat Gaussian signals showing theoretical curves and results of computer simulation. ($F_s = f_s/f_o$ is the ratio of sampling frequency to bandwidth.)

IV. RC SHAPED GAUSSIAN SIGNALS

If a flat Gaussian signal bandlimited to the frequency range $(0, f_o)$ is passed through a low-pass RC filter, then the one-sided power spectrum of the output is

$$F(f) = \frac{2\pi\alpha}{\tan^{-1}\left(\dfrac{2\pi f_o}{\alpha}\right)} \times \frac{1}{(2\pi f)^2 + \alpha^2} \qquad 0 < f < f_o, \qquad (6)$$

where we assume a mean square value of unity and $\alpha = 1/RC$. The RC

spectrum given by (6) is relatively flat from $f = 0$ to a corner frequency $f_c = \alpha/2\pi$ at which it rolls off to assume a slope of -6 db/octave up to the cutoff frequency f_o. It is shown in Appendix B that if α is small enough then we may approximate the autocovariance function $\psi(\tau)$ by

$$
\psi(\tau) = \frac{\dfrac{\pi}{2} e^{-\alpha\tau} - \alpha\tau \left(\dfrac{\cos 2\pi f_o\tau}{2\pi f_o\tau} + \mathrm{Si}\ (2\pi f_o\tau) - \dfrac{\pi}{2} \right)}{\dfrac{\pi}{2} - \dfrac{\alpha}{2\pi f_o}} \qquad \tau \geqq 0,
\tag{7}
$$

$$\psi(-\tau) = \psi(\tau).$$

The values of b_o and b_2 for this RC Gaussian signal are found from (17) to be

$$
b_o = \frac{2\pi f_o\alpha}{\tan^{-1}\left(\dfrac{2\pi f_o}{\alpha}\right)} - \alpha^2,
\tag{8}
$$

$$
b_2 = \frac{(2\pi f_o)^3\alpha - 6\pi f_o\alpha^3}{3\tan^{-1}\left(\dfrac{2\pi f_o}{\alpha}\right)} + \alpha^4.
\tag{9}
$$

Using the above expressions we can find the S/N resulting when an RC shaped signal is transmitted through a ΔM system. Figs. 5 and 6 show S/N versus $kf_s/f_o = kF_s$ for $\alpha = 0.25\ f_o$ and $\alpha = 0.068\ f_o$, respectively. These values for α were chosen because this causes the signal spectra to have roughly the same shape as the envelope of a *Picturephone* signal (using current standards) and a black and white entertainment TV signal (FCC standard), respectively. We assume here that the *Picturephone* signal would be bandlimited to 375 kc before encoding. Computer analysis of a composite video signal with current *Picturephone* standards indicates that the *Picturephone* spectrum has a corner at about

$$0.25 \times 375\ \mathrm{kc}/2\pi \cong 15\ \mathrm{kc}.$$

In the U.S., standard entertainment black and white TV is approximately bandlimited to 4.5 mc and has a corner at about 0.068×4.5 mc/$2\pi \cong 49$ kc.[*] These corner frequencies are slightly dependent on picture material. Although television signals have strong periodic components, the frequencies involved are so low that their periodic nature does not influence the S/N ratio. The spectrum of the quantizing noise, however, is affected by this periodicity, for, in general, periodic sampling of periodic signals produces quantizing noise which has periodic com-

---

[*] An unpublished study by W. N. Toy shows that this corner frequency may lie between 40 and 60 kc depending on picture material.
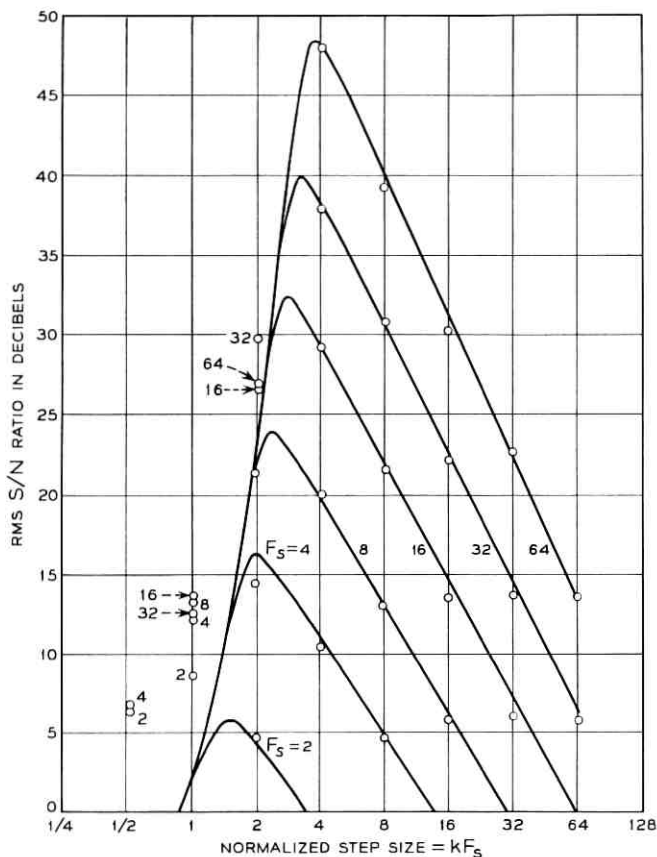
Fig. 5 — S/N for RC shaped Gaussian signals with $\alpha = 0.25 f_o$.

ponents. Although Figs. 5 and 6 apply specifically to Gaussian input signals, they give estimates of the performance of basic ΔM systems when used to transmit *Picturephone* signals and standard TV signals respectively. Fig. 11 which compares four of the curves in Fig. 5 with a computer simulation of an actual *Picturephone* visual telephone system using typical picture material shows that these estimates are good ones.

V. COMPARISON OF PCM AND ΔM FOR GAUSSIAN INPUTS

In Fig. 7, the S/N ratios for standard PCM and optimum basic ΔM systems with Gaussian input signals are compared. Bennett[1] showed that, under conditions usually encountered in practical systems, the rms
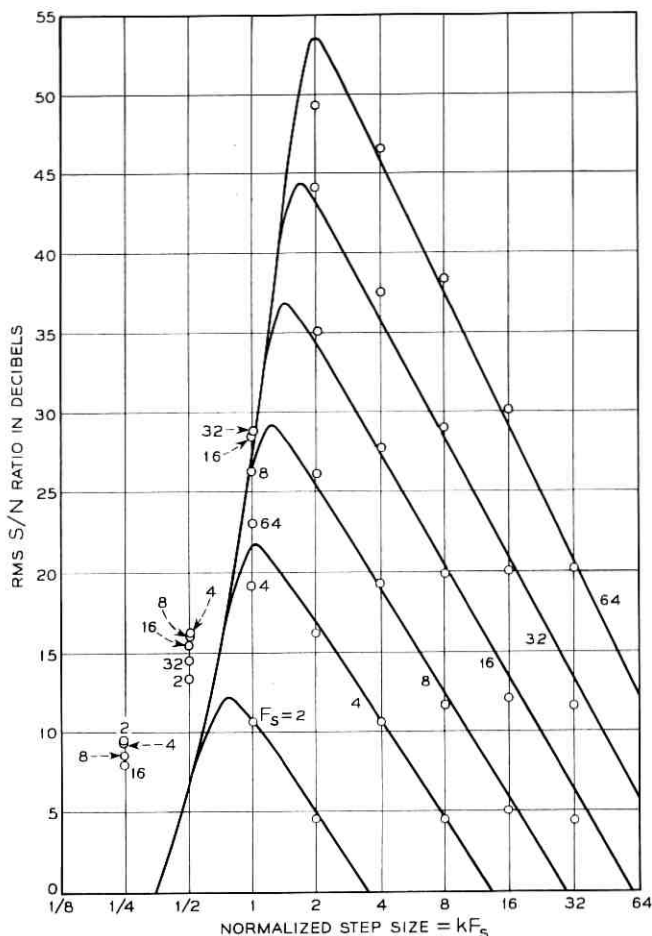
Fig. 6 — S/N for RC shaped Gaussian signals with $\alpha = 0.068 f_o$.

value of the quantizing noise for Nyquist rate sampled PCM is $E_o/\sqrt{12}$ where E_o is the step size. If n, the number of quantizing digits, is not too small, then E_o is equal to $E_p/2^n$, where E_p is the peak-to-peak value of the incoming signal. Therefore, the rms S/N ratio in db for PCM is

$$D = 20 \log \left(\frac{\sigma}{E_p} \sqrt{12} \right) + 20 \log 2^n,$$

where σ/E_p is the ratio of the signal's rms value to its peak value. If we encode only the values of the signal which lie between -4σ and
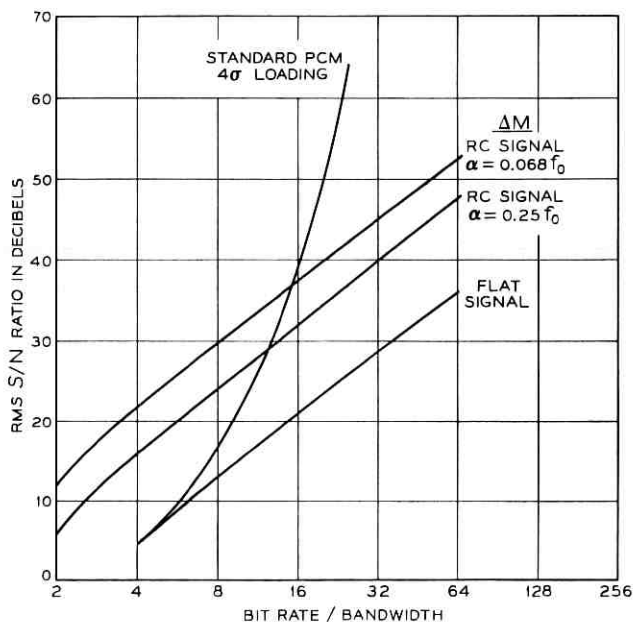
Fig. 7 — Comparison of ΔM and standard PCM for bandlimited Gaussian signals.

4σ and neglect values outside of this range then $E_p = 8\sigma$ and the formula for S/N ratio in db becomes

$$D \cong -7.3 + 6n.$$

This is called 4σ loading. Although 4σ loading is used for comparison in Fig. 7, this is not optimum loading. For PCM, the loading which gives the highest value of S/N is dependent on the number of digits, n, used to encode each sample value. PCM with a fixed amount of loading (regardless of n) provides a realistic comparison with ΔM in systems, such as television, where no amplitude overload is allowed. For other applications, however, restricting the PCM system to a fixed amount of loading may not provide a valid comparison between PCM and ΔM.

Although the curve shown in Fig. 7 for PCM is continuous, it is actually defined only when the bit rate is an even multiple of the bandwidth because we have assumed that the sampling rate is always twice the bandwidth.

VI. COMPUTER SIMULATION WITH GAUSSIAN SIGNALS

The basic ΔM system of Fig. 1 was simulated on an IBM 7094 digital computer and the resulting S/N ratios are shown as points on Figs. 4,

5, and 6. Flat bandlimited signals sampled at the Nyquist rate were easily simulated by simply using independent random numbers with a Gaussian distribution and unit variance. For convenience, we assumed that $f_0 = 1$. A flat signal sampled at R times the Nyquist rate is simulated by filtering the random samples with a digital filter whose cutoff frequency is $1/R$. A discussion of sampled data filters is given in Ref. 7. Digital sharp cutoff filters, like their continuous counterparts, are not easily realized. The filters used all had the general shape given in Fig. 8. The filter shown is down 3 db at 0.25 and we call the bandwidth 0.25 for this reason. This filter would be used when simulating ΔM systems whose sampling frequency is 8 times the bandwidth (4 times the Nyquist rate). Other filters used had exactly the same shape when plotted on a log scale but, of course, had different 3-db points. These low-pass filters were nonrecursive filters which were simulated by finding a sequence of numbers which represented the filter's impulse response. Filtering was
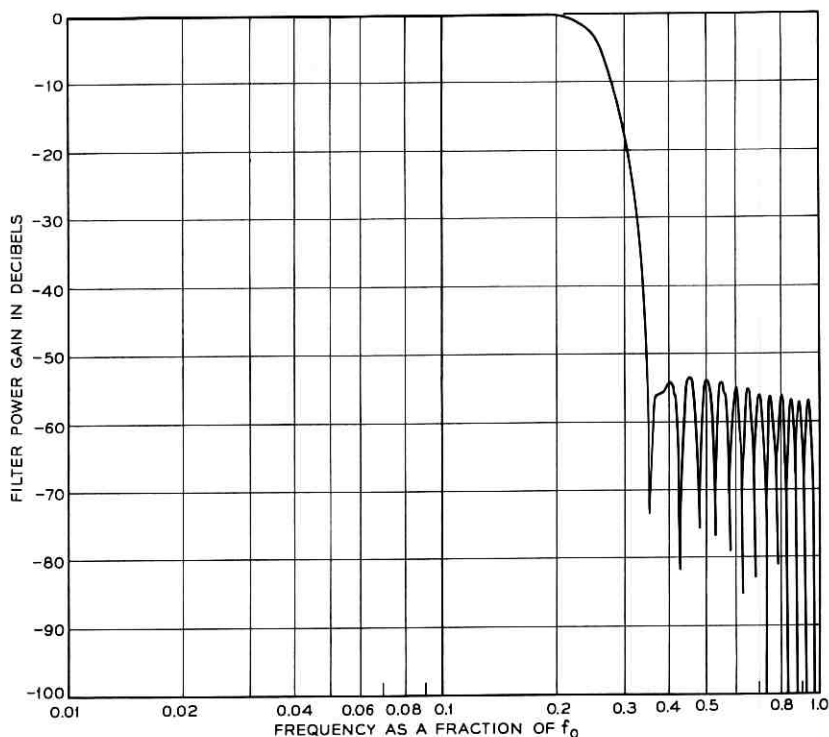
Fig. 8 — Power spectrum of low-pass filter with a bandwidth of $\frac{1}{4} f_o$ or $\frac{1}{8} f_s$.

accomplished by convolving the samples representing the signal with this sequence.

The RC shaped signals were simulated by passing the random samples representing flat noise through a digital simulation of a low-pass RC network.

VII. SIMULATION OF THE *PICTUREPHONE* SYSTEM

The basic ΔM system shown in Fig. 1 is impractical because errors introduced in the transmission medium will not decay out. To prevent the accumulation of errors from severely degrading the signal and to improve the operation of the system even when no errors are present, it is necessary to place a leak in the feedback loop represented by an amplifier with gain β less than unity. The ΔM system with leak added is shown in Fig. 9. This system was simulated on the computer and a signal similar to the *Picturephone* signal was encoded and decoded by it.

The input signal used was a television-like signal obtained by scanning a square slide with a slow-speed flying spot scanner, sampling the output, and encoding the samples into 11-bit PCM. The PCM samples were recorded on magnetic tape suitable as an input to the IBM 7094 digital computer.[8] The sampling frequency was synchronous with the line frequency. The slide used to produce the signal was a head and shoulders view of a girl similar to what might be expected on a *Picturephone* call. In this way, a signal was produced which represented a *Picturephone* signal. Current standards for the *Picturephone* system produce a 271-line picture with 2-to-1 interlace. The frame rate is 30 per second. The horizontal and vertical blanking pulses are 21 and 1000 μsec, respectively. The simulated signal was subjected to filtering so
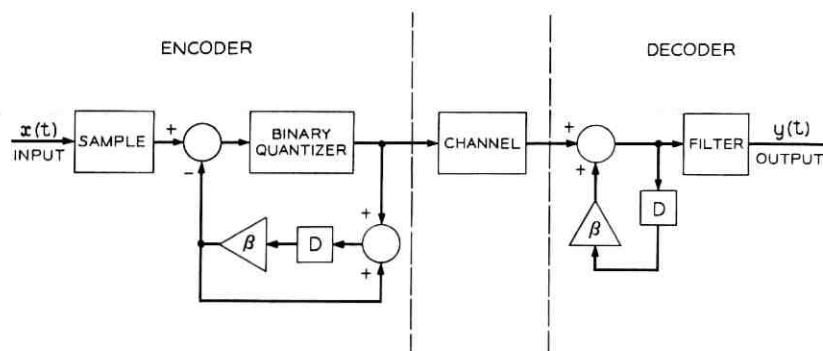
Fig. 9 — ΔM system with leak β.

that it was equivalent to a Picturephone signal which had been passed through a sharp cutoff filter with a bandwidth of 375 kc. The bandwidth then is considered to be 375 kc and sampling at R times the bandwidth means sampling at a rate of $R \times 375 \times 10^3$ samples per second.

The power spectrum of the composite signal (video and blanking pulses) on tape was found by computing the Fourier transform of its autocovariance function. The envelope of the power spectrum could be roughly approximated by the spectrum of (4) with an α of about 0.25. The spectrum, however, had the irregularities typical of a TV signal.

The slope overload produced by ΔM for smaller step sizes, occurs primarily during blanking intervals, and is not visible on the picture tube. For this reason, S/N ratios were found both for the composite signal and for the video part of the signal. In the region of interest, the S/N ratios for the video part of the signal are a few db above those for the composite signal.

Fig. 10 shows S/N ratios obtained from the simulation using the *Picturephone* signal on magnetic tape. The scale on the left of Fig. 10 gives rms composite signal to rms noise ratios. The scale on the right of Fig. 10 gives peak-to-peak composite signal to rms noise ratios because this is the quantity usually measured in television systems. The peak-to-peak composite signal to rms noise ratios are 11.6 db greater than the rms signal to rms noise ratios because the peak-to-peak value of the composite signal used is 11.6 db greater than its rms value. The relationship between three metrics associated with the input are as follows:

	relative value	db
peak-to-peak of composite signal	3.79	11.6
rms of composite signal	1	0
rms of video part of signal	0.512	−5.8

For each sampling rate in Fig. 10, there are two curves. In the solid curves the rms value of the noise in only the video part of the signal is used. The dotted curves use the rms value of the noise in the whole composite signal (video plus sync). Using only the noise in the video part leads to a better metric of picture quality because, as long as sync is maintained, noise in the sync pulses does not degrade the resulting television picture.

In Fig. 10 the actual bit rates are shown. For example, a bit rate of 6 megabits means sampling at 16 times the bandwidth since $16 \times 375 \times 10^3 = 6 \times 10^6$. The S/N ratios of the video signal varied only slightly with leak factor, β, as long as β was near 1. The values of β used were those which gave the best S/N ratios. These values are shown on Fig. 10
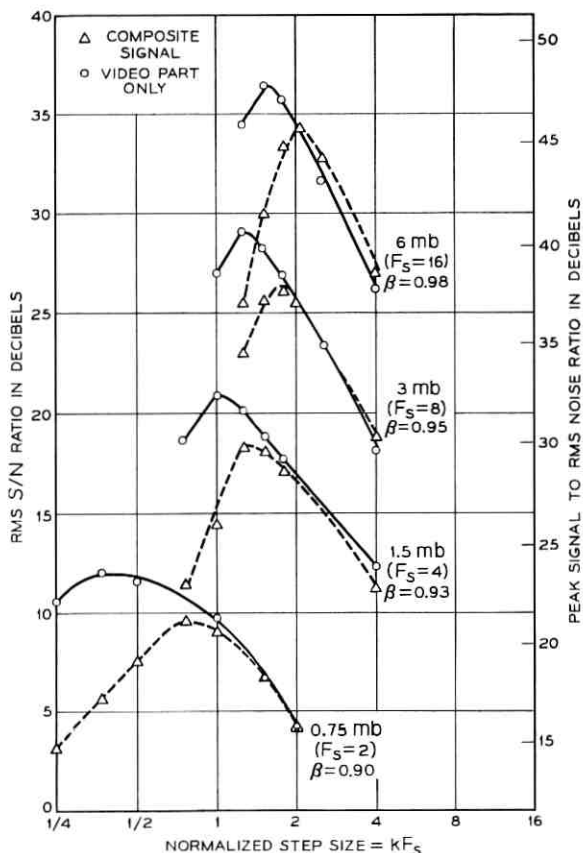
Fig. 10 — Simulated *Picturephone* systems. (Scale on the right assumes a signal whose peak-to-peak value is 11.6 db higher than its rms value.)

and also apply to the points on Fig. 11. It will be shown in a subsequent paper[9] how the optimum value of β is related to the covariance between adjacent sample values.

For the video, the optimum step sizes yielded peak-to-peak signal to rms noise ratios of 48.0, 40.8, 32.5, and 23.7 db for sampling rates of $16 f_o$(6 mb), $8 f_o$(3 mb), $4 f_o$(1.5 mb), and $2 f_o$(0.75 mb), respectively.

Fig. 11 was plotted to show the close agreement of the simulated *Picturephone* video results (with leak) to the theoretical results (without leak) for RC Gaussian signals with the same spectrum envelope as a *Picturephone* signal ($\alpha = 0.25 f_o$). The points in Fig. 11 are the same as those in Fig. 10 connected by the solid curves. They have been trans-
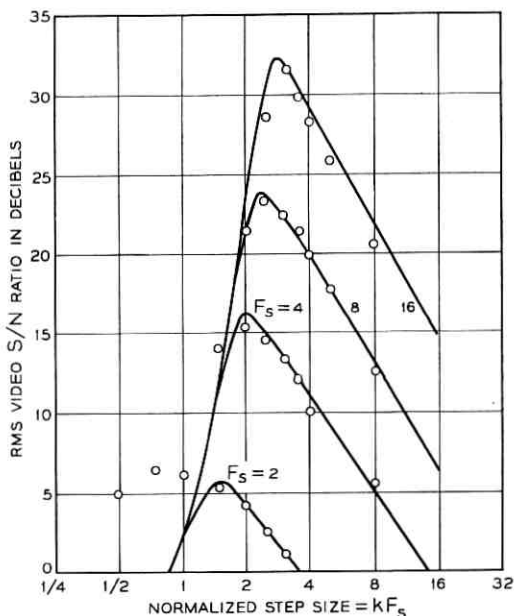
Fig. 11 — Comparison of simulated *Picturephone* video signals (points) to theoretical Gaussian results (solid curves) for $\alpha = 0.25 f_0$.

lated vertically by 5.8 db because the rms value of the video is 5.8 db less than the rms value of the composite signal, and they have been shifted to the right by a factor of $1/0.512$ because the normalized step size is expressed in terms of the rms value of the signal. In previous figures, the rms value of the signal meant the rms value of the composite signal which is 1, but in Fig. 11 we are dealing with the rms value of the video which is 0.512.

In Fig. 12, the peak-to-peak composite signal to rms noise ratios for the simulation of ΔM are compared with those for standard PCM systems. For n-digit standard PCM, the ratio of peak-to-peak signal to rms noise in db is

$$D_{pp} = 20 \log \sqrt{12} + 20 \log 2^n$$

$$\approx 10.8 + 6n.$$

In PCM, about 3 db can be gained by assigning only one or two levels to the sync pulses and using the remaining available levels to encode the video part of the signal. This has not been taken into consideration in the above formula or in Fig. 12.
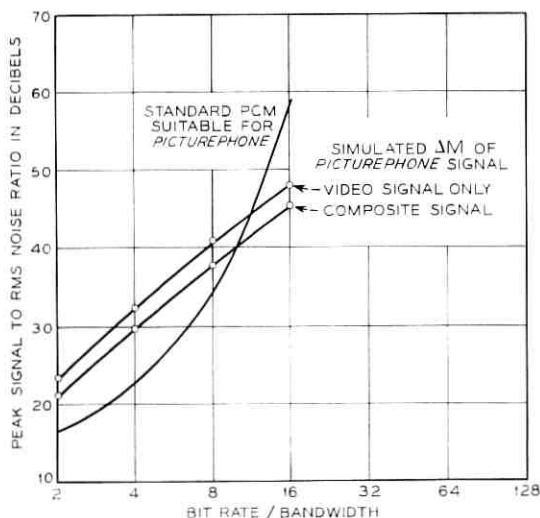
Fig. 12 — Comparison of simulated ΔM *Picturephone* system to standard PCM.

VIII. ESTIMATES OF S/N RATIOS FOR ΔM OF ENTERTAINMENT TELEVISION

The curves of Fig. 6 allow us to obtain a rough estimate of the S/N ratios possible for monochrome entertainment television systems (FCC standard). For the *Picturephone* signal used in the simulation, the rms video was 17.4 db below the peak-to-peak value of the composite signal. A comparison between *Picturephone* standards and entertainment television standards suggests that this is also a reasonable number for entertainment television. Moreover, since this number is dependent on picture material, we can rest comfortably in the knowledge that we can surely find a picture whose rms video is 17.4 db below its peak-to-peak value. It should be possible to transmit such a picture with peak-to-peak composite signal to video rms noise ratios of about 54, 46, 38, and 29 db at bit rates of 16, 8, 4, and 2 times the bandwidth, respectively. These ratios were found by adding 17.4 db to the peak values of the curves in Fig. 6.

IX. INTERPRETATION OF S/N RATIOS FOR TELEVISION SYSTEMS

It is well known that the quality of a television picture cannot be judged by its S/N ratio alone. In fact, such a judgment may be quite misleading. The quality of a picture contaminated with additive flat Gaussian noise may be quite different from that of the same picture

contaminated by ΔM quantizing noise even if the S/N ratios are identical.

Quantizing noise in standard PCM exhibits itself in television pictures as contouring. If the number of digits used is high enough, typically 7 or 8 for monochrome entertainment television, then the eye cannot detect contouring and no degradation due to quantizing noise is noticeable. In ΔM, quantizing noise in television signals exhibits itself subjectively in four ways — as grainy noise, slope overload, contouring, and edge busyness. The fact that the noise is present in four subjectively different forms may be a significant advantage for ΔM. An observer normally judges the quality of a television picture by the most severe degradation that he sees rather than by jointly considering several different types of degradation. ΔM takes advantage of this. In a subjectively optimum ΔM system the step size, sampling rate, and filter characteristics are chosen to spread the degradation into these four categories to produce the best subjective picture. In earlier computations, we considered all noise to be either granular noise N_g or overload noise N_o. In this section, we have further divided granular noise into three different categories — grainy noise, contouring, and edge busyness—because this N_g exhibits itself as three subjectively distinguishable phenomena. Granular quantizing noise tends to have a rectangular amplitude distribution and is likely to be less annoying than an equivalent amount of additive noise with a Gaussian amplitude distribution.

Slope overload noise will appear subjectively like a loss of bandwidth since the rise time of white to black transitions is increased. The snow or salt and pepper effect so ubiquitous in TV systems is what we are calling grainy noise. Contouring occurs since there are only a finite number of steady levels or flat tones which can be established by a ΔM system (if the leak β is unity the number of levels is one less than the peak-to-peak value of the signal divided by the step size). Edge busyness exhibits itself as a busyness at vertical edges, i.e., vertical white to black transitions, when the sampling rate and line rate are not synchronized. Due to the lack of synchronization and the finite time between samples these transitions do not occur in a straight line on successive lines and frames.

X. MULTI-LEVEL QUANTIZING

If the quantizer shown in Fig. 1 is not a 2-level device, then the formula for N_o in (3) must be modified. If we define an n-digit uniform quantizer to be one which quantizes its input into the nearest one of the

2^n levels $\pm k$, $\pm 3k$, $\cdots$, $\pm(2^n - 1)k$, then overload noise does not occur until $|x'(t)|$ becomes greater than $(2^n - 1)kf_s$. To modify N_o in (3) then to accommodate a uniform n-level quantizer we simply replace k by $(2^n - 1)k$. The expression for N_g does not need to be modified.

XI. SUMMARY AND CONCLUSIONS

An analytical solution for the S/N ratio as a function of step size and bit rate is presented for a signal with an arbitrary spectrum and Gaussian amplitude distribution. The correctness of the solution has been demonstrated by computer simulation of some delta modulation systems. Computer simulations with low bandwidth television signals have shown that the formula is accurate for actual video signals whose amplitude distribution is not necessarily Gaussian. These analytical results will allow us to predict what values of S/N ratio may be obtained at various bit rates for many types of signals.

Some computer simulations demonstrated that properly designed ΔM systems can transmit 375-kc *Picturephone* signals with peak signal to rms noise ratios as high as 24, 32, 40, and 48 db for bit rates of 2, 4, 8, and 16 times the bandwidth, respectively. Estimates of the S/N ratios possible for 4.5-mc black and white entertainment television are about 29, 38, 46, and 54 db for the above bit rates, respectively. These S/N ratios are somewhat dependent on picture material. Although S/N ratios are an important indicator of system performance, final judgments about a system's ability to transmit television pictures must be based on subjective viewing tests.

The quantizing noise in television ΔM systems distributes itself into 4 visually distinguishable categories. This suggests that ΔM quantizing noise may be subjectively less objectionable than an equivalent amount of noise introduced by other means.

Any comparison between the relative performance of ΔM and standard PCM depends on the characteristics of the signal to be transmitted. Generally, however, for signals whose spectra decrease with frequency, ΔM is superior by the S/N criterion to standard PCM when low quality reproduction of the signal is allowed. For high-quality systems, standard PCM gives better results than ΔM. This is due to the fact that in ΔM doubling the bit rate gives only about an 8-db gain in S/N ratio. In standard PCM, increasing the number of bits per sample by 1 increases the S/N ratio by 6 db. The relative performance of ΔM and standard PCM for two types of signals is illustrated in Figs. 7 and 12.

APPENDIX A [*]

Noise Burst, Steep-Slope Approximation to Δ-Modulation Noise

When the step size is not too large, most of the output noise in a delta modulation system is produced in bursts. The bursts occur when the time derivative of the input exceeds the maximum slope permitted by the system. An approximation for the average value of the power in this type of noise is given here. It turns out that the analysis is quite similar to that used to study the distribution of fade lengths in radio transmission (see (1) of Ref. 10).

The material given here was worked out jointly by Mr. O'Neal and myself. The concepts and approximations associated with the delta modulation system are due to him. My part consisted chiefly in supplying the steps suggested by the analogy with the fading problem.

The problem is the following. Let the input voltage be a Gaussian process $x(t)$ with (one-sided) power spectrum $F(f)$. Let the output of the system be $y(t)$. Most of the time $y(t)$ will be equal to $x(t)$. During intervals of this sort, the absolute value of $x'(t) = dx(t)/dt$ is less than some given positive quantity x_o'. The intervals during which $y(t) \neq x(t)$ start at the instants $|x'(t)|$ increases through the value x_o'. Let t_o denote the starting time of a particular interval of this type and suppose, for convenience, that $x'(t_o)$ is positive so that $x'(t_o) = x_o'$. Throughout the interval $y(t)$ is defined to be $x(t_o) + (t - t_o)x_o'$, and increases linearly with time. The interval lasts as long as $x(t)$ exceeds $y(t)$. It ends at time t_1 when $x(t)$ and $y(t)$ again become equal;

$$x(t_1) = y(t_1) = x(t_o) + (t_1 - t_o)x_o'. \tag{10}$$

For intervals starting with $x_o'(t_o) = -x_o'$, $y(t)$ is defined similarly by $y(t) = x(t_o) - (t - t_o)x_o'$.

The output noise is defined to be

$$n(t) = x(t) - y(t). \tag{11}$$

[*] This appendix was written by S. O. Rice.

Since $n(t)$ will be zero much of the time, the noise tends to occur in short bursts. The average noise power is

$$\overline{n^2(t)} = \lim_{T \to \infty} \frac{1}{T} \int_0^T n^2(t) \, di. \tag{12}$$

We seek an approximation for $\overline{n^2(t)}$ which holds when $x_o{}'$ is large compared to the rms value of $x'(t)$.

When $x_o{}'$ is large, the interval $t_1 - t_o$ tends to be small and an expression for its length may be obtained by considering the expansion of $x(t)$ about t_o. Here, and in much of the following, we take $x'(t_o)$ to be positive:

$$x(t) = x(t_o) + (t - t_o)x_o{}' + \frac{(t - t_o)^2}{2!} x''(t_o)$$
$$+ \frac{(t - t_o)^3}{3!} x'''(t_o) + \cdots \tag{13}$$

$$0 = \frac{(t_1 - t_o)^2}{2!} \left(x''(t_o) + \frac{t_1 - t_o}{3} x'''(t_o) \cdots \right) \tag{14}$$

$$t_1 - t_o = -\frac{3x''(t_o)}{x'''(t_o)} + \cdots. \tag{15}$$

In going from the first equation to the second we have set $t = t_1$ and used the end-of-interval relation (10). When $x_o{}'$ is large we can expect $x'''(t_o)$ to be large and negative while $x''(t_o)$ remains of order 1. This is shown in the following paragraph.

To begin with, consider the special case $x = \sin \omega t$ with t near zero. Then x and its time derivatives are such that $x \approx 0$, $x' \approx \omega$, $x'' \approx 0$, $x''' \approx -\omega^3$, etc. Our Gaussian $x(t)$ and its derivatives behave in somewhat the same way when $x'(t)$ is large. Let $\xi = x'(t)$, $\eta = x''(t)$, $\zeta = x'''(t)$ denote the first three derivatives at time t of an $x(t)$ chosen at random from the ensemble of $x(t)$'s. It may be shown that their joint probability density is

$$\frac{(2\pi)^{-3/2}}{\sqrt{b_2 B}} \exp\left[-\frac{\xi^2}{2b_o} - \frac{\eta^2}{2b_2} - \frac{(\zeta + b_2 b_o{}^{-1}\xi)^2}{2Bb_o{}^{-1}} \right], \tag{16}$$

where b_o and b_2 are the respective variances of $x'(t)$ and $x''(t)$, and

$$b_n = \int_0^\infty (2\pi f)^{n+2} F(f) \, df, \qquad n = 0, 2, 4$$
$$B = b_o b_4 - b_2{}^2 \tag{17}$$

where $F(f)$ is the power spectrum of $x(t)$. When $x'(t)$ is held fixed at

the large value x_o', (16) shows that the average value of $x'''(t)$ is $-b_2 x_o'/b_o$. If x_o' is so large that this average value is large compared to the standard deviation $\sqrt{B/b_o}$, we are led to approximate $x'''(t)$ in expression (15) in the interval $t_1 - t_o$ by its average value. Making the further approximation of neglecting the higher order terms in (15) gives

$$t_1 - t_o \approx \frac{3 b_o x''(t_o)}{b_2 x_o'} \tag{18}$$

for the length of the interval during which $x(t)$ exceeds the output $y(t)$.

The noise energy in the burst corresponding to the interval $t_1 - t_o$ is

$$
\begin{aligned}
\int_{t_o}^{t_1} n^2(t)\, dt &= \int_{t_o}^{t_1} [x(t) - y(t)]^2\, dt \\
&= \int_{t_o}^{t_1} [x(t) - x(t_o) - (t - t_o)x_o']^2\, dt \\
&\approx \int_{t_o}^{t_1} \left[\frac{(t - t_o)^2}{2!} x''(t_o) + \frac{(t - t_o)^3}{3!} x'''(t_o) \right]^2 dt \\
&\approx \frac{81}{140} \left(\frac{b_o}{b_2 x_o'} \right)^5 [x''(t_o)]^7 .
\end{aligned}
\tag{19}
$$

In going to the last line, the approximation (18) for $t_1 - t_o$ is used and $x'''(t_o)$ is replaced by $-b_2 x_o'/b_o$. It is helpful to make the change of variable $t - t_o = (t_1 - t_o)z$.

Expression (19) gives the noise energy in a burst for which the initial value of $x''(t)$ is equal to $x''(t_o)$. As we go from burst to burst, $x''(t_o)$ will fluctuate but it will always be positive for the type of interval $(x'(t_o) = x_o' > 0)$ we are considering. This is because $x'(t)$ is increasing as it passes upward through the value x_o' at time t_o.

The next step is to find the average noise energy in a burst. When a member $x(t)$ is picked at random from the ensemble of $x(t)$'s, the chance that $x'(t)$ will increase through the value x_o' during t_o, $t_o + dt$ with slope between x'' and $x'' + dx''$ is $x'' p(x_o', x'') dx''\, dt$, where

$$p(\xi, \eta) = \frac{(2\pi)^{-1}}{\sqrt{b_o b_2}} \exp\left[-\frac{\xi^2}{2 b_o} - \frac{\eta^2}{2 b_2} \right]$$

is the joint probability density of $x'(t)$ and $x''(t)$ (see Section 3.5 of Ref. 11). When the ensemble of $x(t)$'s consists of an extremely large number M of members, the number which have the above behavior is approximately $(M\, dt) x'' p(x_o', x'') dx''$. The total number M_o which pass upward through x_o' during $t_o, t_o + dt$ is obtained by integrating from $x'' = 0$ to $x'' = \infty$:

$$M_o = \frac{(M\,dt)}{2\pi} \left(\frac{b_2}{b_o}\right)^{\frac{1}{2}} \exp\left(-\frac{x_o'^2}{2b_o}\right).$$

Since the noise energy in a burst is proportional to x''^7 we average it over the M_o members:

$$\text{ave } x''^7 = \frac{1}{M_o} \int_0^\infty x''^7 (M\,dt)[x''p(x_o',x'')\,dx'']$$

$$= (2b_2)^{7/2}\Gamma(9/2).$$

Combining this with (19) gives

$$\text{ave} \int_{t_o}^{t_1} n^2(t)\,dt \approx \frac{\sqrt{2\pi}}{8}\left(\frac{3b_o}{x_o'}\right)^5 b_2^{-3/2} \tag{20}$$

for the average noise energy in a burst.

Our final assumption is that a noise burst occurs every time $x'(t)$ increases through x_o' or decreases through $-x_o'$. The true number of bursts tends to be less than this because such crossings can occur when a burst is in progress. From noise theory,[11] the expected number of such crossings in one second is

$$2\frac{1}{2\pi}\left(\frac{b_2}{b_o}\right)^{\frac{1}{2}} \exp\left(-\frac{x_o'^2}{2b_0}\right). \tag{21}$$

Multiplying by the average burst energy (20) then gives

$$\overline{n^2(t)} \approx \frac{1}{4\sqrt{2\pi}}\left(\frac{b_o^2}{b_2}\right)\left(\frac{3b_o^{\frac{1}{2}}}{x_o'}\right)^5 \exp\left(-\frac{x_o'^2}{2b_o}\right) \tag{22}$$

which is the approximation sought for the average noise power.

The right-hand side of (22) has the dimension of $(\text{volt})^2$ since the dimensions of x_o', b_o, b_2, are volt/sec, (volt/sec)^2, (volt/sec^2)^2, respectively.

APPENDIX B

Computation of $\psi(\tau)$ for a Bandlimited RC Signal

By a bandlimited RC signal we mean a signal which will result if white noise is passed through a low-pass RC filter and then bandlimited to the interval $(0,f_0)$. The one-sided power spectrum of such a signal with unit variance is

$$F(f) = \frac{2\pi}{\alpha \tan^{-1}\left(\dfrac{2\pi f_o}{\alpha}\right)} \times \frac{\alpha^2}{(2\pi f)^2 + \alpha^2} \qquad 0 < f < f_o$$

$$F(f) = 0 \qquad f \geqq f_o.$$

where $\alpha = 1/RC$.

The autocovariance function of a bandlimited RC signal with unit variance is

$$\psi(\tau) = \int_0^\infty F(f) \cos 2\pi f\tau \, df$$

$$\psi(\tau) = K\left[\int_0^\infty \frac{\alpha^2}{(2\pi f)^2 + \alpha^2} \cos 2\pi f\tau \, df \right. \tag{23}$$

$$\left. - \int_{f_o}^\infty \frac{\alpha^2}{(2\pi f)^2 + \alpha^2} \cos 2\pi f\tau \, df \right],$$

where

$$K = \frac{2\pi}{\alpha \tan^{-1}(2\pi f_o/\alpha)}.$$

The first integral can be evaluated by contour integration and is found to be $(\alpha/4) \exp(-\alpha|\tau|)$. If α is small enough then the second integral can be approximated by

$$\int_{f_o}^\infty \frac{\alpha^2}{(2\pi f)^2 + \alpha^2} \cos 2\pi f\tau \, df$$

$$\cong \alpha^2 \int_{f_o}^\infty \frac{1}{(2\pi f)^2} \cos 2\pi f\tau \, df \tag{24}$$

$$\cong \frac{\alpha^2 |\tau|}{2\pi} \left[\frac{\cos 2\pi f_o |\tau|}{2\pi f_o |\tau|} + \text{Si} \ (2\pi f_o |\tau|) - \frac{\pi}{2} \right].$$

Therefore,

$$\psi(\tau) \cong K\left[\frac{\alpha}{4} e^{-\alpha|\tau|} - \frac{\alpha^2 |\tau|}{2\pi} \left(\frac{\cos 2\pi f_o |\tau|}{2\pi f_o |\tau|} + \text{Si} \ (2\pi f_o |\tau|) - \frac{\pi}{2} \right) \right],$$

where Si is the sine integral function. The above approximation of $\psi(\tau)$ does not have $\psi(0) = 1$ which is the necessary requirement of unit variance. To restore this requirement we divide the above expression by $\psi(0)$. Therefore, the autocovariance function for a bandlimited RC signal with unit variance may be approximated by

$$\psi(\tau) \cong \frac{\frac{\pi}{2} e^{-\alpha|\tau|} - \alpha |\tau| \left(\frac{\cos 2\pi f_o |\tau|}{2\pi f_o |\tau|} + \text{Si} \ (2\pi f_o |\tau|) - \frac{\pi}{2} \right)}{\frac{\pi}{2} - \frac{\alpha}{2\pi f_o}}.$$

Although the above approximation is convenient for computational purposes, an exact expression for $\psi(\tau)$ can be found. Instead of approxi-

mating the second integral on the right-hand side of (23), it can be integrated exactly giving

$$\frac{\alpha}{4\pi} \text{ Im } [e^{-\alpha\tau}E_1(-\alpha\tau - i2\pi f_o\tau) - e^{\alpha\tau}E_1(\alpha\tau - i2\pi f_o\tau)],$$

where E_1 is the exponential integral. An alternate way of arriving at the approximation in (24) is to expand the E_1 functions in the above expression about $-i2\pi f_o\tau$ and take the limit as α becomes small.

REFERENCES

1. Bennett, W. R., Spectra of Quantized Signals, B.S.T.J., 27, July, 1948, pp. 446–472.
2. de Jager, F., Delta Modulation, A method of PCM Transmission Using a 1-Unit Code, Philips Res. Rep. 7, 1952, pp. 442–466.
3. Van de Weg, H., Quantizing Noise of a Single Integration Delta Modulation System with an N-Digit Code, Philips Res. Rep. 8, 1953, pp. 367–385.
4. Zetterberg, L., A Comparison Between Delta and Pulse Code Modulation, Ericsson Technics, 2, No. 1, 1955, pp. 95–154.
5. Cutler, C. C., Differential Quantization of Communication Signals, Patent No. 2,605,361, July 29, 1952.
6. Graham, R. E., Predictive Quantizing of Television Signals, IRE Wescon Convention Record, Part 4, 1958, pp. 147–157.
7. Kaiser, J. F., Design Methods for Sampled Data Filters, Proceedings of the First Allerton Conference on Circuit and System Theory, J. B. Cruz, editor, U. of Illinois Press, Urbana, Ill., 1963.
8. Graham, R. E. and Kelly, J. L., Jr., A Computer Simulation Chain for Research on Picture Coding, IRE Wescon Convention Record, Part 4, Aug., 1958, pp. 41–46.
9. O'Neal, J. B., Jr., Predictive Quantizing Systems (Differential Pulse Code Modulation) for Television Signals, to be published.
10. Rice, S. O., Distribution of Fades in Radio Transmission, B.S.T.J., 37, May, 1958, pp. 581–635.
11. Rice, S. O., Mathematical Analysis of Random Noise, B.S.T.J., 23, 1944, pp. 282–332; 24, 1945, pp. 46–156.

Phase Principle for Detecting Narrow-Band Gaussian Signals

By A. J. RAINAL

This paper describes a phase principle for detecting a weak, narrow-band Gaussian signal in the presence of receiver noise. The phase principle leads to a phase detector which performs 2.5 db worse than the time-honored square-law detector when gain fluctuations are negligible. However, when gain fluctuations are significant the phase detector can perform better than the square-law detector. The phase principle can be implemented by using radio interferometer type receivers or monopulse radar-type receivers.

I. INTRODUCTION

In many branches of science and technology one is often confronted with the problem of detecting a weak, narrow-band Gaussian signal in the presence of receiver noise. For example, this problem occurs in the fields of radio and radar astronomy, radar detection, and radio communication. The classical solution to this problem utilizes the time-honored square-law detector. The output of the square-law detector is proportional to the total power applied at its input. One detects the presence of a Gaussian signal in the presence of receiver noise by monitoring the total power. When the total power is relatively high the signal is supposed to be present. Present-day radiometers use this principle.

In this paper we shall describe a phase principle for detecting a narrow-band Gaussian signal in the presence of receiver noise. We shall show that the phase principle leads to a phase detector whose performance is comparable to the square-law detector when gain fluctuations are negligible. Furthermore, the phase detector is relatively insensitive to system gain fluctuations; whereas the square-law detector is highly sensitive to system gain fluctuations. That is, the phase detector enjoys this important property shared by the polarity-coincidence correlator,[1,2] the phase detector analyzed by Huggins and Middleton,[3] and the zero-cross-

ing detector.[4] The latter two detectors are suitable for detecting an extremely narrow-band signal immersed in narrow-band noise, and they are insensitive to a "white" Gaussian signal.

II. IMPLEMENTATION AND RELATIVE PERFORMANCE OF THE PHASE DETECTOR

Fig. 1 illustrates a simplified implementation of the phase detector for detecting a narrow-band Gaussian signal. We assume that two receivers are available for detection purposes. $S(t)$, and $N_1(t)$ and $N_2(t)$ represent zero mean, independent, narrow-band Gaussian processes. $N_1(t)$ and $N_2(t)$ are considered to be receiver noises of equal variances. $S(t)$ represents the narrow-band Gaussian signal to be detected. η_i represents the ith independent sample of the phase difference between $S(t) + N_1(t)$ and $S(t) + N_2(t)$. η_i is taken to be in the primary interval $(-\pi, \pi)$. After n such samples the output $\eta^\dagger$ of the phase detector is given by

$$\eta^\dagger = \frac{1}{n} \sum_{i=1}^{n} \cos \eta_i . \tag{1}$$

One compares $\eta^\dagger$ with some constant threshold value Λ_1 and decides that signal is present if $\eta^\dagger > \Lambda_1$. Otherwise the signal is supposed to be absent.

We shall compare the performance of the phase detector with the performance of the square-law detector on the basis of the "deflection criterion." [6] In general, if f_{s+N} and f_N represent the output of a detector with and without signal, respectively, then the "deflection criterion" bases the performance of the detector on the detection index
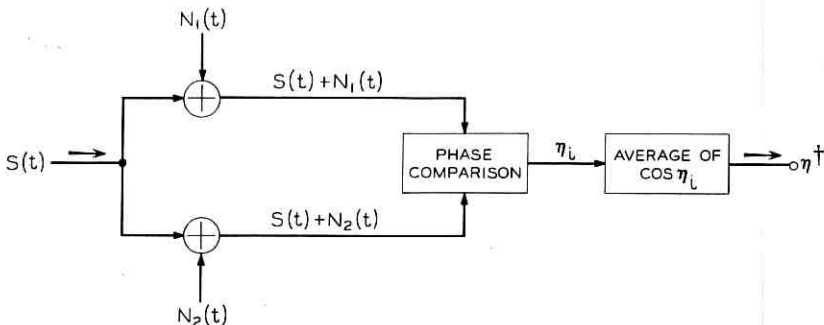
Fig. 1 — Simplified implementation of the phase detector for detecting a narrow-band Gaussian signal. ($S(t)$, $N_1(t)$, and $N_2(t)$ represent independent, narrow-band Gaussian processes.)

k where

$$k \equiv \frac{|Ef_{s+N} - Ef_N|}{[\text{Var } f_{s+N} + \text{Var } f_N]^{\frac{1}{2}}} \tag{2}$$

$$E = \text{Expectation}$$

$$\text{Var} = \text{Variance.}$$

This form of the detection index was also used in Ref. 3. Incidentally, comparing the detectors on the basis of the detection index when large sample sizes and weak signals are involved is equivalent to comparing the detectors on the basis of probability of error and probability of false alarm. This equivalence is demonstrated in Ref. 4.

General statistical properties of η_i were derived in Ref. 5. Using these results we find that

$$E \cos \eta_i = \frac{\pi l}{4} \, {}_2F_1\left(\frac{1}{2}, \frac{1}{2}; 2; l^2\right) \tag{3}$$

$$E \cos^2 \eta_i = \frac{1}{2} + \frac{l^2}{4} \, {}_2F_1(1, 1; 3; l^2) \tag{4}$$

where ${}_2F_1$ is the Gaussian hypergeometric function

$$_2F_1(\alpha, \beta; \gamma; x) \equiv 1 + \frac{\alpha\beta}{\gamma} x + \frac{\alpha(\alpha + 1)\beta(\beta + 1)}{\gamma(\gamma + 1)} \frac{x^2}{2!} + \cdots$$

and

$$l = \frac{a}{1 + a}$$

$$a = \frac{\text{Var } S(t)}{\text{Var } N_1(t)} = \frac{\text{Var } S(t)}{\text{Var } N_2(t)}.$$

Thus,

$$E\eta^\dagger = E \cos \eta_i \tag{5}$$

$$\text{Var } \eta^\dagger = \frac{\text{Var } \cos \eta_i}{n} = \frac{E[\cos^2 \eta_i] - E^2[\cos \eta_i]}{n}. \tag{6}$$

Thus, for small values of "a", the only case of interest in this paper, the detection index k for the phase detector is given by

$$k = \frac{E\eta^\dagger}{[2 \text{ Var } \eta^\dagger]^{\frac{1}{2}}} = \frac{\pi a \sqrt{n}}{4}. \tag{7}$$

The output, I_n, of a square-law detector operating on $2n$ independent samples of the Gaussian sum signal $N_1(t) + N_2(t) + 2S(t)$ has the following mean and variance[7]:

$$EI_n = 2 [\text{Var } N_1(t) + 2 \text{ Var } S(t)] \tag{8}$$

$$\text{Var } I_n = \frac{4 [\text{Var } N_1(t) + 2 \text{ Var } S(t)]^2}{n}. \tag{9}$$

Thus, for small values of "a" the detection index k_1 for the square-law detector is given by

$$k_1 = \frac{4 \text{ Var } S(t)}{\left[\dfrac{8 \text{ Var}^2 N_1(t)}{n}\right]^{\frac{1}{2}}} = a\sqrt{2n}. \tag{10}$$

Incidentally, the square-law detector operating on the Gaussian sum signal is equivalent to the Neyman-Pearson detector of reference 2.

For equal detector performances the detection indices must be equal. Thus, from (7) and (10) we see that the performance of the square-law detector, in terms of signal-to-noise power ratio "a," is approximately 2.5 db better than the performance of the phase detector when gain fluctuations are negligible. Clearly, when gain fluctuations are significant the phase detector can perform better than the square-law detector since the phase difference η_i is relatively insensitive to gain fluctuations. The phase detector can be implemented by using radio interferometer-type receivers or monopulse radar-type receivers.[5]

It will now be shown that the test statistic $\eta^\dagger$ defined by (1) is the optimum test statistic for processing n independent samples of the phase difference η_i. Equation (34) of Ref. 5 gives the probability density $p_2(\eta)$ of each independent sample η_i as

$$p_2(\eta) = \frac{1 - l^2}{2\pi} (1 - \beta_2{}^2)^{-3/2} \left[\beta_2 \sin^{-1} \beta_2 + \frac{\pi \beta_2}{2} + \sqrt{1 - \beta_2{}^2}\right] \tag{11}$$

where

$$\beta_2 = l \cos \eta$$

$$l = \frac{a}{1 + a}.$$

By using (11) for small values of "a" and applying the likelihood-ratio test[8,9] associated with n independent samples of η_i one decides that a signal is present only if

$$\log \frac{\prod_{i=1}^{n} \frac{1}{2\pi} \left(1 + \frac{\pi}{2} a \cos \eta_i \right)}{\left(\frac{1}{2\pi} \right)^n} > \Lambda_0 , \tag{12}$$

or

$$\sum_{i=1}^{n} \log \left(1 + \frac{\pi a}{2} \cos \eta_i \right) \doteq \frac{\pi}{2} a \sum_{i=1}^{n} \cos \eta_i > \Lambda_0 , \tag{13}$$

or

$$\frac{1}{n} \sum_{i=1}^{n} \cos \eta_i = \eta^\dagger > \Lambda_1 \tag{14}$$

where Λ_0 and Λ_1 are constant threshold values. This establishes the optimum property of $\eta^\dagger$.

III. CHARACTERISTICS OF THE PHASE DETECTOR

Let us summarize the important characteristics of the phase detector:

(*i*) The phase detector is relatively insensitive to system gain fluctuations.

(*ii*) For detecting weak signals, the performance of the phase detector is comparable to the performance of the square-law detector even with no gain fluctuations. With significant gain fluctuations, the phase detector can perform better than the square-law detector. Furthermore, unlimited post-detection integration is permitted with the phase detector.

(*iii*) The narrow-band signal applied to the phase detector may be a "white" Gaussian signal, a sinusoidal signal, or an arbitrary narrow-band Gaussian signal.

(*iv*) The phase detector can be implemented by using radio interferometer-type receivers or monopulse radar-type receivers.

(*v*) The phase detector utilizes two receivers.

IV. ACKNOWLEDGMENT

The author wishes to thank A. R. Eckler and I. Jacobs for some valuable suggestions.

REFERENCES

1. Faran, J. J., Jr. and Hills, R., Jr., Correlators for Signal Reception, Acoustics Res. Lab., Harvard University, Cambridge, Mass., Tech. Memo. No. **27**, September 15, 1952.

2. Wolff, S. S., Thomas, J. B., and Williams, T. R., The Polarity-Coincidence Correlator: A Nonparametric Detection Device, Trans. IRE Prof Group Inform. Theor., *IT-8*, No. 1, January, 1962, pp. 5–9.
3. Huggins, W. H. and Middleton, D., A Comparison of the Phase and Amplitude Principles in Signal Detection, Proc. Nat. Elec. Conf., *XI*, October, 1955, pp. 304–317.
4. Rainal, A. J., Zero-Crossing Principle for Detecting Narrow-Band Signals. Submitted to IEEE Trans. Instrum. Meas.
5. Rainal, A. J., Monopulse Radars Excited by Gaussian Signals. To appear in IEEE Trans. Aerosp. and Electronic Systems.
6. Lawson, J. L. and Uhlenbeck, G. E., Threshold Signals, MIT Radiation Laboratory Series, *24*.
7. Rice, S. O., Mathematical Analysis of Random Noise, B.S.T.J. *24*, Jan., 1945, p. 112, equations (4.1–14) and (4.1–15).
8. Helstron, C. W., *Statistical Theory of Signal Detection,* Pergamon Press, London, England, 1960, Chap. III.
9. Davenport, W. B., Jr. and Root, W. L., *Random Signals and Noise,* McGraw-Hill Book Company, Inc., New York, New York, 1958, Chap. 14.

Sequential Decoding — The Computation Problem*

By J. E. SAVAGE

Sequential decoding is a technique for encoding and decoding at moderate cost with a decoding reliability which approximates that of the optimum, and expensive, maximum-likelihood decoder. The several known sequential decoding algorithms enjoy a cost advantage over the maximum-likelihood decoder because they allow the level of the channel noise to regulate the level of the decoding computation. Since the average level of the required decoding computation for sequential decoders is small for source rates below a rate R_{comp} , such a decoder can be realized for these rates with a relatively small logic unit and a buffer. The logic unit is normally designed to handle computation rates which are less than two or three times the average computation rate; the buffer serves to store data during those noisy periods when the required computation rate exceeds the computation rate of the logic unit.

If the periods of high computation, which are caused by noise, are too frequent or too long, the buffer, which is necessarily finite in capacity, will fill and overflow. Since data are lost during an overflow, continuity in the decoding process cannot be maintained. The decoder, then, cannot continue to decode without error. For this reason, buffer overflow is an important event. In addition, since errors in the absence of overflow are much less frequent than are overflows themselves, the overflow event is of primary concern in the design of a sequential decoder.

This paper presents some recent analytical results concerning the probability of a buffer overflow. In particular, it is shown that this probability is relatively insensitive to both the buffer capacity and the maximum speed of the logic unit for moderate capacities and speeds. By contrast, it is shown that the overflow probability decreases rapidly with a decrease in the source

rate and is more than squared by a halving of this rate. These sensitivities are basic to sequential decoding; they exist because the required computation level is large during intervals of high channel noise and grows exponentially with the length of such an interval. It is also shown that the dependence of the overflow probability on the source rate is intimately related to exponents appearing in the coding theorem. In addition, the results presented agree with the limited experimental evidence available.

I. INTRODUCTION

Sequential decoding procedures are important because they achieve, at modest cost, a decoding error rate which approximates the error rate of the optimum and expensive maximum-likelihood decoder. Sequential decoding procedures have this near-optimum performance at modest cost because they allow the level of the channel noise to determine the level of the decoding computation. The level of the decoding computation is a function of the source rate as well as the channel noise and if the source rate is held at less than a computational cutoff rate, R_{comp} , the computation level *on the average* will be small.[1,2,16] Thus, a sequential decoder may be constructed from a logic unit capable of handling two or three times the average computation rate and from a buffer to store data during those noisy periods which require a computation rate which exceeds that of the basic decoding machine. The maximum likelihood decoder, however, always requires a very high computation rate and, in effect, is designed to handle the peak noise levels.

The buffer portion of the decoder stores data during periods of high computation and since it has finite capacity, it will fill and overflow if the high computation intervals are too frequent or too long. If and when a buffer overflow occurs, the decoder cannot continue to decode reliably since data which are important to the continuing decoding process are lost. Consequently, a buffer overflow forces a halt in the decoding process while both the encoding and decoding processes are restarted.

While errors occur after the onset of overflow, they may also occur in the absence of overflow. For a properly chosen code, however, it can be argued that errors in the absence of overflow occur much less frequently than do overflow, themselves. Consequently, it can be argued— and, indeed, it is found in practice—that the buffer overflow event is of primary concern in the design of a sequential decoder.

In this paper, we present some recent results[3] concerning the probability of a buffer overflow. In particular, we show by upperbounding this probability that it is relatively insensitive to machine speed and to the storage capacity of the buffer for moderate speeds and capacities. By

contrast, it is shown that the overflow probability decreases rapidly with a decrease in the source rate and that this probability is more than squared by a halving of the rate. It is found that these sensitivities are basic to sequential decoding and arise because the computation per decoded digit is large during intervals of high channel noise and grows exponentially with the length of such an interval. We show that the dependence of the overflow probability on the source rate is intimately connected with exponents found in the coding theorem.[4,5] In addition, the results represented here agree with the limited experimental evidence available.[6]

We assume throughout this paper that the encoding and decoding are done for a discrete memoryless channel (DMC) characterized by the channel transition probabilities

$$\{P\,(y_j\,|\,x_k), \qquad 1 \leqq k \leqq K, \qquad 1 \leqq j \leqq J\}$$

where x_k represents a letter from the channel input alphabet and y_j represents a letter from the channel output alphabet. The results for the DMC apply with qualifications to other channels.

In the following sections we introduce the Fano algorithm,[2] the vehicle for this study of sequential decoding.

II. THE DECODING PROCEDURE

2.1 Tree Codes

The Fano algorithm decodes data encoded from tree codes. We assume that this data arrives from a source as a sequence of digits and we make the assumption that these digits are statistically independent and are drawn from the b-letter alphabet, $A = \{a_1, a_2, \cdots, a_b\}$. A sequence of source digits drawn from this alphabet is encoded with a tree code as follows (see Fig. 1): A branch from the first node of the tree is selected which corresponds to the value of the first digit produced by the source. The same is true for the second and later source outputs. Thus, in the example of Fig. 1, the source sequence $(1, 0, 2, \cdots)$ with letters from the alphabet $\{0, 1, 2\}$ selects the sequence $(112, 010, 122, \cdots)$ from the tree. The digits on these branches are then transmitted over the DMC.

We assume that each branch of the tree contains l channel symbols so that the source rate in bits per channel transmission is defined as

$$R = \log_2 b/l. \tag{1}$$

A variety of rates can be generated with tree codes.
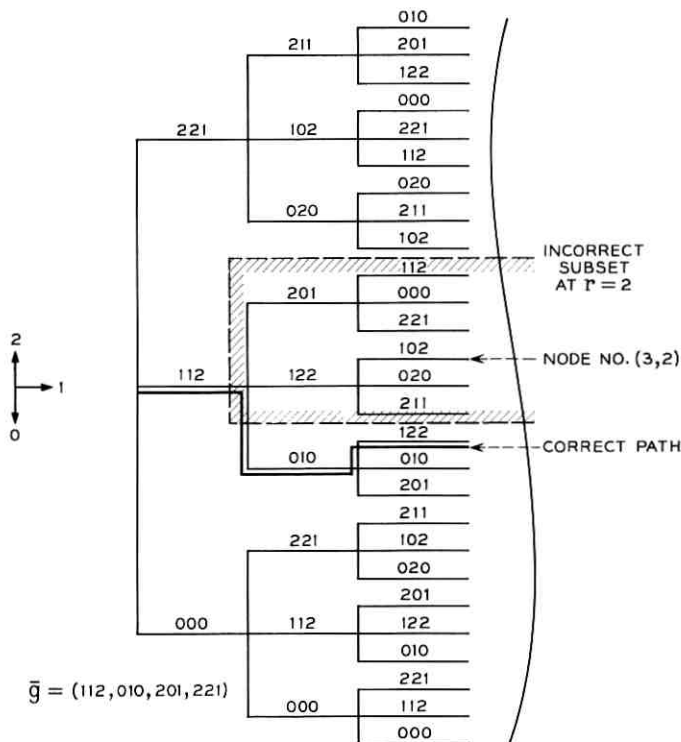
Fig. 1 — Tree code.

A class of tree codes which may be generated with a small amount of equipment is known as convolutional codes. Convolutional codes are generated with shift registers, multipliers and adders. An example of a convolutional encoder is given in Fig. 2 where circles represent multiplication and addition is taken modulo $b = 3$. This example generates the tree code of Fig. 1. Although we do not restrict the results of this paper to convolutional codes, it suffices to say that they can be decoded with sequential decoders with a small resultant error rate.[1,16]

2.2 The Metric

The Fano algorithm decodes by comparing the received channel sequence to paths in the tree code in search of a path which "matches well" to the received sequence. A "match" is measured with a "metric." *

---

* This is not a metric in the mathematical sense since it does not satisfy any of the rules for a metric. The word metric is used here to indicate the relative match (or mismatch) between the received channel sequence and a tree path.

Let $\bar{u}_s$, $\bar{v}_s$ represent a tree path and the received sequence, respectively, where each has s branches. Then, for the purposes of this paper we define the metric between $\bar{u}_s$, $\bar{v}_s$, $d(\bar{u}_s, \bar{v}_s)$, as

$$d(\bar{u}_s, \bar{v}_s) = \sum_{r=1}^{s} \sum_{h=1}^{l} \left[\log_2 \left\{ \frac{P(v_{rh} \mid u_{rh})}{f(v_{rh})} \right\} - R \right] \tag{2}$$

where u_{rh}, v_{rh} are the hth digits on the rth branches of $\bar{u}_s$, $\bar{v}_s$, respectively. $P(v_{rh}/u_{rh})$ is a channel transition probability. The function (v_{rh}) for $v_{rh} = y_j$ is given as

$$f(y_j) = \sum_{k=1}^{K} p_k P(y_j \mid x_k). \tag{3}$$

This function may be viewed as the probability of channel output y_j when the channel inputs are assigned with probabilities $\{p_k\}$. (The function $f(y_j)$ and the probability assignment $\{p_k\}$ are chosen because they fit naturally into the random code bound to be presented later.)

This choice of metric is used because it lends itself to analysis and is a metric with which the Fano algorithm will operate. We now study this metric and observe from a simple combination of terms in (2) that $d(\bar{u}_s, \bar{v}_s)$ is monotonically increasing in increasing $P[\bar{v}_s \mid \bar{u}_s]$ which is the probability of receiving the sequence $\bar{v}_s$ when the sequence $\bar{u}_s$ is transmitted. This fact plus the fact that all tree paths with the same number of branches are assumed equiprobable imply that $P[\bar{v}_s \mid \bar{u}_s]$ is propor-
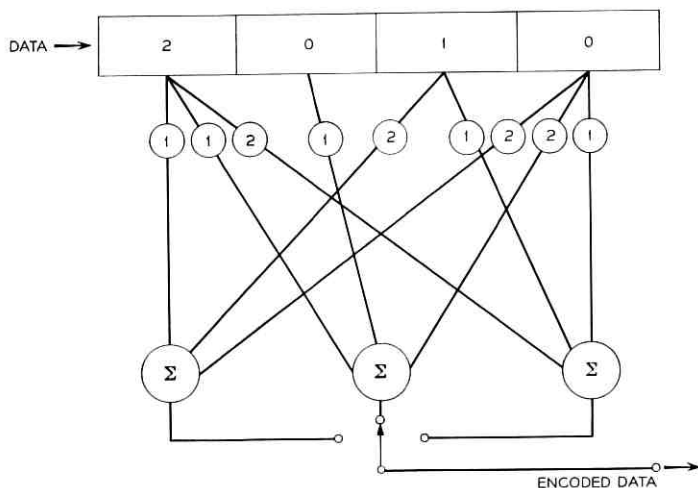
Fig. 2 — Convolutional encoder.

tional from Baye's Rule, to $P[\bar{u}_s \mid \bar{v}_s]$, the *a posteriori* probability of sequence $\bar{u}_s$ given that sequence $\bar{v}_s$ is received. Equivalently, this implies that $d(\bar{u}_s, \bar{v}_s)$ is monotonically increasing in the *a posteriori* probability of tree path $\bar{u}_s$. Thus, as the decoder progresses into the tree we expect $d(\bar{u}_s, \bar{v}_s)$ to increase if $\bar{u}_s$ represents the correct path (see Fig. 3). However, if the decoder branches onto an incorrect path, we expect the path to decrease in probability (for a properly chosen code) and to see $d(\bar{u}_s, \bar{v}_s)$ decrease (see Fig. 3). Although this behavior is typical, occasional noisy intervals will cause the correct path to decrease in metric and searching will be required to distinguish it from incorrect paths.
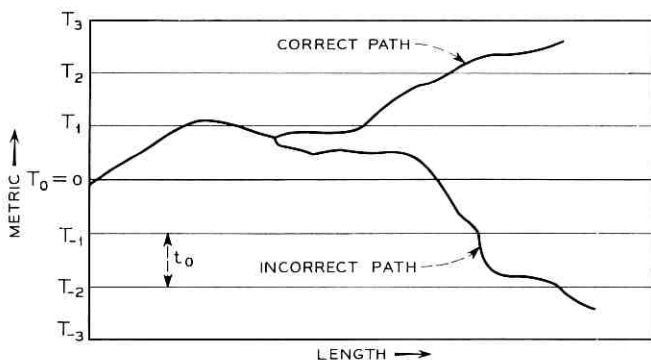
Fig. 3 — Criteria and typical paths.

2.3 *The Fano Algorithm*

The Fano algorithm is a set of rules for searching tree paths using the metric given by (2).* Since the algorithm is designed to find the transmitted tree path, it is programmed to follow a path which grows in metric. A path will be said to grow in metric if it crosses an increasing sequence of thresholds, such as those of Fig. 3.

The decoder is also programmed to search for other paths when the path being followed begins to decrease in metric and crosses a threshold from above. Such a decrease signals the presence of channel noise and indicates that searching will be required to distinguish between the correct path and incorrect paths.

The rules governing such a search, as well as the rules for determining which path to follow when two or more paths increase in metric, are given

---

* Other metrics with the same properties will also work.

by the flow chart† of Fig. 4. In that chart, a "most probable" branch at a node is that branch for which the increase in the metric is largest.

The "running threshold", which is simply called "threshold" in the flow chart, is really a sequence of thresholds which always lies below the node being examined in the decoder (see Fig. 5). It is used to determine whether the path being extended increases or decreases in metric. In
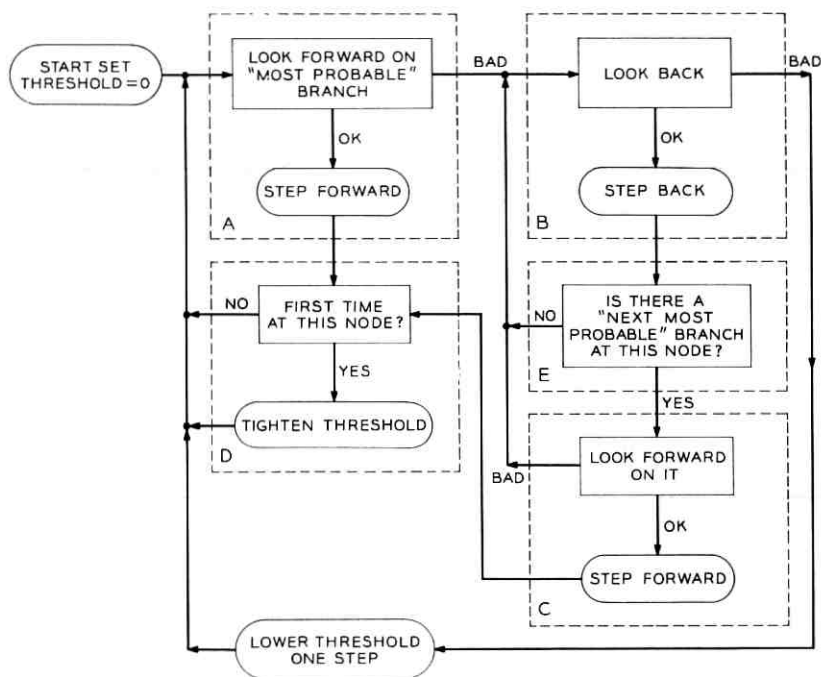
Fig. 4 — Flow chart of the Fano algorithm.

operations A, B, and C the metric on a node is compared with the running threshold. The indicators OK and BAD signify, respectively, that the metric is above or below this threshold.

In operation D, the statement "tighten threshold" means that the running threshold is to be increased until it lies just below the value of the metric on the node reached by the decoder. Notice that the threshold is increased only when a node is reached for the first time. Otherwise looping would occur.

---

† This chart is based on a chart suggested by Prof. I. M. Jacobs of M.I.T. It is equivalent to the flow chart of Ref. 2.
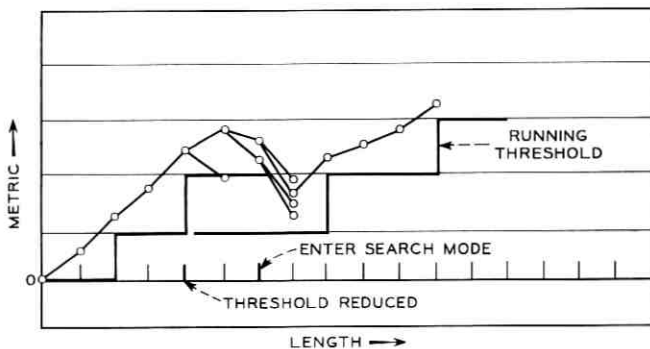
Fig. 5 — Threshold reduction, $b = 2$.

To further clarify the operations of the flow chart, we make the following observations: (i) Forward searching on a path whose path metric continues to grow is performed by operations A and D, (ii) the searching required after the searched path crosses the running threshold *from above* is performed by operations B, E, C, and D, (iii) the running threshold is reduced *only* if it is found that all paths cross this threshold from above (see Fig. 5). This last observation deserves expansion. When the decoder observes that the path under examination violates the running threshold, it looks back, one node at a time, to find a path which it might extend forward. If, after a number of backward and forward moves, the decoder decides that all paths examined violate the running threshold, it reduces the value of this threshold and repeats the search until a path is found which remains above the new lower value of the threshold. (If there is more than one such path, the decoder follows that path which has the "most probable" branches.) The decoder then continues to extend this path.

We now go on to discuss a particular buffer design and to examine the dynamics of the decoding operation. We shall return to the discussion of this section in a following section while discussing a random variable of computation.

2.4 *Dynamics of the Decoder*

A buffer designed to smooth the delay experienced by data arriving at the decoder is shown in Fig. 6. Data arrives from the left, is stored in sections corresponding to tree branches and progresses through the buffer at the rate at which it arrives. Storage is reserved below each branch for tentative source decisions. A safety zone is provided so that,

should a buffer overflow occur, data in this section will be declared unreliable and not released to the user.

Two pointers are shown on the buffer of Fig. 6. With these pointers the decoder operation may be traced. The "search" pointer locates the received branch currently being examined. The "extreme" pointer labels the latest branch ever examined. When the channel is relatively noise-free the two pointers hover at the left-hand side of the buffer. During a noisy interval, searching is required and the search pointer drifts to the right and away from the extreme pointer while the extreme pointer drifts to the right at the data rate. The two pointers become superimposed and move to the left after the noisy period has been passed. (We assume that the decoder has a computation rate which is twice or three times the average required computation rate.)

Should the channel experience a severely noisy period, the search pointer may drift to the far right-hand side of the buffer at which time the decoder will quite probably release an erroneous source decision to the safety zone. This spells trouble because thereafter the decoder searches on incorrect paths and is likely to do a large amount of continuous searching. Additional decoding errors will then be released to the user. This event we call buffer overflow.

Since buffer overflow can be detected by the location of the search pointer, the user can be so informed. However, no known techniques exist for retrieving the decoder from the overflow state once it has entered this state other than a restarting of the decoding process. This
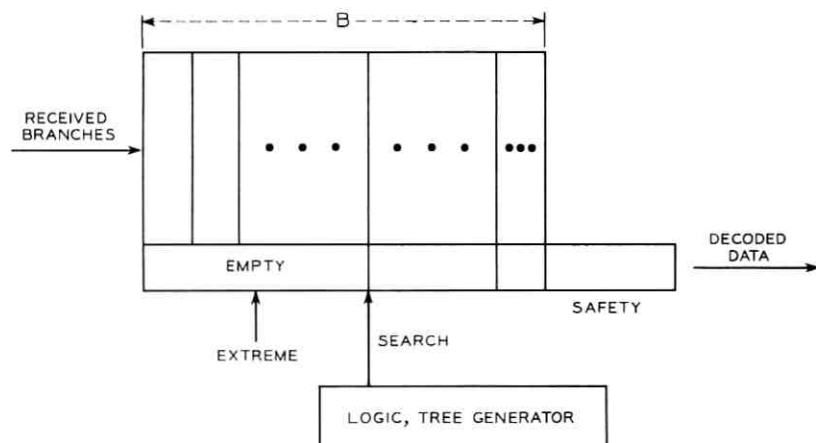
Fig. 6 — Buffer.

implies that either a feedback link has to be available or that periodic restarting is employed. Overflow, then, is a serious event. Since it can be argued the probability of an overflow is generally much larger (for a properly chosen code) than the probability of an error without overflow, it is, therefore, a most important consideration in the design of a sequential decoder.

In the next section we begin the analytical treatment of the overflow probability. Our intent is to indicate the dependence of this probability on the encoder and decoder parameters.

2.5 *Static Computation*

The overflow probability, $P_{BF}(N)$, is defined as the probability that the buffer overflows on or before the Nth source decision is released to the safety zone. It is this probability which is of primary concern in the design of the decoder. Unfortunately, both experimental[7] and analytical[3] investigations of $P_{BF}(N)$ have produced only estimates of this probability and these estimates depend upon a heuristic connection between $P_{BF}(N)$ and probabilities which have either been determined experimentally or bounded analytically. We shall be concerned with the analytical bounds and shall present an interpretation of these bounds.

Since $P_{BF}(N)$ is not amenable to direct analysis we shall be concerned with a random variable of computation which we call "static" computation. This is a computation associated with *a node of the correct path*. We assume that the decoder reaches a node of the correct path, say the gth, and we define static computation, C, as the number of computations required on the gth correct node and on all nodes on paths branching from this correct node except nodes on the correct path. This set of nodes is called the "incorrect subset" associated with the gth correct node. (See Fig. 1 where $g = 2$). A computation on a node is defined as a forward or backward "look" from a node (See the flow chart of Fig. 4).

The analytical results of this paper are concerned with bounds on the cumulative probability distribution of the random variable of static computation C, namely, $P[C \geq L]$. We shall determine the behavior of $P[C \geq L]$ with the distribution parameter L. Before we do so, however, we develop an upper bound to C to be used later in developing an upper bound to $P[C \geq L]$. We begin by labeling nodes in the incorrect subset.

Each node in the gth incorrect subset can be labeled uniquely with a doublet (m, s). We take the index s as a measure of the "penetration"

of a node in the incorrect subset. We say a node has penetration s if it is separated from the correct node by s branches. The correct node itself is at penetration zero. The index m indicates the position of nodes at penetration s counting from the bottom of the incorrect subset (see Fig. 1 where node $(3, 2)$ is shown). We define $M(s)$ as the number of nodes at penetration s and have $1 \leq m \leq M(s)$ where

$$M(s) = \begin{cases} 1 & s = 0 \\ (b - 1)b^{s-1} & s > 0 \end{cases} \tag{4}$$

and b is the number of branches at a node. (Note that $M(0) = 1$ since the correct node has penetration zero.) Then, each node is uniquely labeled by a doublet (m,s).

To develop an upper bound to the random variable C we continue the discussion of Section 2.3. Assuming that we have reached the gth node of the correct path, defining D as the smallest value of the path metric on the remaining portion of the correct path and letting T_D be the threshold just below D (see Fig. 7), we see from observation (*iii*) of Section 2.3 that no threshold lying below T_D is ever used. A lower threshold would be required if all paths eventually crossed T_D but, by definition, at least one path, the correct path, remains completely above T_D.

Consider a particular incorrect node (m,s) with metric $d_0 + d^*(m,s)$, where d_0 is the value of the metric on the path terminated by the gth correct node and $d^*(m,s)$ is the remainder. If the thresholds are defined by $T_i = it_0$, $t_0 > 0$, $- \infty < i < \infty$, and if $d_0 + d^*(m,s)$ is separated from T_D by k such thresholds (including T_D), then the decoder can
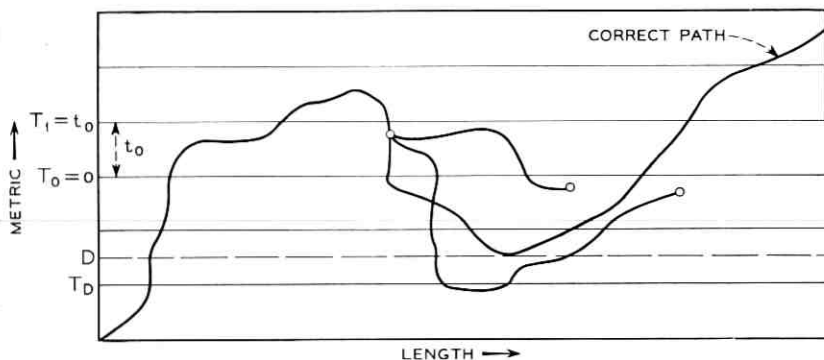
Fig. 7 — Typical path trajectories and the minimum threshold, T_D.

look at node (m,s) with *at most* k thresholds.[†] It can be shown that with each threshold no more than $(b + 1)$ computations can be performed at node (m,s), i.e., one backward look and b forward looks from (m,s). Since this is the case, we can define a random variable which counts the number of thresholds between the value of the metric on node (m,s) and threshold T_D and we can use this random variable to bound C. To simplify the analysis, however, we shall define a random variable $z_{i,s}(m)$ which allows us to *overbound* the number of thresholds between the value of the metric on node (m,s) and threshold T_D, including T_D. Represent the metric on the correct path of length $g + r$ by $d_0 + d_c(\bar{u}_r, \bar{v}_r)$ where $\bar{u}_r$, $\bar{v}_r$ are the portions of the correct and received paths extending beyond the gth node, respectively. Then, we have the following definition for $z_{i,s}(m)$:

$$z_{i,s}(m) = \begin{cases} 1 & d^*(m,s) \geq T_{i-1}, \quad d_c(\bar{u}_r, \bar{v}_r) \leq T_{i+1}, \\ & \quad \text{some } r \geq 0 \\ 0 & \text{otherwise.} \end{cases} \tag{5}$$

We now argue that $\sum_{i=-\infty}^{\infty} z_{i,s}(m)$ overbounds the number of thresholds between the value of the metric on node (m,s), $d_0 + d^*(m,s)$, and threshold T_D, including this threshold. Let d_0, the value of the path metric on the correct path up to and including the gth node, be between thresholds T and $T + t_0$. Then, if the metric on node (m,s) were $T + t_0$ instead of d_0, the number of thresholds with which (m,s) would be examined would be increased. Similarly, if the path metric on the correct path of length $g + r$, $d_0 + d_c(\bar{u}_r, \bar{v}_r)$, were replaced by $T + d_c(\bar{u}_r, v_r)$, the computation on node (m,s) would again be increased. These observations are used to define $z_{i,s}(m)$ in such a way that $\sum_{i=-\infty}^{\infty} z_{i,s}(m)$ overbounds the number of thresholds between (m,s) and T_D.

We have stated that no more than $(b + 1)$ computations are needed for each threshold lying between (m,s) and T_D. Then, we overbound the random variable of static computation on nodes of the gth incorrect subset, C, by

$$C \leq (b + 1) \sum_{i=-\infty}^{\infty} \sum_{s=0}^{\infty} \sum_{m=1}^{\lceil M(s) \rceil} z_{i,s}(m). \tag{6}$$

This bound will be used in overbounding $P[C \geq L]$.

In Section III the analytical results will be delineated and interpreted and the upper bound to $P[C \geq L]$ will be derived.

[†] This may be deduced from the flow chart of Fig. 4.

III. THE DISTRIBUTION OF STATIC COMPUTATION

Static computation has been defined as the computation performed in a particular incorrect subset of the tree code. A lower bound to the probability distribution of this random variable has been obtained, and is presented elsewhere.[3] An abbreviated derivation of an upper bound to this distribution will be presented in a following section. The essence of the lower bound argument is contained in the following section.

3.1 *Behavior of the Distribution*

It has been found[3,7] that the distribution of static computation, $P[C \geq L]$ behaves as $L^{-\beta}$ for large L. We shall now present several simple intuitive arguments which explain this behavior.

If noise causes a large dip in the value of the correct path metric in the neighborhood of the gth correct node (see Fig. 7) then, the decoder will not be able to discriminate between the correct path and incorrect paths. Thus, much computation will be required. Since the number of paths in the incorrect subset grows exponentially with penetration into this subset, the number of computations required will grow roughly as an exponential in the length of the correct path dip or the duration of the interval of high channel noise. Hence, the static computation grows exponentially with an interval of high channel noise. On the other hand, an interval of high channel occurs on the DMC with a probability which decreases exponentially with its length. It is the balance between these two exponentials which is responsible for the behavior of the distribution of static computation. Random variables with distributions of this type are known as Paretian random variables and they appear in random walk problems,[6] in the distribution of incomes,[8] in error clustering on the telephone channels[15] and many other places.[14]

3.2 *Random Code Bound on the Distribution*

The technique used in this section to overbound the distribution of computation contains two major steps. In the first step, the distribution is bounded in terms of the moments of computation using a generalization of Chebysheff's Inequality. In the second step, the moments of computation are averaged over the ensemble of all tree codes. Together the two steps generate a random code bound to the distribution. This argument shows the existence of codes having a particular upper bound to their distribution function. The generalized Chebysheff Inequality is stated below.

Lemma 1: Let C be a positive random variable. Then,

$$P[C \geq L] \leq \overline{C^p}/L^p, \qquad p \geq 0. \tag{7}$$

The "tightness" of this inequality is indicated by two examples. (i) For the discrete random variable which assumes values 0 and c_0 with probabilities $1 - a$ and a, respectively, the bound is exact when $L = c_0$. (ii) For the continuous random variable which assumes values greater than or equal to one with probability density $\beta/c^{\beta+1}$, the exact form of $P[C \geq L]$ is $1/L^\beta$ and the bound is $\beta/(\beta - p)L^p$ for $p < \beta$. Therefore, as p approaches β the coefficient in the bound becomes indefinitely large while the exponent approaches the true exponent. Since the distribution of *static computation* is Paretian, this same behavior appears in the random code bound derived in this section.

The random variable of computation C has been overbounded by (6). It should be clear that moments of the bound on C will be difficult to evaluate due to the many crossterms. Much of the difficulty is avoided through the use of Minkowski's Inequality[9] which is stated below.

Lemma 2: Let $x_1 , x_2 , \cdots , x_n$ be a set of positive random variables. Then, for $p \geq 1$ and for every n we have

$$\overline{\left(\sum_{i=1}^{n} x_i\right)^p}^{1/p} \leq \sum_{i=1}^{n} \overline{x_i^p}^{1/p}. \tag{8}$$

Applying this inequality to the bound on C we have

$$\overline{C^p}^{1/p} \leq (b + 1) \sum_{i=0}^{\infty} \sum_{s=0}^{\infty} \overline{\left(\sum_{m=1}^{M(s)} z_{i,s}(m)\right)^p}^{1/p}$$
$$+ (b + 1) \sum_{i=0}^{\infty} \sum_{s=0}^{\infty} \overline{\left(\sum_{m=1}^{M(s)} z_{-i,s}(m)\right)^p}^{1/p}. \tag{9}$$

In this form, moments are taken of the sum of the random variables $z_{i,s}(m)$, $1 \leq m \leq M(s)$, with both the threshold T_i and the penetration s fixed. (See the definition of $z_{i,s}(m)$ in (5).)

To further bound $\overline{C^p}$ we make the following expansion for integer values of p where the indices i and s are omitted:

$$\overline{\left(\sum_{m=1}^{M(s)} z(m)\right)^p} = \sum_{m_1=1}^{M(s)} \cdots \sum_{m_p=1}^{M(s)} \overline{z(m_1)z(m_2) \cdots z(m_p)}. \tag{10}$$

Since such an expansion does not hold for noninteger p, we limit our attention hereafter to integer p. We now proceed through several counting arguments to put (10) in a manageable form.

Since the random variable $z(m_1) z(m_2) \cdots z(m_p)$ assumes the value 1 only when all implied events occur simultaneously, the expectation in the right-hand side of (10) is the probability of the joint occurrence of all implied events. Now it can be seen for $p = 4$, say, that

$$z(5)z(1)z(16)z(5) = z(16)z(5)z(5)z(1) = z(1)z(5)z(16)$$

since $z(\cdot) = 1$ or 0 (so that $z(5)z(5) = z(5)$). Hence, $z(m_1) \cdots z(m_p)$ is independent of the order of the m_i and equals $z(\theta_1) \cdots z(\theta_t)$ where $\theta_1, \cdots, \theta_t$ are the *distinct* elements among $m_1, m_2, \cdots, m_p$. Consequently we can write*

$$\sum_{m_1=1}^{M(s)} \cdots \sum_{m_p=1}^{M(s)} \overline{z(m_1) \cdots z(m_p)}$$
$$= \sum_{t=1}^{\text{Min}(M(s),p)} \sum_{\substack{\text{All sets of } t \\ \text{distinct elements} \\ \{\theta_1, \cdots, \theta_t\}}} W(t,p) z(\theta_1) \cdots z(\theta_t) \qquad (11)$$

where $W(t,p)$ is the number of p-tuples $(m_1, m_2, \cdots, m_p)$ which contain t distinct elements. We now bound $W(t,p)$.

$W(t,p)$ may be viewed as the number of ways of placing one ball in each of p distinguishable cells where the balls are of t different colors and each color must appear at least once. The number of such collections of p balls is less than the number of collections one would have if we include the situations where one or more colors do not appear. This larger number is the number of ways of placing t different elements in each of p distinguishable cells, or t^p. Therefore, $W(t,p) \leqq t^p$.

To underbound $W(t,p)$ we now establish that $W(t,p) \geqq tW(t,p-1)$. Consider $W(t,p-1)$, the number of ways $(p-1)$ balls of t different colors may be placed in $(p-1)$ distinguishable cells with no cell empty. Consider extending the collection by placing one additional ball with one of the t colors in a pth cell. This new collection contains $tW(t,p-1)$ items. It cannot contain more items than does the collection of $W(t,p)$ items because one color appears at least twice and every other color at least once, establishing the desired inequality. Iterating this inequality $(p-t)$ times and observing that $W(t,t) = t!$, we have $W(t,p) \geqq t^{p-t}t!$. The two bounds are summarized in the following Lemma:

Lemma 3: For $t \leqq p$ we have

$$\sqrt{2\pi t}\, e^{-t} t^p \leqq W(t,p) \leqq t^p \qquad (12)$$

---

* The upper limit on t indicates that $(m_1, \cdots, m_p)$ contains no more than the smaller of $M(s)$ and p different elements.

Proof: We use the fact[6] that

$$t! \geq t^t \sqrt{2\pi t} \, e^{-t}.$$ Q.E.D.

The two bounds indicate that $W(t,p)$ grows with t primarily as t^p for large p.

Before we proceed to the next counting argument we motivate our use of this next argument by presenting a result which is too long to be derived here.[3] The probability $z_{i,s}(\theta_1) \cdots z_{i,s}(\theta_t)$ is the probability that nodes $(\theta_1, s), \cdots, (\theta_t, s)$, all at penetration s in the gth incorrect subset, simultaneously lie in metric above threshold $T_{i-1} = (i-1) t_0$ while the correct path falls below T_{i+1} somewhere following the gth correct node (see (5)). An overbound to this probability is given below. The average of the product of the z's is taken over the ensemble of channel transitions and the *set of all tree codes*. It is at this point that the random code technique is used.

$$\overline{z_{i,s}(\theta_1) \cdots z_{i,s}(\theta_t)} \leq \{2^{t_0[t/(1+t)-\sigma_0]} \, 2^{-it_0[t/(1+t)+\sigma_0]}$$

$$\cdot 2^{[slt/(1+t)](R_t-R)}\} \cdot \{2^{-\alpha l R_t}\} \left\{ \sum_{r_0=1}^{\infty} 2^{-r_0 l [\sigma_0 R - \mu_t(\sigma_0)]} \right\}.$$ (13)

Here α *is the number of branches on the paths terminated by nodes* (θ_1, s), $\cdots, (\theta_t, s)$, exclusive of branches preceding the gth correct node, and

$$\mu_t(\sigma_0) \triangleq \frac{1}{1+t} \log_2 \sum_{j=1}^{J} f(y_j) \left(\sum_{k=1}^{K} p_k \left[\frac{P(y_j | x_k)}{f(y_j)} \right]^{1+\sigma_0} \right)^{1+t}$$ (14)

$$f(y_j) \triangleq \sum_{k=1}^{K} p_k P(y_j | x_k)$$

where $\sigma_0 \leq 0$. Also,

$$R_t \triangleq -\frac{1}{t} \log_2 \sum_{j=1}^{J} \left(\sum_{k=1}^{K} p_k P(y_j | x_k)^{1/1+t} \right)^{1+t}.$$ (15)

The probability assignment $\{p_k\}$ is the assignment given to digits in a code when using the *random code argument*. In the bound of (13) there exists a value of σ_0, $-(t)/(1+t) < \sigma_0 \leq 0$, for which the sum on r_0 converges, as long as $R < R_t$. Examination of (13) will show that the bound depends on the paths terminated by nodes $(\theta_1, s), (\theta_2, s), \cdots$, (θ_t, s) only through α, the number of branches which they contain, exclusive of branches preceding the gth correct node. (For example, see Fig. 8 where a set of paths is indicated with checks and the branches which they contain are labeled with 1.) This being the case, we must
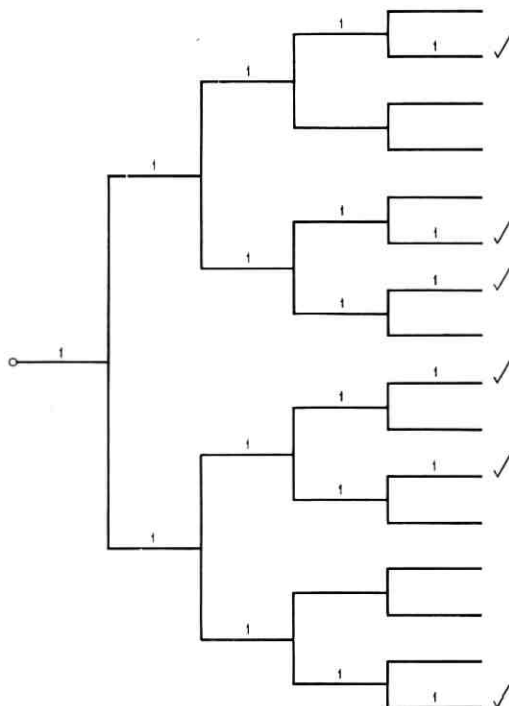
Fig. 8 — Topology of tree paths.

then group together in (13) all paths having the same number, α, of branches. Call this number of paths $N_t(\alpha)$. The following lemma provides a bound on $N_t(\alpha)$.

Lemma 4:
$$N_t(\alpha) \leqq (t-1)!(s-1)^{t-2}2^{\alpha l R}. \tag{16}$$

Proof: The proof is by construction. We first show that

$$N_t(\alpha) \leqq (t-1)!s^{t-2}2^{\alpha l R} \quad \text{for} \quad s \geqq 1.$$

Consider placing the t paths in the tree, one by one. The first of the t paths placed in the incorrect subset of the tree (containing $M(s) \leqq b^s$ paths) may assume no more than b^s positions. A second path connecting with the first, but having d_1 separate branches, may assume any one of b^{d_1} positions since its point of connection to the first path is fixed by its length d_1. A third path with d_2 branches distinct from the first two may connect to either path and terminate in b^{d_2} positions, that is, it can assume no more than $2\ b^{d_2}$ places. The tth path having

d_{t-1} branches may terminate in any one of $b^{d_{t-1}}$ positions; hence, can be situated in no more than $(t - 1) b^{d_{t-1}}$ places. Thus, given that the second path has d_1 branches distinct from the first, that the third path has d_2 branches distinct from the first and second, etc., the number of arrangements of the t paths cannot exceed $(t - 1)! b^\alpha$ where

$$\alpha = s + d_1 + \cdots + d_{t-1},$$

the number of branches on these paths. All that remains is to determine the number of ways that values may be assigned to $d_1, d_2, \cdots, d_{t-2}$. (Note that d_{t-1} is fixed given α and $d_1, d_2, \cdots, d_{t-2}$.) Since each number d_i represents a portion of a path, $1 \leq d_i \leq s$, we may assign values to $d_1, d_2, \cdots, d_{t-2}$ in no more than s^{t-2} ways. Hence, the number of arrangements of t paths containing α branches cannot exceed $(t - 1)! s^{t-2} b^\alpha$. Observing that $b = 2^{lR}$ by (1) we have the desired result for $s \geq 1$. We also have $s \leq \alpha \leq st$ since one path contains s branches and the number of branches on all paths cannot exceed st. Now, when $s = 0$, the bound on $N_t(\alpha)$ is zero. We must have $N_t(\alpha) = 1$ when $s = 0$, so that we replace s by $(s + 1)$.   Q.E.D.

Combining all terms we have the following random code bound on the moments of static computation:

$$\overline{C^p}^{1/p} \leq \left[\sum_{s=0}^{\infty} (s + 1)^{1-1/p} 2 \exp\left(\frac{-sl(R_p - R)}{p(1 + p)} \right) \right] (2^{l_0(1-\sigma)} p p!)^{1/p}$$

$$\times \left\{ \left(\sum_{r=1}^{\infty} 2 \exp\{-rl[\sigma R - \mu_p(\sigma)]\} \right)^{1/p} \left[\sum_{i=0}^{\infty} 2 \right. \right.$$

$$\left. \exp\left(-\frac{il_0(\frac{1}{2} + \sigma)}{p} \right) \right] \tag{17}$$

$$+ \left(\sum_{r=1}^{\infty} 2 \exp\{-rl[\sigma'R - \mu_p(\sigma')]\} \right)^{1/p} \left[\sum_{i=0}^{\infty} 2 \right.$$

$$\left. \left. \exp\left(+\frac{il_0(p/(1 + p) + \sigma')}{p} \right) \right] \right\}.$$

It can be shown[3] that σ and σ' can be chosen for $R < R_p$ such that $\sigma > -\frac{1}{2}, \sigma' < -(p)/(1 + p), \sigma R - \mu_p(\sigma) > 0$ and $\sigma'R - \mu_p(\sigma') > 0$, that is, such that the bound converges for $R < R_p$.

We now have enough results available to draw the central conclusion concerning moments of the random variable of static computation, C. For integer p, $\overline{C^p}$, as an average over the ensemble of all tree codes, is finite for source rates R strictly less than the rate R_p (given by (15)). Since it can be shown that $R_1 \geq R_2 \geq R_3 \geq \cdots \geq 0$, we have for any

given rate R that moments $\bar{C}$, $\overline{C^2}$, $\cdots$, $\overline{C^k}$ are bounded where k is the largest integer such that $R < R_k$. We cannot determine from this bounding argument whether moments $\overline{C^{k+1}}$, $\overline{C^{k+2}}$, etc. are finite or not.

Returning to Chebysheff's Inequality we overbound the cumulative probability distribution of the random variable of static computation, $P[C \geqq L]$, using the bounds on the moments.

Theorem 1: With a probability of at least 0.9, a tree code drawn from the ensemble of tree codes will have a distribution of static computation, $P[C \geqq L]$, which is bounded by $10\overline{C^k}/L^k$ where k is the largest integer such that $R \leqq R_k$, R is the source rate, R_k is given by

$$R_k = -\frac{1}{k}\log_2\sum_{j=1}^{J}\left(\sum_{k=1}^{K}p_kP(y_j\,|\,x_k)^{1/1+k}\right)^{1+k} \tag{18}$$

and $\overline{C^k}$ is the random code bound on the moments of static computation. For any larger k a finite bound on $\overline{C^k}$ is not known.

Proof: Over the ensemble of tree codes $P[C \geqq L]$ is a random variable. Then, if we let x represent $P[C \geqq L]$, we have

$$\bar{x} \geqq \sum_{x \geqq 10\bar{x}} xp(x) \geqq 10\bar{x}P[x \geqq 10\bar{x}]$$

from which we have that $P[x < 10\bar{x}] \geqq 0.9$.

Q.E.D.

This theorem summarizes the major result of this section which is that the distribution of computation decreases as fast as L^{-k} where k is the largest integer such that $R < R_k$. We note that $\overline{C^k}$ becomes indefinitely large as R approaches R_k. This was predicted by the discussion which followed the introduction of Chebysheff's Inequality.

In the next section we interpret the bounds on the distribution of static computation and relate these bounds to the probability of a buffer overflow.

IV. STATIC COMPUTATION AND THE OVERFLOW PROBABILITY

The upper bound to the distribution of computation given above and a lower bound presented elsewhere[3] both are algebraic functions of the distribution parameter, that is, $P[C \geqq L]$ behaves as $L^{-\beta}$, $\beta > 0$, for large L. In the following sections we define a quantity called the "computation exponent" which extracts from $P[C \geqq L]$ its behavior with L. The computation exponent is compared to known exponents on the probability of error and with some experimental data. Also, a heuristic connection between the overflow probability and the distribution of

static computation is established. We begin with a discussion of the computation exponent.

4.1 *The Computation Exponent*

The "computation exponent," $e(R)$, as defined below, is a measure of the tail behavior of $P[C \geq L]$, that is, its behavior with L for large L.

$$e(R) \triangleq R \left\{ \lim_{L \to \infty} \frac{- \log P[C \geq L]}{\log L} \right\}. \qquad (19)$$

If $P[C \geq L]$ behaves as $L^{-\beta}$ for large L, then $\beta = e(R)/R$. We consider the computation exponent $e(R)$ rather than β because $e(R)$ is a bounded function while β is not. We now state bounds that have been obtained on $e(R)$ by over- and under-bounding $P[C \geq L]$. We note that a channel is "completely connected" if all of its transition probabilities are nonzero, i.e., all output symbols can be "reached" from every input symbol, the normal physical situation.

Theorem 2: Codes do not exist for the completely connected DMC which have a computation exponent greater than $\bar{e}(R)$ where[3]

$$\bar{e}(R) \triangleq (-\sigma)(R - I_{\min}) \qquad (20)$$

and σ, $-1 \leq \sigma \leq 0$, is the solution to

$$R = \max_k \frac{\gamma_k(\sigma)}{\sigma}. \qquad (21)$$

Here, $\gamma_k(\sigma)$ is given by

$$\gamma_k(\sigma) \triangleq \log_2 \sum_{j=1}^{J} P(y_j \mid x_k)^{1+\sigma} f(y_j)^{-\sigma}$$

$$I_{\min} \triangleq \min_{j,k} \log_2 \frac{P(y_j \mid x_k)}{f(y_j)} \qquad (22)$$

and

$$f(y_j) = \sum_{k=1}^{K} p_k P\left(\frac{y_j}{x_k}\right).$$

Theorem 3: On the DMC, codes exist which have a computation exponent greater than or equal to $\underline{e}(R)$ where

$$\underline{e}(R) = pR \qquad (23)$$

and $p = 1, 2, 3, \cdots$, is found from $R_{p+1} \leq R < R_p$. R_p is given by (18).

The probability assignment $\{p_k\}$ appears in the random code argument and in the definition of the metric through the function $f(y_j)$. Although this will not be done here, one can choose $\{p_k\}$ to maximize $\varrho(R)$.

As an example, the two bounds are sketched in Fig. 9 for the Binary Symmetric Channel (BSC) with crossover probability of $p_0 = 0.01$. In that figure we have chosen $p_k = \frac{1}{2}$, $k = 1, 2$. For this probability assignment $\bar{e}(R)$ is zero for R greater than or equal to channel capacity. For other assignments $\bar{e}(R)$ may intercept the rate axis at a rate which exceeds channel capacity.

4.2 *An Experimental Result, A Conjecture and An Interpretation*

Recently a computer simulation was made of the Fano algorithm for a number of channels including the BSC. This simulation study[7] was performed at the M.I.T. Lincoln Laboratory under the direction of K. L. Jordan. Mr. Jordan has generously provided the author with data from a particular simulation of a BSC with crossover probability of $p_0 = 0.01$.

In this simulation, a convolutional tree code of the type described in Section 2.1 with $b = 2$ was used (hence; source rates of $R = 1/l$, l an integer were available). The generator for this tree code was optimized in the manner found in Ref. 1.
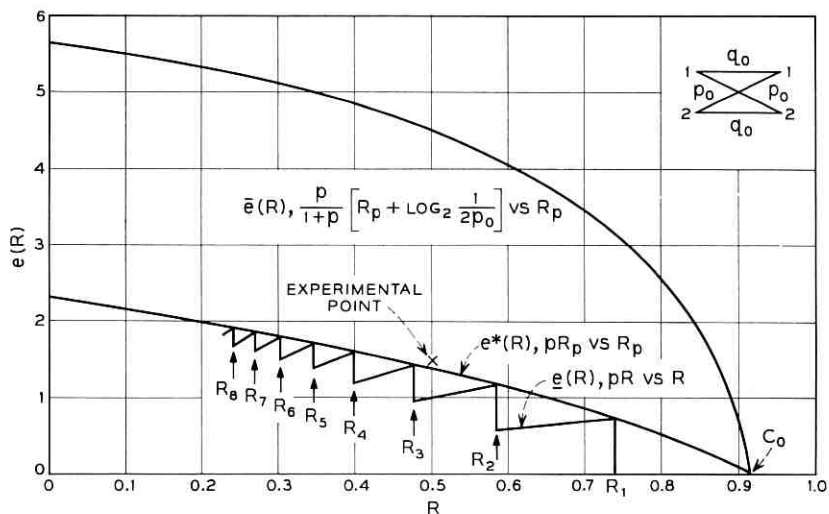
Fig. 9 — Computation exponent bounds for the BSC with $p_0 = 0.01$.

An empirical distribution of a particular random variable of computation was measured. This random variable differs from static computation somewhat but one can argue heuristically that it is within a small multiple of the random variable of static computation when either random variable is large. The random variable measured in the simulation is the number of computations required to advance one node into the tree. For example, when the channel is not noisy, a forward "look" will indicate that a forward move is possible and only one computation will be necessary; however, if the channel is noisy, the decoder may have to do much backward searching before a path is found upon which the point of deepest penetration into the tree can be increased.

The empirical distribution of computation is shown in Fig. 10 for $R = \frac{1}{2}$. The corresponding computation exponent for this rate is shown in Fig. 9. The data from which the empirical distribution was determined represents the transmission of over one million channel digits. Although data at rates $R = \frac{1}{3}, \frac{1}{4}$ was available, it was not deemed reliable and not used because few cases of large computation occurred.

The experimental computation exponent and the derivation of the lower bound to $e(R)$, namely $\varrho(R)$, leads one to conjecture a "true" value for the computation exponent.
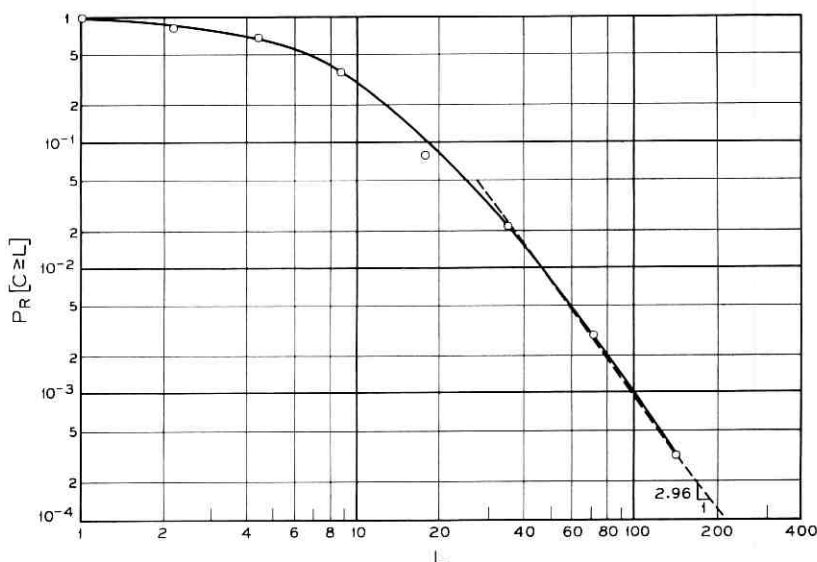
Fig. 10 — Empirical distribution of computation.

Conjecture:† For the metric used in this paper the computation exponent for the Fano algorithm cannot exceed $e^*(R)$ and there exists codes with this computation exponent where $e^*(R)$ is given by

$$e^*(R) = pR_p \quad \text{for} \quad R = R_p \tag{24}$$

Here p assumes all nonnegative, real values and R_p is given by (18). Here we use that probability assignment $\{p_k\}$, for each p that maximizes R_p.

The conjectured exponent for the BSC is shown in Fig. 9. The experimental point and $e^*(R)$ at $R = \frac{1}{2}$ differ by 5 percent, an excellent match.

The conjectured exponent has an interesting interpretation in terms of the probability of error with "List Decoding."[10,11] With list decoding, the decoder makes a list of the k *a posteriori* most probable codewords. If this list does not contain the transmitted codeword, an error is said to occur. Random code bounds have been obtained on this probability of error. This probability of error has an exponent which we call $E_k(R)$ for list size k (see Fig. 11). $E_k(R)$ may be found from an exponent $E_\infty(R)$ by $E_k(R) = E_\infty(R)$ for $R_k^* \leq R$ where R_k^* is the rate at which $E_\infty(R)$ has slope $-k$ and for $R < R_k^*$, $E_k(R)$ is the tangent to $E_\infty(R)$ at $R = R_k^*$. The rate-axis intercept of this straight line is R_k.

The "list decoding exponent", $E_\infty(R)$, depends on the random code assignment probabilities $\{p_k\}$. If that set $\{p_k\}$ is chosen for each rate which maximizes $E_\infty(R)$, we have the "sphere-packing"[13] exponent. (See Fig. 11.) This is an exponent on the probability of a block decoding error which cannot be exceeded by any block code with any decoding algorithm even when a feedback channel is available. Thus, the "list decoding exponent" and the "sphere-packing exponent" are fundamental.

The conjectured computation exponent, $e^*(R)$, can now be related to $E_\infty(R)$. To find $e^*(R)$ draw a line from R on the rate-axis which is tangent to $E_\infty(R)$. (See Fig. 12.) This line intersects the exponent axis. The rate-axis intercept and the exponent-axis intercept define a point on $e^*(R)$. Using this construction procedure every point on $e^*(R)$ may

---

† Note added in the preparation of this paper: Recently I. M. Jacobs and E. Berlekamp have underbounded the probability of buffer overflow or undetected error using lower bounds to the probability of error with list decoding. They have found that this bound has a computation exponent which agrees with the conjectured exponent given above and have shown that this bound grows linearly with the number of source digits processed by the decoder before overflow. Also, H. Yudkin has recently upper bounded the moments of static computation for integer and noninteger moments. The computation exponent implied by these bounds establishes the conjecture.
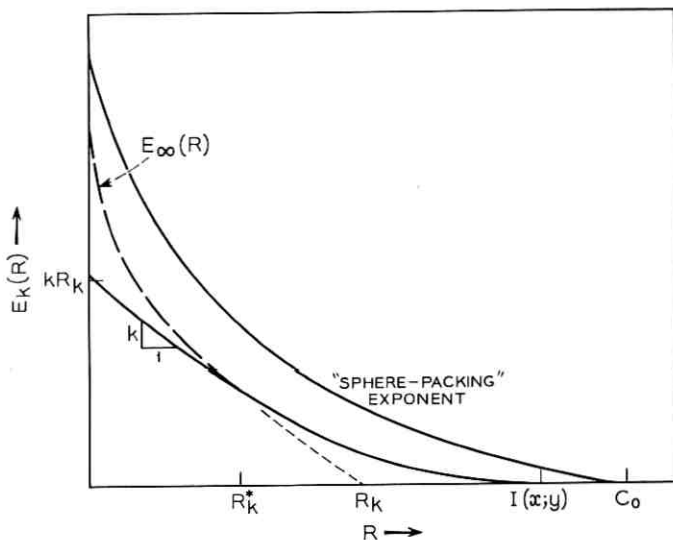
Fig. 11 — List decoding exponent.

be generated. Hence, $e^*(R)$ *may be obtained by a simple and natural construction from* $E_\infty(R)$.

4.3 *Heuristic Connection With The Overflow Probability*

In this section we establish a heuristic connection between $P[C \geq L]$ and the probability of a buffer overflow $P_{BF}(N)$, the probability of an overflow before the Nth source decision is released to the safety zone.

We begin by noting that $P_{BF}(N)$ is monotone increasing in N, hence that $P_{BF}(N) \geq P_{BF}(1)$. We first relate $P_{BF}(1)$ and $P_R[C \geq L]$.

Referring to Fig. 7, an example of a correct path trajectory which causes large static computation, we develop the following argument. If the random variable of static computation, C, is large, most of the computation will be performed on nodes which are close to the reference node. For computation to be performed on nodes distant from the reference node, the correct path must dip sufficiently at some distant point so that it returns at least to the level of the reference node. (Incorrect paths typically decrease in metric.) Since the correct path increases on the average, such a dip must be very large and thus occurs with much smaller probability than do dips close to the reference node.

If most of the static computation is done on nodes close to the reference node, we may associate such computation with dips in the correct

path. Then, since all incorrect subsets in the neighborhood of a path dip will have approximately equal amounts of computation done in them, the total computation due to a correct path dip will be a small multiple of the static computation in a particular incorrect subset in the neighborhood of the dip. Consequently, if about N_{av} incorrect subsets have equal computation in them, say C_0, and $N_{av}C_0$ is enough computation to cause overflow on the first decoded digit, then, heuristically, $P_{BF}(1) \cong P[C \geq C_0]$. To find C_0, assume that the buffer can store B tree branches of l digits each, that each channel digit arrives in τ_{ch} seconds, and that the decoder can perform one computation in τ_0 seconds. Then, the search pointer will be forced back to the safety zone if more than $lB\tau_{ch}/\tau_0$ computations are needed to decode the first digit. Setting $N_{av}C_0 = lB\tau_{ch}/\tau_0$ we have

$$P_{BF}(1) \cong P[C \geq lB\tau_{ch}/N_{av}\tau_0] \qquad (25)$$

as our heuristic approximation.

If dips in the correct path are infrequent and if the decoder operates at about twice or three times the speed required to do the average computation in real time, then we may approximate $P_{BF}(N)$ by assuming independence of the dips which cause overflow and have

$$P_{BF}(N) \cong NP_{BF}(1) \qquad (26)$$

This last argument is weak and should, at best, serve as a rule of thumb.
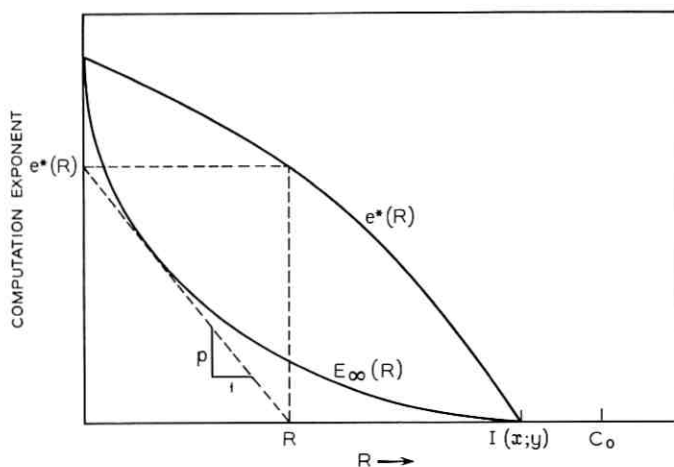
Fig. 12 — Construction for $e^*(R)$.

The argument leading to the connection between $P_{BF}(1)$ and the distribution of static computation is stronger and is partially supported by the experimental evidence cited above.

From (24), (25), (26), and the fact that the distribution of static computation is Paretian, we deduce that the overflow probability, *when it is small*, behaves as $N[N_{av}\tau_0/lB\tau_{ch}]^\beta$ where β is related to the computation exponent $e(R)$ by $\beta(R) = e(R)/R$. Thus, it is clear that the overflow probability is relatively insensitive to the buffer size B and the machine speed $1/\tau_0$ but that it depends heavily on the source rate R. (Note that changing the duration of the channel symbols, τ_{ch}, is tantamount to changing the channel and thus $e(R)$.) Since $e(R)$ increases with decreasing rate, we deduce that $\beta(R)$ is more than doubled by a halving of the information rate or that the overflow probability is more than squared.

V. CONCLUSIONS

It has been said that the buffer overflow probability is of primary concern in the design of a sequential decoder. We have examined this buffer overflow probability and have shown that it is relatively insensitive to the buffer capacity and to machine speed for moderate speeds and capacities. We have also indicated that the overflow probability is a strong function of the source rate. In addition, bounds on the dependence of the overflow probability on the source rate were given and related to exponents presented in the coding theorem.

We have argued that the particular sensitivites of the overflow probability exist because the distribution of static computation is an algebraic function of the distribution parameter; i.e., $P[C \geqq L]$ behaves as $L^{-\beta}$, $\beta > 0$, for large L. In turn, it has been observed that such behavior arises because the random variable of static computation assumes exponentially large values with exponentially small probabilities. This exponential growth of computation has been shown to be basic to sequential decoding.[3]

While the probability of overflow is relatively insensitive to many of the machine parameters, these parameters can be so chosen and the source rate can be so restricted that the probability of a buffer overflow can be made very small. To achieve the small overflow probabilities, the source rate for many channels need not be restricted to be less than about 90 percent of R_1.[7] (R_1 is generally known as R_{comp}, the computational cutoff rate defined by Wozencraft.[1] For many channels, R_{comp} is a substantial fraction of channel capacity.)

VI. ACKNOWLEDGMENTS

REFERENCES

1. Wozencraft, J. M. and Reiffen, B., *Sequential Decoding*, M.I.T. Press and John Wiley and Sons, Inc., New York, London, 1961.
2. Fano, R. M., A Heuristic Discussion of Probabilistic Decoding, IEEE Trans., *IT-9*, 1963, pp. 64–74.
3. Savage, J. E., The Computation Problem with Sequential Decoding, Ph. D. Thesis, Department of Electrical Engineering, M.I.T., February, 1965, also published as Technical Report No. 371, M.I.T., Lincoln Laboratory, Lexington, Mass., 1965, and as Technical Report No. 439, M.I.T., Research Laboratory of Electronics, Cambridge, Mass., 1965.
4. Shannon, C. E. and Weaver, W., *Mathematical Theory of Communication*, U. of Illinois Press, Urbana, Ill., 1949.
5. Gallager, R. G., A Simple Derivation of the Coding Theorem and Some Applications, IEEE Trans., *IT-11*, 1965, pp. 3–18.
6. Feller, W., *An Introduction to Probability Theory and Its Applications*, 2nd Ed., John Wiley and Sons, Inc., New York, 1957, Chap. 2.
7. Jordan, K. L., Jr., Performance of Sequential Decoding with Efficient Modulation, to be published in IEEE Trans. of the Communication Systems Group.
8. Mandelbrot, B. M., The Pareto-Levy Law and the Distributions of Income, Int. Econ. Rev., *1*, May, 1960.
9. Hardy, G. H., Littlewood, J. E., and Polya, G., *Inequalities*, University Press, Cambridge, England, 1959.
10. Wozencraft, J. M., List Decoding, Quarterly Progress Report 48, Research Laboratory of Electronics, M.I.T., January 15, 1958.
11. Elias, P., List Decoding for Noisy Channels, Technical Report 335, Research Laboratory of Electronics, September 20, 1957.
12. Gallager, R. G., unpublished notes.
13. Fano, R. M., *Transmission of Information*, M.I.T. Press and John Wiley and Sons, New York, 1961.
14. Zipl, G. K., *Human Behavior and the Principle of Least Effort*, Addison-Wesley Press, Reading, Mass., 1949.
15. Mandelbrot, B., Self-Similar Error Clusters in Communication Systems and the Concept of Conditional Stationarity, IEEE Trans., *COM-13*, March, 1965.
16. Wozencraft, J. M. and Jacobs, I. M., *Principles of Communication Engineering*, John Wiley and Sons, Inc., New York, 1965.

A Mathematical Model of a Vibrating Soil-Foundation System

By G. F. WEISSMANN

The displacement amplitudes and the phase angles of vertically vibrating rigid circular plates on an elastic isotropic homogeneous half-space have been expressed in terms of the mass of the plate, the static spring constant multiplied by a frequency-dependent function, and a damping term. The results have been modified to apply to vibrating soil-foundation systems. The effects of hysteresis damping, nonlinear load-deflection characteristics of soils, the static prepressure, the change of soil properties with depth, and the difference between static and dynamic stress-strain relations of soils have been considered. The mathematical model has been compared with data on vibrations of circular foundations. The agreement between the model and the experimental data for cohesive soils is very good.

I. INTRODUCTION

Numerous attempts have been made to develop a mathematical model capable of representing the steady-state vibrations of a soil-foundation system. E. Reissner[1] solved the problem of vertical vibrations of a rigid circular plate on a semi-infinite elastic solid. A sign error in his work was discovered by O. J. Šechter[2] who presented also a corrected analytical solution for this case. T. Y. Sung[3] continued this work for different pressure distributions between the plate and the solid. G. N. Bycroft[4] presented approximate solutions of the steady-state vibrations for the degrees of freedom of a rigid circular plate on an elastic isotropic half-space and on an elastic stratum. Since the mathematical solutions become rather difficult, this approach has been used only for a strongly idealized soil, namely the semi-infinite elastic isotropic solid. Another approach to this problem is the determination of a simplified mathematical model capable of describing the vibrations of a soil-foundation system. O. J. Šechter[2] showed that the amplitude-frequency response curve of a vibrating system consisting of constant mass, viscous damping force, and linear spring constant differs only slightly from that

177

caused by vertical vibrations of a circular plate on an elastic half-space, provided the mass of the plate is multiplied by a factor and the damping coefficient is chosen appropriately. This approach has been extended by M. Novák[5,6] who introduced a frequency independent nonlinear restoring force. G. Ehlers[7] attempted to simulate the soil-foundation system by assuming the foundation to be supported by a truncated pyramid of soil. This approach was used also by A. Pauw,[8] and H. A. Balakrishna Rao and C. N. Nagaraj.[9] However, none of the above mentioned models was capable of representing the amplitude-frequency response curves of several soil-foundation systems investigated by R. K. Bernhard and J. Finelli,[10] who concluded that an equivalent system could not be analogous to a simple spring-mass system with viscous damping and linear elasticity.

The purpose of this paper is to present a quasilinear system sufficiently adaptable to represent the amplitude-frequency response and phase angle-frequency curves of circular foundations on soil.

II. THE VIBRATIONS OF CIRCULAR FOUNDATIONS ON AN ELASTIC HALF-SPACE*

The vertical steady-state vibrations of circular foundations on a homogeneous elastic isotropic half-space have been investigated analytically by E. Reissner,[1] O. J. Šechter,[2] T. Y. Sung,[3] and G. N. Bycroft.[4] According to their work the displacement amplitude becomes

$$y_0 = \frac{F_0}{Gr_0} \sqrt{\frac{f_1^2 + f_2^2}{(1 + b_0 a_0^2 f_1)^2 + (b_0 a_0^2 f_2)^2}}. \tag{1}$$

The phase angle is

$$\tan \Phi = - \frac{f_2}{f_1 + b_0 a_0^2 (f_1^2 + f_2^2)}, \tag{2}$$

where

y_0 = displacement amplitude of foundation,
F_0 = force amplitude of harmonic exciting force,
G = shear modulus of half-space,
r_0 = radius of circular foundation,
b_0 = $m_0/\rho r_0^3$ = mass ratio,
m_0 = mass of circular foundation,
ρ = mass density of half-space,
a_0 = $r_0 \omega \sqrt{\rho/G_s}$ = frequency factor,

* The letter symbols used in this paper are defined where they first appear and are arranged alphabetically, for convenience or reference, in the Appendix.

Φ = phase angle between exciting force and displacement,

G_s = dynamic shear modulus of half-space,

ω = angular frequency,

f_1 and f_2 are functions of the dimensionless frequency factor a_0, of Poisson's ratio ν of the half-space and of the assumed pressure distribution between the half-space and the foundation.

T. Y. Sung[3] determined the functions f_1 and f_2 for different contact pressure distributions and different Poisson's ratios in terms of power series of the frequency factor a_0 for $a_0 \leq 1.5$. The values of these functions for a pressure distribution caused by a rigid circular plate are shown in Fig. 1. The functions f_1 and f_2 as determined by G. N. Bycroft[4] differ somewhat from those used in this paper which are based on T. Y. Sung's[3] work. It should be noted that for zero frequency, f_1 approaches a finite value and f_2 becomes equal to zero.

For zero frequency, (1) becomes

$$y_{os} = -\frac{F_0}{Gr_0} f_{10} \tag{3}$$
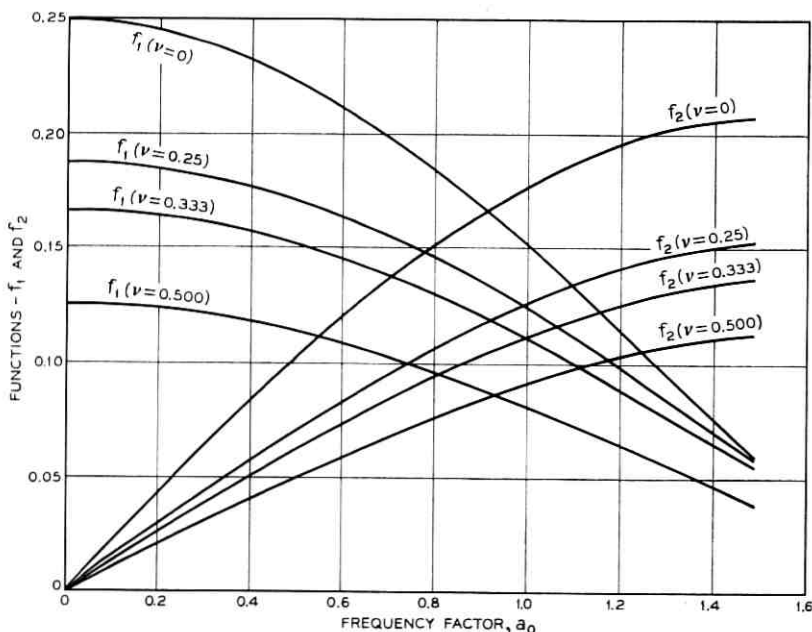
Fig. 1 — Functions f_1 and f_2 for rigid circular plates.

where

$y_{0s} = \lim\limits_{\omega \to 0} y_0 =$ displacement of foundation due to static load F_0, and

$f_{10} = \lim\limits_{a_0 \to 0} f_1 =$ value of f_1 for zero frequency.

From Fig. 1 it follows that the value of f_{10} can be expressed as

$$-f_{10} = \frac{1 - \nu}{4}. \tag{4}$$

Substituting (4) in (3) results in an expression for the displacement of a rigid circular plate on a homogeneous elastic half-space due to a vertical static force. This expression is identical to that derived by Boussinesq[11] in 1885.

It is readily verified that (1) and (2) can be written as

$$y_0 = \frac{F_0}{\sqrt{[C_s \alpha - m_0 \omega^2]^2 + [C_s \beta]^2}} \tag{5}$$

$$\tan \Phi = \frac{C_s \beta}{C_s \alpha - m_0 \omega^2} \tag{6}$$

where

$$C_s = -\frac{G r_0}{f_{10}} = \frac{4 G r_0}{1 - \nu} = \lim\limits_{\omega \to 0} \frac{F_0}{y_0} \tag{7}$$

$$\alpha = \frac{f_1 f_{10}}{f_1^2 + f_2^2} = -\frac{1 - \nu}{4} \frac{f_1}{f_1^2 + f_2^2} \tag{8}$$

$$\beta = -\frac{f_2 f_{10}}{f_1^2 + f_2^2} = \frac{1 - \nu}{4} \frac{f_2}{f_1^2 + f_2^2}. \tag{9}$$

C_s represents the static spring constant of a rigid circular plate on an elastic isotropic homogeneous half-space. Its magnitude depends on the shear modulus and Poisson's ratio of the half-space and on the radius of the rigid plate.

α and β are functions of the frequency factor a_0 and of Poisson's ratio ν as shown in Fig. 2. They have been computed using the values of f_1 and f_2 shown in Fig. 1. The values of the functions α and β for $\nu = 0$ and $\nu = \frac{1}{3}$ are plotted in Fig. 2 only, because the values for $\nu = \frac{1}{4}$ and $\nu = \frac{1}{2}$ fall between those shown. Since $a_0 = r_0 \omega \sqrt{\rho / G_s}$, the functions α and β depend on the magnitude of the radius of the plate, r_0, the frequency, ω, the dynamic shear modulus, G_s, of the half-space, and the mass-density ρ, of the half-space.

$$\alpha = -\frac{1-\nu}{4}\frac{f_1}{f_1^2+f_2^2}$$

$$\beta = \frac{1-\nu}{4}\frac{f_2}{f_1^2+f_2^2}$$

FREQUENCY FACTOR $a_0 = r_0\,\omega\sqrt{\rho/G\,\text{s}}$

Fig. 2 — Functions α and β vs frequency factor a_0.

The square root of the ratio of the dynamic shear modulus, G_s, to the mass-density, ρ, represents the shear wave velocity, v_s,

$$v_s = \sqrt{\frac{G_s}{\rho}}. \tag{10}$$

It should be mentioned that, for many materials, the dynamic shear modulus, G_s, as obtained from wave velocity measurements, is larger than the shear modulus, G, determined by means of static or slow dynamic tests.

For large shear wave velocities, the function α approaches one and β approaches zero. For this case, (5) represents the displacement amplitude and (6) the phase angle of a linear vibrating system without damping. This system consists of the mass of the plate, a weightless spring with a spring constant defined by (7), and a harmonic exciting force. It becomes apparent that the functions α and β modify this simple system to account for the additional effect of the mass-density of the half-space.

The functions α and β, as shown in Fig. 2, can be expressed with

sufficient accuracy as follows:

$$\alpha = 1 - \varepsilon a_0^2 = 1 - \varepsilon \left(\frac{r_0}{v_s}\right)^2 \omega^2 \tag{11}$$

$$\beta = b_1 a_0 = b_1 \left(\frac{r_0}{v_s}\right)\omega \tag{12}$$

where ε and b_1 are appropriately selected constants. The values of ε and b_1 depend on Poisson's ratio; ε varies between 0.26 and 0.30, and β between 0.76 and 0.85.

III. THE PARTICIPATING MASS OF THE HALF-SPACE

H. Lorenz[12] introduced the concept of the participating soil mass in order to explain some results of foundation vibration tests. O. J. Šechter[2] proved that the vertical vibration of a circular plate on an elastic half-space can be expressed, with sufficient accuracy, by means of a constant mass, a viscous damping force, and a spring constant. The mass consists of the mass of the plate, m_0, multiplied by a factor which accounts for the mass of the half-space vibrating in-phase with the plate. The displacement amplitudes and the phase angles of such a system can be written as

$$y_0 = \frac{F_0}{\sqrt{[C_s - \bar{m}\omega^2]^2 + [b\omega]^2}} \tag{13}$$

$$\tan \Phi = \frac{b\omega}{C_s - \bar{m}\omega^2} \tag{14}$$

where
$\bar{m} = m_0 + m_s = $ constant mass,
$m_s = $ participating mass of half-space, and
$b \quad = $ damping constant.

Equations (13) and (14) are identical to (5) and (6), provided the constant mass and the damping constant are selected as follows:

$$\bar{m} = m_0 \left[1 + \varepsilon \frac{C_s}{m_0}\left(\frac{r_0}{v_s}\right)^2\right] \tag{15}$$

$$b = b_1 \frac{r_0}{v_s} C_s . \tag{16}$$

This identity is readily shown by substitution of (15) and (16) in (13) and (14).

IV. DYNAMIC STIFFNESS

Some investigators, such as W. Heukelom,[13,14] expressed the results of foundation vibration tests in terms of the dynamic stiffness and the phase angle. The dynamic stiffness is defined as the ratio of the force amplitude between the foundation and the subsoil to the resulting displacement amplitudes. The steady-state vibrations of a rigid circular plate on an elastic half-space shall now be expressed in these terms.

The force acting at the surface of the half-space can be expressed as

$$\bar{F} = F - m_0 \ddot{y} \tag{17}$$

where

$\bar{F} = \bar{F}_0 e^{i(\omega t + \Psi)}$ = force acting between plate and half-space,

$\bar{F}_0$ = force amplitude acting between plate and half-space,

Ψ = phase angle between $\bar{F}$ and the resulting displacement,

$F = F_0 e^{i(\omega t + \Phi)}$ = exciting force acting on plate,

$y = y_0 e^{i\omega t}$ = displacement of plate,

$\ddot{y} = -y_0 \omega^2 e^{i\omega t}$ = acceleration of plate,

Φ = phase angle between F and the resulting displacement,

$i = \sqrt{-1}$.

The force amplitude acting between the plate and the half-space becomes

$$\bar{F}_0 = \sqrt{F_0^2 + 2F_0 m_0 y_0 \omega^2 \cos \Phi + (m_0 y_0 \omega^2)^2} \tag{18}$$

and for the phase angle between the force acting at the surface of the half-space and the displacement, the following expression is obtained:

$$\tan \Psi = \frac{F_0 \sin \Phi}{F_0 \cos \Phi + m_0 y_0 \omega^2}. \tag{19}$$

The dynamic stiffness is defined as the ratio of the force amplitude acting between the plate and the half-space and the resulting displacement amplitude and becomes, by means of (18),

$$S = \frac{\bar{F}_0}{y_0} = \frac{F_0}{y_0} \sqrt{1 + 2\frac{m_0 y_0}{F_0} \omega^2 \cos \Phi + \left(\frac{m_0 y_0 \omega^2}{F_0}\right)^2} \tag{20}$$

where

S = dynamic stiffness.

Substituting y_0 and Φ, expressed by means of (5) and (6), in (20), the dynamic stiffness becomes

$$S = C_s \sqrt{\alpha^2 + \beta^2} \tag{21}$$

and by substitution of (5) and (6) in (19), the following expression is

obtained for the phase angle Ψ:

$$\tan \Psi = \frac{\beta}{\alpha}. \tag{22}$$

Substitution of the values for α and β from Fig. 2 or of the approximate expression for α and β given by (11) and (12) in (21) shows that the dynamic stiffness of the half-space is essentially equal to the static stiffness or the static spring constant, C_s. The effect of α and β on the dynamic stiffness is negligibly small.

Substitution of α and β in (22) shows that the phase angle between the force acting at the surface of the half-space and the displacement remains always smaller than 90 degrees for values of the frequency factor, a_0, smaller or equal to 1.5.

V. DAMPING

Energy propagation to infinity provides the only damping of the vibrations of a rigid circular plate on an ideally elastic homogeneous half-space. The energy dissipated per cycle becomes

$$D_s = \oint F \, dy \tag{23}$$

where
D_s = dissipated energy per cycle,
F = $F_0 \sin (\omega t + \Phi)$,
y = $y_0 \sin \omega t$.

By substitution of (5) and (6) in (23) the following is obtained:

$$D_s = \pi C_s \beta y_0^2. \tag{24}$$

The energy required for the deformation of the half-space becomes

$$U_s = \tfrac{1}{2} C_s \alpha y_0^2 \tag{25}$$

where
U_s = energy required for the deformation of the half-space.

It should be noted that the energy required for the deformation of the half-space is equal to the maximum energy stored in the half-space reduced by the inertia effects of the half-space.

The loss coefficient of the circular plate on the ideally elastic half-space shall be defined as

$$\eta_s = \frac{D_s}{2\pi U_s} = \frac{\beta}{\alpha} \tag{26}$$

where

η_s = loss coefficient of vibrating circular plate.

The loss coefficient of the circular plate on the elastic half-space should be identical to the phase angle between the force amplitude acting between the plate and the half-space and the resulting displacement amplitude shown in (22).

It should be pointed out that both the dissipated energy and the energy of the half-space are proportional to the static spring constant C_s. The loss coefficient of the vibrating system, however, is a function of α and β alone. α and β are defined by means of (8) and (9). Equations (11) and (12) are approximate expressions of α and β.

The medium of the half-space was considered to be ideally elastic and hence, the propagation of energy to infinity provided the only source of energy dissipation. However, engineering materials and particularly soils are not ideally elastic but dissipate energy due to internal friction if subjected to cyclic stresses. The author and R. R. Hart[15] determined the specific damping capacity or the coefficient of energy absorption of some granular soils by means of laboratory tests. The specific damping capacity is defined as the amount of energy absorbed by a unit volume of the material per unit of energy spent for deformation per cycle. The specific damping capacity for these granular soils varied between 0.4 and 0.9. D. D. Barkan[16] reported values between 0.64 and 0.79 for sand. For clayey soils the damping capacity varied between 0.2 and 0.6. Furthermore, it was established that the specific damping capacity of sandy and clayey soils does not depend on the rate of stress application, the frequency of changes in the stress, the maximum alternating stress, or the static prestresses. The loss coefficient is obtained by division of the specific damping capacity by 2π.

$$\eta = \frac{\Psi_0}{2\pi} \tag{27}$$

where

η = loss coefficient of material

Ψ_0 = specific damping capacity of material.

The loss coefficient, η, is considered to be a basic property of a material. The difference between the loss coefficient of a material, η, and the loss coefficient of a vibrating system, η_s, should be noted.

G. N. Bycroft[4] investigated the effect of internal friction of the medium of the half-space on the functions f_1 and f_2 shown in Fig. 1. f_1 becomes numerically smaller and f_2 greater for small values of the frequency factor, a_0. Changes of f_1 and f_2 affect the function α and β shown

in Fig. 2 and defined by means of (8) and (9). The effect of such a change on the function α is rather small and α can still be expressed, with sufficient accuracy, by means of (11). The function β becomes approximately

$$\beta = \eta + b_1 a_0 = \eta + b_1 \frac{r_0 \omega}{v_s}. \tag{28}$$

For small values of the frequency factor, a_0, or for high shear wave velocities and small radii of the plates, the effect of the loss coefficient of the medium becomes significant.

An approximate expression of the loss coefficient of the vibrating circular plate is obtained by substitution of (11) and (28) in (26)

$$\eta_s = \frac{\eta + b_1 a_0}{1 - \varepsilon a_0{}^2} = \frac{\eta + b_1 \left(\dfrac{r_0 \omega}{v_s}\right)}{1 - \varepsilon \left(\dfrac{r_0 \omega}{v_s}\right)^2}. \tag{29}$$

For zero frequency, the loss coefficient of the plate becomes equal to the loss coefficient of the medium of the half-space. This is true only if the loss coefficient of the material is independent of the magnitude of the applied static and cyclic stresses. The author[17] measured the loss coefficient of circular plates on clayey silt subjected to slowly alternating loads. The results varied between 0.1 and 0.15. Considering the additional friction between the plate and the soil, the results agree well with those obtained by laboratory tests of sandy and clayey soils as reported by the author[15] and by D. D. Barkan.[16]

VI. NONLINEAR RESTORING FORCE

The static spring constant of a rigid circular plate on an elastic isotropic homogeneous half-space has been expressed by means of (7). For this idealized medium, the deflection is a single-valued linear function of the applied force. For engineering materials, and particularly for soils, this relationship becomes considerably more complex. Due to the effect of hysteresis damping, the deformation caused by the application of an alternating force is no longer a single-valued function. Two different forces cause the same deformation under the condition of loading and unloading. Furthermore, the average of these two forces may be a nonlinear function of the deformation and/or the rate of deformation. Other factors, such as static preloads and change of the properties of the half-space with depth, further complicate the force-deformation relation.

In view of the mathematical complexity of strongly nonlinear vibration problems, it shall be assumed that the nonlinearities of the force-displacement function within a limited range are small. For this case the nonlinear force-displacement function can be expressed with sufficient accuracy by means of an equivalent linear function.

$$F_s = f(y) \approx C_s(y_0)y \quad \text{for} \quad -y_0 \leqq y \leqq y_0 \tag{30}$$

where

$F_s \quad = f(y) =$ nonlinear force-displacement function, and

$C_s(y_0) =$ amplitude dependent spring constant.

The spring constant, C_s, should be selected in such a manner that the stored energy at the displacement amplitude of both the nonlinear and the equivalent linear systems are equal.

$$U = \int_0^{y_0} F_s dy = \int_0^{y_0} f(y)dy = \tfrac{1}{2}C_s(y_0)y_0^2 \tag{31}$$

where

$U =$ stored energy.

The spring constant as a function of the displacement amplitude is readily obtained by solving (31) with respect to C_s. The static spring constant can frequently be expressed by the following empirical equation:

$$C_s = C_0 y_0^{-n} \tag{32}$$

where

C_0 and n are appropriately selected constants.

It should be noted that (32) is an empirical function which has been used successfully by the author[17] to express the amplitude, dependent load-deflection characteristics of circular plates on some soils. Other functions may be more suitable to define these characteristics for different soils.

The amplitude-frequency response curves and the phase angle frequency curves of circular plates on a quasielastic homogeneous isotropic half-space with hysteresis damping are obtained by substitution of (11), (28), and (32) in (5) and (6). For the amplitude-frequency response curves, biquadratic equations of the frequency as a function of the amplitudes are obtained.

VII. THE VIBRATING SOIL-FOUNDATION SYSTEM

The load-deflection characteristics of circular rigid plates on soil are generally expressed in terms of the coefficient of subgrade reaction

which is defined as the ratio of the average applied stress to the resulting displacement. The spring constant of a rigid circular plate on soil becomes then

$$C_s = \pi r_0^2 k_s \qquad (33)$$

where

k_s = coefficient of subgrade reaction.

By means of (7) and (33) the coefficient of subgrade reaction of circular rigid plates on an elastic isotropic homogeneous half-space can be expressed as

$$k_s = \frac{4G}{\pi(1 - \nu)r_0}. \qquad (34)$$

For this case, the coefficient of subgrade reaction becomes inversely proportional to the radius of the plate.

The author[17] determined the coefficient of subgrade reaction of a silty clay experimentally. Circular plates of different radii, r_0, were loaded to produce various average prepressures, $\bar{p}$, between the plate and the subsoil. This static prepressure was maintained until the creep settlements of the plates became negligibly small. An average stress, $\bar{\sigma}_n$, was then repeatedly added to and subtracted from the prepressure, $\bar{p}$. The resulting displacements were measured. Fig. 3 shows the results schematically. The coefficient of subgrade reaction, k_s, is calculated by dividing the alternating stress amplitude, $\bar{\sigma}_n$, by the corresponding vertical displacement, y_n. The results may be summarized as follows:

(i) The coefficient of subgrade reaction decreased with an increase of the alternating stress amplitude, $\bar{\sigma}_n$.

(ii) An increase of the static prepressure, $\bar{p}$, caused an increase of the coefficient of subgrade reaction.

(iii) An increase of the radius, r_0, caused a decrease of the coefficient of subgrade reaction; however, this decrease was generally smaller than (34), valid for the elastic half-space, would indicate.

The author and S. R. White[18] have shown that the dependence of the coefficient of subgrade reaction on the static prepressure can be rather significant for some soils.

S. D. Wilson and E. A. Sibley[19] have shown that the shear modulus increases with an increase of the rate of load application. A modulus value determined from velocity measurements was almost an order of magnitude higher than that determined by means of static compression tests. Typical data reported by R. V. Whitman[20] show a similar phenomenon. Only for sands, the shear modulii obtained by seismic tests
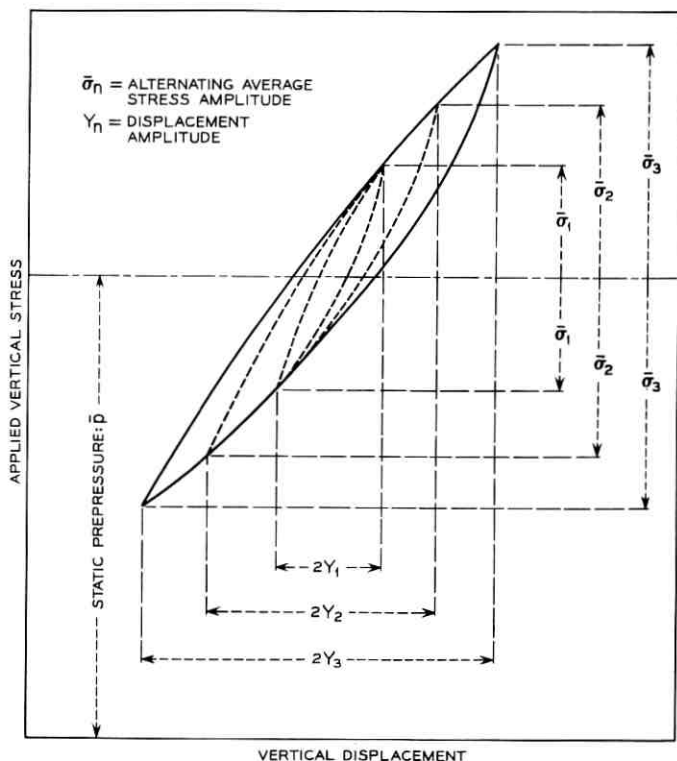
Fig. 3 — Coefficient of subgrade reaction.

did not differ much from that determined by means of static compression tests. Based on these results, it appears reasonable to assume that the coefficient of subgrade reaction of some soils increases also with an increased frequency of the load application.

Because the static prepressure, $\bar{p}$, and the radius, r_0, of the foundation are important parameters affecting the magnitude of the coefficient of subgrade reaction, k_s, the mass, m_0, of the foundation should be expressed as

$$m_0 = \frac{1}{g} \pi r_0^2 \bar{p} \tag{35}$$

where

$g = $ acceleration of gravity.

Substituting (11), (28), (33), and (35) in (5) and (6), the following

expressions for the displacement amplitude, y_0, and the phase angle, Φ, are obtained:

$$y_0 = \frac{F_0}{\pi r_0^2 k_s \sqrt{\left[1 - \{1 + \varepsilon\bar{a}_0^2\} \dfrac{\bar{p}}{k_s g} \omega^2\right]^2 + \left[\eta + b_1 \dfrac{r_0}{v_s} \omega\right]^2}} \quad (36)$$

$$\tan \Phi = \frac{\eta + b_1 \dfrac{r_0}{v_s} \omega}{1 - \{1 + \varepsilon\bar{a}_0^2\} \dfrac{\bar{p}}{k_s g} \omega^2} \quad (37)$$

where

$$\bar{a}_0 = \frac{r_0}{v_s} \sqrt{\frac{k_s g}{\bar{p}}}. \quad (38)$$

The resonance frequency becomes

$$\omega_0 = \sqrt{\frac{k_s g}{\bar{p}\{1 + \varepsilon\bar{a}_0^2\}}} = \sqrt{\frac{k_s g}{\bar{p}\left[1 + \varepsilon \dfrac{r_0^2}{v_s^2} \dfrac{k_s g}{\bar{p}}\right]}}. \quad (39)$$

In order to estimate the magnitude of $\bar{a}_0$, (10) and (34) are substituted in (38) to yield

$$\bar{a}_0 = \frac{r_0}{v_s} \sqrt{\frac{k_s g}{\bar{p}}} = \sqrt{\frac{4\rho g G r_0}{\pi(1 - \nu)G_s \bar{p}}} = \sqrt{\frac{4\gamma r_0 G}{\pi(1 - \nu)\bar{p}G_s}} \quad (40)$$

where

$\gamma = \rho g$ = density of soil.

For most soils, with the exception of sand, the shear modulus obtained by means of slow vibration tests is smaller than that obtained by seismic velocity measurements and hence $G/G_s < 1$. The specific weight of soils, γ, is generally smaller than the average contact pressure between the foundation and the subsoil, $\bar{p}$, and therefore $\gamma/\bar{p} < 1$. Since the foundation is considered to be rigid, the magnitude of the radius, r_0, must be limited. An increase of the radius r_0 would require a corresponding increase of the average contact pressure, $\bar{p}$. Hence, it is reasonable to assume that $\bar{a}_0$ is, for many materials, a small quantity and that $\varepsilon\bar{a}_0$ is then small compared to one. For this case, (39) can be simplified to

$$\omega_0 \approx \sqrt{k_s g / \bar{p}}. \quad (41)$$

The amplitude at resonance, y_{0r}, for a constant exciting force, F_0, follows from (36)

$$y_{0r} = \frac{F_0}{\pi r_0^2 k_s \left[\eta + b_1 \dfrac{r_0}{v_s} \omega_0 \right]} \tag{42}$$

and for a centrifugal exciting force $F_0 = m_1 e_0 \omega_0^2$ where m_1 is the eccentric mass and e_0 the eccentricity of the rotating weights:

$$y_{0r} = \frac{m_1 e_0 \omega_0^2}{\pi r_0^2 k_s \left[\eta + b_1 \dfrac{r_0 \omega_0}{v_s} \right]} = \frac{m_1 e_0 g}{\pi r_0^2 \bar{p}} \frac{\left[1 - \varepsilon \left(\dfrac{r_0 \omega_0}{v_s} \right)^2 \right]}{\left[\eta + b_1 \left(\dfrac{r_0 \omega_0}{v_s} \right) \right]}. \tag{43}$$

The loss coefficient at resonance can be expressed by means of (29) and (43) as

$$\eta_s = \frac{\eta + b_1 \left(\dfrac{r_0 \omega_0}{v_s} \right)}{1 - \varepsilon \left(\dfrac{r_0 \omega_0}{v_s} \right)^2} = \frac{m_1 e_0 g}{\pi r_0^2 \bar{p} y_{0r}} = \frac{m_1 e_0}{m_0 y_{0r}}. \tag{44}$$

It is now hypothesized that (36) and (37) describe the amplitude-frequency response and the phase angle-frequency relation of a rigid circular foundation on soil, provided the coefficient of subgrade reaction, k_s, the shear wave velocity, v_s, and the loss coefficient of the soil y, are determined experimentally and the constants ε and b_1 are selected according to the model of the rigid circular plate on the elastic half-space as 0.26 and 0.76, respectively. For sand, with its relatively low shear wave velocity, the term $r_0 \omega_0 / v_s$ may exceed 1.5 and (36) to (39) are no longer applicable.

The validity of this hypothesis can only be established by the evaluation of the data obtained by means of vibration tests.

VIII. THE EVALUATION OF VIBRATION TEST DATA

Vertical vibration tests of rigid circular foundations on soil were conducted by H. Lorenz[12,23] in Germany, D. D. Barkan[16] in the U.S.S.R., M. Novák[5,6] in Czechoslovakia, W. Heukelom[13,14] in the Netherlands, F. J. Converse[22] of California Institute of Technology, and Z. B. Fry[21] of the U. S. Army Engineer Waterways Experiment Station. R. K. Bernhard and J. Finelli[10] of Rutgers University used a rigid square foundation.

A vertical sinusoidal exciting force, F, was applied to the foundation and the resulting displacements were measured. Generally, these displacements could be expressed with sufficient accuracy in terms of a sinusoidal function.

The weight of the foundation and its dimensions are considered to be known quantities. They can be expressed in terms of the average contact pressure between the foundation and the subsoil and the radius of the foundation. In case of square foundations, the radius of an equivalent circular foundation with the same contact area as the square foundation was used.

The exciting force amplitude, F_0, is also considered to be a known function of the frequency. For all these reported tests, the exciting force has been produced by means of eccentrically rotating weights and therefore, can be expressed as $F_0 = m_1 e_0 \omega^2$.

The following experimental data can be obtained from a well conducted foundation vibration test:

(i) The displacement amplitude-frequency response curve, $y_0(\omega)$, and

(ii) The phase angle-frequency curve, $\Phi(\omega)$.

However, the measurements of the phase angle-frequency curve is relatively difficult, and a number of investigators did not determine these data. In some cases only the resonance frequency was measured.

Solving (5) and (6) with respect to $C_s\alpha$ and $C_s\beta$ the following equations are obtained:

$$C_s\alpha = \frac{F_0}{y_0}\left[\frac{m_0 y_0 \omega^2}{F_0} + \cos \Phi\right] = \pi r_0^2 k_s\alpha \tag{45}$$

$$C_s\beta = \frac{F_0}{y_0}\sin \Phi = \pi r_0^2 k_s\beta. \tag{46}$$

$k_s\alpha$ shall be defined as the "dynamic coefficient of subgrade reaction." By means of (45) and (46) it is always possible to calculate the parameters $C_s\alpha$ and $C_s\beta$, provided the mass of the foundation, m_0, is known and the force amplitude-frequency relation, $F_0(\omega)$, the displacement amplitude-frequency relation, $y_0(\omega)$, and the phase angle-frequency relation, $\Phi(\omega)$, have been determined experimentally.

Substitution of these values for $C_s\alpha$ and $C_s\beta$ back in (5) and (6) will obviously result in a perfect fit of the calculated amplitude-frequency response curve and the phase angle-frequency curve with the experimental data. However, according to (33), C_s is a function of the coefficient of subgrade reaction, k_s. The coefficient of subgrade reaction, k_s, in turn is, as discussed previously, a function of the displacement amplitude, y_0, and of the frequency, ω. Due to the large amplitude changes occurring close to the resonance frequency, even small nonlinearities of the stress-displacement relation may cause a considerable change of the

magnitude of the coefficient of subgrade reaction. From a single amplitude-frequency response curve and the corresponding phase angle-frequency curve, it is impossible to determine the effect of the displacement amplitude on the parameters $C_s\alpha$ and $C_s\beta$. However, if the exciting force amplitude is changed a number of amplitude-frequency response curves and phase angle-frequency curves are obtained, and it is possible to evaluate points of constant frequency at different displacement amplitudes or of constant displacement amplitudes at different frequencies. In this manner, the effect of frequency and amplitude on the parameters $C_s\alpha$ and $C_s\beta$ can be determined.

The loss coefficient, η_s, of the vibrating system is defined by means of (26). Substitution of (45) and (46) in (26) results in

$$\eta_s = \frac{\sin \Phi}{\left[\dfrac{m_0 y_0 \omega^2}{F_0} + \cos \Phi \right]}. \tag{47}$$

It should be noted that for phase angles Φ greater than $\pi/2$, the denominator in (47) becomes a difference, and small experimental errors will have a considerable effect on the calculated magnitude of the loss coefficient, η_s. Furthermore, (47) shows again that the loss coefficient does not depend on the spring constant, C_s.

If the phase angle-frequency data are not available, $C_s\alpha$ and $C_s\beta$ can be calculated from the amplitude-frequency response curve for specific frequencies only. For low frequencies, the phase angle Φ can be assumed to be approximately equal to zero, at high frequencies equal to π, and at resonance equal to $\pi/2$. Unfortunately, for a centrifugal exciting force, the displacement amplitudes at low frequencies are rather small and the data become relatively inaccurate; at high frequencies, the exciting force amplitude frequently exceeds the weight of the foundations and no data are taken. It is always possible to select frequency dependent functions in such a manner that an amplitude-frequency response curve calculated by means of (5) will fit the experimental data. This is possible for any arbitrary amplitude dependent function, $C_s(y_0)$. However, there is no physical significance in fitting one particular amplitude-frequency response curve. A mathematical model capable of describing the vibrations of a vibrating soil-foundation system should not only fit the amplitude-frequency response curve and the phase angle-frequency curve of one particular test but should also predict the effect of a change in radius, r_0, of the foundation, of a change of the static contact pressure, $\bar{p}$, and of a change of the exciting force amplitude, F_0.

IX. RESONANCE DATA OF VERTICAL STEADY-STATE VIBRATIONS OF RIGID FOUNDATIONS

A direct comparison of the data of vibrating rigid foundations shown in the literature is complicated by the different units and nomenclature used to express the results of these tests. In order to facilitate such a comparison, data obtained at resonance have been collected and are presented in Table I, using uniform units and nomenclature.

The authors of the publications used are listed in Column 2 of the table.

The type of soil is shown in Column 3.

The radius, r_0, of circular foundations is shown in Column 4 and is expressed in feet. In case of a square foundation, such as used by R. K. Bernhard and J. Finelli,[10] the radius of an equivalent circular foundation with the same contact area as the square foundation was used.

The average static contact pressure, $\bar{p}$, between the foundation and the subsoil is shown in Column 5 and is expressed in pounds per square foot.

Column 6 shows the angular resonance frequency, ω_0, expressed in radians per second. Resonance occurs if the phase angle between the exciting force and the resulting displacement is equal to $\pi/2$ or 90 degrees. For centrifugal excitation, resonance is sometimes determined by the tangent to the amplitude-frequency response curve through the origin. This is correct only for a linear damping force; however, the possible error is small. Even the difference of the frequency at maximum amplitude and the resonance frequency remains relatively small.

The exciting force amplitude, F_0, is listed in Column 7 in terms of pounds. H. Lorenz[23] and R. K. Bernhard and J. Finelli[10] reported some results for which the exciting force at resonance becomes greater than the weight of the foundation. These data are not included in Table I.

Column 8 shows the displacement amplitude at resonance in inches multiplied by 10^3.

The loss coefficient at resonance, a dimensionless quantity, is listed in Column 9 and has been calculated by means of (44).

The compression and shear wave velocities, v_c, and, v_s, are shown in Column 10 and are expressed in feet per second.

Column 11 shows the coefficient of subgrade reactions, k_s, which is defined as the ratio of the average stress caused by a static force acting on a rigid circular or square plate to the resulting displacement. The coefficient of subgrade reaction is expressed in pounds per square foot per inch.

The type of data reported by the investigators are listed in Column 12.

Table I shows clearly the need for more complete reporting of the obtained test data and of associated significant soil parameters.

Some typical values of the compression and shear wave velocities for different soils have been listed by D. D. Barkan[16] and are shown in Table II.

X. EXPERIMENTAL VERIFICATION OF THEORY

Equation (29) shall now be used to predict the loss coefficient, η_s, of vibrating rigid circular foundations. The results shall be compared with the loss coefficient, η_s, obtained by substitution of foundation vibration data in (47).

Z. B. Fry[21] of the U. S. Army Waterways Experiment Station reported the results of vibration tests of rigid circular foundations on a silty clay. Fig. 4 shows a typical amplitude-frequency response curve and the corresponding phase angle-frequency curve. An average shear wave velocity $v_s = 475$ ft/sec was determined for this soil.

Fig. 5 shows the loss coefficient, η_s, obtained by substitution of the shear wave velocity, v_s, in (29). A loss coefficient of the soil of $\eta = 0.1$ was assumed, and, based on the model of the rigid circular plate on an elastic half-space, the constants $\varepsilon = 0.26$ and $b_1 = 0.76$ were used. Furthermore, for a number of frequencies, the loss coefficient, η_s, was calculated by substitution of the data shown in Fig. 4 in (47). The agreement between the predicted and experimentally determined values of the loss coefficient is very good. The data show that the loss coefficient is affected to some degree by the magnitude of the exciting force amplitude.

The loss coefficient at resonance can be calculated by means of (44). The resonance frequencies, ω_0, and the displacement amplitudes at resonance, y_{0r}, of foundations having different radii, r_0, contact pressures, $\bar{p}$, and exciting force amplitudes, F_0, are listed in Table I. The data reported by Z. B. Fry[21] for silty clay having a shear wave velocity $v_s = 475$ ft/sec are listed from numbers H-1a to H-10d. The loss coefficients, η_s, at resonance are shown in Fig. 6 as a function of the product of radius and resonance frequency, $r_0\omega_0$. The agreement between the loss coefficient predicted by means of (29) and these experimental values is excellent.

The resonance data obtained by M. Novák are shown in Table I (A-1a to A-10c). The tests were conducted on a loess loam. The loss coefficients calculated by means of (44) are shown in Fig. 7. Unfortunately, the shear wave velocity, v_s, was not reported. Therefore, a

Table I—Resonance Data of Vertical Foundation Vibration Tests

1 No.	2 Reference	3 Soil	4 Radius of Foundation r_0 [ft]	5 Average Static Contact Pressure $\bar{p}$ [lb/ft²]	6 Angular Resonance Frequency ω [Rad/sec]	7 Exciting Force Amplitude at Resonance $F_0 = m_1 e \omega_0^2$ [lb]	8 Displacement Amplitude at Resonance y_{0c} [in ×10⁻³]	9 Loss Coefficient of Soil-Foundation System at Resonance η_t [−]	10 Compression Wave Velocity v_c [ft/sec]	10 Shear Wave Velocity v_s [ft/sec]	11 Coefficient of Subgrade Reaction k_s [lb/ft²/in]	12 Type of Available Data
A-1a	M. Novák[5]	Loess Loam	1.85	445	187	479	2.4	0.454				Amplitude-Frequency Response Curves
b					183	870	5.2	0.402				
c					173	1,515	10.0	0.406				
d					162	1,975	14.5	0.420				
e					158	1,825	14.9	0.409				
f					150	2,220	18.7	0.425				
2a				346	200	549	2.8	0.698				
b					187	911	5.7	0.652				
c					171	1,475	12.4	0.581				
3a				248	210	602	3.0	0.665				
b					178	1,600	14.3	0.511				
4a			1.60	625	160	351	3.4	0.310				
b					151	578	6.6	0.301				
c					140	990	12.9	0.298				
5a			1.31	987	132	238	4.2	0.237				
b					124	402	8.6	0.220				
c					115	667	17.5	0.210				
d					113	963	24.8	0.221				
6a				692	149	304	5.1	0.277				Resonance Frequency and Amplitude at Resonance
b					143	531	10.2	0.266				
c					132	880	21.6	0.243				
7a				397	118)?	427	7.5	0.325				
b					165)?	708	15.8	0.298				

Ref	Author	Soil	d					Amplitude	Resonance Freq. and Amplitude at Resonance	Amplitude-Frequency Response Curves
b					162	1,323	5.2	0.450		
c					157	1,860	6.1	0.571		
9a				3?9	188	584	1.6	0.552		
b					182	861	3.3	0.500		
c					170	1,460	6.9	0.456		
d					162	1,980	10.2	0.470		
10a				262	213	622	1.7	0.719		
b					205	1,095	3.7	0.640		
c					191	1,844	8.3	0.554		
B-1a	M. Novák[5]	Sandy Clay	1.85	420	203	1,070	7.9	0.281		
b					190	1,433	11.5	0.295		
c					181	1,658	14.5	0.298		
C-1	D. D. Barkan[16]	15 feet saturated clay on sand	2.61	1,670	88			0.290	22.90	
2			3.70	968	60			0.266	12.75	
3			5.23	770	69			0.362	10.68	
D-1	D. D. Barkan[16]	Soft saturated silty clay	1.30	1,335	73			0.142	18.30	
2			1.85	1,045	69			0.116	13.10	
3			2.27	916	70			0.102	10.95	
E-1	D. D. Barkan[16]	Loess	1.66	1,090	159				74.00	
2			2.19	1,550	107				56.20	
3			2.62	1,105	117				53.70	
4			3.70	874	121				42.70	
F-1	D. D. Barkan[16]	Fine saturated sand	1.85	762	95				20.60	
2a			3.70	421	143				23.20	
b					181				39.30	
3			5.25	692	130				28.90	
4			7.16	490	124				20.80	
5a			1.85	1,390				0.264		
b								0.380		
c								0.350		
6				3,360				0.320		
G-1	R. K. Bernhard and J. Finelli[9]	Gravel with silt	1.50	222	188	562	14.8	0.278		

TABLE I—Continued

No.	Reference	Soil	Radius of Foundation r_0 [ft]	Average Static Contact Pressure $\bar{p}$ [lb/ft²]	Angular Resonance Frequency ω_0 [Rad/sec]	Exciting Force at Resonance Amplitude $F_0 = m_e e \omega_0^2$ [lb]	Displacement Amplitude at Resonance z_{0r} [in $\times 10^{-3}$]	Loss Coefficient of Soil-Foundation System at Resonance η_s [—]	Compression Wave Velocity v_c [ft/sec]	Shear Wave Velocity v_s [ft/sec]	Coefficient of Subgrade Reaction k_s [lb/ft²/in]	Type of Available Data
H-1a	Waterways Experiment Station[21]	Silty Clay	2.58	1,478	86.7	2,780	10.0	0.365	1,000	475		
b					78.5	4,540	25.2	0.361				
c					72.5	5,870	40.0	0.345				
d					70.3	7,245	69.5	0.259				
2a				1,478	90.4	3,025	10.0	0.462				
b					80.4	4,765	23.5	0.410				
c					77.9	6,720	43.0	0.321				
d					73.5	7,920	62.8	0.292				
3a				1,225	94.8	3,325	12.0	0.464				
b					85.4	5,375	28.5	0.390				
c					78.5	6,820	48.5	0.343				
d					74.1	8,055	68.3	0.324				
4a				1,225	94.2	3,285	13.8	0.404				
b					82.9	5,060	31.9	0.349				
c					77.9	6,720	49.5	0.336				
d					74.7	8,185	77.0	0.287				
5a			3.65	738	115.6	4,950	4.5	1.027				
b					106.8	8,405	10.3	0.884				
c					101.7	11,450	16.3	0.847				
d					95.4	13,350	18.2	1.005				
6a				612	117.4	5,105	4.6	1.210				
b					110.5	8,995	10.8	1.030				
c					105.5	12,320	18.6	0.896				
d					101.1	14,990	24.6	0.892				

								250	1,044
7a		4.50	492	127.5	3.7	6,020	1.256		
b				120.6	8.1	10,720	1.130		
c				106.8	12.0	12,630	1.150		
d				105.5	17.5	16,330	1.050		
8a			612	113.0	3.4	4,725	1.095		
b				105.5	6.8	8,200	1.090		
c				110.5	11.4	13,520	0.976		
d				105.5	16.3	16,330	0.903		
9a		5.17	369	106.1	2.4	4,165	1.925		
b				103.0	5.1	7,820	1.880		
c				99.2	7.7	10,890	1.820		
d				98.0	9.1	14,090	2.030		
10a			612	98.6	2.0	3,600	1.395		
b				97.3	4.3	6,975	1.292		
c				91.1	6.6	9,190	1.260		
d				95.4	9.7	13,350	1.140		
I-1a	Nonplastic uni-form fine sand	2.58	1,225	100.5	8.6	3,740	0.649	250	1,044
b				94.2	17.0	6,540	0.653		
c				94.2	25.2	9,825	0.661		
d				95.4	31.4	13,350	0.704		
2a		3.65	738	100.5	6.2	3,740	0.745		
b				95.4	12.2	6,705	0.754		
c				94.8	17.6	9,945	0.783		
d				94.2	22.8	13,020	0.803		
3a			612	99.2	9.2	3,645	0.610		
b				96.7	17.4	6,890	0.638		
c				95.4	24.0	10,070	0.693		
d				94.2	27.2	13,020	0.813		
4a			738	105.5	5.6	4,120	0.826		
b				101.7	10.3	7,625	0.893		
c				100.5	15.0	11,180	0.919		
d				98.6	20.8	14,260	0.880		
5a			612	108.0	9.9	4,320	0.564		
b				104.2	15.4	8,005	0.722		
c				102.4	19.2	11,610	0.868		
d				101.1	21.0	14,990	1.052		

Waterways Experiment Station[21]

TABLE I—Continued

No.	Reference	Soil	Radius of Foundation r_0 [ft]	Average Static Contact Pressure $\bar{p}$ [lb/ft²]	Angular Resonance Frequency $\bar{\omega}$ [Rad/sec]	Exciting Force at Resonance Amplitude $F_0 = m_1 e \omega_0^2$ [lb]	Displacement Amplitude at Resonance z_{0r} [in × 10^{-3}]	Loss Coefficient of Soil-Foundation System at Resonance η_s [-]	Compression Wave Velocity v_c [ft/sec]	Shear Wave Velocity v_s [ft/sec]	Coefficient of Subgrade Reaction k_s [lb/ft²/in]	Type of Available Data
I-continued	Waterways Experiment station[21] continued.	Nonplastic uniform fine sand continued.	4.50	492								Amplitude-Frequency Response Curves and Phase Angle-Frequency Curves
6a					100.5	3,740	9.2	0.502				
b					95.4	6,705	15.6	0.590				
c					93.6	9,700	23.0	0.600				
d					92.3	12,500	24.6	0.744				
7a				612	98.6	3,600	5.6	0.666				
b					92.9	6,360	11.8	0.629				
c					90.4	9,045	17.4	0.638				
d					89.2	11,670	21.8	0.677				
8a			5.17	369	102.4	3,880	8.5	0.543				
b					99.2	7,250	14.4	0.639				
c					96.1	10,220	19.0	0.726				
d					94.8	13,180	23.2	0.778				
9a				612	100.5	3,740	9.35	0.641				
b					94.2	6,540	9.10	0.612				
c					92.3	9,430	13.5	0.616				
d					90.4	11,980	18.0	0.615				
J-1a	F. J. Converse[22]	Sandpit	0.654	578	141	300						
b					147	300						
c					147	300						
d					136	300						
e					141	400						
f					141	400						
g					131	500						
h					136	500						

				Frequency at Maximum Amplitude
J-11	139			500
j	133			600
k	125			600
2a	139	837	0.800	300
b	134			450
c	128			600
3a	141	274		450
b	149			300
c	140			450
d	146			300
e	138			450
4	144	304		300
5a	128	389		600
b	144			300
c	141			450
d	133			600
e	131			750
6a	128	405		600
b	134			750
c	131			750
7a	136	532		300
b	141			300
c	147			300
d	141			300
e	136			450
f	128			450
g	131			450
h	136			450
i	136			450
j	128			600
k	131			600
l	133			600
m	131			600
n	128			750
o	126			750
p	123			750
q	121			800
r	121			800
s	126			800

TABLE I—Continued

No.	Reference	Soil	Radius of Foundation r_0 [ft]	Average Static Contact Pressure $\bar{p}$ [lb/ft²]	Angular Resonance Frequency ω_n [Rad/sec]	Exciting Force Amplitude at Resonance $F_0 = m_1 e_1 \omega_n^2$ [lb]	Displacement Amplitude at Resonance s_{v_r} [in × 10^{-3}]	Loss Coefficient of Soil-Foundation System at Resonance η_s [—]	Compression Wave Velocity v_c [ft/sec]	Shear Wave Velocity v_s [ft/sec]	Coefficient of Subgrade Reaction k_s [lb/ft²/in]	Type of Available Data
K-1	F. J. Converse[22]	Beach Sand	0.800	222	163	300						Frequency at Maximum Amplitude
2a				387	163	300						
b					141	600						
3			1.875	100	157	650						
L-1a	H. Lorenz[23]	Peat	0.925	1,230	63.3							Resonance of Frequency
b					69.0							
2a			1.85	307	74.0							
b					82.2							
M-1	H. Lorenz[23]	Medium Sand	0.925	1,150	95.4							
2			1.850	287	109.3							
N-1	H. Lorenz[23]	Clayey Sand	0.925	1,253	135.3							
2			1.850	314	143.0							
P-1a	H. Lorenz[23]	?	1.85	556	122	5,200	98	0.192				Resonance Frequency and Amplitude of Resonance
b					113	4,320	118	0.175				
c					113	4,320	83	0.193				
d					113	4,320	130	0.177				
e					113	5,200	118	0.175				
f					122		130					
g							130					
2a			0.925	556	132	962	42.7	0.308				Amplitude-Frequency Re-
b					112	1,110	26.5	0.327				

202

Soil	Compression wave velocity [ft/sec]	Shear wave velocity [ft/sec]
Moist clay	4920	500
Loess at natural moisture	2630	850
Dense sand and gravel	1575	820
Fine-grained sand	985	360
Medium-grained sand	1800	525
Medium-sized gravel	2460	590
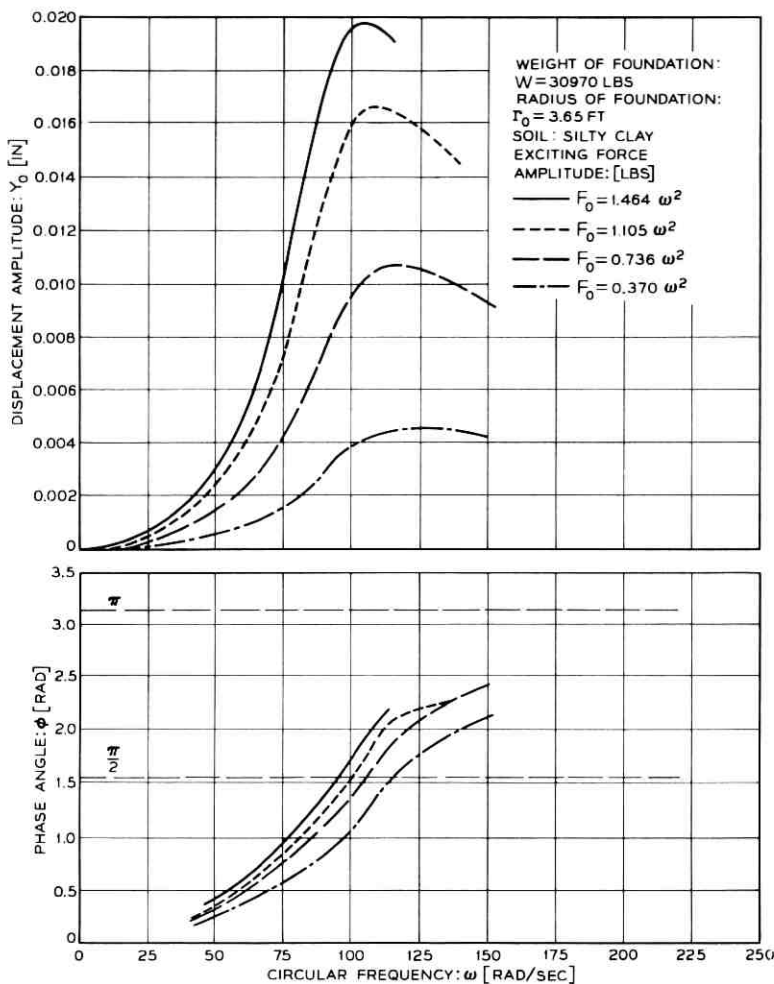
Fig. 4 — Typical amplitude-frequency response curve and phase angle-frequency curve of rigid circular foundation on silty clay.
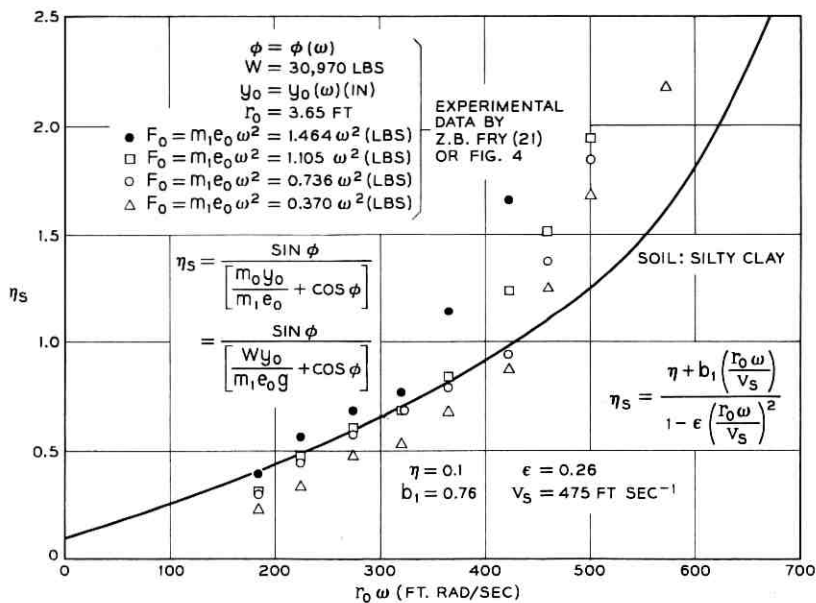
Fig. 5 — Loss coefficient of a vibrating circular foundation on silty clay.
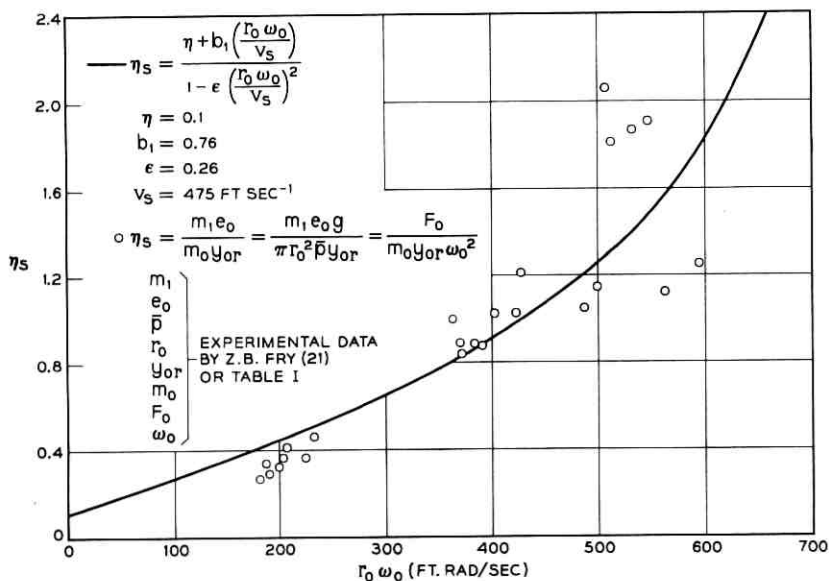
Fig. 6 — Loss coefficients at resonance of circular foundations on silty clay.

number of different shear wave velocities were substituted in (29) and the resulting curves are also shown in Fig. 7. Table II shows a value of the shear wave velocity of loess $v_s = 850$ ft/sec. The agreement of the predicted values of the loss coefficient and the experimentally determined values at resonance are again very good.

Z. B. Fry[21] reported also the results of vibration tests on sand. The resonance data, the radii, and the contact pressures are listed in Table I (I-1a to I-9d). A typical displacement amplitude-frequency response curve and the corresponding phase angle-frequency curve is shown in Fig. 8. The loss coefficients, η_s, were calculated by means of (47) and are shown in Fig. 9. No loss coefficient was predicted because the experimentally determined shear wave velocity decreased with an increase of the frequency. Fig. 10 shows the loss coefficients at resonance of foundations having different radii and contact pressures. The loss coefficient at resonance appears to be approximately constant. Fig. 11 shows the loss coefficients calculated by means of (47) for two foundations having different radii. The figure shows that for this sand, the loss coefficient is independent of the radius of the foundation. In order to obtain the constant loss coefficient at resonance shown in Fig. 10, the resonance frequency must be constant too. The resonance frequencies listed in Table I for this case are indeed almost constant.
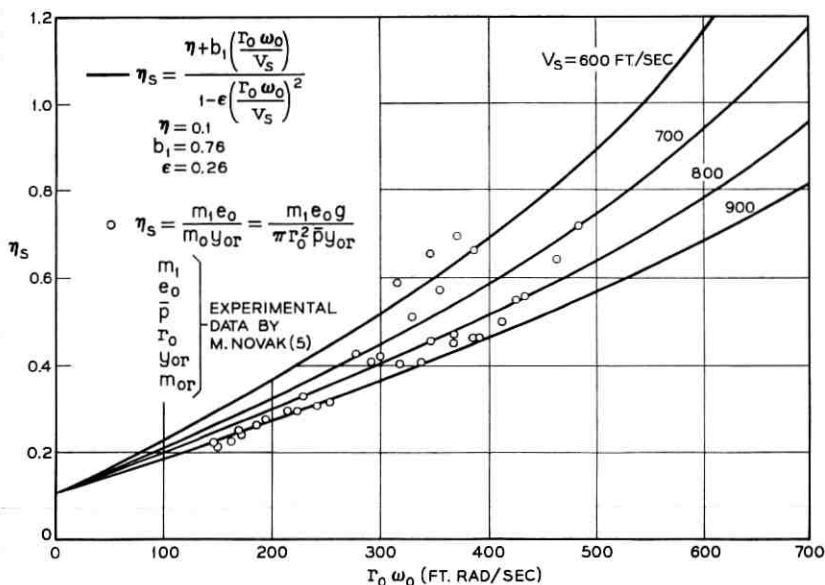
Fig. 7 — Loss coefficients at resonance of circular foundations on loess loam.
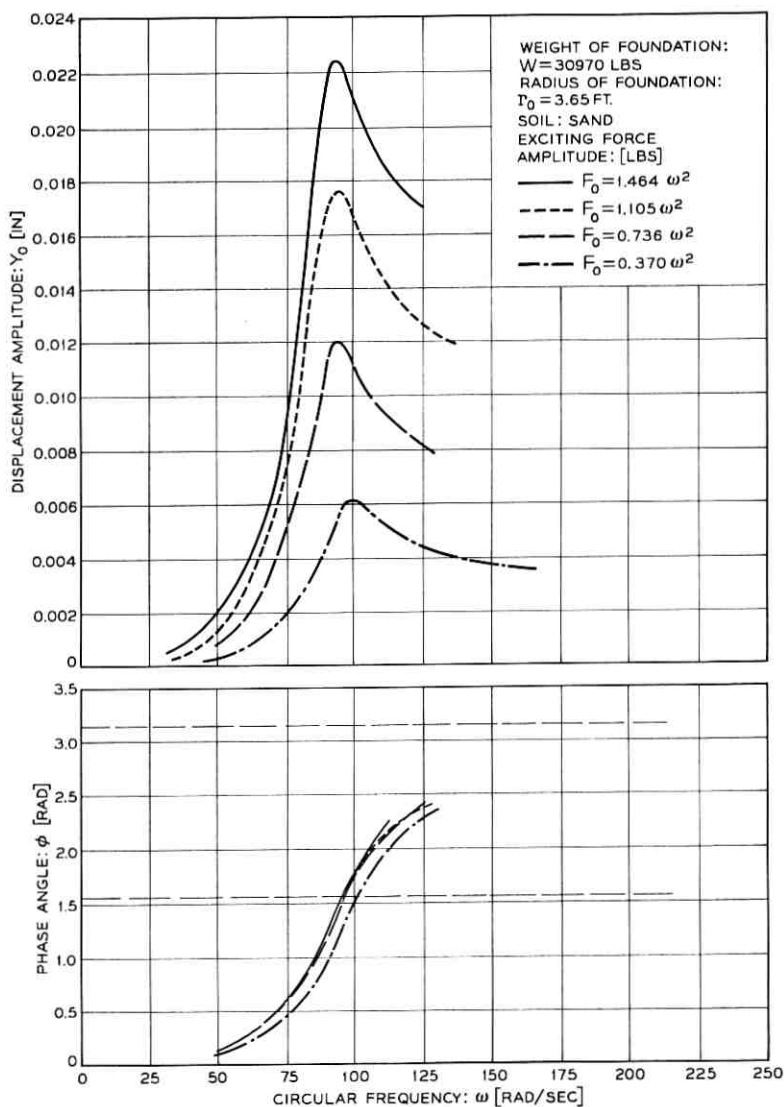
Fig. 8 — Typical amplitude-frequency response curve and phase angle-frequency curve of rigid circular foundation on sand.

Fig. 9 — Loss coefficient of a vibrating circular foundation on sand.

In figure:

$$\eta_s = \frac{\sin\phi}{\left[\dfrac{m_0 Y_0}{m_1 e_0} + \cos\phi\right]} = \frac{\sin\phi}{\left[\dfrac{W Y_0}{m_1 e_0 g} + \cos\phi\right]}$$

$\phi = \phi(\omega)$
$W = 30970$ LBS
$Y_0 = Y_0(\omega)$ [IN.]
$r_0 = 3.65$ FT.

- $F_0 = m_1 e_0 \omega^2 = 1.464\ \omega^2$ [LBS]
- $\triangle\ F_0 = m_1 e_0 \omega^2 = 1.105\ \omega^2$ [LBS]
- $\circ\ F_0 = m_1 e_0 \omega^2 = 0.736\ \omega^2$ [LBS]
- $\square\ F_0 = m_1 e_0 \omega^2 = 0.370\ \omega^2$ [LBS]

EXPERIMENTAL DATA BY Z.B. FRY [21]
OR FIG. 8

SOIL: SAND

Y-axis: η_s (0 to 2.4)
X-axis: $r_0\omega$ [FT. RAD/SEC] (0 to 500)

Fig. 10 — Loss coefficients at resonance of circular foundations on sand.

In figure:

- $\circ\ \bar{p} = 1225$ LB/FT^2, $r_0 = 2.58$ FT
- $\times\ \bar{p} = 738$ LB/FT^2, $r_0 = 3.65$ FT
- $\bullet\ \bar{p} = 612$ LB/FT^2
- $\blacktriangle\ \bar{p} = 492$ LB/FT^2, $\blacksquare\ \bar{p} = 612$ LB/FT^2 } $r_0 = 4.50$ FT
- $\triangle\ \bar{p} = 369$ LB/FT^2, $\square\ \bar{p} = 612$ LB/FT^2 } $r_0 = 5.17$ FT

DATA BY Z.B. FRY (21) OR
TABLE I, NO. I 1a ÷ I 9d

$$\eta_s = \frac{m_1 e_0}{m_0 y_{or}} = \frac{m_1 e_0 g}{\pi r_0^2 \bar{p}\, y_{or}}$$

Y-axis: η_s (0 to 1.6)
X-axis: $r_0\omega_0$ (FT. RAD/SEC) (200 to 650)

207
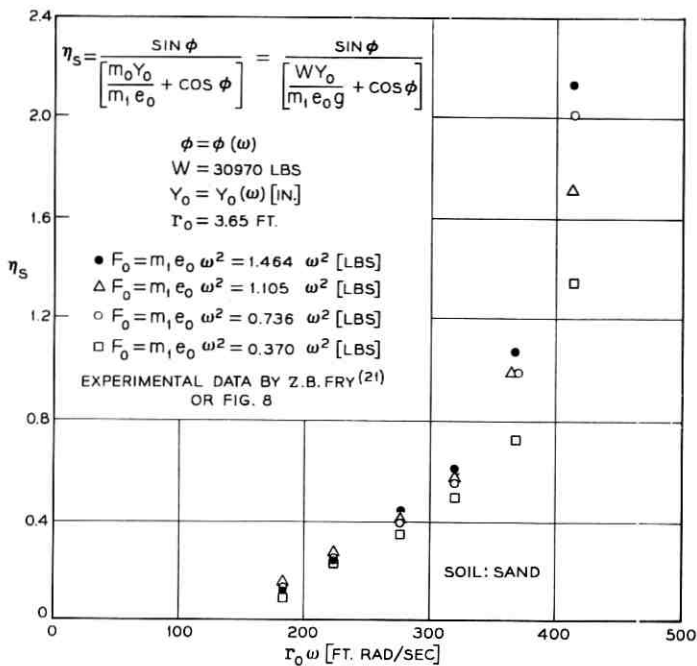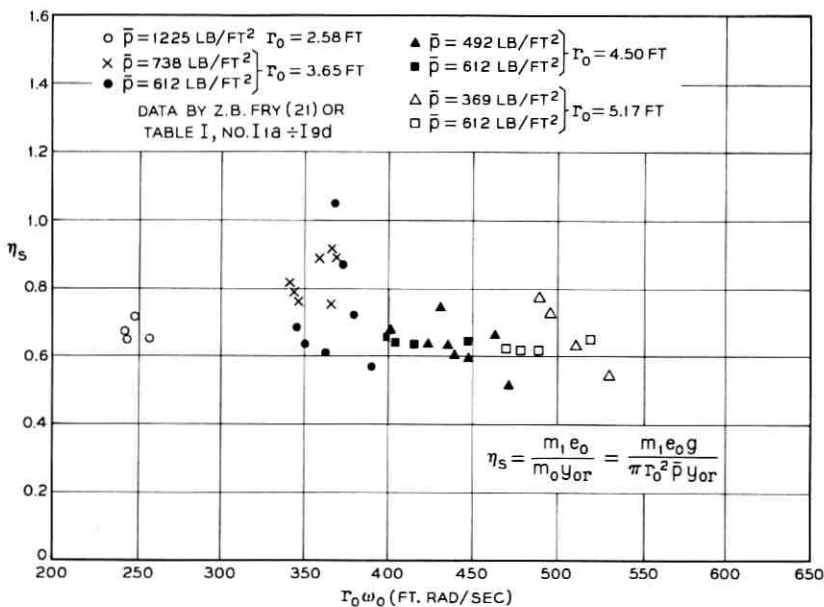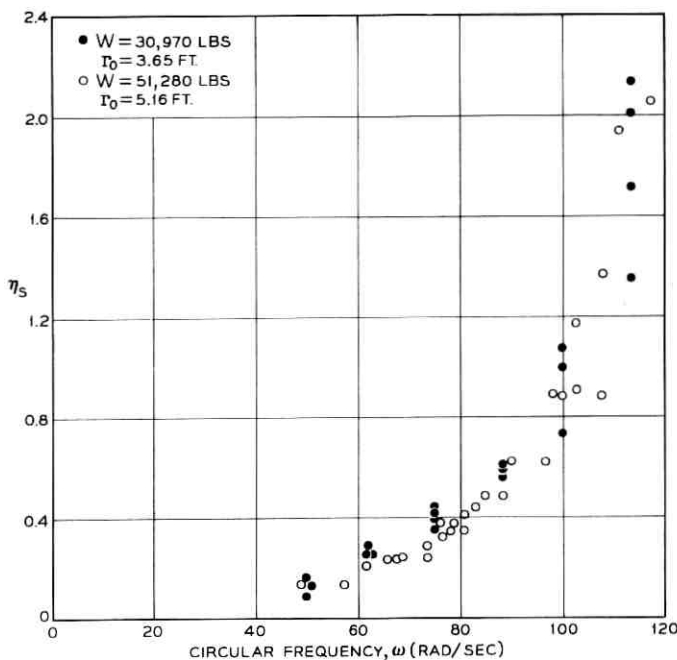
Fig. 11 — Loss coefficients of two different foundations on sand.

It may be concluded that the proposed mathematical model is capable of predicting the loss-coefficient, η_s, of a vibrating circular rigid foundation on a cohesive soil. For sand, however, this model is not applicable, and a different mechanism must be assumed in order to explain the independence of the loss coefficient from the magnitude of the radius of the foundation. The assumption of a dynamic arching effect causing the vibration of a large sand mass of a definite radius may provide an intuitive explanation.

The resonance frequency of the proposed mathematical model can be determined by means of (39). The resonance frequency depends on the coefficient of subgrade reaction, k_s, the static contact pressure, $\bar{p}$, the radius of the foundation, r_0, and the shear wave velocity, v_s. Equation (39) can frequently be replaced by (41), which neglects the inertia effects of the soil. It has been shown that these effects are relatively small for cohesive soils and foundations of small radii. The coefficient of subgrade reaction at the resonance frequency is generally slightly higher than the statically determined value. Hence, neglect of the effect

of the rate of loading in the numerator of (39) is often compensated by neglecting the inertia effects in the denominator.

The assumption, that the resonance frequency can be calculated by means of (41), is supported by the data obtained by D. D. Barkan[16] shown in Table I (B-1a to F-4). The calculated values of the resonance frequency, based on static load-deflection tests, agree well with the experimentally determined values. The error in percent is shown in Fig. 12 as a function of the radius of the foundation. The error does not exceed 20 percent. In general, the predicted values of the resonance frequency are higher than the experimentally determined ones. This was to be expected because the inertia effects of the soil are neglected in (41). Possible experimental errors may have caused the four predicted resonance frequencies shown in Fig. 12 which were lower than the experimentally determined values.

Unfortunately, to the best of the author's knowledge, only D. D. Barkan[16] determined the static coefficient of subgrade reaction in connection with vibration tests of circular foundations. However, the dynamic coefficient of subgrade reaction can be calculated by means of (45) provided the exciting force, displacement amplitude, and the phase angle are known experimentally determined functions of the frequency. The data shown in Fig. 4 were substituted in (45) and the dynamic coefficient of subgrade reaction was calculated for three different displacement amplitudes. The results are shown in Fig. 13. There is an expected scattering of the data. However, it may be concluded that the dynamic coefficient of subgrade reaction, $k_s\alpha$, decreases with an increase
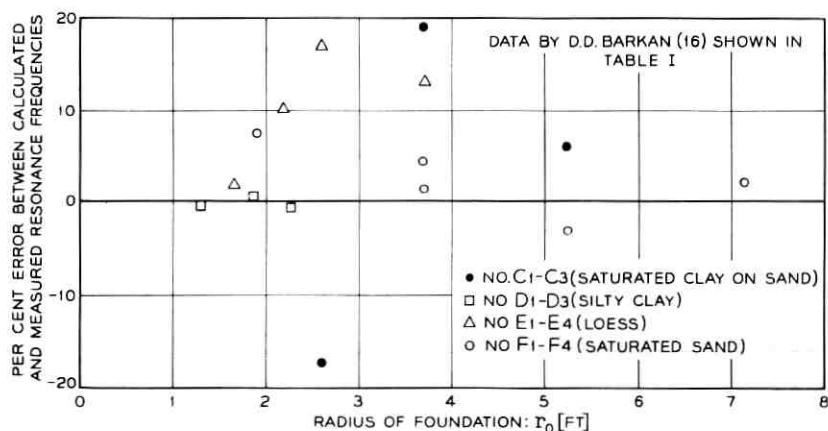
Fig. 12 — Error between calculated and measured resonance frequencies.
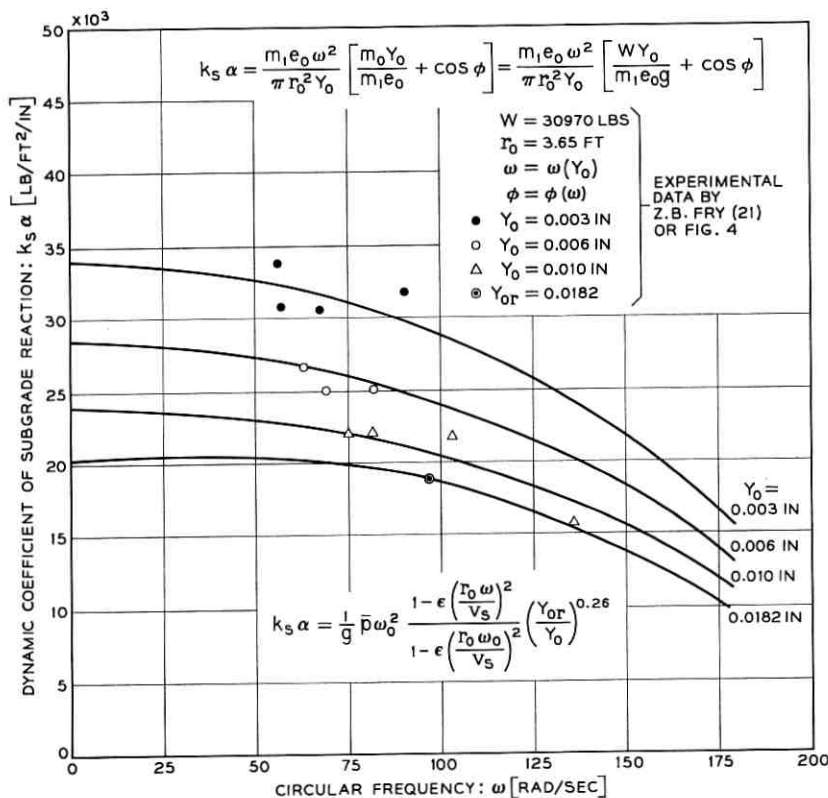
Fig. 13 — Dynamic coefficients of subgrade reaction as a function of the angular frequency for different displacement amplitudes on silty clay.

of the frequency, ω, at a constant displacement amplitude, y_0. Changes of the displacement amplitudes result, however, in significant changes of the coefficient of subgrade reaction.

Fig. 14 demonstrates the dependence of the dynamic coefficient of subgrade reaction on the displacement amplitude. The dynamic coefficient of subgrade reaction decreases with an increase of the displacement amplitude. For a constant frequency, the coefficient of subgrade reaction as a function of the displacement amplitude can be expressed with sufficient accuracy by the following empirical equation:

$$\frac{k_s}{k_s{}^*} = \left(\frac{y_0{}^*}{y_0}\right)^n \tag{48}$$

where

n = 0.26 = experimental constant,

k_s^* = coefficient of subgrade reaction at displacement amplitude y_0^*, and

y_0^* = displacement amplitude used as reference amplitude.

The maximum displacement amplitude at resonance, $y_{0r} = 0.0182$ in., is shown in Fig. 4 or in Table I, No. 5d and shall be used as reference amplitude ($y_0^* = y_{0r}$). Resonance occurred at $\omega_0^* = 95.4$ Rad. sec^{-1}. Solving (39) with respect to the coefficient of subgrade reaction, one obtains

$$k_s^* = \frac{\bar{p}^* \omega_0^{*2}}{g\left[1 - \varepsilon \left(\dfrac{r_0^* \omega_0^*}{v_s}\right)^2\right]} \tag{49}$$

provided the resonance frequency, ω_0^*, the shear wave velocity, v_s, the
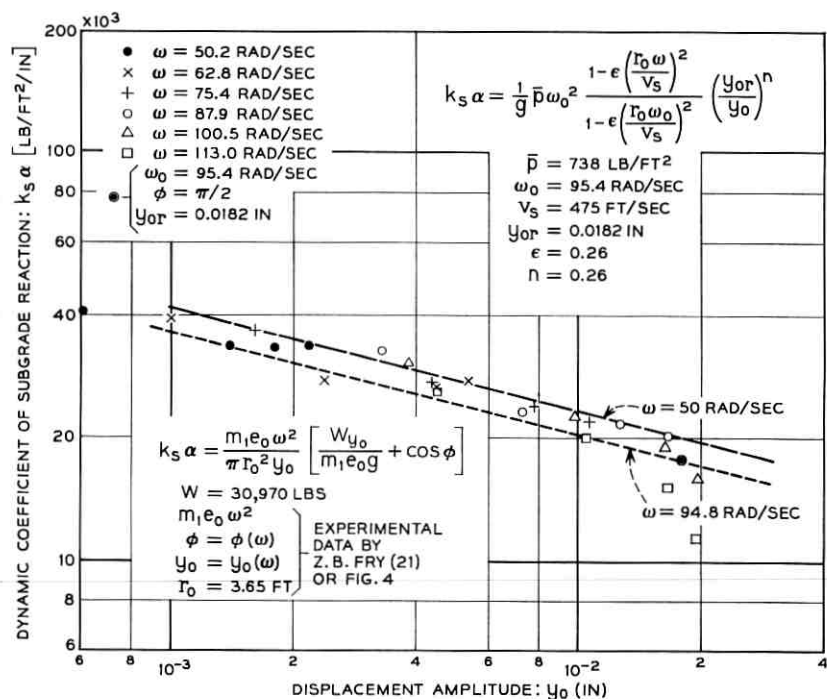
Fig. 14 — Dynamic coefficients of subgrade reaction as a function of the displacement amplitudes for different frequencies on silty clay.

average contact pressure, $\bar{p}^*$, and the radius, r_0^*, of the reference foundation are known quantities.

By means of (11), (48), and (49) the dynamic coefficient of subgrade reaction $k_s\alpha$ can be written as follows

$$k_s\alpha = \frac{\bar{p}^*\omega_0^{*2}}{g} \frac{\left[1 - \varepsilon\left(\frac{r_0^*\omega}{v_s}\right)^2\right]}{\left[1 - \varepsilon\left(\frac{r_0^*\omega_0^*}{v_s}\right)^2\right]}\left(\frac{y_0^*}{y_0}\right)^n. \tag{50}$$

Equation (50) is plotted in Fig. 13 for four values of the displacement amplitude, y_0, and in Fig. 14 for two values of the angular frequency, ω. A comparison of the data obtained by means of (45) with the plot of (50) shows that the results are compatible; however, the scattering of the experimental data prevents a direct verification of (50).

So far, the radius of the foundation, r_0, and the subsoil were assumed to remain constant. Now, however, the effect of a change of the radius and the contact pressure on the natural frequency of rigid circular foundations shall be considered. From (39) follows

$$\frac{\omega_0}{\omega_0^*} = \sqrt{\left(\frac{k_s}{k_s^*}\right)\left(\frac{\bar{p}^*}{\bar{p}}\right)\left[\frac{1 + \varepsilon\left(\frac{r_0^*}{v_s}\right)^2\frac{k_s^*g}{\bar{p}^*}}{1 + \varepsilon\left(\frac{r_0^*}{v_s}\right)^2\frac{k_s^*g}{\bar{p}^*}\left(\frac{r_0}{r_0^*}\right)^2\left(\frac{k_s}{k_s^*}\right)\left(\frac{\bar{p}^*}{\bar{p}}\right)}\right]}. \tag{51}$$

The asterisk indicates known quantities used for a reference foundation.

The coefficient of subgrade reaction is, as mentioned before, a function of the displacement amplitude, the radius of the foundation, the contact pressure, and the rate of loading. The author[17] proposed the following expression for the coefficient of subgrade reaction subjected to fluctuating loads

$$\frac{k_s}{k_s^*} = \left(\frac{y_0^*}{y_0}\right)^n\left[(1 - c^*)\left(\frac{r_0^*}{r_0}\right)^{(1-r)} + c^*\left(\frac{\bar{p}}{\bar{p}^*}\right)^p\right] \tag{52}$$

where n, r, c^*, and p are experimentally determined constants. If these constants are assumed to be zero, then (52) is proportional to (34) which is valid for the case of the elastic half-space, n indicates the amplitude dependent nonlinearity of the coefficient of subgrade reaction. An increase of the stiffness of the soil with depth is considered by the term $(r_0^*/r_0)^{(1-r)}$, and the effect of the contact pressure is indicated by $(\bar{p}/\bar{p}^*)^p$. It shall be assumed that the coefficients of subgrade reaction for fluc-

tuating loads were determined at a frequency in the range of the reso-
nance frequencies of the vibrating foundations. Hence, no provision is
made in (52) for the effect of the rate of loading. Substituting (52) in
(51) one obtains

$$
\frac{\omega_0}{\omega_0{}^*} = \left(\frac{y_{0r}{}^*}{y_{0r}}\right)^{n/2} \left(\frac{\bar{p}^*}{\bar{p}}\right)^{\frac{1}{2}} \left(\frac{r_0{}^*}{r_0}\right)^{\frac{1}{2}(1-r)} \left[1 - c^* + c^* \left(\frac{\bar{p}}{\bar{p}^*}\right)^p \left(\frac{r_0}{r_0{}^*}\right)^{(1-r)} \right]^{\frac{1}{2}}
$$

$$
\times \left[\frac{1 + \varepsilon \left(\frac{r_0{}^*}{v_s}\right)^2 \frac{k_s{}^* g}{\bar{p}^*}}{1 + \varepsilon \left(\frac{r_0{}^*}{v_s}\right)^2 \frac{k_s{}^* g}{\bar{p}^*} \left(\frac{y_{0r}{}^*}{y_{0r}}\right)^n \left(\frac{r_0}{r_0{}^*}\right)^{1+r} \left(\frac{\bar{p}^*}{\bar{p}}\right)} \cdot \left[1 - c^* + c^* \left(\frac{\bar{p}}{\bar{p}^*}\right)\left(\frac{r_0}{r_0{}^*}\right)^{(1-r)}\right] \right]^{\frac{1}{2}}. \quad (53)
$$

Fig. 15 shows the angular resonance frequencies of the rigid circular
foundations reported by Z. B. Fry[21] for silty clay as a function of the
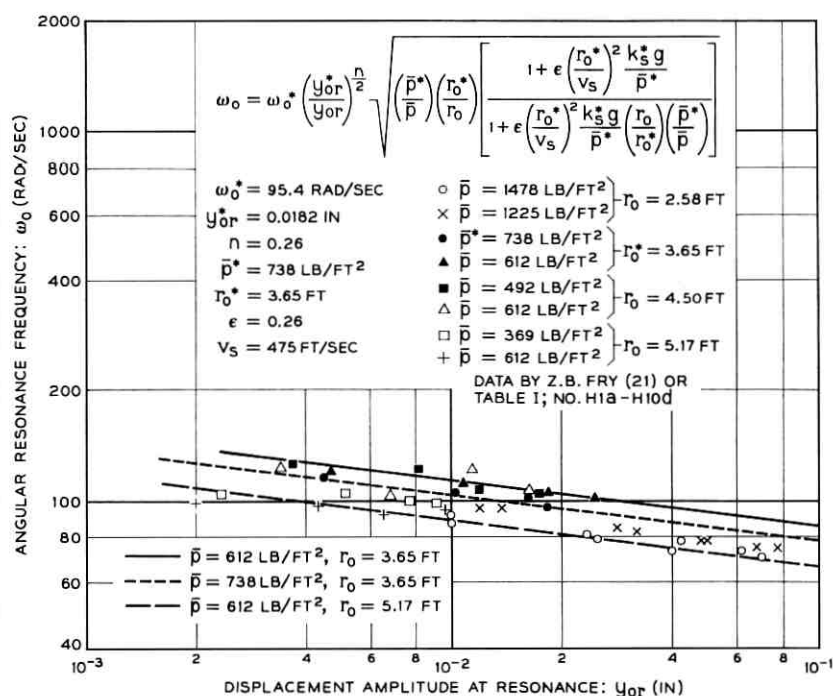
Fig. 15 — Resonance frequencies of rigid circular foundations on silty clay.

displacement amplitude at resonance. These data are listed in Table I, No. H-1a to H-10d. Z. B. Fry[21] reports furthermore, that the shear modulus determined by seismic methods does not change significantly with depth below the surface for this silty clay. Hence, it may be assumed that the constant, r, in (52) and (53) becomes approximately zero. Furthermore, it can be assumed that the effect of the static contact pressure can be neglected, since the overburden does not increase the shear modulus significantly. Hence, c^* is assumed to be small compared to unity. With these assumptions, (53) simplifies to

$$\frac{\omega_0}{\omega_0^*} = \left(\frac{y_{0r}^*}{y_{0r}}\right)^{n/2} \left(\frac{\bar{p}^*}{\bar{p}}\right)^{\frac{1}{2}} \left(\frac{r_0^*}{r_0}\right)^{\frac{1}{2}}$$

$$\cdot \left[\frac{1 + \varepsilon \left(\frac{r_0^*}{v_s}\right)^2 \frac{k_s^* g}{\bar{p}^*}}{1 + \varepsilon \left(\frac{r_0^*}{v_s}\right)^2 \frac{k_s^* g}{\bar{p}^*} \left(\frac{r_c}{r_0^*}\right) \left(\frac{\bar{p}^*}{\bar{p}}\right) \left(\frac{y_{0r}^*}{y_{0r}}\right)^n}\right]^{\frac{1}{2}} \quad (54)$$

where
ω_0^* = 95.4 Rad/sec = angular resonance frequency of reference foundation for maximum exciting force listed in Table I, No. H-5d,

y_{0r}^* = 0.0182 in. = amplitude at resonance of reference foundation,

r_0^* = 3.65 ft = radius of reference foundation,

$\bar{p}^*$ = 738 lb/ft^2 = average static contact pressure of reference foundation,

ε = 0.26,

g = 386 in./sec^2 = acceleration of gravity,

v_s = 475 ft/sec = shear wave velocity,

n = 0.26 = experimental constant determined from Fig. 14, and

k_s^* = coefficient of subgrade reaction for reference foundation calculated by (49).

For the contact pressure $\bar{p} = \bar{p}^* = 738$ lbs/ft^2 and the radius $r_0 = r_0^* = 3.65$ ft, the angular resonance frequency of the reference foundation is obtained and shown in Fig. 15 as a function of the displacement amplitude at resonance, y_{0r}. This curve fits the corresponding experimental data very well, which was to be expected from the results shown in Fig. 14. For a contact pressure $\bar{p} = 612$ lbs/ft^2 and a radius $r_0 = 3.65$ ft the maximum values of the angular resonance frequencies of the here considered foundations are obtained. For $\bar{p} = 612$ lbs/ft^2 and $r_0 =$

5.17 ft follow the minimum values. They are also shown in Fig. 15 as functions of the displacement amplitude at resonance. The experimental data and the curves computed by means of (54) show good agreement. It should be realized that the changes of the radii and the contact pressures were relatively small and their effects on the resonance frequency appear to be in the same order of magnitude as the possible experimental errors of measuring the resonance frequency. However, the dependence of the resonance frequency on the displacement amplitude is clearly demonstrated.

The resonance frequencies obtained by M. Novák on a loess loam are listed in Table I, No. A-1a to A-10c. They are shown in Fig. 16 as a function of the displacement amplitude at resonance. Again it is apparent, that the resonance frequency decreases with an increase of the displacement amplitude; however, not as rapidly as in Fig. 15. Unfortunately, no detailed description of the soil properties is available; however, it has been shown in Fig. 7 that an assumed shear wave velocity $v_s = 800$ ft/sec allowed the prediction of the loss coefficient with good accuracy. Hence, the term $\varepsilon (r_0/v_s)^2$ becomes small compared to

The plotted formula reads:

$$\omega_0 = \omega_0^* \left(\frac{y_{or}^*}{y_{or}}\right)^{\frac{n}{2}} \left(\frac{\bar{p}^*}{\bar{p}}\right)^{\frac{1}{2}(1-p)}$$

$\omega_0^* = 113$ RAD/SEC
$y_{or}^* = 0.0248$ IN
$\bar{p}^* = 978$ LB/FT^2
$n = 0.18$
$p = 0.38$

○ $\bar{p} = 987$ LB/FT^2	$r_0 = 1.31$ FT
× $\bar{p} = 692$ LB/FT^2	
● $\bar{p} = 625$ LB/FT^2	$r_0 = 1.60$ FT
▲ $\bar{p} = 445$ LB/FT^2	
■ $\bar{p} = 346$ LB/FT^2	$r_0 = 1.85$ FT
△ $\bar{p} = 248$ LB/FT^2	
□ $\bar{p} = 514$ LB/FT^2	
+ $\bar{p} = 379$ LB/FT^2	$r_0 = 2.27$ FT
▽ $\bar{p} = 262$ LB/FT^2	

DATA BY M. NOVAK (5)
OR TABLE I, NO. A1a – A10C

$\bar{p} = \bar{p}^* = 987$ LB/FT^2
$\bar{p} = 514$ LB/FT^2
$\bar{p} = 248$ LB/FT^2

ANGULAR RESONANCE FREQUENCY: ω_0 (RAD/SEC)

DISPLACEMENT AMPLITUDE AT RESONANCE: y_{or} (IN)

Fig. 16 — Resonance frequencies of rigid circular foundations on loess loam.

one and can be neglected in (53). Equation (53) can then be written

$$\frac{\omega_0}{\omega_0^*} = \left(\frac{y_{0r}^*}{y_{0r}}\right)^{n/2} \left(\frac{\bar{p}^*}{\bar{p}}\right)^{\frac{1}{2}} \left[(1 - c^*)\left(\frac{r_0^*}{r_0}\right)^{(1-r)} + c^*\left(\frac{\bar{p}}{\bar{p}^*}\right)^p\right]^{\frac{1}{2}}. \quad (55)$$

For each set of data shown in Fig. 16 follows $n = 0.18$. Assuming $c^* \approx 1$ and $p = 0.38$, (55) becomes

$$\frac{\omega_0}{\omega_0^*} = \left(\frac{y_{0r}^*}{y_{0r}}\right)^{n/2} \left(\frac{\bar{p}^*}{\bar{p}}\right)^{\frac{1}{2}(1-p)} = \left(\frac{y_{0r}^*}{y_{0r}}\right)^{0.09} \left(\frac{\bar{p}^*}{\bar{p}}\right)^{0.31}. \quad (56)$$

Equation (56) shows the effect of a change of the displacement amplitude and of the contact pressure on the resonance frequency for the data shown in Fig. 15. The agreement between the resonance frequencies calculated by use of (56) and the experimental data is excellent.

The assumption of $c^* \approx 1$ in (56) results in a resonance frequency which is not affected by a change of the radius of the foundation. Since this is possible only if the overburden increases the stiffness of the soil, the stiffness of the soil must also be affected by the magnitude of the contact pressure $\bar{p}$. Hence, an experimental constant $p = 0.38$, which indicates the effect of the contact pressure on the stiffness of the soil, is reasonable.

The effect of a change of the radius of the foundation on the resonance frequency shall now be discussed. The resonance frequencies of the foundations described by (54) decrease with an increase of the radius. The decrease of the resonance frequency is approximately proportional to the square root of the radius. A similar relationship between the resonance frequency and the radius of the foundation was established by G. P. Tschebotarioff[24] who evaluated the performance records of a limited number of existing engine foundations. However, foundations, which are described by (56), are independent of the radius. H. Lorenz[23] reported an increase of the resonance frequency due to an increase of the radius. This apparent contradiction is readily explained by the proven nonlinearity of the coefficient of subgrade reaction. The exciting force in all test results here reported was produced by eccentrically rotating weights. Therefore, the ratio of the displacement amplitudes at resonance becomes, by means of (43),

$$\frac{y_{0r}^*}{y_{0r}} = \left(\frac{m_1^* e_0^*}{m_1 e_0}\right)\left(\frac{\omega_0^*}{\omega_0}\right)^2 \left(\frac{k_s}{k_s^*}\right)\left(\frac{r_0}{r_0^*}\right)^2$$

$$\cdot \left[\frac{\eta + b_1 \dfrac{r_0^* \omega_0^*}{v_s}\left(\dfrac{r_0}{r_0^*}\right)\left(\dfrac{\omega_0}{\omega_0^*}\right)}{\eta + b_1 \dfrac{r_0^* \omega_0^*}{v_s}}\right]. \quad (57)$$

Substituting (57) in (52) and solving for the ratio of the displacement amplitudes at resonance and substituting this ratio in (53) the following expression for the resonance frequency is obtained:

$$\frac{\omega_0}{\omega_0^*} = \left(\frac{m_1^* e_0^*}{m_1 e_0}\right)^{n/2} \left(\frac{r_0^*}{r_0}\right)^{\frac{1}{2}(1-r-2n)} \left(\frac{\bar{p}^*}{\bar{p}}\right)^{\frac{1}{2}(1-n)}$$

$$\cdot \left[1 - c^* + c^* \left(\frac{r_0}{r_0^*}\right)^{(1-r)} \left(\frac{\bar{p}}{\bar{p}^*}\right)^p\right]^{\frac{1}{2}} c_1^{n/2} c_2^{\frac{1}{2}(1-n)} \tag{58}$$

where

$$c_1 = \frac{\eta + b_1 \frac{r_0^* \omega_0^*}{v_s} \left(\frac{y_{0r}^*}{y_{0r}}\right)^{n/2} \left(\frac{r_0}{r_0^*}\right)^{\frac{1}{2}(1+r)} \left(\frac{\bar{p}^*}{\bar{p}}\right)^{\frac{1}{2}} c_2^{\frac{1}{2}} \cdot \left[1 - c^* + c^* \left(\frac{r_0}{r_0^*}\right)^{(1-r)} \left(\frac{\bar{p}}{\bar{p}^*}\right)^p\right]^{\frac{1}{2}}}{\eta + b_1 \frac{r_0^* \omega_0^*}{v_s}}$$

$$c_2 = \frac{1 + \varepsilon \left(\frac{r_0^*}{v_s}\right)^2 \frac{k_s^* g}{\bar{p}^*}}{1 + \varepsilon \left(\frac{r_0^*}{v_s}\right)^2 \frac{k_s^* g}{\bar{p}^*} \left(\frac{y_{0r}^*}{y_{0r}}\right)^n \left(\frac{r_0}{r_0^*}\right)^{1+r} \left(\frac{\bar{p}^*}{\bar{p}}\right) \cdot \left[1 - c^* + c^* \left(\frac{r_0}{r_0^*}\right)^{(1-r)} \left(\frac{\bar{p}}{\bar{p}^*}\right)^p\right]} .$$

Since $n \ll 1$, $(y_{0r}^*/y_{0r})^n$, and $c_1^{n/2}$ are approximately equal to one. For $c^* = 0$, (58) becomes

$$\frac{\omega_0}{\omega_0^*} = \left(\frac{m_1^* e_0^*}{m_1 e_0}\right)^{n/2} \left(\frac{r_0^*}{r_0}\right)^{\frac{1}{2}(1-r-2n)} \left(\frac{\bar{p}^*}{\bar{p}}\right)^{\frac{1}{2}(1-n)}$$

$$\cdot \left[\frac{1 + \varepsilon \left(\frac{r_0^*}{v_s}\right) \frac{k_s^* g}{\bar{p}^*}}{1 + \varepsilon \left(\frac{r_0^*}{v_s}\right)^2 \frac{k_s^* g}{\bar{p}^*} \left(\frac{r_0}{r_0^*}\right)^{(1+r)} \left(\frac{\bar{p}^*}{\bar{p}}\right)}\right]^{-\frac{1}{2}(1-n)} \tag{59}$$

For $c^* = 1$, it follows

$$\frac{\omega_0}{\omega_0^*} = \left(\frac{m_1^* e_0^*}{m_1 e_0}\right)^{n/2} \left(\frac{r_0}{r_0^*}\right)^n \left(\frac{\bar{p}^*}{\bar{p}}\right)^{\frac{1}{2}(1-n-p)}$$

$$\cdot \left[\frac{1 + \varepsilon \left(\frac{r_0^*}{v_s}\right)^2 \frac{k_s^* g}{\bar{p}^*}}{1 + \varepsilon \left(\frac{r_0^*}{v_s}\right) \frac{k_s^* g}{\bar{p}^*} \left(\frac{r_0}{r_0^*}\right)^2 \left(\frac{\bar{p}^*}{\bar{p}}\right)^{(1-p)}}\right]^{-\frac{1}{2}(1-n)} \tag{60}$$

The resonance frequencies of vibrating foundations which are expressed in terms of (59) are affected by the nonlinearity of the coefficient of subgrade reaction. For relatively small foundation radii and relatively large nonlinearities expressed by the experimental constant, n, an increase of the radius may result in an increase of the resonance frequency. For large foundation radii and small nonlinearities, however, the frequency should decrease for an increase of the radius. Resonance frequencies expressed in terms of (60) should show an increase of the resonance frequency with an increase of the radius.

Equations (59) and (60) show also the effect of the contact pressure, $\bar{p}$, on the resonance frequency. Generally, the resonance frequency decreases for an increase of the contact pressure, however, at a rate less than expected from purely elastic considerations. The nonlinearities expressed by the experimental constant, n, in (59) and (60) reduces the effect of the contact pressure which is proportional to the mass of the foundation. The stiffening effect of the contact pressure is expressed by the experimental constant, p. The value of $p = 0.38$ was used to express the data shown in Fig. 16. In the plate bearing tests conducted by the author and S. R. White[18], a value of $p = 1.859$ was obtained. For such a soil, an increase of the resonance frequency with an increase of the static contact pressure should be expected. In other words, the increase of the mass of the vibrating system is more than compensated by the resulting increase of the stiffness.

It may be stated, that the proposed mathematical model is not only not contradicted by the available experimental data obtained on silty clay and loess loam, but that there is a satisfactory amount of evidence supporting this theory.

Equation (45) was also used to calculate the dynamic coefficient of subgrade reaction for sand. The amplitude-frequency response curve and the phase angle-frequency curve shown in Fig. 8 were used for the calculation. The dynamic coefficient of subgrade reaction, $k_s\alpha$, divided by the contact pressure, $\bar{p}$, and multiplied by the acceleration of gravity is shown in Fig. 17 as a function of the frequency. The data show a strong dependence on the frequency. The dynamic coefficient of subgrade reaction decreases rapidly if the frequency is increased. This phenomenon was to be expected, because the loss coefficient increased rapidly with an increase of the frequency as shown in Figs. 9 and 11. However, the shape of the dynamic coefficient of subgrade reaction-frequency curve does not agree with the shape of the function α shown in Fig. 2. Hence, the proposed mathematical model of the vibrating rigid circular foundation is not applicable to foundation-sand systems. The dynamic coefficient

of subgrade reaction was also determined for two additional foundations. The amplitude-frequency response curves and the phase angle-frequency curves of these foundations were also provided by Z. B. Fry[21] of the U.S. Waterways Experiment Station. The dynamic coefficients of subgrade reaction divided by the contact pressure and multiplied by the acceleration of gravity for these additional foundations are also shown in Fig. 17. There appears to be a difference of the dynamic coefficient of subgrade reaction divided by the contact pressure for low frequencies. For higher frequencies, however, the data are practically identical. This implies a coefficient of subgrade reaction proportional to the contact pressure and independent of the radius of the foundation. The intersection of the ω^2-curve with the data indicates the resonance frequency. For the three sets of data shown in Fig. 17, the resonance frequency appears to be constant. In order to verify this assumption, all the resonance frequencies reported by Z. B. Fry[21] are shown in Fig. 18 as a func-

$$\frac{C_s}{m_0}\alpha = \frac{k_s g}{\bar{p}}\alpha = \frac{m_1 e_0}{m_0 y_0}\omega^2\left[\frac{m_0 y_0}{m_1 e_0} + \cos\phi\right] = \frac{m_1 e_0 g}{W y_0}\left[\frac{W y_0}{m_1 e_0 g} + \cos\phi\right]$$

- $W = 30{,}970$ LBS
  $r_0 = 3.65$ FT $\phi = \phi(\omega)$
- $W = 51{,}280$ LBS $y_0 = y_0(\omega)$
  $r_0 = 5.16$ FT
                          TAKEN FROM DATA
- $W = 25{,}640$ LBS   BY Z.B. FRY (21)
 $r_0 = 2.58$ FT
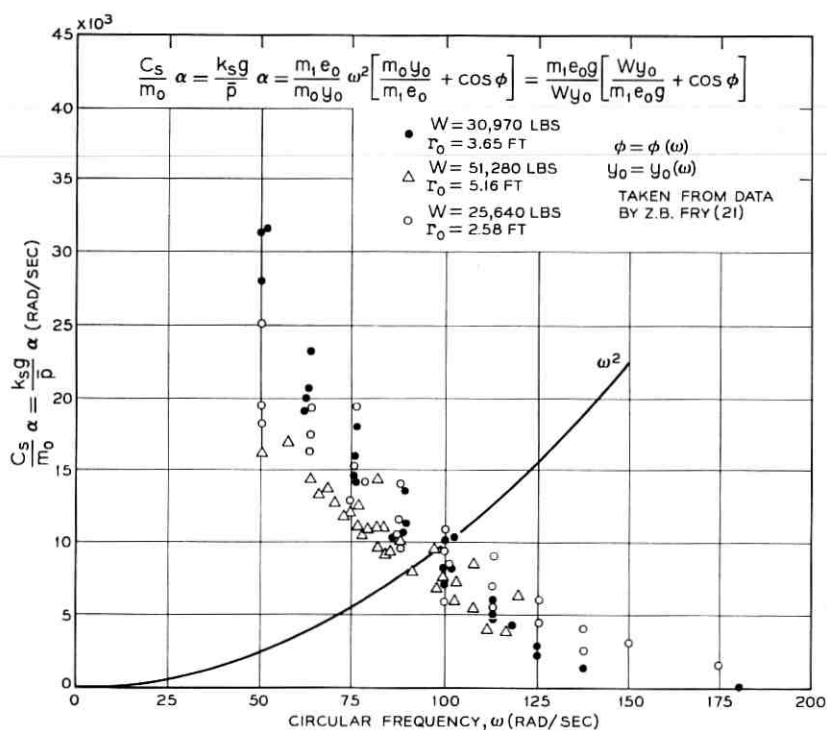
Fig. 17 — Dynamic coefficients of subgrade reaction as a function of the frequency on sand for three different foundations.
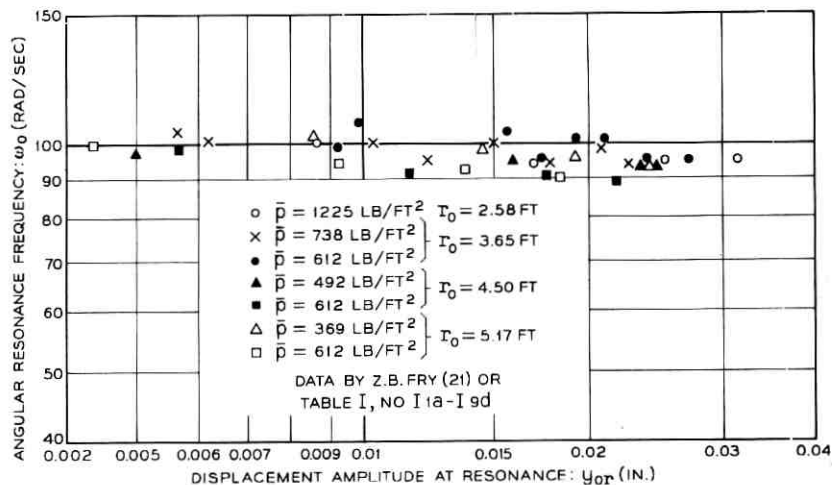
Fig. 18 — Resonance frequencies of rigid circular foundations on sand.

tion of the displacement amplitudes. For all practical purposes, the resonance frequencies for these circular foundations on sand are constant, independent of displacement amplitude, radius, and contact pressure. The data by F. J. Converse[22] listed in Table I, No. J-1a to J-7s, show a dependence on the applied force amplitude but appear to be relatively independent of the contact pressure and the radius. A mechanism describing the vibrations of circular foundations on sand must be different from the here proposed mathematical model. Arching of sand has probably a significant effect on the vibrations of foundation-sand systems. For engineering purposes, it appears to be sufficient to determine the resonance frequency and the loss coefficient with a small vibrator and to assume an identical resonance frequency and loss coefficient of the planned foundation. The suggestion by G. P. Tschebotarioff[25] of providing cavities near the four corners of machine foundation blocks which could be filled, or emptied, to change the weight of the block by 15 to 20 percent would have no or only an insignificant effect on the resonance frequency and the loss coefficient of foundations on sand.

The effective mass of a vibrating rigid circular plate on an elastic isotropic homogeneous half-space is determined by (15). The mass of the half-space vibrating in phase with the plate becomes

$$m_s = \varepsilon C_s \left(\frac{r_0}{v_s}\right)^2 \qquad (61)$$

where

m_s = mass of half-space vibrating in phase with plate.

The ratio of the soil mass to the mass of the plate becomes, by means of (61), (33), and (35),

$$\frac{m_s}{m_0} = \varepsilon \frac{k_s g}{\bar{p}} \left(\frac{r_0}{v_s}\right)^2. \tag{62}$$

Substitution of (49) in (62) gives

$$\frac{m_s}{m_0} = \frac{\varepsilon \left(\dfrac{r_0 \omega_0}{v_s}\right)^2}{1 - \varepsilon \left(\dfrac{r_0 \omega_0}{v_s}\right)^2}. \tag{63}$$

The validity of (63) is limited to values of $r_0\omega_0/v_s \leqq 1.5$. For this value, the ratio of the participating soil mass to the mass of the vibrating plate becomes 1.41. For most vibrating foundations listed in Table I, this ratio becomes considerably smaller and the participating soil mass, m_s, becomes insignificantly small for small foundations. This conclusion is apparently contradicted by the theoretical and experimental investigations of W. Heukelom.[13,14] However, it is readily shown, that the amplitude dependent nonlinearity of the soil, which he recognized but neglected, can account for this apparent contradiction. The dynamic stiffness can be calculated by means of (20) from experimentally determined displacement amplitudes and phase angles. The vibration data obtained by Z. B. Fry[21] shall be used again to calculate the dynamic stiffness. The displacement amplitude-frequency curve as well as some values of the dynamic stiffness, calculated by means of (20), are shown in Fig. 19. No provision was made to account for the nonlinearity of the load-deflection characteristic of the soil. W. Heukelom[13,14] fitted to such experimental data the following function:

$$S = S \big|_{\omega=0} - m_s \omega^2 \qquad \text{for} \quad \omega \leqq \omega_0$$

$$= S \big|_{\omega=0} - m_s \left(\frac{\omega_0}{\omega}\right)^3 \omega^2 \qquad \text{for} \quad \omega_0 \leqq \omega.$$

The constants $S \big|_{\omega=0}$ and m_s, representing the static stiffness and the participating soil mass, can be selected to fit the experimental data very well indeed. This equation would indicate a constant participating soil mass, m_s, for frequencies below the resonance frequency and a participating soil mass, $m_s (\omega_0/\omega)^3$, decreasing with an increase of the frequency for frequencies greater than the resonance frequency. The magnitude of
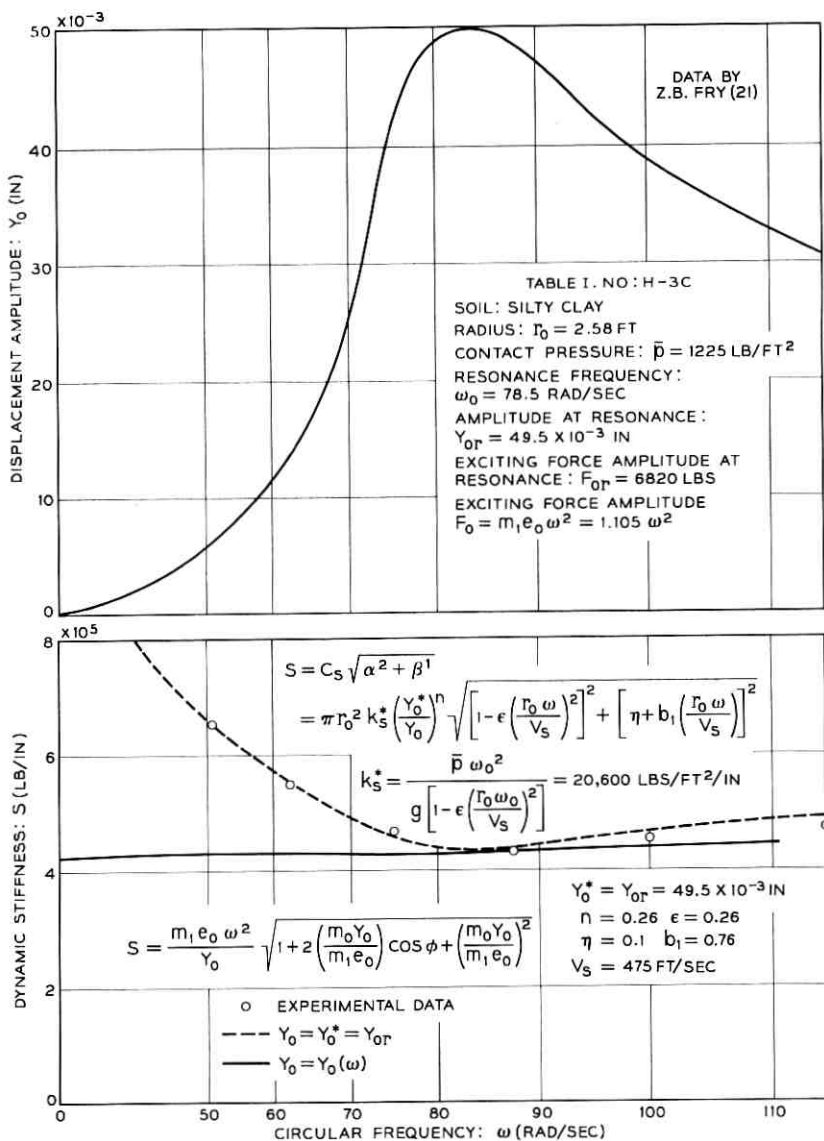
Fig. 19 — Effect of the displacement amplitude on the dynamic stiffness.

the participating soil mass becomes considerably larger than that obtained by (63).

The dynamic stiffness of the proposed mathematical model is obtained by substitution of (33), (28), and (11) in (21)

$$S = \pi r_0^2 k_s \sqrt{\left[1 - \varepsilon \left(\frac{r_0 \omega}{v_s} \right)^2 \right]^2 + \left[\eta + b_1 \left(\frac{r_0 \omega}{v_s} \right) \right]^2} \qquad (64)$$

and by substitution of (48) as

$$S = \pi r_0^2 k_s^* \left(\frac{y_0^*}{y_0} \right)^n \sqrt{\left[1 - \varepsilon \left(\frac{r_0 \omega}{v_s} \right)^2 \right]^2 + \left[\eta + b_1 \left(\frac{r_0 \omega}{v_s} \right) \right]^2}. \qquad (65)$$

where k_s^* is determined from (49). For the resonance frequency, $\pi r_0^2 k_s$ becomes 420,000 lbs/in. The displacement amplitude at resonance $y_{0r} = y_0^* = 0.0495$ in. and the experimental constant $n = 0.26$ are used for the calculations. The solid line in Fig. 19 indicates the dynamic stiffness for a constant displacement amplitude $y_0 = y_0^* = y_{0r}$. As is to be expected, this curve fits the data only at the resonance frequency. The dotted line, however, shows the corrections made to account for the amplitude dependence of the dynamic stiffness expressed by $(y_0^*/y_0)^n$. The displacement amplitude, y_0, at each frequency is taken from the displacement amplitude-frequency curve also shown in Fig. 19. The dotted curve fits the experimental data very well. It should be noted here that this curve was rationally developed and not obtained by direct fitting of data. It may be concluded that the reduction of the dynamic stiffness close to resonance is caused by the amplitude dependent non-linearity of the load deflection characteristic of the soil-foundation system and not by a frequency dependent mass or a frequency dependent coefficient of subgrade reaction. Even a small nonlinearity will cause a significant change of the dynamic stiffness close to resonance due to the large amplitude changes occurring in this frequency range. Again, the proposed mathematical model is applicable only for cohesive soils and no attempt was made to calculate the dynamic stiffness of sand-foundation systems.

XI. SUMMARY AND CONCLUSIONS

The displacement amplitudes and the phase angles of vertically vibrating rigid circular foundations on soil have been expressed in terms of the average static contact pressure between the foundation and the subsoil, the coefficient of subgrade reaction for fluctuating loads, the magnitude and frequency of the exciting force, the radius of the founda-

tion, the loss coefficient of the soil, the shear wave velocity, and two theoretically derived constants accounting for the inertia effects of the soil. The nonlinear stress-deflection characteristic of the coefficient of subgrade reaction as well as the dependence of the coefficient of subgrade reaction on the radius of the foundation and the average contact pressure between the foundation and the subsoil have been considered. The derived mathematical model describes, as a limiting idealized case, the vibrations of rigid circular plates on an elastic isotropic homogeneous solid. Furthermore, it is capable of expressing the static load-deflection characteristics of rigid circular foundation on soil and, as a limiting case, on an elastic half-space.

Based on this mathematical model, the following behavior of a vibrating soil-foundation system should be expected:

   (i) An increase of the exciting force amplitude results in a decrease of the resonance frequency of the vibrating foundation. This effect is caused by the nonlinearity of the coefficient of subgrade reaction.

  (ii) An increase of the radius of the foundation when maintaining a constant contact pressure and exciting force can result in either an increase or a decrease of the resonance frequency of the vibrating soil-foundation system. For large foundations an increase of the radius will generally result in a decrease of the resonance frequency. For smaller foundations the nonlinearity of the coefficient of subgrade reaction and the increase of the stiffness of the soil with depth may cause an increase of the resonance frequency for an increase of the radius of the foundation. For small nonlinearities of the coefficient of subgrade reaction and small increases of the stiffness of the soil with depth, an increase of the radius of the foundation will cause a decrease of the resonance frequency.

 (iii) An increase of the contact pressure will generally lower the resonance frequency, however, less than would be expected from purely elastic considerations. The nonlinearity of the coefficient of subgrade reaction and the increase of the coefficient of subgrade reaction with an increase of the applied static contact pressure explain this phenomenon. For some soils an increase of the contact pressure could possibly result in an increase of the resonance frequency if the coefficient of subgrade reaction increases very rapidly with an increase of the static contact pressure.

  (iv) The loss coefficient, expressing the damping of the vibrating

system, increases with an increase of the radius of the foundation. The inertia effects of the soil or of an elastic half-space account for this behavior.

(v) The displacement amplitudes increase less than proportional to the amplitudes of the exciting force. Again, the nonlinearity of the coefficient of subgrade reaction explains this phenomenon.

The predicted behavior of a vibrating soil-foundation system is well supported by the available experimental evidence. An evaluation of experimentally determined amplitude-frequency response curves and phase angle-frequency curves support, furthermore, the validity of the proposed mathematical model for cohesive soils. It is shown, that the soil mass vibrating in-phase with the foundation is considerably smaller than was previously expected. It should be noted, however, that this mathematical model is not applicable to foundations on sand. For this case, the resonance frequency and the loss coefficient, remain practically constant, independent of changes of the radius of the foundation or the contact pressure.

APPENDIX

Notation

The following letter symbols have been adopted for use in this paper:

C_s = static spring constant of rigid circular plate on elastic half-space or load-displacement relation of circular foundation on soil.

C_0 = experimentally determined constant used to express the non-linearity of load-displacement relation of circular foundations on soil.

D_s = dissipated energy per cycle.

$F = F_0 e^{i(\omega t + \Phi)}$ = harmonic exciting force acting on plate or foundation.

F_0 = amplitude of exciting force acting on plate or foundation.

$F_s = f(y)$ = nonlinear force-displacement function.

$\bar{F} = \bar{F}_0 e^{i(\omega t + \Psi)}$ = force acting between plate or foundation and half-space or subsoil.

$\bar{F}_0$ = force amplitude acting between plate or foundation and half-space or subsoil.

G = shear modulus of elastic half-space.

G_s = dynamic shear modulus of half-space.

$S = \bar{F}_0/y_0$ = dynamic stiffness.

U = stored energy.

U_s = energy required for the deformation of the half-space.

$a_0 = r_0\omega \sqrt{\rho/G_s}$ = frequency factor.

$a_{0r} = r_0\omega_0 \sqrt{\rho/G_s}$ = frequency factor at resonance.

$\bar{a}_0 = (r_0/v_s) \sqrt{C_s/m_0} = (r_0/v_s) \sqrt{k_s g/\bar{p}}$.

b = damping constant of linear vibrating system.

$b_1 = 0.76$ = constant used to approximate function β.

$b_0 = m_0/\rho r_0^3$ = mass ratio.

C^* = experimental constant used to express the coefficient of subgrade reaction.

e = base of natural logarithms.

e_0 = eccentricity of rotating masses of vibrator.

f_1 = function of the frequency factor and Poisson's ratio.

$f_{10} = \lim_{a_0 \to 0} f_1$

f_2 = function of the frequency factor and Poisson's ratio.

g = acceleration of gravity.

$i = \sqrt{-1}$.

k_s = coefficient of subgrade reaction.

m_1 = eccentric mass of vibrator.

m_0 = mass of circular plate or foundation.

$\bar{m} = m_0 + m_s$ = effective vibrating mass.

m_s = participating soil mass.

n = experimental constant used to express the nonlinear load-displacement relation of circular foundations on soil.

$\bar{p}$ = average static contact pressure between foundation and subsoil.

p = experimental constant used to express the increase of the coefficient of subgrade reaction with an increase of the static contact pressure.

r_0 = radius of rigid circular plate or foundation.

r = experimental constant used to express the increase of the stiffness of soil with depth below ground level.

t = time.

v_s = shear wave velocity of soil.

v_c = compression wave velocity of soil.

y = displacement of plate or foundation.

y_0 = displacement amplitude of plate or foundation.

$\ddot{y}$ = acceleration of plate or foundation.

y_{0s} = displacement of foundation due to static load.

y_{0r} = displacement amplitude of plate or foundation at resonance.

Φ = phase angle between exciting force and displacement of plate or foundation.

Ψ = phase angle between force acting between the plate and the halfspace and the resulting displacement.

Ψ_0 = specific damping capacity of soil.

$\alpha = f_1 f_{10} / (f_1^2 + f_2^2)$ = function expressing the inertia effect of the half-space on the restoring force.

$\alpha_0 = \alpha(a_{0r})$.

$\beta = f_2 f_{10} / (f_1^2 + f_2^2)$ = function expressing energy losses due to wave propagation.

γ = density of half-space or soil.

ε = constant used to approximate function α.

η = loss coefficient of soil.

$\eta_s = D_s / 2\pi U_s$ = loss coefficient of vibrating plate or foundation.

ν = Poisson's ratio of half-space or soil.

ρ = mass density of half-space or soil.

ω = angular or circular frequency of vibrating system.

ω_0 = angular resonance frequency.

* The asterisk is used as a superscript to designate fixed known or experimentally determined quantities.

REFERENCES

1. Reissner, E., Stationäre, axial symmetrische, durch eine schüttelnde Masse erregte Schwingungen eines homogenen elastischen Halbraumes, Ing. Archiv., 7, 1963, pp. 381-396.
2. Sechter, O. J., Sbornik Trudov, Vibracii Sooruzenij i Fundamentov, No. 12, Strojevojenmorizdat, Moskva, 1948, pp. 72-83.
3. Sung, T. Y., Vibrations in Semi-infinite Solids due to Periodic Surface Loading, Symposium on Dynamic Testing of Soils, ASTM Special Technical Publication No. 156, 1953, pp. 35-63.
4. Bycroft, G. N., Forced Vibrations of a Rigid Circular Plate on a Semi-infinite Elastic Space and on an Elastic Stratum, Phil. Trans. of the Royal Soc. of London, Series A, 248, Math. and Phy. Sci., 1956, pp. 327-368.
5. Novák, M., Über die Nichtlinearität der Verticalschwingungen von starren Körpern auf dem Baugrunde, Acta Technica, Rocnik 2, Nakladatelstvi CSAV, Praha II, CSR, 1957, pp. 365-409 and 456-492.
6. Novák, M., The Vibrations of Massive Foundations on Soil, International Association of Bridge and Structural Engineering, XX, 1960, pp. 263-281.
7. Ehlers, G., Der Baugrund als Federung in schwingenden Systemen, Beton und Eisen, 41, 1942, pp. 197-203.
8. Pauw, A., A Dynamic Analogy for Foundation-Soil Systems, Symposium on Dynamic Testing of Soils, ASTM Special Technical Publication No. 156, 1953, pp. 90-112.
9. Balakrishna Rao, H. A. and Nagaraj, C. N., A New Method for Predicting the Natural Frequency of Foundation-Soil Systems, The Structural Engineer, 38, 1960, pp. 310-316.
10. Bernhard, R. K. and Finelli, J., Pilot Studies on Soil Dynamics, Symposium on Dynamic Testing of Soils, ASTM Special Technical Publication No. 156, 1953, pp. 211-253.
11. Timoshenko, S. and Goodier, J. N., *Theory of Elasticity*, McGraw-Hill Book Company, Inc., 1951.
12. Lorenz, H., Neue Ergebnisse der dynamischen Baugrunduntersuchung, Zeitschrift Verein Deutscher Ingenieure, 79, 1934, pp. 379-385.
13. Heukelom, W., Analysis of Dynamic Deflexions of Soils and Pavements, Geotechnique, XI, 1961, pp. 224-243.

14. Heukelom, W., Investigation of the Mechanical Elements Governing the Stiffness of Road Constructions, Koninklijke/Shell-Laboratorium, Amsterdam, Report No. M-23020, 1957.
15. Weissmann, G. F. and Hart, R. R., Damping Capacity of Some Granular Soils, ASTM Special Techn. Publication No. 305, 1961, pp. 45–54.
16. Barkan, D. D., *Dynamics of Bases and Foundations*, McGraw-Hill Book Company, Inc., 1960.
17. Weissmann, G. F., Determination of the Coefficient of Subgrade Soil Reaction, Materials Research and Standards, *5*, No. 2, 1965, pp. 71–75.
18. Weissmann, G. F. and White, S. R., Small Angular Deflexions of Rigid Foundations, Geotechnique, *11*, 1961, pp. 186–201.
19. Wilson, S. D. and Sibley, E. A., Ground Displacements Resulting from Air-Blast Loadings, Proc. ASCE, *88*, No. SM6, 1962, pp. 1–32.
20. Whitman, R. V., Effects of Viscosity and Inelasticity upon Stress Waves through Confined Soil, Shock, Vibration and Associated Environments, Bulletin No. 32, August, 1963, Protective Construction, Part III, pp. 107–123.
21. Fry, Z. B., Development and Evaluation of Soil Bearing Capacity Foundations of Structures; Field Vibratory Tests Data, Waterways Experiment Station, Technical Report No. 3-632, Report 1, 1963.
22. Converse, F. J., Compaction of Sand at Resonance Frequency, Symposium on Dynamic Testing of Soils, ASTM Spec. Techn. Publication No. 156. 1953, pp. 124–137.
23. Lorenz, H., *Grundbau Dynamik*, Springer Verlag, 1960.
24. Tschebotarioff, G. P., Performance Records of Engine Foundations, ASTM Spec. Techn. Publication No. 156, 1953, pp. 163–173.
25. Tschebotarioff, G. P., *Soil-Mechanics, Foundations, and Earth Structures*, McGraw-Hill Book Company, Inc., 1951.

Contributors To This Issue

R. W. FRIIS, B.S.E.E., 1930, University of Minnesota; Bell Telephone Laboratories, 1930—. He was first concerned with the development of HF and UHF radio equipment for use in the Bell System to span natural barriers. Before and during World War II he took part in the early development and evaluation of several types of microwave radar designed for fire control and gun laying applications and the development of radar counter measure transmitters. Since 1945 he has been concerned with the development and design of various microwave radio relay systems beginning with the initial New York-Boston TD(X) experimental system. He is presently Head, Microwave Equipment Department, and is a Registered Professional Engineer-New York. Senior Member, IEEE.

J. JAN JANSEN, SB and SM, 1939, Massachusetts Institute of Technology; Bell Telephone Laboratories 1939—. His early assignments included circuit design work for the television terminals for the L1 coaxial system and the A1 video transmission system. During World War II he was engaged in military work for several airborne radar systems. After the war he participated in the design of the A2A video system and the television terminals for the L3 coaxial system. Since 1957 he has headed groups at the Merrimack Valley Laboratory in the development of the L3 system, the T1 carrier system, and microwave radio systems. Member, Sigma Xi, Eta Kappa Nu, IEEE.

R. M. JENSEN, B.S. in E.E., 1937, Purdue University; Bell Telephone Laboratories, 1937—. He was first engaged in development of audio equipment and subsequently worked in the Quality Assurance Department. In 1938 he was assigned to development of L-type multiplex networks and during World War II he was concerned with the development of tuned amplifiers, coaxial filters, and crystal-controlled oscillators. After the war he resumed development of multiplex networks and in 1956 was assigned to the development of microwave networks and became a supervisor in 1959. Since 1964 he has supervised a group

engaged in equipment design of TL-2/TM-1 Radio Relay, TD-3 Radio Relay, and 3A FM Terminals. Member, Sigma Pi Sigma.

HAROLD T. KING, B.A., 1930, Harvard University; Bell Telephone Laboratories, 1930—. Mr. King was involved in the development of the early Bell System carrier systems. He served five years in the U.S. Army during World War II attaining the rank of Lt. Colonel. Upon his return to the Laboratories, Mr. King was engaged in the development of the N and O carrier systems, then supervised a group in the development of the T1 System. At present, he supervises a group in the development of short-haul microwave radio systems.

E. A. J. MARCATILI, Aeronautical Engineer, 1947, and E.E., 1948, University of Cordoba (Argentina); research staff, University of Cordoba, 1947–54; Bell Telephone Laboratories, 1954—. He has been engaged in theory and design of filters in multimode waveguides and in waveguide systems research. More recently he has concentrated in the study of optical transmission media. Member, IEEE.

J. B. O'NEAL, JR., B.E.E., 1957, Georgia Institute of Technology; M.E.E., 1960, University of South Carolina; Ph.D., 1963, University of Florida; Bell Telephone Laboratories, 1964—. While employed at the Martin Company in 1959–60, he worked on random access communications systems. He is currently engaged in studies to determine efficient coding techniques for converting analog television signals into digital form. Member, IEEE, Eta Kappa Nu; associate member, Sigma Xi.

ATTILIO J. RAINAL, University of Alaska, University of Dayton, 1950–52; B.S.E.Sc., 1956, Pennsylvania State University; M.S.E.E., 1959, Drexel Institute of Technology; DR. ENG., 1963, Johns Hopkins University; Bell Telephone Laboratories, 1964–. He has been engaged in research on noise theory with application to radar theory. Member, Tau Beta Pi, Eta Kappa Nu, Sigma Tau, Pi Mu Epsilon, Sigma Xi, IEEE.

J. E. SAVAGE, S.B., S.M., 1962 and Ph.D., 1965, Massachusetts Institute of Technology; Bell Telephone Laboratories, 1965—. Mr. Savage has been concerned with problems in coding and communication theory. Member, Tau Beta Pi, Sigma Xi, Eta Kappa Nu, IEEE.

GERD F. WEISSMANN, Dipl.-Ing. in civil eng. 1950, Technical University of Berlin; M.S. eng. mechanics, 1953, Pennsylvania State University; Bell Telephone Laboratories, 1953—. Mr. Weissmann's work at the Laboratories has been in soil mechanics, engineering mechanics, and materials properties and testing. He is the author or coauthor of several papers in these fields. Member, Society for Experimental Stress Analysis, ASTM Committee D-18 on Soils and Rocks for Engineering Purposes, American Society of Civil Engineers.